Mortars: a complex material in cultural heritage

A multi-analytical procedure to characterize historical mortars

by
Dr. Valentina Brunello

Supervisor
Prof. Laura Rampazzi

Co-supervisors
Dr. Cristina Corti
Dr. Antonio Sansonetti

Department of Science and High Technology (DiSAT)
Ph.D. Course in Chemical and Environmental Sciences
XXXII Cycle

UNIVERSITÀ DEGLI STUDI
DELL'INSUBRIA

UNIVERSITÀ DEGLI STUDI
DELL'INSUBRIA

Department of Science and High Technology (DiSAT)
Ph.D. Course in Chemical and Environmental Sciences
XXXII Cycle

Mortars: a complex material in cultural heritage

A multi-analytical procedure to characterize historical mortars

by
Dr. Valentina Brunello
730251

Supervisor
Prof. Laura Rampazzi

Co-supervisors
Dr. Cristina Corti
Dr. Antonio Sansonetti

Progetto grafico di ©Valentina Brunello

INDEX

LIST OF ABBREVIATIONS AND SYMBOLS

3D	Three-dimensional
A	Aluminium oxide (Al_2O_3), or alumina
ATR	Attenuated total reflectance
AFt	$C_6A\hat{S}_3H_{32}$, sometimes with substitution of Fe with Al, and/or CO_3^{2-} with SO_4^{2-} (mineralogy: calcium trisulfoaluminate hydrate or ettringite)
BSE	Backscattered electron
C	Calcium oxide (CaO) or lime
C_3S	Tricalcium silicate ($3CaO\ SiO_2$) (mineralogy: alite)
C_2S	Dicalcium silicate ($2CaO\ SiO_2$) (mineralogy: belite or larnite)
C_3A	Tricalcium aluminate ($3CaO\ Al_2O_3$) (mineralogy: celite)
C_4AF	Tetracalcium alumino ferrite ($4CaO\ Al_2O_3\ Fe_2O_3$) (mineralogy: brownmillerite)
CCN	Cement chemist notation
$CaCO_3$	Calcium carbonate (mineralogy: calcite)
$Ca(OH)_2$	Calcium hydroxide (mineralogy: portlandite)
C-A-H	Calcium aluminate hydrate
$CaSO_4\ 2H_2O$	Calcium sulfate dihydrate (mineralogy: gypsum)
$CaSO_4\ 0.5H_2O$	Calcium sulfate hemihydrate (mineralogy: bassanite)
$CaSO_4$	Calcium sulfate (anhydrous state) (mineralogy: anhydrite)
CEM I	Cement Portland type I (raw material)
CEM IV	Cement pozzolanic type IV (raw material)
CP	Cross polarization
CSH	Calcium silicate hydrate
DSC	Differential scanning calorimetry
EDS	Energy dispersive spectroscopy
ER-FTIR	External reflection Fourier transform infrared spectroscopy
ESEM	Environmental scanning electron microscope
F	Iron oxide (Fe_2O_3)
FTIR	Fourier transform infrared spectroscopy
LA-ICP-MS	Laser ablation - inductively coupled plasma - mass spectrometry
MAS	Magic angle spinning
MIP	Mercury intrusion porosimetry
NHL 3.5	Natural hydraulic lime type 3.5
NMR	Nuclear magnetic resonance
ppl	Plane polarized light
PXRD	Powder X-ray diffraction

S	Silicon dioxide (SiO_2) or silica
$\hat{S}$	Sulfur trioxide (SO_3)
SE	Secondary electrons
TG	Thermogravimetry
TXRF	Total reflection X-ray fluorescence
xpl	Cross polarized light
XRF	X-ray fluorescence
µCT	Micro computed tomography
µFTIR	Micro Fourier transform infrared spectroscopy

ABSTRACT AND STRUCTURE OF THE THESIS

This thesis deals with the identification of mortars composition in a cultural and historical context. In detail, the main concern was to collect information for proposing an analytical procedure able to define the mortar typology, balancing advantages, drawbacks, time and costs. In addition, several new techniques have been recently introduced in conservation science and the aim of this research is also to consider these new competences too.

To understand the interactions between components of mortars, in Chapter 1 a general overview of the subject is given with a description of the materials and of the historical background, based on the review of the large bibliography taken into account. In Chapter 2 the methods used for the preparation of the model samples and the final composition are explained. Moreover, the analytical techniques used in this research (optical microscopy and petrographic analysis, powder X-ray diffraction, infrared spectroscopy, Raman spectroscopy, environmental scanning electron microscopy, thermal analysis, mercury intrusion porosimetry and computed tomography) are described, specifying the setting of the instruments.
In Chapter 3 the results of the characterization of the raw materials and of the model samples are shown, the most meaningful results are shown for each technique. The discussion of the experimental data is presented in Chapter 4, and some analytical protocols are proposed, described and explained. In the last chapter, Chapter 5, the conclusions and the future development of this research are underlined.

CHAPTER 1

Introduction

Building materials are used both in historical and in contemporary architecture. They are an important element of the landscape we live, and witnessed our history and for these reasons, it is important to study them for better conservation of the architectural objects they comprise. They could be, in the meanwhile, very simple but contain, in reality, complex compositional and micro-structural issues.

Building materials may be divided into two main groups: natural and artificial. The first refers to materials that are used as they are found in nature (e.g. stones); the second one refers to materials produced by humans from a transformational process using natural materials by which they assume different consistencies and functions from the raw materials, examples are ceramics, mortars, plasters and stucco works. The studies of past recipes used to produce artificial building materials could improve techniques used in understanding of new material technologies. In this work the term "recipe" will be used to denote mix proportions and used in the preparation of the artificial building material.

In this research our attention was focused on mortar materials. According to "UNI 10924 (2001), *Malte per elementi costruttivi e decorativi: classificazione e terminologia*", mortars are "a mixture of inorganic or organic binders, predominantly fine aggregates, water and in some cases organic and/or inorganic additives (or mixture of binder only and water). They are mixed in proportions such as to give to the mixture, in the fresh state a suitable workability and, in the hardened state adequate physical characteristics (porosity, water permeability etc.), mechanical characteristics (strength, deformability, adhesion, etc.), appearance, and durability."

In order to create restoration mortars which are as compatible as possible with the original, both the composition of a mortar and the knowledge of the construction techniques used in the past is required to give accurate historical-technological information. The case studies require the analysis of the composition of the mortars for various reasons, for example, for archeological interest in classifying samples from various sites and historical stratigraphy or to recall the history of the samples and sites analysed. It is important to know the technology in a specific historical period, geographic area and culture and for comparing the past knowledge with the new ones. The identification of the original composition is important in the study of original materials or for restoration purposes, for the restoration objective the composition of mortars is a key point in order to design an effective restoration plan and the removal of recent materials if it is necessary. The identification of the mortar composition is important to identify the state of conservation of mortars and decay phenomena and to plan the proper analytical campaign and conservation work.

The composition of mortars is extremely variable, depending on the historical period and on the geographical area (different raw materials); thus the identification of the mixture presents considerable challenges. In fact, the recipes were traditionally not written, but they were usually transmitted from one worker to another. Very often in the past the recipes were defined by best practice derived using the raw

materials present in the region. Even though the recipes were sometimes written in manuals, a lot of misunderstanding in the proportion used or in the choice of the terminology has been created, because the authors remained generic: commonly just a rough ratio of the materials was indicated. Coming to contemporary uses, more specific recipes can be found, especially in the case of mortars modern cement.
Thanks to research studies, we have a wide knowledge of the various compositions that may be found in historical samples, but we do not have the certainty of the original composition. In literature several case studies have shown how the composition could vary influencing the different techniques and analytical procedures used to detect the material composition. An important and critical point regards the absence of a standardized approach allowing a more precise comparison among the results. Several studies use distinct techniques and often the results are not comparable each others because of the different approach and method used.
Since building materials are usually in contact with the atmosphere, the decay due to time and weathering processes may alter the original composition, introducing some newly formed compounds. Water, wind, pollution, biological agents and other causes may lead to chemical and physical reactions and then to material alteration. All these phenomena make the recovering of the original composition more difficult, especially in case of mortars.
The core idea of this project was inspired by the need for robust and reliable analytical methods for the characterisation of mortars. In particular, the main concern was to collect information on the type of analytical techniques that had been used, the preparation of the samples and the results elaboration. In addition, new instruments are now available to conservation science, which could improve the knowledge we have of historical mortars. This research investigates the different performance of various techniques applied to the characterization of mortar materials. In order to test the analytical techniques, and to create an analytical protocol a series of model mortar samples was designed, prepared using known raw materials. A wide bibliographical search has been carried out in order to collect the main and the most widespread ancient and modern recipes of mortars preparation. For this purpose several manuals and articles have been taken into account. Based on these results and on the recipes found, the mortars specimens have been designed and prepared. Finding pure and suitable raw materials was a critical point, as they are available only from few specialized building materials suppliers.

The binders chosen were:
- lime putty,
- hydrated lime,
- gypsum.

These materials have been selected because they are the most common mortar binders used in the past, and/or they are still used in restoration practice. Two cement binders have also been chosen (Portland cement CEM I and pozzolanic cement CEM IV) and natural hydraulic lime 3.5. Portland cement was selected because it is the most common commercially used cement, while pozzolanic cement was chosen for its peculiar composition, whose performances in mortar mixes could be of some interest in restoration field. On the other hand natural hydraulic lime 3.5 is one of the commercial natural hydraulic binders available nowadays. Two kinds of aggregate have been then selected: quartz and carbonate sand, the most widespread types in modern and past technologies. Furthermore, a particular attention to the influence

of the aggregate composition in the analytical results was considered, thus also for this reason these two types of aggregate were used. Our need to use a pure calcite aggregate is due to the need to exclude the presence of Si from the aggregate from the possible results, on the contrary for the same reason we used almost pure quartz sand without carbonate phases. The proportions used in the project have been chosen among the literature and used in proportions weight/weight in order to be able to reproduce the mixtures in the future with the same ratios.

In this study, different techniques have been compared in order to evaluate their advantages and drawbacks when applied to these materials. A specific focus was given to the new nondestructive analysis, like portable infrared spectroscopy. The main advantage, in the use of portable instruments, lies in the possibility to characterize the artwork surface in case of difficult or impossible sampling.

In literature some studies have been done on an analytical method for mortars' characterization, but they proved to be too ambiguous, often indicating only which type of analysis could be carried out without suggesting a procedure. Moreover, these attempts to create protocols generally do not consider the new technologies. Therefore, within this project we want to explore in depth the potentiality of analytical chemistry and suggest a protocol for mortar analysis, testing various sets of specimens of tailor-made mixtures, considering the different response of each technique to standard specimens and testing the results on samples of historical materials.

One of the main problems in mortars analysis is the identification of the binders' composition and of the aggregates. The aggregate components are easier to characterize, even if some analytical uncertainty could arise when the analyst is called to distinguish very fine particles, due to the influence of the surrounding binder phase and depending on the analytical technique used. The identification of the aggregate is easier with microscopical analysis thanks to the visualization, while in PXRD or FTIR, where all the components are mixed together, it is harder.

Consequently, it is hard to define the composition of the two components. In fact, the most common procedure to separate the binder from the aggregate consists in heating the sample or in an acid attack. In the first case, we cannot be sure that this method manages to separate also the smallest grains, while in the second scenario, if we have a carbonate aggregate, the acid digestion will dissolve also this component. If the samples are ground into a powder in analysis as PXRD and FTIR, then the discrimination between the signals from the aggregate and the ones from the binder becomes more difficult. Other analyses such as optical and electron microscopies that work at different spatial resolutions could help with the identification of these components. However these analyses are limited by size of sample field of view.

Another problem is the identification of hydraulic phases present in a sample of mortar. In fact, some of these phases could be classified as gel (ie. not crystalline), hence it is not possible to identify them with the traditional powder X-ray diffraction; however with the use of other techniques, their identification could be ambiguous, for example Raman spectroscopy on cements could produce fluorescence.

Another significant problem about mortar study is due to the likelihood of mixed mortars analysis. In the past, and also in some restoration practice, several binders could be used mixed together, being still used now to improve the properties of the materials. Some examples regard the mortars in which binders are composed by lime and gypsum or by lime and cement. From an analytical point of view, this is a problem concerning the identification of the overall composition.

According to the international standards, the protocols for the analysis of historical mortars usually in-

clude chemical procedures that involve samples dissolution and therefore a destructive approach, ruling out the possibility of using the samples for further studies.
This is an important point due to the usual small size of the available historical samples; in order to get a suitable identification of all the components the best procedure involves performing different analyses with different instruments on the same sample to gather as much information as possible. Moreover, some studies have shown how it is difficult to interpret wet chemistry results on mortars if previous knowledge of the type of mortars is lacking, since using only the elemental composition the precise identification of the type of mortar is hard.
For a better identification of each of the components of the materials it is important to design precisely the analytical sequence, which allows creating a methodological approach choosing the best succession of techniques in order to use and to optimize the results, the time and the costs.
Because of these reasons and of the ambiguity in the analysis of mortars still present, we attempted an implementation proposing a series of model samples with known composition studied with various analytical techniques. By doing this we want to test the response of each technique to the different samples compositions. In the following paragraphs, several approaches in the analysis of the different types of mortars will be discussed, including microscopy, spectroscopy, and mineralogical studies.

Overview of mortar materials

Mortar is made of a mixture of a binder and aggregate and sometimes additives. Binder materials are substances used to compact and join the inert component. The aggregate has the double function to prevent the binder from cracking during the drying process and to favor the evaporation of water from the mortar. The aggregate fraction is usually made of quartz or carbonate sand (or combination dominated by these materials) [1,2].

There are different types of mortar, commonly distinguished as air or hydraulic mortars, depending on the type of binder:

- aerial binders that harden in the presence of air (lime or gypsum);
- hydraulic binders that can harden both in presence of air or water (natural hydraulic lime, cements).

Aerial binders

Gypsum

Bassanite, that is the partially unhydrated phase of gypsum, is usually produced by the heating of gypsum rock mineral. When gypsum ($CaSO_4$ $2H_2O$) is heated at 130°C, it begins to lose part of its water and transforms into semi-hydrated $CaSO_4$ $½H_2O$ (bassanite); under these conditions it can be rehydrated easily. If heated above 200°C, it completely loses the water molecules and turns into anhydrite, which does not easily rehydrate.
The gypsum firing process allows different materials to be obtained, depending on the heating temperature. Two allotropic varieties are known for semi-hydrate gypsum, a rapid-setting α and a slow-setting β [3].

Gypsum behaviour between 128°C and 163°C:

$CaSO_4$ $2H_2O$ -> $CaSO_4$ $½H_2O$ + 3 $½H_2O$ at 128°C

$CaSO_4$ $½H_2O$ -> $CaSO_4$ + $½H_2O$ at 163°C

Ready-to-use plaster is obtained at temperatures between 120-180°C [mainly composed of bassanite ($CaSO_4$ $½H_2O$)], and commonly employed in stuccos and models. At a temperature between 200-250°C, anhydrite with a slower setting is obtained, mainly used for masonry.
Over 500°C-600°C calcium sulphate becomes insoluble in water due to a partial superficial vitrification of the particles. The product is called "dead chalk" (or "overcooked plaster" or "burnt plaster") [3], and reacts with water or sets very slowly. The dead chalk is called insoluble anhydrite or anhydrite β. Instead, anhydrite obtained after cooking at temperatures around 163°C is called anhydrite α and tends to hydrate itself, being an unstable form.
When the temperature reaches 600°C, the plaster is completely dehydrated and it requires a long setting time. At temperatures between 800-1000°C another type of gypsum is obtained, mainly composed of $CaSO_4$, which is similar to anhydrite but with a very slow setting. Over 1000°C there is a partial dissociation of the insoluble anhydrous calcium sulfate to produce calcium oxide or quicklime and basic calcium sulfate [3–5].
When water is added to bassanite the re-hydration process takes place in order to form again gypsum.

$CaSO_4$ $½H_2O$ + 3 ½ H_2O -> $CaSO_4$ $2H_2O$

Lime

The most commonly used air binder is calcium hydroxide $Ca(OH)_2$ (slaked lime). It is derived from the calcination of carbonate rocks (limestone, lime marble or calcareous shell fragments) at a temperature not exceeding 850°C. CaO (lime oxide), which is commonly called quicklime, is obtained by calcination at about 1000°C of limestone:

$CaCO_3 \rightarrow CaO + CO_2$

The quicklime (CaO) is then hydrated to obtain the slaked lime (calcium hydroxide):
$CaO + H_2O \rightarrow Ca(OH)_2$

Once the lime is slaked (slaked lime), it can be mixed with aggregates (such as cocci, sand, etc…) to improve its properties. Indeed, without these aggregates, lime laid in thick layers is cracked during the drying process, due to volume reduction, thereby losing its adhesive properties.
During the wet slaking process quicklime is matured under water to obtain a very plastic material, rich in H_2O, which is called lime putty. For as long as storage lasts, the crystals of calcium hydroxide become smaller and finer.
On the contrary, during the dry slaking only the amount of water strictly necessary for hydrating is added to the lime and a floury product is obtained.
After the slaking process, two phases occur: a period of setting, in which the dough loses the first fluidity and becomes the desired shape, followed by later hardening, when the mass progressively increases its mechanical strength as the reaction between calcium hydroxide and atmospheric carbon anhydride leads to the formation of calcium carbonate and water:

$Ca(OH)_2 + CO_2 \rightarrow CaCO_3 + H_2O$

The process is called carbonation and is very slow. The rate of reaction depends on the size and shape of the grains and is also influenced by the type of limestone and the presence of impurities in the materials [4–6].

Hydraulic binders

Natural hydraulic lime (NHL) and cement

Natural hydraulic lime (NHL) is a lime binder with hydraulic properties obtained by burning siliceous or argillaceous limestone or calcareous marls at temperatures below 800-1200°C. After the heating, the product is impure quicklime that also contains hydraulic phases. The hydraulic phases (Ca-silicate and aluminate phase) give water resistance to the binder. The main mineralogical phases are: $Ca(OH)_2$, C_2S, amorphous aluminate and un-reactive phases.
Hydraulic mortars based on aerial lime are complex systems, whose properties are known from ancient times. The Romans needed mortars that could set in the presence of water too and thus introduced the use of Pozzuoli's volcanic ash (i.e. Roman cement). This was taken from the north part of the Naples bay, in the volcanic area of the Flegrei fields and Vesuvio. The ash was added to the lime air, obtaining a hydraulic lime or also called pozzolanic lime mortars. The ash is very rich in alumina Al_2O_3 and silicates, which react with lime hydroxide giving water resistant products. A similar transformation is obtained by mixing aerial lime with the finely ground materials as ceramics (i.e. terracotta, cocciopesto) contain a lot of quartz and minerals, such as aluminum silicates, which give hydraulic properties [4,5,7,8].

Portland cement was the first cement produced in the mid-1840s in England. The name "Portland" was given because of the supposed similarity with white or pale/gray limestone quarried in the Island of Portland. In the first half of 19th century the cement was burnt in shaft kilns and then cooled slowly, but from the 20th century rotary kilns were used. In modern Portland cement, whose composition is different from the first Portland cement, a percentage of gypsum (about 5%) is added to control the setting. The EN 197-1 normative defines the different type of cements that are commercially available.
In modern cements the amount of clinker (clinker is the name of the results of the heating of the limestones and clay minerals over 1450°C) has decreased and been substituted with blast furnace, fly ash, or micro-silica, to increase the performance of the cements at lower price. Moreover, these materials could reduce CO_2 emissions that occur in the clinker production. Portland cement is made by the mixture, the grinding and the heating of limestone and clay minerals in rotary kilns at a temperature of 1450-1550°C. A partial fusion occurs and clinker nodules are produced. Then the clinker is finely ground and mixed with calcium sulphate. Table 1 describes the cement chemist notation, that is used to express chemical composition [9].

CCN	formula	name
C	CaO	Calcium oxide, or lime
S	SiO_2	Silicon dioxide, or silica
A	Al_2O_3	Aluminium oxide, or alumina
F	Fe_2O_3	Iron oxide
T	TiO_2	Titanium dioxide, or titania
M	MgO	Magnesium oxide, or periclase
K	K_2O	Potassium oxide
N	Na_2O	Sodium oxide
H	H_2O	Water
Ĉ	CO_2	Carbon dioxide
Ŝ	SO_3	Sulfur trioxide
P	P_2O_5	Phosphorus hemi-pentoxide

Table 1. The table describes the cement chemist notation (CCN)..

The main unhydrated cement phases are alite ($3CaO\ SiO_2$) (C_3S) 50-70%, belite ($2CaO\ SiO_2$) (C_2S) 15-30%, tricalcium aluminate ($3CaO\ Al_2O_3$) (C_3A) 5-10% and ferrite ($4CaO\ Al_2O_3\ Fe_2O_3$) (tetracalcium alumino ferrite C_4AF) 5-10% and gypsum ($CaSO_4\ 2H_2O$) ($C\hat{S}H_2$) 5% (table 2).

CNN	formula	name	mineral phase
C_3S	$3CaO\ SiO_2$	Tricalcium silicate	Alite/Hatrurite
C_2S	$2CaO\ SiO_2$	Dicalcium silicate	Belite/Larnite
C_3A	$3CaO\ Al_2O_3$	Tricalcium aluminate	Aluminate or Celite
C_4AF	$4CaO\ Al_2O_3\ Fe_2O_3$	Tetracalcium alumino ferrite	Ferrite/Brownmillerite

Table 2. The main unhydrated cement minerals.

When water is added to cement many reactions take place. In the first minutes of hydration ettringite (CCN) ($C_6A\hat{S}_3H_{32}$) ($Ca_6Al_2S_3O_{18}$ $32H_2O$) forms, followed by portlandite (*CH*) ($Ca(OH)_2$). Later, the hydration of calcium silicates takes place, forming different small crystals of calcium silicates hydrates indicated to as (CCN) *C-S-H*. The crystal structure of calcium silicates hydrates is not well resolved but usually *C-S-H* is similar to the following crystals: tobermorite ($Ca_5H_2(Si_3O_9)_2$ $4H_2O$)) or jennite ($Ca_9(Si_3O_9)_2(OH)_6$ $8H_2O$) (table 3 and 4).

$2C_3S$	+	$6H$	->	$C_3S_2H_3$ or (*C-S-H*)	+	3 *CH*
$2Ca_3$ SiO_2	+	$6H_2O$	->	$Ca_3Si_2O_4(OH)_6$	+	$3Ca(OH)_2$
alite	+	water	->	(*C-S-H*) gel phase tobermorite	+	portlandite

Table 3. Description of alite hydration process. Legenda. First row: CCN notation. Second row: chemical formula and mineral name.

$2C_2S$	+	$4H$	->	$C_3S_2H_3$ or (*C-S-H*)	+	*CH*
$2Ca_2$ SiO_2	+	$4H_2O$	->	$Ca_3Si_2O_4(OH)_6$	+	$Ca(OH)_2$
belite	+	water	->	(*C-S-H*) gel phase tobermorite	+	portlandite

Table 4. Description of belite hydration process. Legenda. First row: CCN notation. Second row: chemical formula and mineral name.

In the absence of gypsum in the cement paste, the setting and hardening would take place too quickly; the tricalcium aluminate in the presence of water tends to hydrate immediately with the formation of a gel around the C_3A crystals. After that, the gel becomes hexagonal crystals (C_2AH_6 and C_4AH_{19}), and then it transforms in the cubic C_3AH_6. Gypsum is added to the cement clinker to moderate the reaction in the cement paste. During the hydration (table 5), gypsum reacts quickly with C_3A forming the ettringite phase on the surface of C_3A crystals which retards the hydration. This ettringite is commonly termed primary ettringite or *AFt* [9–12].

C_3A	+	$3C\hat{S}H_2$		+	$26H$	->	$C_6A\hat{S}_3$ $32H$
3CaO Al_2O_3	+	$3CaSO_4$ $2H_2O$		+	$26H_2O$	->	$Ca_6Al_2S_3O_{18}$ $32H_2O$
tricalcium aluminate	+	gypsum		+	water	->	ettringite

Table 5. Description of the formation of ettringite. Legenda. First row: CCN notation. Second row: chemical formula and mineral name.

Also *AFm* (calcium monosulfoaluminate) phases are hydration products of calcium aluminate phases. The general formula for *AFm* phases is $[Ca_2(Al,Fe)(OH)_6]$ X xH_2O, where X stands for a charged anion (OH^-, SO_4^{2-} or CO_3^{-2}). AFm phase could be schematically represented as sheets of $M(OH)_6$ (octahedral ions like brucite or portlandite) with 1/3 of M^{2+} replaced by a trivalent ion like Al or Fe, giving to the layers a strong positive charge that creates a larger space between the layers and attracts anions and water molecules. Common phases are the group of C_4AH_x, $C_4A\hat{S}H_x$ [9–12]. C_4AF hydration reaction is similar to that of C_3A and the reactivity is also influenced by the presence of gypsum, which slows down the hydration.

Mixed mortars

Mixed mortars are a type of mortars in which different binders are used, these being mixed together to improve the properties of the material. The variability of mixed mortars is shown in many manuals and case studies [3,8,12].

For example, gypsum and aerial lime were mixed together in equal proportion with the addition of sand to use this mixture in different uses. Manuals like Turco's manual [3] underline how the addition of gypsum to lime increases the speed of hardening of lime, and also lends higher adherence to the mortar if compared to a mortar with lime alone [3,13]. Mixing gypsum and hydraulic lime in different proportion is used to improve the setting time and the resistance to decay caused by humidity. Another example of mixed mortars is represented by the mixture of aerial and hydraulic lime to obtain a mortar that can set also in presence of humidity [12]. Later with the discovery of cement and its wide use, the practice of mixing cement binders with lime became common where the masonry is exposed to rain or humidity [8,12].

References

[1] R.P.J. van Hees, L. Binda, I. Papayianni, Toumbakari, Characterisation and damage analysis of old mortars, Mater. Struct. 37 (2004) 644–648. doi:10.1007/BF02483293.

[2] L. Binda, G. Baronio, S.E.D. of the P. di Milano, Studies on Mortars Sampled from Historic Buildings: Selected Papers 1983 - 1999, Structural Engineering Department of the Politecnico di Milano, 1983.

[3] A. Turco, Il gesso, Hoepli, 1990.

[4] C. Montagni, I leganti, in: UTET (Ed.), Mater. per Restauro e La Manutenzione, 2000: pp. 177–190.

[5] C. Arcolao, Le ricette del restauro: malte, intonaci, stucchi dal XV al XIX secolo, Marsilio Editori, 1998.

[6] A. Rattazzi, Conosci il grassello di calce? Origine, produzione e impiego del grassello in architettura, nell'arte e nel restauro, Edicom, 2007. http://books.google.es/books?id=4zq_HwAACAAJ.

[7] Ente italiano di normazione, UNI EN 459-1:2015 Building lime - Part 1: Definitions, specifications and conformity criteria, (2015).

[8] U. Menicali, I materiali per l'edilizia storica. Tecnologia e impiego dei materiali tradizionali, Roma, 1992.

[9] H.F.W. Taylor, Cement chemistry. 2nd ed., 1997. doi:10.1016/S0958-9465(98)00023-7.

[10] T. Matschei, B. Lothenbach, F.P. Glasser, The AFm phase in Portland cement, Cem. Concr. Res. 37 (2007) 118–130. doi:10.1016/j.cemconres.2006.10.010.

[11] H.R. Wenk, A. Bulakh, Minerals: Their Constitution and Origin, Cambridge University Press, 2004. https://books.google.it/books?id=IcH2liK0JOYC.

[12] E. Pecchioni, F. Fratini, E. Cantisani, Le Malte Antiche e Moderne tra Tradizione ed Innovazione, Pàtron, Bologna, 2008.

[13] C. Genestar, C. Pons, Ancient covering plaster mortars from several convents and Islamic and Gothic palaces in Palma de Mallorca (Spain). Analytical characterisation, J. Cult. Herit. 4 (2003) 291–298. doi:10.1016/j.culher.2003.02.001.

State of the art

In order to follow our objective a first level of literature was analysed searching for previous attempts in creating a shared procedure to analyze mortars. The attention was especially focused on the different analytical approach with the aim to identify the most representative analysis of the overall composition and features of the samples [1–9]. Several attempts to standardise and create an analytical protocol have been proposed in literature [1,3,4,8,10–12].

For example RILEM TC 203-RHM [1], focused on repair mortars, shows how to analyse those already existing on buildings, and gives general instructions on how to make a good reintegration mortar. RILEM, in their technical report, considered the environmental conditions, the classification of decay patterns and other parameters essential to build a reintegration mortar, such as colour, porosity pattern, and the size distribution of the aggregate.

RILEM TC 167-COM [12], gives an ample overview on the methodologies of characterisation of historic mortars. The report presents indications of the characteristic of old mortars in relation to their repair, then it presents different methods of characterisation: "in-situ visual analysis and practical sampling of historic mortars, mineralogical characterization of historic mortars, chemical characterization of historic mortars, mechanical tests on mortars and assemblages and porosity of mortars", and in the end it treats degradation processes and case of studies. They consider optical microscopy, scanning electron microscopy, X-ray diffraction and acid dissolution and wet chemistry techniques. They underline as the wet chemistry analysis, if used independently, lacks information. In this RILEM report also the porosity characterisation is considered. They report the criticism already underlined by Diamond, for MIP and present the other measurement for the specific surface like BET, tomography and NMR. Middendorf et al [13] give an interesting review of the microscopic analysis like SEM-EDS and WDS, thin section analysis, thermogravimetry, differential scanning calorimetry and X-ray diffraction on mortars and cements, in the second chapter (2.2) of RILEM TC 167-COM "Characterisation of Old Mortars with Respect to Their Repair". In this review, thanks to some examples from the case studies, they also proposed a flow chart similar to the one made by Alessandrini [11] and Veiga et al [4] in which a general approach to the analysis of mortars and cements is suggested and they explains schematically which type of information could be obtained from each technique. He focused mainly on microscopy analysis (SEM-EDX), TG-DSC and separation of binder from the aggregate. In the second chapter (2.3), Middendorf et al. concentrate also on chemical characterisation of historical mortars [3] focusing on elemental composition in destructive way for the sample, like dissolution, extractions, heat treatments, etc.. In RILEM TC-167 the mechanical tests were also taken into account, both on site and in laboratory, but a big restriction of the application of mechanical tests on historical mortars is the small dimensions of the samples taken from historical buildings, which limit the applicable analyses.

Normal 27/88 [14], in 1988 suggested a general procedure to characterize mortars by means of analytical techniques. The Normal committee suggested the mechanical separation between binder and aggregate and their characterisation with XRD, infrared spectroscopy, DTA and thermogravimetry, but Normal commission did not consider the difficulties and the problems that this separation can lead to.

Moreover, they suggested the preparation of thin sections or cross sections but the SEM analysis have been recommended only on these last ones. Furthermore, this protocol lacks information on the analytical results and how these are useful to identify one type of mortar from another. In addition, with the new technology, other analyses could be added to the ones listed in this Standard.

Alessandrini et al. provided a flow chart to suggest which analyses could be performed and which information can be deduced by each technique. They differentiate between bulk analysis and powder analysis. They propose also a second flow chart where they introduce the analytical sequence for the chemical characterisation of a mortar, suggesting a series of extraction, filtration, and heat treatments. The first flow chart lacks in the mineralogical and chemical information that can define one type of mortar from an another, while the second flow chart is very specific but it shows only methods that dissolve the samples. In cultural heritage, due to the small samples, the loss of the sample could be a restriction in the choice of the analysis [11].

Another scheme of the sequence to identify the composition of ancient mortars is presented by Rosario Veiga et al. [4]. They suggest as the first step after sampling stereomicroscope observation, then XRD for the "nature of the components", TGA-DSC for the lime content, SEM-EDX for morphological components and deterioration and FTIR for the identification of the nature of the organic compounds. In parallel they suggest the use of wet chemistry analysis for the identification of soluble salts and to measure the grain size distribution. Several observations can be made on this scheme, first of all the preparation of thin sections requires a certain amount of sample that not always is possible to collect. Secondly XRD does not characterize each of the phases, as in the case of hydraulic compounds, these present problems, moreover SEM-EDX can also help in the identification of hydration/carbonation rims and also of the hydraulic compounds. Furthermore, FTIR can additionally identify inorganic compounds and not only the organic fraction. For what concerns the wet chemistry treatment suggested should be considered with care because these techniques require the dissolution of the samples, and in the case of historical mortars this is a restriction.

Goins et al. [8] underlined on one hand how the ASTM C114 (American Society for Testing and Materials) and the wet chemical tests exhibit the inability to distinguish the soluble silicates in cements and on the other hand they also evidenced that the acid digestion technique for the separation and analysis of aggregate could incur problems when the aggregate is partially or total composed by carbonate phases. The authors of this article claim that the X-ray fluorescence is a good alternative method for the identification of oxides and that these methods do not give the mineralogical composition of the material.

Van Balen et al. proposed [9] two methods for the identification of hydraulic binders. They focused on the comparison of the results with XRD and DTA/TGA analysis and the use of complementary procedures as the acid attacks in order to quantify soluble silica and they perform a pozzolanicity test. They do not consider the problem that in the case of mixed mortars; the signals of hydraulic phases could be weaker and not visible.

Martinet et al. [10] proposed a complementary methodology for mortar analysis, combining examination under optical microscope, thermogravimetric analysis, X-ray diffraction, SEM-EDX analysis with chemical analysis of the acid soluble fraction. They compare the results from the above-mentioned techniques and propose the use of specific software for determining the mortars composition.

Alvarez et al. [15] did a comparative analysis of different methods for the attack of mortars with silicate aggregate with diluted HCl. They compared the cold attack with the hot attack saying that the latter is more effective while the cold attack is suspected to be able to solubilize only a part of the binder.

The ASTM C114 standard [16] provide a series of test method to perform the chemical analysis of hydraulic cements. This standard refers only to wet chemistry methods to estimate each component of the cement like: silicon dioxide, ferric oxide, phosphorus pentoxide, titanium dioxide, aluminum oxide, calcium oxide, magnesium oxide, sulfur, and other oxides. Also the UNI 11088 [17], UNI 11089 [18] and UNI 11189 [19] establish the chemical procedure and the calculations that should be done for the identification of the chemical compounds. These procedures are time consuming and require a certain amount of samples that at the end of the analysis will be destructed, reducing the possibility to perform other analyses on the same samples. It is a destructive analysis that for cultural heritage samples could be a severe restriction. Moreover from the oxides it is not always easy to go back to the mineralogical composition of the mortar.

The second phase of the literature research was on the mix proportion and methods of past and modern mortars "recipes". Several manuals and scientific literature were examined, several case studies have shown how the composition could vary and the different ways and techniques that are used to detect the material composition. The main manuals of Leon Battista Alberti, Vitruvio, Plinio il Vecchio, Francesco Milizia, Andrea Palladio and many others have been considered in this study [20–29]. In these manuals a lot of misunderstanding emerged regarding the proportion used or in the use of the terminology. Usually just an estimated ratio of the materials was indicated. In our times, especially in the case of cements, a wide range of normative with well-defined proportions is present and also the methods to test the compositions are fully highlighted [30,31]. It is important to underline that the UNI EN 196-2, just cited, is applicable for cements without historical interest, because as the other norms for the mortars, it implies destructive analyses of the sample, based on wet chemistry. Also the results and the studies reported in the articles and case studies have been considered in the study of past recipes [32–45]. Some case studies are exemplified in the following paragraph, having chosen the most representative among the huge quantity present in literature. For example Elert et al. [32] focus their attention on lime mortars in the field of conservation of buildings. They take into consideration from the calcination of the raw materials until the re-carbonation of the lime, taking also into account the hydration of lime and the aging of lime putty Moropoulou et al. [33] explain, through a case study, the different mortar technologies analyzing them with mineralogical and chemical analysis.

A third phase of literature was examined to identify the analytical techniques applied to the characterization of mortars. Aerial mortars composed by hydrated lime, lime putty and gypsum mortars are usually identified using petrographic microscopy, X-ray diffraction, or with the help of other more detailed analytical techniques such as scanning electron microscopy (SEM), thermal analysis DSC, TG and FTIR. For hydraulic mortars such as natural hydraulic lime and cements the above mentioned techniques could be used, but also Raman spectroscopy and NMR have an important role according to literature.

Polarized light microscopy (petrographic microscopy) is one of the most common method of mortar analysis. Thin section observations are important because they give an optical visualization of the sample providing information on the structure and the minerals present in it and often used to analyze building materials and geological samples. This method requires a long and careful preparation in order to obtain

the correct thickness of the sample, which is required for this type of analysis. This technique exploits the optical properties of minerals when polarized light is passed through them in order to make easier the identification of minerals. Thanks to the optical analysis, the main minerals, the size, the dimensions and shape of the pores (spherical or irregular), aggregate grains and some information on binders can be identified. For this type of analysis, a certain amount of sample is necessary and for this reason its use is not always possible (especially on cultural heritage materials). Some unpublished research by "Forum calce" shows how the interpretation of thin sections could be difficult and strictly dependent by the operator [46]. The use of petrographic analysis are well documented application of microscopy techniques in the study of mortars mineralogical composition [2,33,55–64,47–54]. In his review, Elsen [2] clearly explains the different techniques like polarized light microscopy, polarization fluorescence microscopy, scanning electron microscope applied to mortars and cements. He also focuses on the different nature of the aggregates, binders and hydraulic additives giving a great deal of examples.

Several are the case studies regarding the application of thin section analysis on historical mortars and of their alterations [33,39,56,60,65,66]. Weber et al. [67] provide a complete overview on the microscopical methodologies for the identification of hydraulic binders in historical mortars. They explain a methodological approach from the preparation of the samples to their observation with stereo-microscope, polarizing microscopy and scanning electron microscopy.

In this research, polarized optical microscopy has been applied to mortars samples made with a single binder or on mixed mortars (with two binders); both types of mortars were made using two different types of aggregate (quartz-sand and carbonate-sand) in order to evaluate the influence of the aggregate in the analysis of mortars with known composition. The samples of mortars with aggregate and one single binder have been used as a reference and compared to the mortars with two binders. On these latter the possibility of distinguishing the presence of two mixed binders has been evaluated.

In the last decades this technique has been applied also to the analysis of cements [2,62,67–77] with good results thanks to the identification of cement unhydrated particles in the binder. Optical microscopy is usually employed in combination with scanning electron microscopy or environmental scanning electron microscopy, to confirm or study in depth the phases previously identified with optical microscopy at the highest possible resolution. This happens especially when cements are analyzed, like Pintér or Weber and others authors works [61,64,68,69,73,78–80] shown. In this study an environmental scanning electron microscope (ESEM) has been used: it allows analysing the samples without the need of a coating. The analyses have been performed mostly with back-scattered electrons (BSE). The production of back-scattered electrons is mainly linked to the atomic number of the atoms that constitute the sample, giving images with black/white contrast. The scanning electron microscope analysis has been used to investigate the samples at high resolution in order to evaluate the morphological differences between each mortar and their elemental compositions (EDS detector). Since ESEM analysis is an image analysis, it could give information about the microstructure of the sample investigated adding data to the powder sample analysis performed with other techniques (PXRD, FTIR, TG-DSC). A particular attention was given to the samples blended with cements, in order to verify the possibility of recognizing the cements when they are mixed with other materials.

Powder X-ray diffraction (PXRD) is another largely used technique. It allows the identification of the mineralogical components of a sample. PXRD is an invasive non-destructive analysis; in fact it requires

samples but it is non-destructive because the samples, although in powder, could be used for other investigations after the analysis. In order to perform PXRD analysis on mortars approx 1g of powdered sample is required. Once the powder is analysed the information obtained will represent the overall bulk of the sample. PXRD analyses are performed to obtain the mineralogical reference composition of the samples. PXRD is widely applied to mortars [37,78,81–86] and cements [70,80,87–93] in several examples. The research of Aranda et al. [89] represent a valuable and helpful work in the identification and quantifications of phases and hydration products present in ordinary Portland cements. Unfortunately, PXRD presents some restrictions in the analysis of hydrated phases of cements, because these are usually in gel form, not well crystallised, and thus they are difficult to identify with this technique.

Infrared spectroscopy is a vibrational technique that allows studying the vibrational movements of atoms in the molecules of a sample. It is often used in combination with PXRD or petrographic microscopy to detect the chemical composition of the samples [37,78,83–85,94]. It is usually used in different modalities like attenuated total reflection mode and transmission. These are two bench-top modes of analysis that require a small amount of powder sample.

In this research study, three different FTIR instruments are compared to evaluate their drawbacks and advantages applied to mortars. FTIR in transmission mode was compared to attenuated total reflectance (ATR) mode and to portable infrared spectroscopy in external reflection mode (ER-FTIR).

A comparison between different infrared spectroscopic modalities of analysis was already studied by Delgado et al. [95] applied to cement minerals and hydrated products. They compare transmission, photoacoustic spectroscopy and diffuse reflectance infrared (DRIFT). They underlined as the three techniques provide similar results but infrared in transmission mode is more "labour-intensive" compared to the other two. Moreover Ghosh and Handoo [96] provide an interesting and early review on the use of infrared and Raman spectroscopy applied to the identification of cements components, before and after the hydration. Hughes et al. studied the identification of cements compounds with DRIFT technique providing the characteristic absorbance bands for cement minerals [97]. Yu et al. studied in near-, mid- and far-infrared spectroscopy the calcium silicate hydrate (*C-S-H*), $Ca(OH)_2$, tobermorite and jennite minerals while Ren et al. [93] studied the structure of tricalcium silicate with infrared spectroscopy and X-ray diffraction. Bensted et al. [98] and Gastaldi et al. [99] provide interesting studies on the application of infrared spectroscopy in the assignation of the bands of ettringite, Gastaldi in particular, focused their attention in the near-infrared identification of ettringite bands.

ER-FTIR is a relatively new non-invasive technique that allows performing infrared analysis with portable instruments without sampling the object of the analysis. It is based on the reflection of incident infrared radiation. The peaks obtained with this technique could be harder to interpret than the ones found with other infrared techniques because of the presence of inverted and derivatives peaks. They appear because Fresnel's law rules the reflection connecting the absorption index (k) and the refractive index (n). When $k < 1$ a derivative-like signal is observed; on the other hand, when $k >> 1$ inverted (restrahlen) peaks can be seen. The specimens are composed by a mixture of different components, thus it is not possible to know the specific reflection coefficients of the surfaces [100–102]. Moreover, the reflectance infrared spectrum of the instrument used in this research, has a double wavenumber range compared to transmission infrared spectrum: in fact, it starts at about $300cm^{-1}$ and ends at more than $7000cm^{-1}$; therefore more information could be recorded. The ATR mode spectrum ranges from $600cm^{-1}$ to $4000cm^{-1}$, while

the transmission spectrum x axis scale starts around 400cm^{-1} ending at 4000cm^{-1}. With these differences in the length of the spectrum, we can have a change in the detection peaks related to the presence of one substance which could indeed influence the results. It is known the presence of the so-called "ATR-shift". This phenomenon, in our spectra, appears in the zone between about 1000 and 1450cm^{-1}. In addition to the compositional analysis performed with the three infrared techniques, a part of the research focused on the interaction between the surface roughness and the infrared incident and reflected radiation. Since external reflection has been found to be influenced by the surface roughness [103,104] as in the case of painting films [104–106] and of natural stone [107], the diffuse component of the signals determines its intensity and shape. The signals collected are composed of both surface and volume reflection [108]. The surface component is related to specular reflection of the surface microstructure and depends on the absorption phenomena and on the refractive index, leading to the presence of derivative and restrahlen peaks.

To study the thermal behavior of the mineralogical phases the TG-DSC analysis is usually used in mortar analysis requiring at least 40mg of powdered sample. This technique is used for mortar characterization in several case studies [33,37,94,109,110] or in phase transition in research on cement phase formation [81,82,87,88,91,92,111–118], as Guirado et al. [119] showed in their study where they analyzed the thermal decomposition of hydrated alumina cement (CAH_{10}). These techniques are used in quantitative studies, to reconstruct the proportion of binder/aggregate [33,37,94,110] or to study hydraulic phases [94,110,120]. Ramachandran et al. [121] provided a systematic study of cement raw materials and hydrated phases with differential thermal analysis, and they studied the thermal behavior of hydration of different compound at different time from the beginning of the hydration process. Gabrovsek et al. [112] showed the shift in the decomposition of the carbonates as a function of the hydration time and mineralogical phases. Also Dweck et al. studied the hydration of cement with addition of calcium carbonate with the use of thermal analysis and underline that the analysis with this technique of these types of samples is more challenging than the analysis on samples of only cement. Moropoulou et al. [82] show different examples of the application of thermal analysis on different types of mortars: lime mortar, lime mortar with portlandite, hot lime, modern cement and gypsum mortar. They also demonstrated that the CO_2/H_2O ratio (hydraulic water) in relation with CO_2 expresses the hydraulic character of the mortar. This technique was included in this methodological study to evaluate if this technique could add information on the analysis of mortars compared with those performed with the other techniques and help in the identification of composite mortars. It is known its use in the analysis of mortars but a systematic study of this technique on this material was not done yet.

Cements, the most used analytical techniques to study their composition and chemical characteristic are petrographic microscopy, X-ray diffraction, scanning electron microscopy, infrared spectroscopy and thermogravimetric analysis as already discussed before. In addition, also Raman spectroscopy and MAS NMR are used.

Raman spectroscopy on cementitious materials has already demonstrated a good response, except when it is affected by fluorescence especially on this type of material [69,96,122–132]. In literature it is used for the evaluation of hydration process of cement [123,128,132–138], or for the study of a single phase [122,127,138–146] or also to identify cement and mortars paste composition [69,73,76,85,125,129–131,144–150]. It is important to underline that in most of the above mentioned examples, the authors fo-

cused on the identification of a single phase in model samples, while there are fewer examples on real case studies [85,131]. Schmid et al. [131] have shown the application of Raman micro-spectroscopic imaging in the analysis of historical mortars with promising results. They applied this technique to cement mortars, identifying and giving spatial visualization of the identified phases, for example C_3S, C_3A and $C_xA_yF_z$, or between dolomite and calcite. Higl et al. [123] used the confocal Raman spectroscopy to investigate the hydrated cement microstructure. They synthesized C_3S raw material with known composition, and then they studied the phase formed after its hydration. With this study they identified the most characteristic band for *C-S-H*, portlandite, C_2S and C_3S phases.
In this research Raman spectroscopy was used to evaluate its possible applications in the identification of cement phases in mortars. We wanted to evaluate its application on samples of known composition considered as a real case samples to estimate its applicability. On the other hand, we wanted to prove the use of this technique to identify some phases that cannot be detected by XRD or other techniques because of their minor crystallinity or because out of the range of identification (for example oxides in the case of FTIR analysis). The samples analysed with this technique are cement and natural hydraulic lime powders of raw material (before hydration), cement and natural hydraulic lime samples after the hydration without the aggregate and hydraulic mortars. The hydrated samples without the aggregate have been prepared in order to collect the signals from the pure binder as a reference. Finally, the samples with cement and the aggregate have been analysed to evaluate the aggregate influence on the analysis' results.

Nuclear magnetic resonance is a chemical technique that is largely used in the investigation of liquid compounds. The Magic Angle Spinning Nuclear Magnetic Resonance (MAS NMR) is a solid state NMR spectroscopy technique that is applied to massive samples. Its chemical shifts are very large, if compared to liquid NMR. These signals are large bands that sometimes need a de-convolution process to be interpreted. MAS NMR is influenced by the same variables of the liquid NMR but, since the samples are solids, some interactions are not averaged. Thus the samples are influenced by the anisotropy of the chemical shift and the orientation of the atoms in the solid. The analyses are performed at the so called "magic angle" 54.74°, because the anisotropic dipolar interactions of the sample are reduced and homogenized by introducing rotation of the sample at this specific angle. There are other modes of performing solid state NMR, such as the cross polarization (CP): in this technique the polarization is transferred to the most dilute atoms from the most abundant, in order to amplify their signals. A further technique is the high power decoupling: this implies the decoupling of ^{1}H in order to cancel the possible ^{1}H interaction with the isotope that we are studying (notation $\{^{1}H\}$). Usually these techniques are coupled together, in order to obtain the best signals.
MAS NMR spectroscopy is used to analyse cement pastes. It can be used to study and investigate the structure of calcium silicate hydrate gel as Cong et al. demonstrated in their work [140], by monitoring the ^{17}O sites. The samples of cement, made with different CaO/SiO_2 ratios, have been studied after the isotopic enrichment in the content of ^{17}O. Different chemical bonds (Si-O-Si, Si-O-Ca and Ca-OH) have been monitored in order to study the hydration of *C-S-H*. The chemical bonds in the spectra have been assigned on the basis of the chemical shift only. They identified a zone that is connected to the presence of H_2O because after the heating of the sample the corresponding band disappears. In another article Cong et. al. [151] studied the structure of different types of tobermorite, jennite, and other Ca-silicate phases studying the ^{17}O,^{29}Si and $\{^{1}H\}^{29}Si$ CP-MAS NMR. MAS NMR was also used to monitor the sulphate attack in cement. Peyvandi et al. [152] after the exposure of their cement specimens to a solution of 5% of

sodium sulphate for different times, studied ^{27}Al and ^{29}Si to investigate the changes in the specimens after the attack. They studied ^{29}Si and ^{27}Al because sulphate attack changes the relative proportions of cement hydrates products like ettringite, monosulphate, calcium silicate hydrates. In other cases as Andersen et al. [153] and Mendes et al. [154] they demonstrated how the use of MAS NMR could improve the studies and the characterisation of calcium aluminates and aluminate hydrates. To do that, they mainly studied the ^{27}Al and ^{29}Si isotopes.

In our research this technique was not used because it requires specific instrumentations, experience and ability in the analysis of MAS NMR data. Anyway, it was considered and cited as a powerful technique that could help in the study of cement chemistry and in the hydration processes of these materials. In addition, MAS NMR was not applied to our samples due to the specificity of the techniques and because the study of the single phase hydration was not in our purpose.

Another technique that is often used on mortar materials is the X-ray fluorescence (XRF); it could be portable or bench-top instrument with the advantages and drawbacks of each modality of analysis. Since this technique gives only the elemental composition, without the help of another technique the identification of the typology of the mortar analysed could be difficult. Moreover, for classical portable and some bench-top instruments there is the impossibility of this technique to identify elements lighter than silicon silicon because they are too light; as a consequence the quantitative analysis applied on mortars could be difficult due to the inability of the identification of all the elements. On the other end the bench-top total reflection X-ray fluorescence (TXRF) presents better performances than XRF and could be used for elemental analysis, quantitative and provenance studies, but it requires liquid samples. For example Bonizzoni et al. [155] applied XRF and PXRD on Roman mortars. They also provide a classification of the XRF data thank to dendrogram obtained by the cluster analysis. Ergenç and Fort [156] present a multi-analytical characterisation of Roman mortars; they performed bench-top X-ray fluorescence, powder X-ray diffraction, thermal analysis, scanning electron microscope – EDS, petrographic analysis and stable isotopes analysis. Focusing on XRF analysis, they calculated different ratios like CaO/MgO vs TiO_2/Fe_2O_3 or CaO+MgO vs $SiO_2 + Al_2O_3 + Fe_2O_3$ to classify the samples with more binder and less aggregate between the samples with the opposite ratios. They also focused on trace elements to give an idea on the raw materials. Miriello et al. [64] performed analysis on Pompeian mortars. They performed petrographic analysis, bench-top X-ray fluorescence analysis, laser ablation inductively coupled plasma mass spectrometry, and scanning electron microscope and powder X-ray diffraction. In this study, XRF and LA-ICP-MS data were used for compositional and provenance studies using multivariate analysis.

In our research this technique was not used because it is specific for provenance studies that are not among the specific purposes of the project on our model samples. Certainly in a real case of study it is an important analysis if there is the possibility of the analysis also of the raw materials or mortars of different period to recover the historical background of the excavation for example.

In parallel to the above mentioned analytical techniques, a focus on the study of the microstructure of mortar samples has been carried out. It was done by using computed X-ray tomography (CT) [157–166] and mercury intrusion porosimetry (MIP) [138,163,167–170]. Thanks to X-ray tomography the porosity, the size, the grains distribution of the aggregate and the volume distribution of the binder could be evaluated. Among the techniques considered in this research, X-ray tomography is the most uncommon. In fact it requires specific and expensive equipment, software both for acquisition and elaboration of the

data, and an in depth experience in this field of studies. Computed X-ray tomography have been applied to building materials to investigate the stone decay as showed by Cnudde et al. [171] where they develop a software for 3D analysis, with a resolution of 3.96μm. With this research they studied the porosity, the pore size distribution of the pores of the sample. Moreover they could suppose the presence of four mineral phases visually recognizable. An example of the application of X-ray tomography on mortars is given by Lanzon et al. [166]. They use μCT to characterize modern mortars; they could calculate the total porosity, the equivalent diameter and the partial porosity (porosity variation in longitudinal direction).
Then the results of the porosity distribution have been compared to the traditional mercury intrusion porosimetry results. Computed X-ray tomography is a non-destructive technique. This approach is of major concern studying building materials since it allows subsequent analysis. It was also possible to compare the aggregate's size with the known dimension of the sieved aggregate used to prepare the specimens. At the end, to help the visualization of the result of the μCT analysis, a 3D reconstruction of pores, aggregate and binder was made.
This research produced interesting results that can contribute to the critical and necessary knowledge on artificial building materials. It suggests and analyzes the contribution of each analytical technique used when applied on artificial building materials in cultural heritage context. It studies in depth the advantages and drawbacks of each technique. In addition, mortars were investigated also the pore-issue. The results of this last part underline the benefit and the weakness of pore analysis on this type of material.

References

[1] R.T. Committee, RILEM TC 203-RHM: Repair mortars for historic masonry, Mater. Struct. 45 (2012) 1295–1302. doi:10.1617/s11527-012-9917-z.

[2] J. Elsen, Microscopy of historic mortars-a review, Cem. Concr. Res. 36 (2006) 1416–1424. doi:10.1016/j.cemconres.2005.12.006.

[3] P.B. Middendorf, J.J. Hughes, K. Callebaut, G. Baronio, I. Papayianni, Investigative methods for the characterisation of historic mortars. Part 2: Chemical characterisation, Mater. Struct. - RILEM TC 167-COM Characterisation Old Mortars with Respect to Their Repair. 38 (2005) 771–780. doi:10.1617/14282.

[4] M.R. Veiga, J. Aguiar, A.S. Silva, F. Carvalho, Methodologies for characterisation and repair of mortars of ancient buildings, Hist. Constr. Int. Semin. (2001) 353–362.

[5] J.I. Alvarez, I. Navarro, P.J. Garcia Casado, Thermal, mineralogical and chemical studies of the mortars used in the cathedral of Pamplona (Spain), Thermochim. Acta. 365 (2000) 177–187. doi:10.1016/S0040-6031(00)00624-9.

[6] M.P. Colombini, A. Ceccarini, A. Carmignani, Ion chromatography characterization of polysaccharides in ancient wall paintings, 968 (2002) 79–88.

[7] C.M. Belfiore, G.V. Fichera, G. Ortolano, A. Pezzino, R. Visalli, L. Zappalà, Image processing of the pozzolanic reactions in Roman mortars via X-Ray Map Analyser, Microchem. J. 125 (2016) 242–253. doi:10.1016/j.microc.2015.11.022.

[8] E. Goins, A new protocol for the analysis of historic cementitious material, in: P. Bartos, C. Groot, J.J. Hughes (Eds.), Int. RILEM Work. Hist. Mortars Charact. Tests, RILEM Publications SARL, 1999: pp. 71–79.

[9] K. Van Balen, E.-E. Toumbakari, M.-T. Blanco, J. Aguilera, F. Puertas, C. Sabbioni, G. Zappia, C. Riontino, G. Gobbi, Procedure for a mortar type identification - a proposal, in: P.. BARTOS, C.. GROOT, J. HUGHES (Eds.), Int. Work. Hist. Mortars Charact. Test. Vol. 12, Rilem Publications; Cachan (FR), 2000: pp. 61–70.

[10] G. Martinet, B. Quenee, Proposal for useful methodology for the study of ancient mortars, in: P. Bartos, C. Groot, J. Hughes (Eds.), Int. RILEM Work. Hist. Mortars Charact. Tests Paisley, Scotland, 12th-14th May 1999, 2010: pp. 81–91.

[11] G. Alessandrini, C. Tedeschi, Le malte e la conservazione: conoscenza e normativa, Kermes La Riv. Del Restauro. (2009).

[12] C. Groot, G. Ashall, J. Hughes, Characterisation of Old Mortars With Respect To Their Repair - Final Report of RILEM TC 167-COM, 2004.

[13] B. Middendorf, J.J. Hughes, K. Callebaut, G. Baronio, I. Papayianni, Investigative methods for the characterisation of historic mortars. Part 1: Mineralogical characterisation, Mater. Struct. - RILEM TC 167-COM Characterisation Old Mortars with Respect to Their Repair. 38 (2005) 761–769. doi:10.1617/14281.

[14] Normal 27/88 : Caratterizzazione di una malta, (1988) 10.

[15] J.I. Alvarez, A. Martín, P.J. García Casado, I. Navarro, A. Zornoza, Methodology and validation of a hot hydrochloric acid attack for the characterization of ancient mortars, Cem. Concr. Res. 29 (1999) 1061–1065. doi:10.1016/S0008-8846(99)00090-3.

[16] ASTM International, ASTM C114 - 18 - Standard Test Methods for Chemical Analysis of Hydraulic Cement, (2018). doi:10.1520/C0114-18.

[17] Ente italiano di normalizzazione, UNI 11088:2003 - Cultural heritage - Ancient mortar and mortar for restoration - Chemical characterization of a mortar - Determination of siliceous aggregate and of some soluble analytes content, (2003).

[18] Ente italiano di normazione, UNI 11089:2003 - Cultural heritage - Ancient mortar and mortar for restoration - Estimate of the composition of some kind of mortars, (2003).

[19] Ente italiano di normazione, UNI 11189 Beni culturali – Malte storiche e da restauro – Metodi di prova per la caratterizzazione chimica di una malta – Analisi chimica; Cultural heritage, Historical and repair mortars - Test methods for chemical characterisation of a mortar - Chemical, (2013) 2013.

[20] L.B. Alberti, C. Bartoli, L' architettura, 1667.

[21] V. Pollio, M.H. Morgan, H.L. Warren, Vitruvius, the Ten Books on Architecture, Harvard University Press, 1914.

[22] C. Arcolao, Le ricette del restauro: malte, intonaci, stucchi dal XV al XIX secolo, Marsilio Editori, 1998.

[23] A. Rattazzi, Conosci il grassello di calce? Origine, produzione e impiego del grassello in architettura, nell'arte e nel restauro, Edicom, 2007. http://books.google.es/books?id=4zq_HwAACAAJ.

[24] G. Pesce, A. Rattazzi, Criteri per la scelta di un buon grassello di calce, (2009) 1–7.

[25] G. Alessandrini, Gli intonaci nell'edilizia storica: metodologie analitiche per la caratterizzazione chimica e fisica, in: G. Biscontin (Ed.), Plaster. Hist. Cult. Technol. Proc. Congr. Bressanone, L'intonaco Storia, Cult. e Tecnol. Atti Del Convegno Di Stud. Bressanone 24-27 Giugno 1985, 1985: pp. 147–166.

[26] E. Pecchioni, F. Fratini, E. Cantisani, Le Malte Antiche e Moderne tra Tradizione ed Innovazione, Pàtron, Bologna, 2008.

[27] C. Montagni, I leganti, in: UTET (Ed.), Mater. per Restauro e La Manutenzione, 2000: pp. 177–190.

[28] Turco Antonio, Il gesso, Hoepli, 1996.

[29] L. Zevi, Il manuale del restauro architettonico, Mancosu, 2002.

[30] N. Italiana, UNI EN 197 Composizione, specificazioni e criteri di conformità per cementi comuni, (2001).

[31] UNICEMENTO, UNI EN 196-2 Methods of testing cement - Part 2: Chemical analysis of cement, 2013.

[32] K. R.-N. Elert C.; Pardo, E. S.; Hansen, E.; Cazalla, O., Lime mortars for the conservation of historic buildings, Stud. Conserv. 47 (2002) 62–75.

[33] A. Moropoulou, A. Bakolas, K. Bisbikou, Investigation of the technology of historic mortars, J. Cult. Herit. 1 (2000) 45–58. doi:10.1016/S1296-2074(99)00118-1.

[34] A. Duran, M.D. Robador, M.C. Jimenez De Haro, V. Ramirez-Valle, Study by thermal analysis of mortars belonging to wall paintings corresponding to some historical buildings of Sevillian art, J. Therm. Anal. Calorim. 92 (2008) 353–359. doi:10.1007/s10973-007-8733-0.

[35] P. Faria, F. Henriques, V. Rato, Comparative evaluation of lime mortars for architectural conservation, 9 (2008) 338–346. doi:10.1016/j.culher.2008.03.003.

[36] A. Moropoulou, A. Bakolas, P. Moundoulas, E. Aggelakopoulou, S. Anagnostopoulou, Strength development and lime reaction in mortars for repairing historic masonries, 27 (2005) 289–294. doi:10.1016/j.cemconcomp.2004.02.017.

[37] G. Biscontin, M. Pellizon Birelli, E. Zendri, Characterization of binders employed in the manufacture of Venetian historical mortars, J. Cult. Herit. 3 (2002) 31–37. doi:10.1016/S1296-2074(02)01156-1.

[38] E. Navrátilová, P. Rovnaníková, Pozzolanic properties of brick powders and their effect on the properties of modified lime mortars, Constr. Build. Mater. 120 (2016) 530–539. doi:10.1016/j.conbuildmat.2016.05.062.

[39] P. López-Arce, M. Tagnit-Hammou, B. Menéndez, J.-D. Mertz, A. Kaci, Durability of stone-repair mortars used in historic buildings from Paris, Mater. Struct. 49 (2016) 5097–5115. doi:10.1617/s11527-016-0846-0.

[40] C. Nunes, Z. Slížková, Hydrophobic lime based mortars with linseed oil: Characterization and durability assessment, Cem. Concr. Res. 61–62 (2014) 28–39. doi:10.1016/j.cemconres.2014.03.011.

[41] D. Gulotta, S. Goidanich, C. Tedeschi, T.G. Nijland, L. Toniolo, Commercial NHL-containing mortars for the preservation of historical architecture. Part 1: Compositional and mechanical characterisation, Constr. Build. Mater. 38 (2013) 31–42.

[42] C. Ince, M.A. Carter, M.A. Wilson, A. El-Turki, R.J. Ball, G.C. Allen, N.C. Collier, Analysis of the abstraction of water from freshly mixed jointing mortars in masonry construction, Mater. Struct. 43 (2010) 985–992. doi:10.1617/s11527-009-9560-5.

[43] E. Aggelakopoulou, A. Bakolas, A. Moropoulou, Properties of lime–metakolin mortars for the restoration of historic masonries, Appl. Clay Sci. 53 (2011) 15–19. doi:10.1016/j.clay.2011.04.005.

[44] R. Ylmén, L. Wadsö, I. Panas, Insights into early hydration of Portland limestone cement from infrared spectroscopy and isothermal calorimetry, Cem. Concr. Res. 40 (2010) 1541–1546. doi:10.1016/j.cemconres.2010.06.008.

[45] M.R. Veiga, A. Velosa, A. Magalhães, Experimental applications of mortars with pozzolanic additions: Characterization and performance evaluation, Constr. Build. Mater. 23 (2009) 318–327. doi:10.1016/j.conbuildmat.2007.12.003.

[46] Forum Calce, Personal comunication.

[47] D. Miriello, G.M. Crisci, Image analysis and flatbed scanners. A visual procedure in order to study the macro-porosity of the archaeological and historical mortars, 7 (2006) 186–192. doi:10.1016/j.culher.2006.03.003.

[48] N. Marinoni, A. Pavese, M. Foi, L. Trombino, Characterisation of mortar morphology in thin sections by digital image processing, 35 (2005) 1613–1619. doi:10.1016/j.cemconres.2004.09.015.

[49] F. Carpentier, B. Vandermeulen, High-Resolution Photography for Soil Micromorphology Slide Documentation, 31 (2016) 603–607. doi:10.1002/gea.21563.

[50] C.F. Mora, A.K.H. Kwan, Sphericity, shape factor, and convexity measurement of coarse aggregate for concrete using digital image processing, 30 (2000) 351–358.

[51] C. Blaeuer, A. Kueng, Examples of microscopic analysis of historic mortars by means of polarising light microscopy of dispersions and thin sections, Mater. Charact. 58 (2007) 1199–1207. doi:10.1016/j.matchar.2007.04.023.

[52] A.K.H. Kwan, C.F. Mora, H.C. Chan, Particle shape analysis of coarse aggregate using digital image processing, 29 (1999) 1403–1410.

[53] I. Ahmad Bany Yaseen, H. Al-Amoush, M. Al-Farajat, A. Mayyas, Petrography and mineralogy of Roman mortars from buildings of the ancient city of Jerash, Jordan, Constr. Build. Mater. 38 (2013) 465–471. doi:10.1016/j.conbuildmat.2012.08.022.

[54] A. Pecci, E.C. Le Pera, R. De Luca, M. Angel, M. Ontiveros, G. M. Crisci, D. Miriello, A. Bloise Archaeometric study of mortars and plasters from the Roman City of Pollentia (Mallorca - Balearic Islands), (2015). doi:10.2451/2013PM0021.

[55] C. Gillot, The use of pozzolanic materials in Maya mortars: new evidence from Rio Bec (Campeche, Mexico), J.Archaeol. Sci. 47 (2014) 1–9. doi:10.1016/j.jas.2014.03.037.

[56] D. Miriello, F. Antonelli, C. Apollaro, A. Bloise, N. Bruno, M. Catalano, S. Columbu, G.M. Crisci, R. De Luca, M. Lezzerini, S. Mancuso, A. La Marca, A petro-chemical study of ancient mortars from the archaeological site of Kyme (Turkey), Period. Di Mineral. 84 (2015) 497–517. doi:10.2451/2015PM0028.

[57] Y. Asscher, Y. Goren, A Rapid On-Site Method for Micromorphological Block, 31 (2016) 324–331. doi:10.1002/gea.21561.

[58] R. De Luca, V. Gigliotti, M. Panarello, A. Bloise, G.M. Crisci, D. Miriello, Spectroscopic, microchemical and petrographic analyses of plasters from ancient buildings in Lamezia Terme (Calabria, Southern Italy), Spectrochim. Acta Part A Mol. Biomol. Spectrosc. 153 (2016) 184–193. doi:10.1016/j.saa.2015.08.018.

[59] F. Marra, M. Anzidei, A. Benini, E.D. Ambrosio, M. Gaeta, G. Ventura, A. Cavallo, Petro-chemical features and source areas of volcanic aggregates used in ancient Roman maritime concretes, J. Volcanol. Geotherm. Res. 328 (2016) 59–69. doi:10.1016/j.jvolgeores.2016.10.005.

[60] M. Caroselli, G. Cavallo, A. Felici, S. Luppichini, G. Nicoli, Gypsum in Ticinese stucco artworks of the 16–17th century: Use, characterization, provenance and induced decay phenomena, J. Archaeol. Sci. Reports. 24 (2019) 208–219. doi:10.1016/j.jasrep.2019.01.009.

[61] E. Pecchioni, F. Fratini, E. Cantisani, Atlas of the Ancient Mortars in thin section under optical microscope, 2014.

[62] J. Weber, F. Pintér, K. Thomas, Atlas of thin sections of minerals materials in cultural heritage, (2018).

[63] F. Alawneh, E. Almasri, Investigations of hellenistic mortar from UMM QAIS (Gadara), Jordan, Arqueol. Iberoam. 40 (2018) 81–92.

[64] D. Miriello, D. Barca, A. Bloise, A. Ciarallo, G.M. Crisci, T. De Rose, C. Gattuso, F. Gazineo, M.F. La, Characterisation of archaeological mortars from Pompeii (Campania , Italy) and identification of construction phases by compositional data analysis, J. Archaeol. Sci. 37 (2010) 2207–2223. doi:10.1016/j.jas.2010.03.019.

[65] S. Columbu, A.M. Garau, Mineralogical, petrographic and chemical analysis of geomaterials used in the mortars of Roman Nora theatre (south Sardinia, Italy), Ital. J. Geosci. 136 (2017) 238–262. doi:10.3301/IJG.2017.05.

[66] C. Rodríguez-navarro, Binders in historical buildings: Traditional lime in conservation, (1988) 91–112.

[67] J. Weber, T. Köberle, F. Pintér, Methods of Microscopy to Identify and Characterise Hydraulic Binders in Historic Mortars—A Methodological Approach, in: Hist. Mortars, Springer International Publishing, Cham, 2019: pp. 21–31. doi:10.1007/978-3-319-91606-4_2.

[68] F. Pintér, C. Gosselin, The origin, composition and early age hydration mechanisms of Austrian natural Portland cement, Cem. Concr. Res. 110 (2018) 1–12. doi:10.1016/j.cemconres.2018.04.020.

[69] K. Callebaut, J. Elsen, K. Van Balen, W. Viaene, Nineteenth century hydraulic restoration mortars in the Saint Michael's Church (Leuven, Belgium): Natural hydraulic lime or cement?, Cem. Concr. Res. 31 (2001) 397–403. doi:10.1016/S0008-8846(00)00499-3.

[70] M.J. Varas, M.A. De Buergo, R. Fort, Natural cement as the precursor of Portland cement: Methodology for its identification, Cem. Concr. Res. 35 (2005) 2055–2065. doi:10.3758/BF03336304.

[71] J. Elsen, N. Lens, T. Aarre, D. Quenard, V. Smolej, Determination of the w/c ratio of hardended cement paste and concreate samples on thin sections using automated image analysis techniques, Cem. Concr. Res. 25 (1995) 827–834. doi:0008-8846(95)00073-9.

[72] G.W. Scherer, B. Kutchko, N. Thaulow, A. Duguid, B. Mook, Characterization of cement from a well at Teapot Dome Oil Field: Implications for geological sequestration, Int. J. Greenh. Gas Control. 5 (2011) 115–124. doi:10.1016/j.ijggc.2010.06.010.

[73] J. Weber, N. Gadermayr, R. Kozłowski, D. Mucha, D. Hughes, D. Jaglin, W. Schwarz, Microstructure and mineral composition of Roman cements produced at defined calcination conditions, Mater. Charact. 58 (2007) 1217–1228. doi:10.1016/j.matchar.2007.04.025.

[74] J. Weber, K. Bayer, Historic Mortars, Springer Netherlands, Dordrecht, 2012. doi:10.1007/978-94-007-4635-0.

[75] H.F.W. Taylor, Cement chemistry. 2nd ed., 1997. doi:10.1016/S0958-9465(98)00023-7.

[76] P. Dariz, T. Schmid, Ferruginous phases in 19th century lime and cement mortars: A Raman microspectroscopic study, Mater. Charact. 129 (2017) 9–17. doi:10.1016/j.matchar.2017.04.009.

[77] A. Poole, I. Sims, Concrete Petrography, CRC Press, Taylor & Francis Group, 6000 Broken Sound Parkway NW, Suite 300, Boca Raton, FL 33487-2742, 2015. doi:10.1201/b18688.

[78] L. Rampazzi, B. Rizzo, C. Colombo, C. Conti, M. Realini, U. Bartolucci, M.P. Colombini, A. Spiriti, L. Facchin, The stucco decorations from St. Lorenzo in Laino (Como, Italy): The materials and the techniques employed by the "Magistri Comacini", Anal. Chim. Acta. (2008). doi:10.1016/j.aca.2008.09.052.

[79] M.G. Gandolfi, K. Van Landuyt, P. Taddei, E. Modena, B. Van Meerbeek, C. Prati, Environmental scanning electron microscope connected with energy dispersive X-ray analysis and Raman techniques to study proRoot mineral trioxide aggregate and calcium silicate cements in wet conditions and real time, J. Endod. 36 (2010) 851–857. doi:10.1016/j.joen.2009.12.007.

[80] A. Crumbie, G. Walenta, T. Füllmann, Where is the iron? Clinker microanalysis with XRD Rietveld, optical microscopy/point counting, Bogue and SEM-EDS techniques, Cem. Concr. Res. 36 (2006) 1542–1547. doi:10.1016/j.cemconres.2006.05.031.

[81] N.Y. Mostafa, Z.I. Zaki, O.H. Abd Elkader, Chemical activation of calcium aluminate cement composites cured at elevated temperature, Cem. Concr. Compos. 34 (2012) 1187–1193. doi:10.1016/j.cemconcomp.2012.08.002.

[82] A. Moropoulou, A. Bakolas, K. Bisbikou, Characterization of ancient, byzantine and later historic mortars by thermal and X-ray diffraction techniques, Thermochim. Acta. 269–270 (1995) 779–795. doi:10.1016/0040-6031(95)02571-5.

[83] C. Genestar, C. Pons, Ancient covering plaster mortars from several convents and Islamic and Gothic palaces in Palma de Mallorca (Spain). Analytical characterisation, J. Cult. Herit. 4 (2003) 291–298. doi:10.1016/j.culher.2003.02.001.

[84] Y. Zeng, B. Zhang, X. Liang, A case study and mechanism investigation of typical mortars used on ancient architecture in China, Thermochim. Acta. 473 (2008) 1–6. doi:10.1016/j.tca.2008.03.019.

[85] C. García-Florentino, M. Maguregui, H. Morillas, U. Balziskueta, A. Azcarate, G. Arana, J.M. Madariaga, Portable and Raman imaging usefulness to detect decaying on mortars from Punta Begoña Galleries (Getxo, North of Spain), J. Raman Spectrosc. 47 (2016) 1458–1466. doi:10.1002/jrs.4949.

[86] P. Maravelaki-Kalaitzaki, A. Bakolas, I. Karatasios, V. Kilikoglou, Hydraulic lime mortars for the restoration of historic masonry in Crete, Cem. Concr. Res. 35 (2005) 1577–1586. doi:10.1016/j.cemconres.2004.09.001.

[87] X. Guo, F. Meng, H. Shi, Microstructure and characterization of hydrothermal synthesis of Al-substituted tobermorite, Constr. Build. Mater. 133 (2017) 253–260. doi:10.1016/j.conbuildmat.2016.12.059.

[88] P. Yu, J. Kirkpatrick, Thermal dehydration of tobermorite and jennite, Concr. Sci. Eng. 97 (1999) 117–119. http://10.0.4.87/j.1468-229X.2011.00543_3.x%5Cnhttps://login.e.bibl.liu.se/login?url=https://search.ebscohost.com/login.aspx?direct=true&db=aph&AN=70601905&site=eds-live&scope=site.

[89] M.A.G. Aranda, A.G. De la Torre, L. Leon-Reina, Rietveld Quantitative Phase Analysis of OPC Clinkers, Cements and Hydration Products, Rev. Mineral. Geochemistry. 74 (2012) 169–209. doi:10.2138/rmg.2012.74.5.

[90] J. Lanas, J.L. Pérez Bernal, M.A. Bello, J.I. Alvarez, Mechanical properties of masonry repair dolomitic lime-based mortars, Cem. Concr. Res. 36 (2006) 951–960. doi:10.1016/j.cemconres.2005.10.004.

[91] B. Lothenbach, G. Le, E. Gallucci, K. Scrivener, Influence of limestone on the hydration of Portland cements, 38 (2008) 848–860. doi:10.1016/j.cemconres.2008.01.002.

[92] T. Matschei, B. Lothenbach, F.P. Glasser, Thermodynamic properties of Portland cement hydrates in the system $CaO–Al_2O_3–SiO_2–CaSO_4–CaCO_3–H_2O$, Cem. Concr. Res. 37 (2007) 1379–1410. doi:10.1016/j.cemconres.2007.06.002.

[93] X. Ren, W. Zhang, J. Ye, FTIR study on the polymorphic structure of tricalcium silicate, Cem. Concr. Res. (2017). doi:10.1016/j.cemconres.2016.11.021.

[94] A. Bakolas, G. Biscontin, V. Contardi, E. Franceschi, A. Moropoulou, D. Palazzi, E. Zendri, Thermoanalytical research on traditional mortars in venice, Thermochim. Acta. 269–270 (1995) 817–828. doi:10.1016/0040-6031(95)02574-X.

[95] A.H. Delgado, R.M. Paroli, J.J. Beaudoin, Comparison of IR techniques for the characterization of construction cement minerals and hydrated products, Appl. Spectrosc. (1996). doi:10.1366/0003702963905312.

[96] S.N. Ghosh, S.K. Handoo, Infrared and Raman spectral studies in cement and concrete (review), Cem. Concr. Res. (1980). doi:10.1016/0008-8846(80)90005-8.

[97] T.L. Hughes, C.M. Methven, T.G.J. Jones, S.E. Pelham, P. Fletcher, C. Hall, Determining cement composition by Fourier transform infrared spectroscopy, Adv. Cem. Based Mater. 2 (1995) 91–104. doi:10.1016/1065-7355(94)00031-X.

[98] J. Bensted, S.P. Varma., Studies of ettringite and its derivatives, Cem. Technol. 2 (1971) 71–76.

[99] D. Gastaldi, F. Canonico, E. Boccaleri, Ettringite and calcium sulfoaluminate cement: Investigation of water content by near-infrared spectroscopy, J. Mater. Sci. 44 (2009) 5788–5794. doi:10.1007/s10853-009-3812-1.

[100] C. Miliani, F. Rosi, A. Daveri, B.G. Brunetti, Reflection infrared spectroscopy for the non-invasive in situ study of artists' pigments, Appl. Phys. A Mater. Sci. Process. 106 (2012) 295–307. doi:10.1007/s00339-011-6708-2.

[101] L. Rampazzi, V. Brunello, C. Corti, E. Lissoni, Non-invasive techniques for revealing the palette of the Romantic painter Francesco Hayez, Spectrochim. Acta Part A Mol. Biomol. Spectrosc. 176 (2017) 142–154. doi:10.1016/j.saa.2017.01.011.

[102] V. Brunello, C. Corti, A. Sansonetti, C. Tedeschi, L. Rampazzi, Non-invasive FTIR study of mortar model samples: comparison among innovative and traditional techniques, Eur. Phys. J. Plus. 134 (2019) 270. doi:10.1140/epjp/i2019-12667-1.

[103] I. Arrizabalaga, O. Gómez-Laserna, J.A. Carrero, J. Bustamante, A. Rodríguez, G. Arana, J.M. Madariaga, Diffuse reflectance FTIR database for the interpretation of the spectra obtained with a handheld device on built heritage materials, Anal. Methods. 7 (2015) 1061–1070. doi:10.1039/C4AY02189D.

[104] C. Sessa, H. Bagán, J.F. García, Influence of composition and roughness on the pigment mapping of paintings using mid-infrared fiber optics reflectance spectroscopy (mid-IR FORS) and multivariate calibration, (2014) 6735–6747. doi:10.1007/s00216-014-8091-2.

[105] W. Vetter, M. Schreiner, Characterization of pigment-binding media systems - Comparison of non-invasive in-situ reflection FTIR with transmission FTIR microscopy, (2011) 10–22.

[106] L.B. de Paiva, F.A. Rodrigues, Early-hydration of -Ca_2SiO_4 followed by FTIR/ATR spectroscopy, J. Mater. Sci. 39 (2004) 5841–5843. doi:10.1023/B:JMSC.0000040098.45251.b3.

[107] C. Ricci, C. Miliani, B.G. Brunetti, A. Sgamellotti, Non-invasive identification of surface materials on marble artifacts with fiber optic mid-FTIR reflectance spectroscopy, 69 (2006) 1221–1226. doi:10.1016/j.talanta.2005.12.054.

[108] M. Fabbri, M. Picollo, S. Porcinai, M. Bacci, Mid-infrared fiber-optics reflectance spectroscopy: A non-invasive technique for remote analysis of painted layers. Part II: Statistical analysis of spectra, Appl. Spectrosc. 55 (2001) 428–433. doi:10.1366/0003702011952181.

[109] S. Vecchio, A. La Gmestra, A. Frezza, C. Ferragina, The use of thermoanalytical techniques in the characterization of ancient mortars, Thermochim. Acta. 227 (1993) 215–223. doi:10.1016/0040-6031(93)80264-B.

[110] A. Bakolas, G. Biscontin, A. Moropoulou, E. Zendri, Characterization of structural byzantine mortars by thermogravimetric analysis, Thermochim. Acta. 321 (1998) 151–160. doi:10.1016/S0040-6031(98)00454-7.

[111] C.A. Strydom, D.L. Hudson-Lamb, J.H. Potgieter, E. Dagg, The thermal dehydration of synthetic gypsum, Thermochim. Acta. 269–270 (1995) 631–638. doi:10.1016/0040-6031(95)02521-9.

[112] R. Gabrovšek, T. Vuk, V. Kaučič, Evaluation of the hydration of Portland cement containing various carbonates by means of thermal analysis, Acta Chim. Slov. 53 (2006) 159–165.

[113] Z. Šauman, Carbonization of porous concrete and its main binding components, Cem. Concr. Res. 1 (1971) 645–662. doi:10.1016/0008-8846(71)90019-6.

[114] S. Shaw, C.M. Henderson, B. Komanschek, Dehydration/recrystallization mechanisms, energetics, and kinetics of hydrated calcium silicate minerals: an in situ TGA/DSC and synchrotron radiation SAXS/WAXS study, Chem. Geol. 167 (2000) 141–159. doi:10.1016/S0009-2541(99)00206-5.

[115] D.L. Hudson-Lamb, C.A. Strydom, J.H. Potgieter, The thermal dehydration of natural gypsum and pure calcium sulphate dihydrate (gypsum), Thermochim. Acta. 282–283 (1996) 483–492. doi:10.1016/0040-6031(95)02819-6.

[116] J. Dweck, P.M. Buchler, A.C.V. Coelho, F.K. Cartledge, Hydration of a Portland cement blended with calcium carbonate, Thermochim. Acta. 346 (2000) 105–113. doi:10.1016/S0040-6031(99)00369-X.

[117] L.M. Barcina, A. Espina, M. Sufirez, J.R. Garc, J. Rodr, Characterization of monumental carbonate stones by thermal analysis (TG, DTG and DSC), Science (80-.). 290 (1997) 181–189.

[118] A. Moropoulou, A. Bakolas, K. Bisbikou, Thermal analysis as a method of characterizing ancient ceramic technologies, Thermochim. Acta. 269–270 (1995) 743–753. doi:10.1016/0040-6031(95)02570-7.

[119] F. Guirado, S. Galı´, J.S. Chinchón, Thermal Decomposition of Hydrated Alumina Cement (CAH_{10}), Cem. Concr. Res. 28 (1998) 381–390. doi:10.1016/S0008-8846(98)00007-6.

[120] R.C. Mackenzie, Differential Thermal Analysis: Fundamental aspects, Acad. Press, 1978. https://books.google.it/books?id=-HoyvgAACAAJ.

[121] V.S. Ramachandran, R.F. Feldman, P.J. Sereda, Applications of Differential Thermal Analysis in Cement Chemistry, in: I. Chemical Publishing Company (Ed.), New York, 1969.

[122] J. Bensted, Thaumasite — background and nature in deterioration of cements, mortars and concretes, Cem. Concr. Compos. 21 (1999) 117–121. doi:10.1016/S0958-9465(97)00076-0.

[123] J. Higl, M. Köhler, M. Lindén, Confocal Raman microscopy as a non-destructive tool to study microstructure of hydrating cementitious materials, Cem. Concr. Res. 88 (2016) 136–143. doi:10.1016/j.cemconres.2016.07.005.

[124] C.-S. Deng, C. Breen, J. Yarwood, S. Habesch, J. Phipps, B. Craster, G. Maitland, Ageing of oilfield cement at high humidity: a combined FEG-ESEM and Raman microscopic investigation, J. Mater. Chem. 12 (2002) 3105–3112. doi:10.1039/b203127m.

[125] S.S. Potgieter-Vermaak, J.H. Potgieter, R. Van Grieken, The application of Raman spectrometry to investigate and characterize cement, Part I: A review, Cem. Concr. Res. 36 (2006) 656–662. doi:10.1016/j.cemconres.2005.09.008.

[126] S.S. Potgieter-Vermaak, J.H. Potgieter, M. Belleil, F. Deweerdt, R. Van Grieken, The application of Raman spectrometry to the investigation of cement: Part II: A micro-Raman study of OPC, slag and fly ash, Cem. Concr. Res. 36 (2006) 663–670. doi:10.1016/j.cemconres.2005.09.010.

[127] R.J. Kirkpartick, J.L. Yarger, P.F. McMillan, P. Yu, X. Cong, Raman spectroscopy of C-S-H, tobermorite, and jennite, Adv. Cem. Based Mater. 5 (1997) 93–99. doi:10.1016/S1065-7355(97)00001-1.

[128] D. Torréns-martín, L. Fernández-carrasco, S. Martínez-ramírez, Hydration of calcium aluminates and calcium sulfoaluminate studied by Raman spectroscopy, Cem. Concr. Res. 47 (2013) 43–50. doi:10.1016/j.cemconres.2013.01.015.

[129] D. Torréns-Martín, L. Fernández-Carrasco, S. Martínez-Ramírez, J. Ibáñez, L. Artús, T. Matschei, Raman spectroscopy of anhydrous and hydrated calcium aluminates and sulfoaluminates, J. Am. Ceram. Soc. 96 (2013) 3589–3595. doi:10.1111/jace.12535.

[130] M. Torres-Carrasco, A. del Campo, M.A. de la Rubia, E. Reyes, A. Moragues, J.F. Fernández, New insights in weathering analysis of anhydrous cements by using high spectral and spatial resolution Confocal Raman Microscopy, Cem. Concr. Res. 100 (2017) 119–128. doi:10.1016/j.cemconres.2017.06.003.

[131] T. Schmid, P. Dariz, Chemical imaging of historical mortars by Raman microscopy, Constr. Build. Mater. 114 (2016) 506–516. doi:10.1016/j.conbuildmat.2016.03.153.

[132] J. Ibáñez, L. Artús, R. Cuscó, Á. López, E. Menéndez, M.C. Andrade, Hydration and carbonation of monoclinic C_2S and C_3S studied by Raman spectroscopy, J. Raman Spectrosc. 38 (2007) 61–67. doi:10.1002/jrs.1599.

[133] S. Martinez-Ramirez, M. Frías, C. Domingo, Micro-Raman spectroscopy in white portland cement hydration: Long-term study at room temperature, J. Raman Spectrosc. 37 (2006) 555–561. doi:10.1002/jrs.1428.

[134] M. Tarrida, M. Madon, B. Le Rolland, P. Colombet, An in-situ Raman spectroscopy study of the hydration of tricalcium silicate, Adv. Cem. Based Mater. 2 (1995) 15–20. doi:10.1016/1065-7355(95)90035-7.

[135] I.G. Richardson, A. V. Girão, R. Taylor, S. Jia, Hydration of water- and alkali-activated white Portland cement pastes and blends with low-calcium pulverized fuel ash, Cem. Concr. Res. 83 (2016) 1–18. doi:10.1016/j.cemconres.2016.01.008.

[136] J. Skibsted, C. Hall, Characterization of cement minerals, cements and their reaction products at the atomic and nano scale, Cem. Concr. Res. 38 (2008) 205–225. doi:10.1016/j.cemconres.2007.09.010.

[137] K. Garbev, P. Stemmermann, L. Black, C. Breen, J. Yarwood, B. Gasharova, Structural features of C-S-H(I) and its carbonation in air-A Raman spectroscopic study. Part I: Fresh phases, J. Am. Ceram. Soc. 90 (2007) 900–907. doi:10.1111/j.1551-2916.2006.01428.x.

[138] Y. Aono, F. Matsushita, S. Shibata, Y. Hama, Nano-structural Changes of C-S-H in Hardened Cement Paste during Drying at 50°C, J. Adv. Concr. Technol. 5 (2007) 313–323. doi:10.3151/jact.5.313.

[139] D. Torréns-martín, L.J. Fernandez-carrasco, D. Torr, Raman Spectroscopy of Anhydrous and Hydrated Calcium Aluminates and Sulfoaluminates, (2013). doi:10.1111/jace.12535.

[140] X. Cong, R.J. Kirkpatrick, ^{17}O MAS NMR Investigation of the Structure of Calcium Silicate Hydrate Gel, J. Am. Ceram. Soc. 79 (1996) 1585–1592. doi:10.1111/j.1151-2916.1996.tb08768.x.

[141] T.F. Sevelsted, J. Skibsted, Carbonation of C-S-H and C-A-S-H samples studied by ^{13}C, ^{27}Al and ^{29}Si MAS NMR spectroscopy, Cem. Concr. Res. 71 (2015) 56–65. doi:10.1016/j.cemconres.2015.01.019.

[142] J.L. Perez-Rodriguez, M.D. Robador, M.A. Centeno, B. Siguenza, A. Duran, Wall paintings studied using Raman spectroscopy: A comparative study between various assays of cross sections and external layers, Spectrochim. Acta - Part A Mol. Biomol. Spectrosc. 120 (2014) 602–609. doi:10.1016/j.saa.2013.10.052.

[143] D. Gastaldi, E. Boccaleri, F. Canonico, M. Bianchi, The use of Raman spectroscopy as a versatile characterization tool for calcium sulphoaluminate cements: A compositional and hydration study, J. Mater. Sci. 42 (2007) 8426–8432. doi:10.1007/s10853-007-1790-8.

[144] I.G. Richardson, Tobermorite/jennite- and tobermorite/calcium hydroxide-based models for the structure of C-S-H: applicability to hardened pastes of tricalcium silicate, β-dicalcium silicate, Portland cement, and blends of Portland cement with blast-furnace slag, metakaolin, or silica fume, Cem. Concr. Res. 34 (2004) 1733–1777. doi:10.1016/j.cemconres.2004.05.034.

[145] S. Sahu, D.L. Exline, M.P. Nelson, Identification of thaumasite in concrete by Raman chemical imaging, Cem. Concr. Compos. 24 (2002) 347–350. doi:10.1016/S0958-9465(01)00086-5.

[146] K.N. Jallad, M. Santhanam, M.D. Cohen, D. Ben-Amotz, Chemical mapping of thaumasite formed in sulfate-attacked cement mortar using near-infrared Raman imaging microscopy, Cem. Concr. Res. 31 (2001) 953–958. doi:10.1016/S0008-8846(01)00514-2.

[147] Y. Yue, J. Jing, P.A.M. Basheer, J.J. Boland, Y. Bai, Characterisation of carbonated Portland cement paste with optical fibre excitation Raman spectroscopy, Constr. Build. Mater. 135 (2017) 369–376. doi:10.1016/j.conbuildmat.2017.01.008.

[148] S.P. Newman, S.J. Clifford, P. V. Coveney, V. Gupta, J.D. Blanchard, F. Serafin, D. Ben-Amotz, S. Diamond, Anomalous fluorescence in near-infrared Raman spectroscopy of cementitious materials, Cem. Concr. Res. 35 (2005) 1620–1628. doi:10.1016/j.cemconres.2004.10.001.

[149] S. Martinez-Ramirez, S. Sanchez-Cortes, J. V. Garcia-Ramos, C. Domingo, C. Fortes, M.T. Blanco-Varela, Micro-Raman spectroscopy applied to depth profiles of carbonates formed in lime mortar, Cem. Concr. Res. 33 (2003) 2063–2068. doi:10.1016/S0008-8846(03)00227-8.

[150] F. Liu, Z. Sun, Chemical mapping of cement pastes by using confocal Raman spectroscopy, Front. Struct. Civ. Eng. 10 (2015) 168–173. doi:doi.org/10.1007/s1170.

[151] X. Cong, R.J. Kirkpatrick, ^{29}Si and ^{17}O NMR investigation of the structure of some crystalline calcium silicate hydrates, Adv. Cem. Based Mater. 3 (1996) 133–143. doi:10.1016/S1065-7355(96)90045-0.

[152] A. Peyvandi, D. Holmes, P. Soroushian, A.M. Balachandra, Monitoring of sulfate attack in concrete by Al^{27} and Si^{29} MAS NMR spectroscopy, J. Mater. Civ. Eng. 27 (2014) 04014226. doi:10.1061/(ASCE)MT.1943-5533.0001175.

[153] M.D. Andersen, H.J. Jakobsen, J. Skibsted, A new aluminium-hydrate species in hydrated Portland cements characterized by ^{27}Al and ^{29}Si MAS NMR spectroscopy, Cem. Concr. Res. 36 (2006) 3–17. doi:10.1016/j.cemconres.2005.04.010.

[154] A. Mendes, W.P. Gates, J.G. Sanjayan, F. Collins, NMR, XRD, IR and synchrotron NEXAFS spectroscopic studies of OPC and OPC/slag cement paste hydrates, Mater. Struct. Constr. 44 (2011) 1773–1791. doi:10.1617/s11527-011-9737-6.

[155] L. Bonizzoni, V. Brunello, S. Caglio, Scientific analyses beyond the excavation: studies for a non invasive preliminary approach, (2013) 477–487. doi:10.2451/2013PM0028.

[156] D. Ergenç, R. Fort, Multi-technical characterization of Roman mortars from Complutum, Spain, 147 (2019). doi:10.1016/j.measurement.2019.106876.

[157] V. Cnudde, M.N. Boone, High-resolution X-ray computed tomography in geosciences: A review of the current technology and applications, Earth-Science Rev. 123 (2013) 1–17. doi:10.1016/j.earscirev.2013.04.003.

[158] P. Klobes, H. Riesemeier, K. Meyer, J. Goebbels, K.-H. Hellmuth, Rock porosity determination by combination of X-ray computerized tomography with mercury porosimetry, Fresenius. J. Anal. Chem. 357 (1997) 543–547. doi:10.1007/s002160050210.

[159] B. Laforce, B. Masschaele, M.N. Boone, D. Schaubroeck, M. Dierick, B. Vekemans, C. Walgraeve, C. Janssen, V. Cnudde, L. Van Hoorebeke, L. Vincze, Integrated Three-Dimensional Microanalysis Combining X-Ray Microtomography and X-Ray Fluorescence Methodologies, Anal. Chem. 89 (2017) 10617–10624. doi:10.1021/acs.analchem.7b03205.

[160] B. Masschaele, M. Dierick, D. Van Loo, M.N. Boone, HECTOR : A 240kV micro-CT setup optimized for HECTOR: A 240kV micro-CT setup optimized for research, (2013). doi:10.1088/1742-6596/463/1/012012.

[161] E. Pereira, Evaluation of porosity in mortar by X-ray microtomography (Micro-CT) as an additional tool for mercury intrusion, (2014) 18–28.

[162] V. Cnudde, J.P. Cnudde, C. Dupuis, P.J.S. Jacobs, X-ray micro-CT used for the localization of water repellents and consolidants inside natural building stones, 53 (2004) 259–271. doi:10.1016/j.matchar.2004.08.011.

[163] L. Korat, V. Ducman, A. Legat, B. Mirtič, Characterisation of the pore-forming process in lightweight aggregate based on silica sludge by means of X-ray micro-tomography (micro-CT) and mercury intrusion porosimetry (MIP), Ceram. Int. 39 (2013) 6997–7005. doi:10.1016/j.ceramint.2013.02.037.

[164] S. Hemes, G. Desbois, J.L. Urai, B. Schröppel, J.-O. Schwarz, Multi-scale characterization of porosity in Boom Clay (HADES-level, Mol, Belgium) using a combination of X-ray μ-CT, 2D BIB-SEM and FIB-SEM tomography, Microporous Mesoporous Mater. 208 (2015) 1–20. doi:10.1016/j.micromeso.2015.01.022.

[165] V. Cnudde, J. Dewanckele, M. Boone, T. de Kock, M. Boone, L. Brabant, M. Dusar, M. de Ceukelaire, H. de Clercq, R. Hayen, P. Jacobs, High-resolution X-ray CT for 3D petrography of ferruginous sandstone for an investigation of building stone decay, Microsc. Res. Tech. 74 (2011) 1006–1017. doi:10.1002/jemt.20987.

[166] M. Lanzón, V. Cnudde, T. de Kock, J. Dewanckele, X-ray microtomography (μ-CT) to evaluate microstructure of mortars containing low density additions, Cem. Concr. Compos. 34 (2012) 993–1000. doi:10.1016/j.cemconcomp.2012.06.011.

[167] E. Salavessa, S. Jalali, L.M.O. Sousa, L. Fernandes, A.M. Duarte, Historical plasterwork techniques inspire new formulations, Constr. Build. Mater. (2013). doi:10.1016/j.conbuildmat.2013.07.064.

[168] G. Cultrone, E. Sebastián, K. Elert, M.J. de la Torre, O. Cazalla, C. Rodriguez-Navarro, Influence of mineralogy and firing temperature on the porosity of bricks, J. Eur. Ceram. Soc. 24 (2004) 547–564. doi:10.1016/S0955-2219(03)00249-8.

[169] A.B. Abell, K.L. Willis, D.A. Lange, Mercury intrusion porosimetry and image analysis of cement-based materials, J. Colloid Interface Sci. 211 (1999) 39–44. doi:10.1006/jcis.1998.5986.

[170] T. Cai, Z. Feng, D. Zhou, T. Cai, Z. Feng, D. Zhou, Multi-scale characteristics of coal structure by X-ray computed tomography (X-ray CT), scanning electron microscope (SEM) and mercury intrusion porosimetry (MIP) Multi-scale characteristics of coal structure by x-ray computed tomography (X-ray CT), 025324 (2018). doi:10.1063/1.5021699.

[171] V. Cnudde, J.A.N. Dewanckele, M. Boone, T. De. Kock, M. Boone, L. Brabant, M. Dusar, M.D.E. Ceukelaire, H.D.E. Clercq, R. Hayen, P. Jacobs, High-Resolution X-Ray CT for 3D Petrography of Ferruginous Sandstone for an Investigation of Building Stone Decay, 1017 (2011) 1006–1017. doi:10.1002/jemt.20987.

CHAPTER 2

Materials and Methods

Preparation of specimens

A set of 4.5×2.5×1cm specimens were prepared (tables 6-10) with different mix designs based on recipes selected from the literature [1–26]. The dimension of the samples was chosen to have small samples in order to facilitate the re-carbonation of the binders in the bulk of the samples.

The specimens of pure binder were prepared with dispersing aerial lime putty, Portland cement, pozzolanic cement, natural hydraulic lime or gypsum in a measured amount of water in order to obtain the proper workability [27,28], and then the mix was poured into silicone moulds. The raw materials were taken from those commercially available and traditionally used in restoration practice.

From these prepared specimens of pure binder, the spectra of a single component not influenced by aggregate compound peaks could be recorded. Then the specimens with the aggregate (either carbonate or quartz, to study separately their possible contribution to the aggregate) were prepared. The binder/aggregate ratio was 1:3 (weight/weight) it was closed among the most diffused proportion found in literature. The type of quartz sand used for the specimens was a standard sand (referred to as "quartz sand" in the text) according to UNI EN 196–1 (standard quartz sand with controlled granulometry and constant mineralogical composition). This sand was sieved in order to have a grain size distribution similar to that carbonate sand. The carbonate sand was bought from a supplier specialized in restoration product. The grain size of this type of sand is 0,063-0,5mm and 0,7-1,2mm because of they sell the sand in two different bins. The samples were prepared according to UNI EN 196-1.

The set was prepared in a steady environment room at 20 °C and 65% of RH [29]. The specimens with aerial binders were then removed from the mould and cured in the same environmental conditions for 6 months (65% of RH at 20 °C). The cements and natural hydraulic mortars were cured at 90% of RH and 20 °C, according to EN196 [30]. 6 months were chosen as a compromise between the long carbonation times and the technical times for carrying out the analyzes, furthermore, this aspect was considered during the interpretation of the results. Thus, each specimen presents two different surfaces, and the one originally in contact with the silicon mould was smoother than that in contact with the external air, which was rougher by a naked eye observation. A further roughness level was prepared using coarse sandpaper (P180) on one of the remaining faces in order to study the effect of the roughness in ER-FTIR analysis on a "controlled" surface roughness.

Mixes made of one specific binder

Binder 1 (B1)	Binder 2 (B2)	B/water (w/w)	Label
Lime putty	-	-	**G**
Hydrated lime	-	100:67	**C**
CEM I	-	100:50	**CI**
CEM IV	-	100:50	**CIV**
Gypsum	-	100:55	**Gs**
NHL 3.5	-	100:55	**N**

Mixes made of two specific binders

Binder 1 (B1)	Binder 2 (B2)	B1/B2 (w/w)	B/Water (w/w)	Label
Lime putty	NHL 3.5	50:50	100:27.5	**GN**
Lime putty	CEM I	50:50	100:25	**GCI**
Lime putty	CEM IV	50:50	100:25	**GCIV**
Lime putty	Gypsum	50:50	100:27.5	**GGs**
Hydrated lime	NHL 3.5	50:50	100:61	**CN**
Hydrated lime	CEM I	50:50	100:58.5	**CCI**
Hydrated lime	CEM IV	50:50	100:58.5	**CCIV**
Hydrated lime	Gypsum	50:50	100:61	**CGs**
NHL 3.5	CEM I	50:50	100:52.5	**NCI**
NHL 3.5	CEM IV	50:50	100:52.5	**NCIV**
NHL 3.5	Gypsum	50:50	100:55	**NGs**

Table 6. Model samples made of one specific binder and mixes made of two specific binders.

Mortars with quartz aggregate

Binder	Aggregate	B/Water (w/w)	B/Ag (w/w)	Label
Lime putty	quartz sand	-	1:3	**GQ**
Hydrated lime	quartz sand	100:67	1:3	**CQ**
CEM I	quartz sand	100:50	1:3	**CIQ**
CEM IV	quartz sand	100:50	1:3	**CIVQ**
Gypsum	quartz sand	100:55	1:3	**GsQ**
NHL 3.5	quartz sand	100:55	1:3	**NQ**

Table 7. Model samples made of one specific binder and quartz aggregate.

Mixed mortars with quartz aggregate

Binder 1 (B1)	Binder 2 (B2)	Aggregate	B1/B2 (w/w)	B/Water (w/w)	B/Ag (w/w)	Label
Lime putty	NHL 3.5	quartz sand	50:50	100:31.5	1:3	**GNQ**
Lime putty	CEM I	quartz sand	50:50	100:25	1:3	**GCIQ**
Lime putty	CEM IV	quartz sand	50:50	100:25	1:3	**GCIVQ**
Lime putty	Gypsum	quartz sand	50:50	100:27.5	1:3	**GGsQ**
Hydrated lime	NHL 3.5	quartz sand	50:50	100:61	1:3	**CNQ**
Hydrated lime	CEM I	quartz sand	50:50	100:58	1:3	**CCIQ**
Hydrated lime	CEM IV	quartz sand	50:50	100:58	1:3	**CCIVQ**
Hydrated lime	Gypsum	quartz sand	50:50	100:61	1:3	**CGsQ**
NHL 3.5	CEM I	quartz sand	50:50	100:52.5	1:3	**NCIQ**
NHL 3.5	CEM IV	quartz sand	50:50	100:52.5	1:3	**NCIVQ**
NHL 3.5	Gypsum	quartz sand	50:50	100:55	1:3	**NGsQ**

Table 8. Model samples made of two specific binders and quartz sand.

Mortars with quartz aggregate

Binder	Aggregate	B/Water (w/w)	B/Ag (w/w)	Label
Lime putty	carbonate sand	-	1:3	**GM**
Hydrated lime	carbonate sand	100:67	1:3	**CM**
CEM I	carbonate sand	100:50	1:3	**CIM**
CEM IV	carbonate sand	100:50	1:3	**CIVM**
Gypsum	carbonate sand	100:55	1:3	**GsM**
NHL 3.5	carbonate sand	100:55	1:3	**NM**

Table 9. Model samples made of one specific binder and carbonate sand.

Mixed mortars with quartz aggregate

Binder 1 (B1)	Binder 2 (B2)	Aggregate	B1/B2 (w/w)	B/Water (w/w)	B/Ag (w/w)	Label
Lime putty	NHL 3.5	carbonate sand	50:50	100:31.5	1:3	**GNM**
Lime putty	CEM I	carbonate sand	50:50	100:25	1:3	**GCIM**
Lime putty	CEM IV	carbonate sand	50:50	100:25	1:3	**GCIVM**
Lime putty	Gypsum	carbonate sand	50:50	100:27.5	1:3	**GGsM**
Hydrated lime	NHL 3.5	carbonate sand	50:50	100:61	1:3	**CNM**
Hydrated lime	CEM I	carbonate sand	50:50	100:58	1:3	**CCIM**
Hydrated lime	CEM IV	carbonate sand	50:50	100:58	1:3	**CCIVM**
Hydrated lime	Gypsum	carbonate sand	50:50	100:61	1:3	**CGsM**
NHL 3.5	CEM I	carbonate sand	50:50	100:52.5	1:3	**NCIM**
NHL 3.5	CEM IV	carbonate sand	50:50	100:52.5	1:3	**NCIVM**
NHL 3.5	Gypsum	carbonate sand	50:50	100:55	1:3	**NGsM**

Table 10. Model samples made of two specific binders and carbonate sand.

Analytical techniques

Optical microscopy and petrographic analysis

Optical microscopy was performed with a Zeiss Axioscope A.1 equipped with an Axiocam camera and Axiovision software. The sections were prepared to have 30μm thickness. The abundancy of the different components was measured by point counting using JMicrovision freeware. The point counting analysis was performed with JMicroVision software using 200 points and a random grid. Before performing point counting, the classes of selection were created.

X-Ray Diffractometry (XRD)

For each test, three diffractions were made to study the reproducibility of the method, depositing each time a new aliquot of powder in the circular aluminium sample holder. For a test, three repeated tests were performed on the same powder in the sample older of the same sample always to study the reproducibility of the method. The X-ray diffraction instrument used in this study requires about one gram of finely grounded sample. The obtained diffractograms were analysed using the PDXL2 software, which also enabled the recognition of the phases present by comparing with the ICDD-PDF2 and COD databases. The results obtained were also verified by further comparison with paper databases.
A particular attention was given to samples containing cement. After the first scans with Miniflex were performed some scanes with high resolution XRD D8 Bruker that is 40kv 40A and for a longer time to see if the change of the instrument could improve the results. The results are showed in the next chapter (Chapter 3).
The X-ray diffraction analyses were conducted on samples ground, using a Rigaku Miniflex 300 diffractometer (30 kV, 10 mA, Cu-Kα radiation (λ = 1.5418Å), 5-75° Theta/2-Theta, step scan 0.02°, scan speed 3°/min attachment: Standard; Scan axis Theta/2-Theta; Filter scan range: 5.0000 - 75.0000 deg; CBO selection slit-Incident slit; diffracted beam mono; Length limiting slit 10.0mm; detector receiving slit # 1, 1.250deg; Scan mode CONTINUOUS; receiving slit # 2 0.3mm.). PDXL2 software, supporting the International Centre for Diffraction Data (ICDD) PDF2 databases, was used to identify the phases in each diffractogram, by comparing experimental peaks with reference patterns.
D8 Brucker for long measurements, data parameters:
Bruker AXS D8 Advance diffractometer, acquiring data at room temperature in the 4.0–85.0° 2θ range, with steps of 0.02°, and time per step of 1s. Microcrystalline powders of the samples were deposited in the hollow of a silicon zero-background plate 0.2 mm deep. Data acquisitions of Zn-H/NO_2 S and Zn-H/NO_2/NH_2 S were performed on a vertical-scan Bruker AXS D8 Advance θ:θ diffractometer, equipped with a Lynxeye linear position-sensitive detector, an X-ray tube (CuKa, l = 1.5418 Å), a filter of nickel in the diffracted beam and the following optical components: primary beam Soller slits (2.5°), fixed divergence slit (0.5°), antiscatter slit (8 mm). The generator was set at 40 kV and 40 mA.

Infrared spectroscopy

FTIR analyses in external reflection mode FTIR measurements were conducted using an Alpha Bruker FTIR portable spectrophotometer in reflection mode for contactless measurements and a DTGS detector. Spectra were collected between 7500 and 375cm^{-1} with 4cm^{-1} resolution and 200 scans. The background was periodically acquired using a flat gold mirror. The measured area was about 6 mm in diameter. The finest tuning was achieved via software, looking for the maximum signal directly in the interferogram.

Spectra were processed using the pseudoabsorbance [log(1/R); R = reflectance] as the intensity unit. Data were analyzed using an homemade database of minerals, raw materials and bibliographic resources. For each face of the specimens, five spectra were acquired at different points to evaluate the repetitiveness of the analysis and to examine as much surface as possible in the study.

FTIR analyses in transmission and ATR mode spectra were recorded with a Thermo Scientific Nicolet iS10 instrument in the 4000-600cm^{-1} range (ATR) and 4000-400cm-1 (transmission), with a resolution of 4 cm^{-1}, 32 scans. With regard to the ATR analysis, a diamond crystal was used, while the pellets for transmission mode were prepared using a sample/KBr dilution of 1/20. Prior to each specimen a background analysis was performed, whose spectrum was automatically used to correct the measurement. The samples were ground in an automatic ball grinder for 5-7 minutes at intensity 1 (Pulverisette 0 FRITSCH) [31].

The micro FTIR (μFTIR) analyses were performed by a Thermo Scientific Nicolet Nexus spectrophotometer equipped with a DTGS detector (spectral range 4000–400 cm^{-1}) coupled with a Continuμm™ infrared microscope with mercury cadmium telluride detector (MCT/A) cooled with liquid nitrogen (spectral range 4000–650cm^{-1}). The spectral resolution used was 4cm^{-1}, with accumulations of 128 scans. The samples were embedded in polished cross section and analysed in external reflection mode. The background was collected on a golden coated plate.

Raman Spectroscopy

Micro-Raman analyses on binder specimens were performed with a Bruker Senterra instrument, whose settings were changed from time to time as needed. The specimens were analyzed using the fragments as they are and embed in the epoxy resin. The settings of the instrument are as follows:

The experiments were carried out using a Senterra dispersive Raman microscope (Bruker Optik GmbH). The spectral resolution is about 9-15cm^{-1} (400 grooves/mm gratings). The most used conditions are the following: laser 532 nm, output power 5-50 mW laser, microscope objective 50x LWD e 100x, acquisition time 0.2-10s e 10-80 coadditions, pinhole 50 micron.

When with 532 nm there was florescence (samples N, CIVQ, NQ) the 785nm laser was used, with objective 50x LWD e 100x, acquisition time from 10 to 100 mW, 2-10s 10-50 coadditions, pinhole 50 micron.

Environmental Scanning Electron Microscope (ESEM)

Analysis by Environmental Scanning Electron Microscopy and elemental analysis samples were performed by an electronic microscope from FEI/Philips, model XL30 ESEM in low vacuum mode (1torr H2O) at 20kV acceleration potential, using the backscattered electron detector (BSE). Elemental analysis was performed by an energy dispersive X-ray spectrophotometer from Ametek Element.

Thermal analysis

Termogravimetric analysis and differential scanning calorimetry were performed together, with the same instrument (Netzsch sta 409 pc/pg) on 40 mg of powder for each sample. The powder used for the analysis was taken from the powder previously analysed with XRD. At least 10-40mg of grinded sample are required, for the analysis was used 40mg. A NETZSCH STA 409 PC/PG was used for TG-DSC analysis, with N_2 fluxes of 20 and 40 ml/min respectively with a temperature ratio of 20/10.0(K/min)/900.

Microstructure analysis

The microstructure analysis was focussed on porosity analysis. A selection of the samples made with one binder and the two types of the aggregate were analysed. The choice was performed selecting six samples of mortars with quartz aggregate and one specific type pf mortar and other six samples with the same binder but with carbonate aggregate. This selection was done in order to test the influence of the aggregate in the samples structure and also to study the porosity of the different binder used. In fact in this section the microstructure analysis done with MIP are compared to ones done with X-ray computed tomography to evaluate the similarity and the differences between the two techniques.

Mercury intrusion porosimetry (MIP)

Mercury intrusion porosimetry (MIP) was carried out using a Thermo Scientific PASCAL 140 and PASCAL 240. The measuring range (pressure) is 0.1-200 Mpa, the resolution (pressure) is from 0.01 Mpa to 100 Mpa and from 100 to 200 Mpa. The accuracy >0.2% while the resolution in volume is 0.1 mm3. The measuring range radius is between 7.5 and 3.7 X 10-3 microns. For each specimen two samples were analysed with this technique.

Computed tomography (μ-CT)

X-ray Computed microtomography (μCT) images were measured on the custom-built HECTOR scanner at the Centre for X-ray Tomography of Ghent University (UGCT). This scanner rotates the sample 360° during the analysis, and geometric settings resulted in a voxel size of 10 micron. Images were obtained with an X-ray tube operated at 160kV and 10W, equipped with a 1mm Al filter and by taking 1401 frames. Beam hardening was reduced by the presence of a 1 mm Al filter between the X-ray source and the sample. Octopus Reconstruction and Octopus Analysis were used for reconstruction and image analysis respectively. VGStudio was used for 3D visualizationn [32–35].

For the calculation of the sphericity only voids with at least 3 voxels of equivalent diameter were considered in order to exclude the smallest volumes that could produce error in the calculation. The program Octopus analysis calculates the equivalent diameter as “the diameter of a sphere with the same number of voxels as the object” and the maximum opening as “the diameter of the largest inscribed sphere in the object (only possible if the Distance transform is determined)”.

References

[1] A. Bakolas, G. Biscontin, A. Moropoulou, E. Zendri, Characterization of structural byzantine mortars by thermogravimetric analysis, Thermochim. Acta. 321 (1998) 151–160. doi:10.1016/S0040-6031(98)00454-7.

[2] A. Rattazzi, Conosci il grassello di calce? Origine, produzione e impiego del grassello in architettura, nell'arte e nel restauro, Edicom, 2007. http://books.google.es/books?id=4zq_HwAACAAJ.

[3] C. Arcolao, Le ricette del restauro: malte, intonaci, stucchi dal XV al XIX secolo, Marsilio Editori, 1998.

[4] L. Binda, G. Baronio, S.E.D. of the P. di Milano, Studies on Mortars Sampled from Historic Buildings: Selected Papers 1983 - 1999, Structural Engineering Department of the Politecnico di Milano, 1983.

[5] L. Zevi, Il manuale del restauro architettonico, Mancosu, 2002.

[6] V. Pollio, M.H. Morgan, H.L. Warren, Vitruvius, the Ten Books on Architecture, Harvard University Press, 1914.

[7] C. Cennini, II libro dell'arte, 1971.

[8] Montagna, Giordani, I laganti, n.d.

[9] E. Salavessa, S. Jalali, L.M.O. Sousa, L. Fernandes, A.M. Duarte, Historical plasterwork techniques inspire new formulations, Constr. Build. Mater. (2013). doi:10.1016/j.conbuildmat.2013.07.064.

[10] C. Genestar, C. Pons, Ancient covering plaster mortars from several convents and Islamic and Gothic palaces in Palma de Mallorca (Spain). Analytical characterisation, J. Cult. Herit. 4 (2003) 291–298. doi:10.1016/j.culher.2003.02.001.

[11] Turco Antonio, Il gesso, Hoepli, 1996.

[12] E. Navrátilová, P. Rovnaníková, Pozzolanic properties of brick powders and their effect on the properties of modified lime mortars, Constr. Build. Mater. 120 (2016) 530–539. doi:10.1016/j.conbuildmat.2016.05.062.

[13] D. Gulotta, S. Goidanich, C. Tedeschi, T.G. Nijland, L. Toniolo, Commercial NHL-containing mortars for the preservation of historical architecture. Part 1: Compositional and mechanical characterisation, Constr. Build. Mater. 38 (2013) 31–42.

[14] P. López-Arce, M. Tagnit-Hammou, B. Menéndez, J.-D. Mertz, A. Kaci, Durability of stone-repair mortars used in historic buildings from Paris, Mater. Struct. 49 (2016) 5097–5115. doi:10.1617/s11527-016-0846-0.

[15] J. Hormes, A. Diekamp, W. Klysubun, G.L. Bovenkamp, N. Börste, The characterization of historic mortars: A comparison between powder diffraction and synchrotron radiation based X-ray absorption and X-ray fluorescence spectroscopy, Microchem. J. 125 (2016) 190–195. doi:10.1016/j.microc.2015.11.034.

[16] C. Nunes, Z. Slížková, Hydrophobic lime based mortars with linseed oil: Characterization and durability assessment, Cem. Concr. Res. 61–62 (2014) 28–39. doi:10.1016/j.cemconres.2014.03.011.

[17] C. Ince, M.A. Carter, M.A. Wilson, A. El-Turki, R.J. Ball, G.C. Allen, N.C. Collier, Analysis of the abstraction of water from freshly mixed jointing mortars in masonry construction, Mater. Struct. 43 (2010) 985–992. doi:10.1617/s11527-009-9560-5.

[18] R. Ylmén, L. Wadsö, I. Panas, Insights into early hydration of Portland limestone cement from infrared spectroscopy and isothermal calorimetry, Cem. Concr. Res. 40 (2010) 1541–1546. doi:10.1016/j.cemconres.2010.06.008.

[19] B. Lothenbach, G. Le, E. Gallucci, K. Scrivener, Influence of limestone on the hydration of Portland cements, 38 (2008) 848–860. doi:10.1016/j.cemconres.2008.01.002.

[20] M.R. Veiga, A. Velosa, A. Magalhães, Experimental applications of mortars with pozzolanic additions: Characterization and performance evaluation, Constr. Build. Mater. 23 (2009) 318–327. doi:10.1016/j.conbuildmat.2007.12.003.

[21] E. Pecchioni, F. Fratini, E. Cantisani, Le Malte Antiche e Moderne tra Tradizione ed Innovazione, Pàtron, Bologna, 2008.

[22] M. Arandigoyen, J.I. Alvarez, Pore structure and mechanical properties of cement–lime mortars, Cem. Concr. Res. 37 (2007) 767–775.

[23] A. Moropoulou, A. Bakolas, P. Moundoulas, E. Aggelakopoulou, S. Anagnostopoulou, Strength development and lime reaction in mortars for repairing historic masonries, 27 (2005) 289–294. doi:10.1016/j.cemconcomp.2004.02.017.

[24] J. Lanas, J.L.P. Bernal, M.A. Bello, J.I.A. Galindo, Mechanical properties of natural hydraulic lime-based mortars, Cem. Concr. Res. 34 (2004) 2191–2201. doi:10.1016/j.cemconres.2004.02.005.

[25] A. Bakolas, G. Biscontin, V. Contardi, E. Franceschi, A. Moropoulou, D. Palazzi, E. Zendri, Thermoanalytical research on traditional mortars in venice, Thermochim. Acta. 269–270 (1995) 817–828. doi:10.1016/0040-6031(95)02574-X.

[26] C. Montagni, Materiali per il restauro e la manutenzione, UTET, 2000.

[27] Ente italiano di normazione, UNI EN 459-2:2010 Building lime - Part 2: Test methods, (2010).

[28] Ente italiano di normazione, UNI EN 13279-2:2014 Gypsum binders and gypsum plasters Part 2: Test methods, (2014).

[29] EN 1015-11: 1999 - Methods of Test for Mortar for Masonry, 1999.

[30] EN 196 - Methods of testing cement - Part I, 2005.

[31] V. Brunello, C. Corti, A. Sansonetti, C. Tedeschi, L. Rampazzi, Non-invasive FTIR study of mortar model samples: comparison among innovative and traditional techniques, Eur. Phys. J. Plus. 134 (2019) 270. doi:10.1140/epjp/i2019-12667-1.

[32] J. Vlassenbroeck, M. Dierick, B. Masschaele, V. Cnudde, L. Van Hoorebeke, P. Jacobs, Software tools for quantification of X-ray microtomography at the UGCT, 580 (2007) 442–445. doi:10.1016/j.nima.2007.05.073.

[33] L. Brabant, J. Vlassenbroeck, Y. De Witte, V. Cnudde, M.N. Boone, J. Dewanckele, L. Van Hoorebeke, Three-Dimensional Analysis of High-Resolution X-Ray Computed Tomography Data with Morpho+, Microsc. Microanal. 17 (2011) 252–263. doi:10.1017/S1431927610094389.

[34] B.C. Masschaele, V. Cnudde, M. Dierick, P. Jacobs, UGCT : New X-ray radiography and tomography facility, 580 (2007) 266–269. doi:10.1016/j.nima.2007.05.099.

[35] B. Masschaele, M. Dierick, D. Van Loo, M.N. Boone, HECTOR : A 240kV micro-CT setup optimized for HECTOR : A 240kV micro-CT setup optimized for research, (2013). doi:10.1088/1742-6596/463/1/012012.

CHAPTER 3

RAW MATERIALS CHARACTERIZATION

The raw materials compositions are according to EN 459-1 [1] and EN 197-1 [2]. The X-ray diffraction, infrared spectroscopy and thermal analyses were performed to characterize their compositions, and to have reference sample for future analysis and of the unhydrated phases. Unfortunately it was not possible to analyze lime putty because of its quick hardening; in fact, for example, in powder X-ray diffraction, during the analysis the sample started to carbonate and all the peaks appear shifted and impossible to be interpreted. In any case the analysis was possible on the hydrated paste made with one binder: lime putty. They were analyzed with different techniques to detect impurities or, as in the case of reflection infrared spectroscopy, to study the response of the instruments to these materials.

The raw materials are:

- Lime putty
- Hydrated lime
- Natural hydraulic lime 3.5 (NHL 3.5)
- Portland cement (CEM I)
- Pozzolanic cement (CEM IV)
- Bassanite commercially sold as “gesso alabastrino”
- Quartz sand
- Carbonate sand (commercially sold as “polvere di marmo” with two particle size ranges mixed together 0.063<Ø<0.5 and 0.7<Ø<1.2. They were mixed together because commercially they were sold separately).

Powder X-ray diffraction (PXRD)

The main phases identified are listed in table 11, from the more intense to the less intense. Figures 1 - 3 show the diffraction pattern of CEM IV, CEM I and NHL 3.5 respectively. In some cases some phases could not have been discriminated because of the overlap of the main diffraction peaks. This the case for larnite (C_2S) (Ca_2SiO_4), hatrurite (C_3S) (Ca_3SiO_5) and calcite ($CaCO_3$). Larnite [00-033-0302] presents its main peaks at d-spacing [Å] 2.78 (max intensity), 2.74, 2.61 and 2.18 while hatrurite [01-086-0402] has its main peaks at 3.03, 2.77 (max intensity), 2.75, 2.74, 2.60 and 2.18 d-spacing [Å] in CEM I and CEM IV. Moreover, calcite presents some overlapping with these phases, as its main diffraction peak is at 3.06 d-spacing [Å] where overlaps with one of the most intense peak of hatrurite. The identification of C_3A is more doubtful because this phase presents numerous overlapping diffraction signals with all the other phases and the signals are very weak. The presence of mullite in CEM IV is uncertain because the peaks obtained are not intense, but its occurrence could be due to the presence of fly ashes in this type of cement.

	Mineralogical phases					
Hydrated lime	Calcite	Portlandite	Quartz			
"Gesso alabastrino	Bassanite	Dolomite	Anhydrite	Quartz		
CEM IV	Hatrurite/Larnite/ Calcite	Quartz	Gypsum	Brownmillerite	*C_3A (?)*	Mullite (?)
CEM I	Hatrurite/Larnite/ Calcite	Gypsum	Brownmil-lerite	*C_3A (?)*		
NHL 3.5	Calcite	Quartz	Portlandite	Hatrurite/Larnite		
Quartz sand	Quartz	Feldspar	Micas (?)			
Carbonate sand 0.063-0.5mm	Magnesian Calcite/Calcite	Quartz				
Carbonate sand 0.7-1.2mm	Magnesian Calcite/Calcite	Dolomite	Quartz			

Table 11. The mineralogical phases of the raw materials are written from left to right from the more intense to the weaker.

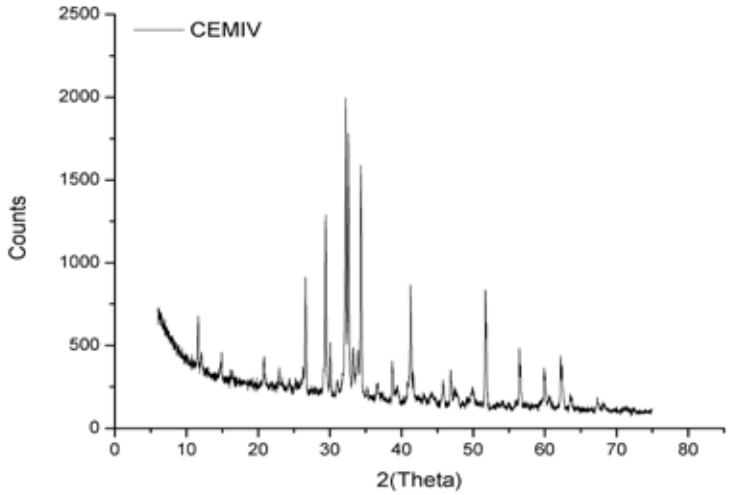

▲ *Figure 1. PXRD pattern of pozzolanic cement (CEMIV) raw material.*

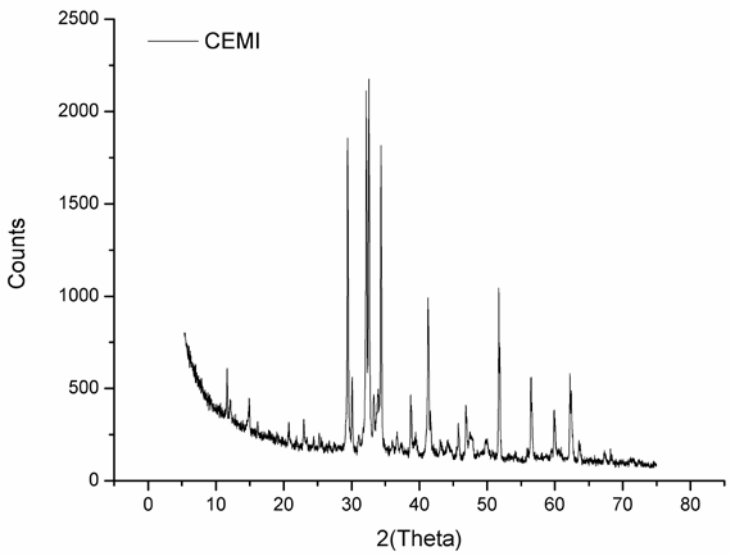

▲ *Figure 2. PXRD pattern of Portland cement (CEMI) raw material.*

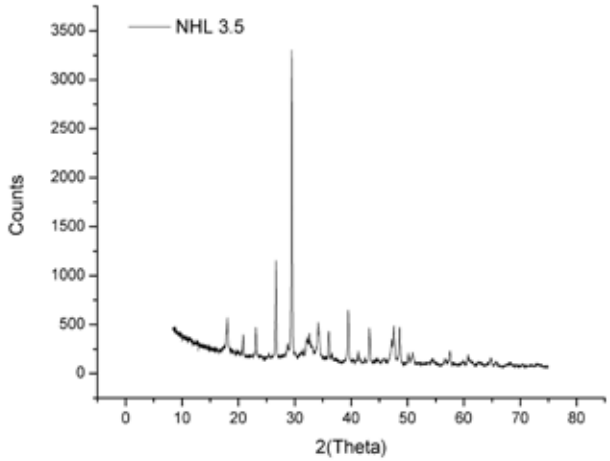

▲ *Figure 3. PXRD pattern of Natural hydraulic lime 3.5 raw material*

Infrared spectroscopy (transmission, ATR and external reflection mode)

Carbonate sand

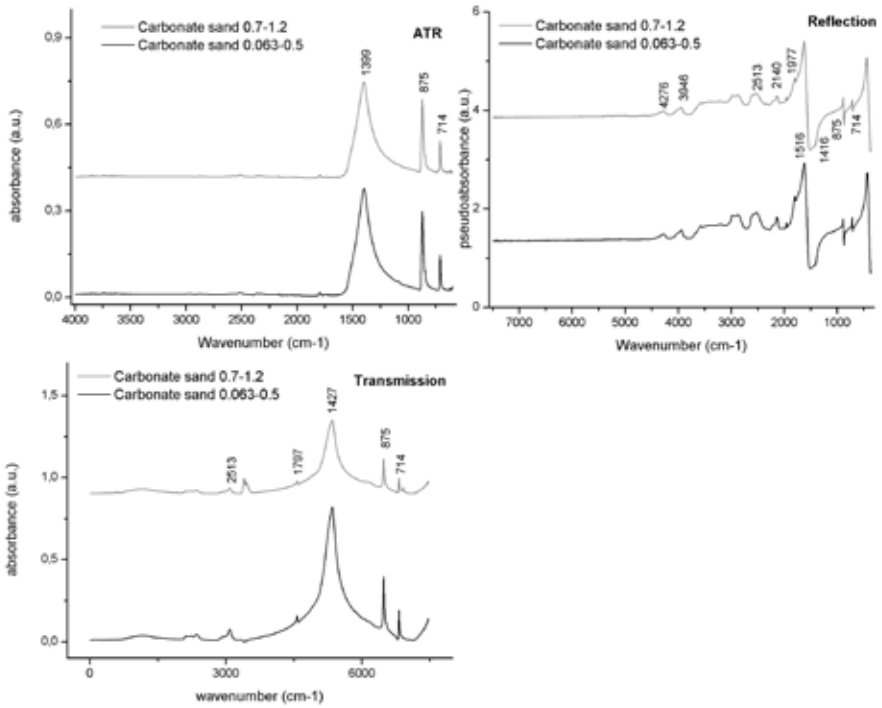

▲ *Figure 4. ATR, transmission and external reflection mode spectra of "Carbonate sand" 0.7 -1.2 (gray) and "Carbonate sand" 0.063 – 0.5 (black) of carbonate sand, with the main peaks.*

Figure 4 shows the spectra of the raw material in ATR, reflection and transmission. The peaks at 714cm^{-1} and 875cm^{-1} are clearly visible in transmission mode; they correspond to υ_4 CO_3^{2-} symmetric in-plane bending and υ_2 CO_3^{2-} out-of-plane asymmetric bending respectively [3–7]. These two signals are also visible in ATR mode (figure 4) and in reflection mode but in the latter, the peaks are derivative-shape. The intense band at 1427cm^{-1}, in transmission, is related to asymmetric stretching υ_3 CO_3^{2-} [3–8]; in ATR mode this peak shifts to 1399cm^{-1} [9] while in reflection mode the peak splits in its characteristic shape (peak at 1516 and 1416cm^{-1}) [10,11]. The peak at 1797cm^{-1} (υ_1+υ_4 CO_3^{2-} and/or overtone υ_2) [6,12–14] is visible in all the three modes of FTIR analysis.

The bands at about 2513cm^{-1} and its shoulder at 2594cm^{-1} are generally assigned to υ_1+υ_3 and/or 2υ_2+υ_4 (CO_3^{2-}) [6,7,10,12,13] is present in all the three FTIR methods used. The signals at 2875cm^{-1} and 2987cm^{-1} (2υ_3 and overtone) [6,14–16], are the same in all the three FTIR modes used, in ATR and transmission there is also a peak at 2924cm^{-1}, which is the combination band 2υ_3+47 [7] or 2υ_3 [6]. The peak at 1088cm-^{1} is assigned to the υ_1 CO_3^{-2} mode [4]. The peak at 3946cm^{-1} and the shoulder at 4005cm^{-1} are assigned to 2υ_3+υ_1 vibrations [17]. The peak at 4276cm^{-1} is the second overtone of υ(CO) [18,19] and the peak at 4630cm^{-1} is assigned to υ_1+υ_2+υ_3 or 3υ_1+2υ_4 [17], while the peak at 5000cm^{-1} is assigned to 2υ_1+2υ_3 of $CaCO_3$ [17].

Quartz sand

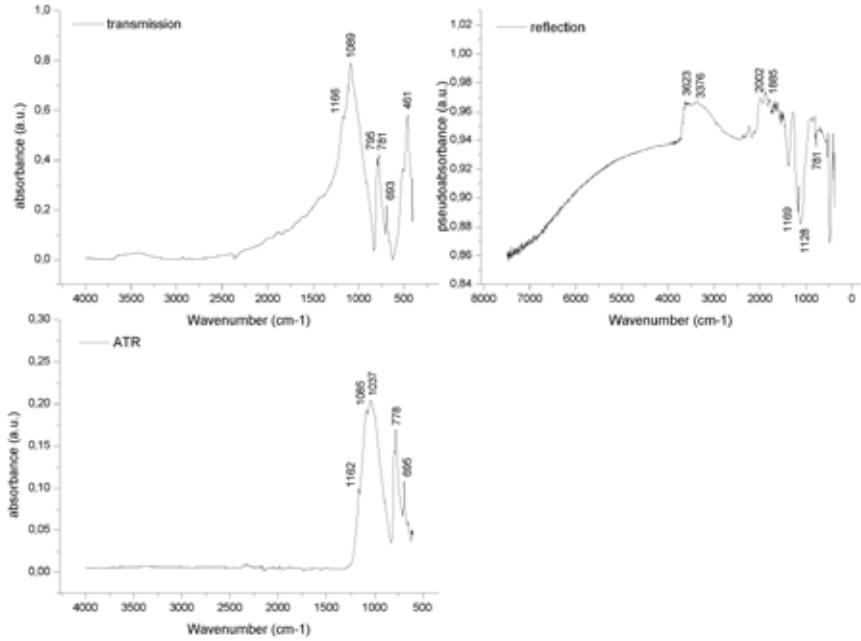

▲*Figure 5. Quartz sand in ATR, transmission and reflection mode FTIR spectroscopy, the main peaks are reported.*

The doublet at 781cm^{-1} and 798cm^{-1} is assigned to the Si–O symmetrical stretching vibrations. It is observed and it is visible in all the spectra (figure 5) [20–22]. The peak at 397cm^{-1} related to quartz [21,23] in transmission is visible. The peak at 461cm^{-1} with its shoulder at 514cm^{-1} (Si–O asymmetrical bending vibration) [20–22] is visible in transmission, while in reflection they are slightly shifted to 481 and 538cm^{-1} respectively. The peaks at 1085cm^{-1} and 1166cm^{-1} from Si–O asymmetrical stretching vibrations [20] are assigned to Si-O asymmetrical stretching vibrations; In ATR mode in this zone it is present also a peak at 1037cm^{-1} and this band could be due a splitting of quartz or to the presence of feldspar in the sand [21]. In reflection mode in the zone centered at 1161cm^{-1}, it is present the splitting at 1128 and 1169cm^{-1}. Also the peaks at 1885 and 2002cm^{-1} are also assigned to quartz phase. In reflection there is a small shoulder at 650cm^{-1} that could be related to the presence of minor feldspar [20–22].

Hydrated lime

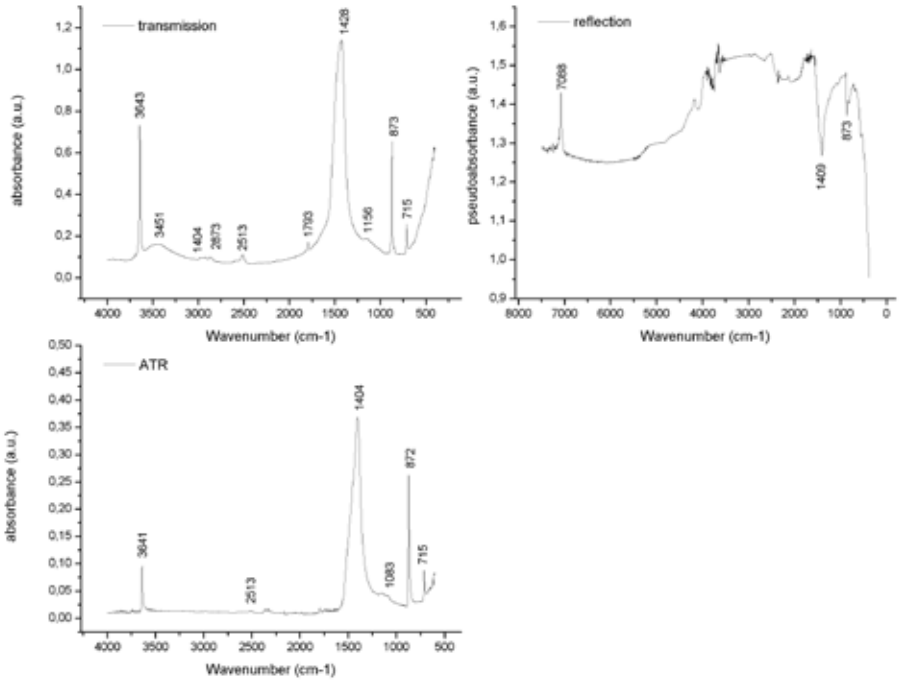

▲ *Figure 6. Hydrated lime spectra, in clockwise order from the bottom left: ATR, transmission and external reflection mode.*

The spectra in transmission and ATR mode are very similar (figure 6). In the hydrated lime there is also $CaCO_3$, as it is confirmed by X-ray diffraction analysis (table 1). In fact the main peaks of $CaCO_3$ are identified: the peaks at 715cm^{-1} (υ_4 CO_3^{2-} symmetric in-plane bending), 1428cm^{-1} (antisymmetric CO_3^{2-} stretching (υ_3)), 1793cm^{-1} (υ_1+υ_4 CO_3^{2-} and/or υ_2 overtone) and the bands at about 2513cm^{-1} and its shoulder at 2594cm^{-1} is generally assigned to υ_1+υ_3 and/or 2υ_2+υ_4 (CO_3^{2-}) [6,7,10,12,13]. The peak at 3643cm^{-1}, assigned to $Ca(OH)_2$ due to the O-H stretching of $Ca(OH)_2$, is also visible [14]. In reflection, this peak is slightly visible in this case because of the noise, but for example in sample C it is visible also in reflection. In reflection an additional peak assigned to $Ca(OH)_2$ is visible, it is at 7088cm^{-1}; its assignment is still uncertain, but it should be the first overtone of $Ca(OH)_2$ stretching mode [24–27].

Portland cement (CEM I)

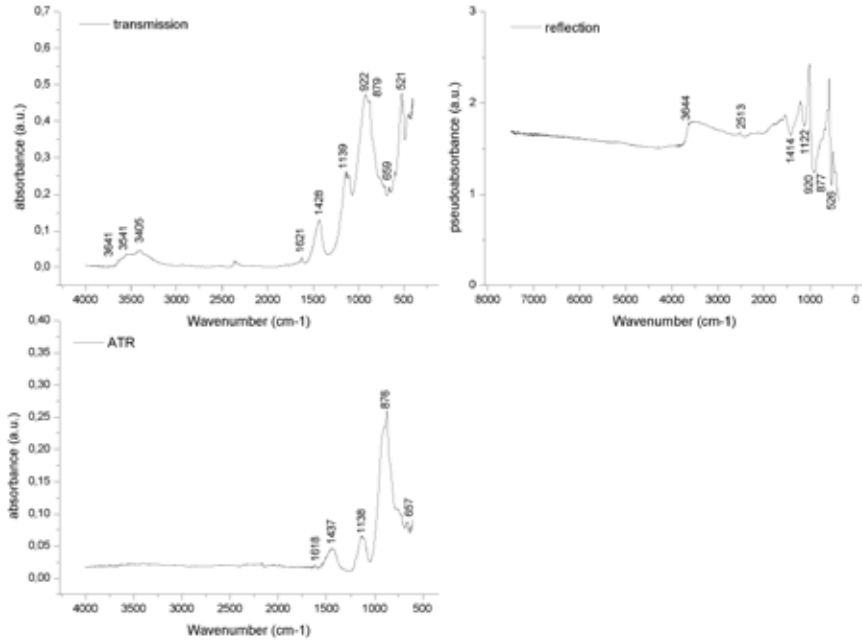

▲*Figure 7. Portland cement (CEM I) spectra, in clockwise order from the bottom left: ATR, transmission and external reflection mode.*

In all the spectra the peaks at 715cm^{-1} (υ_4 CO_3^{2-} symmetric in-plane bending), and 875cm^{-1} (υ_2 CO_3^{2-} out-of-plane asymmetric bending), 1428cm^{-1} (antisymmetric CO_3^{-2} stretching (υ_3)), 1793cm^{-1} (υ_1+υ_4 CO_3^{2-} and/or υ_2 overtone) [3,4,7,13], 2877 and 2985cm^{-1} [7–9,15,16] (overtones and combination bands of the 2υ_3 CO_3^{2-} stretching) are related to the presence of calcite in the sample. In the zone between 2850 and 2950cm^{-1} it could also be that C-H stretching that indicates the presence of organic compounds [3]. Portlandite is present, as it is identified by the peak at 3641cm^{-1}.

In the spectra, in figure 7, bassanite ($CaSO_4$ 0.5H_2O) is probably identified. It is recognized by the absorption signal corresponding to the υ_3 stretching vibrations SO_4^{2-} at 1095cm^{-1} and the shoulder at 1155cm^{-1} [16,28,29]. The peaks at 1124 and 1139cm^{-1} are connected to the presence of gypsum [9,29,30]. In transmission mode the peak at 659cm^{-1} is assigned to υ_4 asymmetric bending SO_4^{2-}, which shifts at 657cm^{-1} in ATR and at 661cm^{-1} in reflection mode; the previous one and the peak at 601cm^{-1}, υ_4 asymmetric bending SO_4^{2-} (in transmission, 597cm^{-1} in reflection, while in ATR it is not visible) could be related to the presence of both gypsum and bassanite. Looking at the zone of OH stretching, the absorption at 3608cm^{-1} could be due to the presence of bassanite [16,28,29]. The presence of sulphates is confirmed also by the bands at 3405 and 3541cm^{-1} (υ_3 and υ_1 H_2O) [16,28–31]. The peaks at 1621 and 1685cm^{-1} are the υ_2 bending H_2O, while the peaks at 3405 and 3541cm^{-1} correspond to υ_3 and υ_1 H_2O [29-31]. The peak at 3643cm^{-1} is assigned to the O-H stretch of portlandite [16,32]. According to Rosi et al [29] the signals at 2093 and 2133cm^{-1} are assigned to combination υ_1+υ_3 bands while the band at 2215cm^{-1} is 2υ_3 vibration of bassanite. The band that is only visible in reflection mode at 5211cm^{-1} is assigned to the presence of bassanite (υ_1/υ_3 OH + υ_2 OH according to Rosi et al.) [29].

Some peaks related to silicates are identified. The peak at 922cm^{-1} and the shoulder at 891cm^{-1} could be assigned to the asymmetric stretching bands (υ_3) of $[SiO_4]^{4-}$ of monoclinic C_3S [30,33] but both peaks could be found also in C_2S [16,30] and in C_3A [30]. In these two last reference articles the shape of the peak is different from the band measured in this study, but small quantities of these phases could be present in the mixture. The peak at 876cm^{-1} could be $CaCO_3$ [4,6,7,17] or an overlapping of signals of $CaCO_3$ and C_2S [16,29,31]. The shoulder at 846cm^{-1} is the symmetric stretching vibration (v_1) $[SiO_4]^{4-}$ C_3S [5,33] or C_2S according to Hughes and Ghosh [16,30].

The signal at 521cm^{-1} corresponds to the out-of-plane bending υ_4 of $[SiO_4]^{4-}$ [16,33], while the ones at 461cm^{-1} (in-plane bending vibration υ_2 of $[SiO_4]^{4-}$) is related to the presence of C_3S [33]. This last one could be also due to the vibrations of AlO^{6-} octahedral groups of C_3A as Ghosh and Handoo in their work [5,30]. The presence of this last phase could be confirmed by the presence of the peak at 406cm^{-1} that is also related to the presence of C_3A [5].

Cement IV (CEM IV)

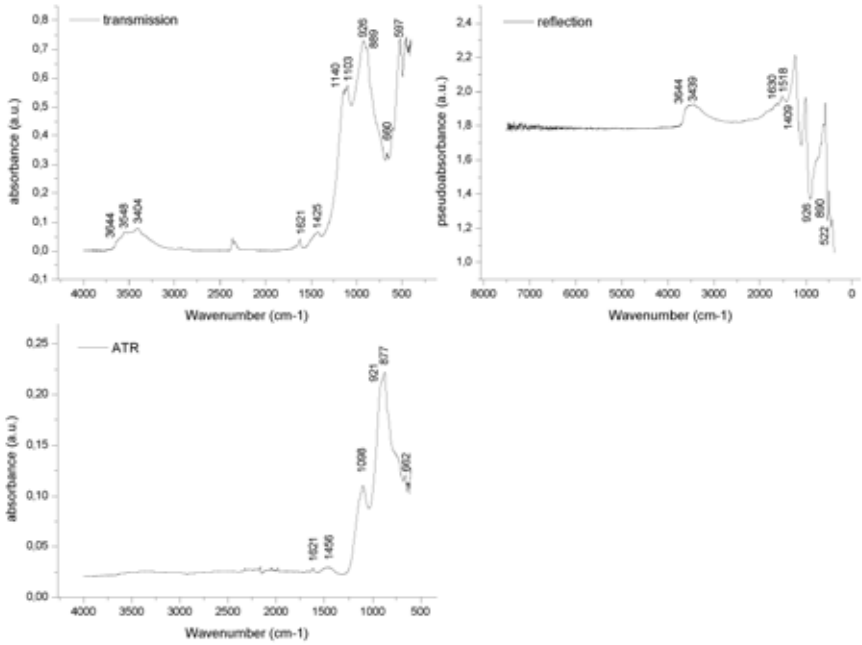

▲ *Figure 8. Pozzolanic cement (CEM IV) spectra, in clockwise order from the bottom left: ATR, transmission and external reflection mode. The main peaks are shown.*

Cement IV presents similar signals to those identified in Portland cement. In fact, also in this cement, the presence of $CaCO_3$ and $Ca(OH)_2$ are visible (figure 8) [16,32]. Also the peaks at 926cm^{-1} and the peak at 889cm^{-1} are present in all the spectra (in reflection they are inverted) [30,33,16]. The shoulder at 846cm^{-1} C_3S [5,33] is the symmetric stretching vibration ($\upsilon 1$) $[SiO_4]^{4-}$, or C_2S, according to Hughes and Ghosh [16,30], is still present.

The sulphates are present as well. Gypsum is identified thank to the peaks at 597cm^{-1} (υ_4 asymmetric bending SO_4^{2-}), 668cm^{-1} (υ_4 asymmetric bending SO_4^{2-}), 1140 and 1126cm^{-1} (υ_3 stretching vibrations SO_4^{2-}), 1626 and 1684cm^{-1} (υ_2 bending H_2O), 3403 and 3543cm^{-1} (υ_3 and υ_1 H_2O) [29-31]. The peak at 1103cm^{-1}, the small peak at 657cm^{-1}, and 3607cm^{-1} could be due to the presence of bassanite [16,28].

Natural hydraulic lime 3.5 (NHL 3.5)

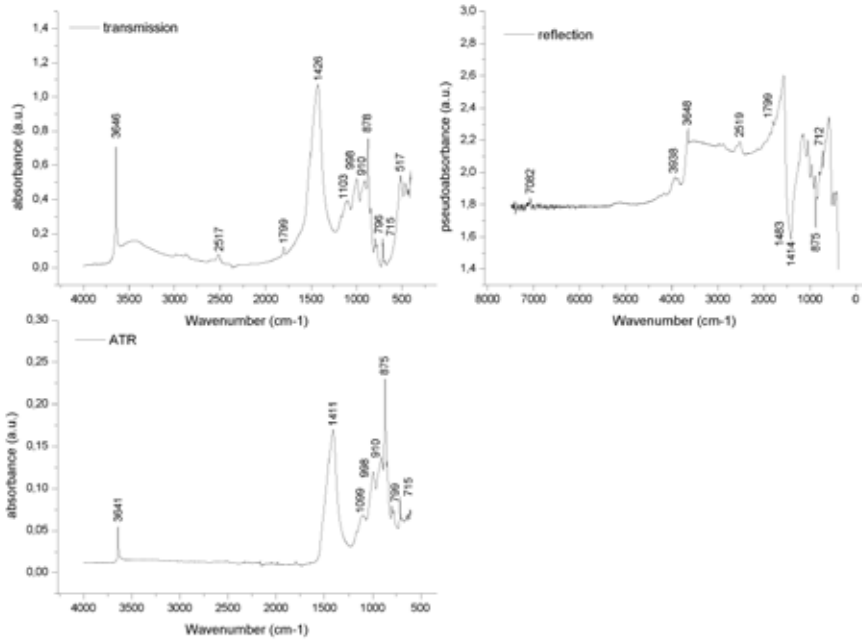

▲ *Figure 9. Natural hydraulic lime (NHL 3.5) spectra, in clockwise order from the bottom left: ATR, transmission and external reflection mode. The main peaks are shown.*

$CaCO_3$, $Ca(OH)_2$ and quartz are visible in the sample (figure 9). Peaks at 712, 847, 1424, 2515 and 3938cm^{-1} are assigned to $CaCO_3$, the peak at 3643cm^{-1} is assigned to $Ca(OH)_2$, while the peaks at 467, 517, 693, 778, 847, 1164cm^{-1} are assigned to quartz [21,23,34] (see paragraphs carbonate sand, hydrated lime and quartz sand for the assignations). The peak at 875cm^{-1} is assigned to $CaCO_3$ [5,14,16,27], but this peak could be also assigned to C_2S according to Hughes, or to C_3A according to Ghosh [16,30]. The peak at 910cm^{-1} could be assigned to C_3S according to Delgado and Ren [14,33], while the peak at 998cm^{-1} could be assigned both to C_2S [5,16] and C_3S phases [33]. 1103cm^{-1} could be due to the presence of sulfates in the material, probably as impurity.

"Gesso Alabastrino" bassanite

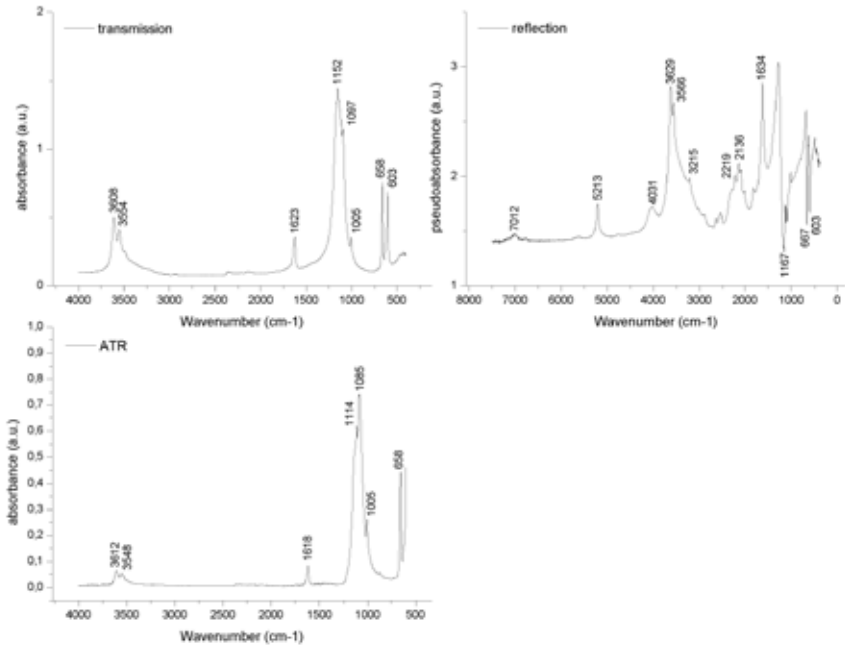

▲ *Figure 10. "Gesso alabastrino" (bassanite) spectra, in clockwise order from the bottom left: ATR, transmission and external reflection mode. The main peaks are shown.*

The doublet 603 and 667cm^{-1} ($\upsilon_4(SO_4)$ and $\upsilon_4(SO_4)$ vibrations [31,35] is well visible in all the spectra (figure 10), even if in ATR mode the spectrum is interrupted in the middle of the peak at 608cm^{-1}. In all the spectra it is well visible the $\upsilon_1(SO_4)$ at 1005cm^{-1} [29]. The antisymmetric stretching υ_3 mode presents the characteristic splitting at 1097 and 1152cm^{-1}. In reflection mode these two peaks are inverted while in ATR they are shifted to 1085 and 1114cm^{-1} respectively. It is also present the peak at 1623-34cm^{-1} (OH bending mode (υ_2)) in all the spectra. The OH stretching region shows the characteristic doublet at 3548 and 3612cm^{-1} [29]. The reflection spectra present additional peaks at 2013cm^{-1} ($2\upsilon_1$ SO_4), 2091 and 2136cm^{-1} ($\upsilon_1 + \upsilon_3$ SO_4), 2219cm^{-1} ($2\upsilon_3$ SO_4) and 5213cm^{-1} (υ_1/υ_3 OH + υ_2 OH), which are assigned to bassanite.

Thermogravimetric analysis and differential scanning calorimetry (TG-DSC)

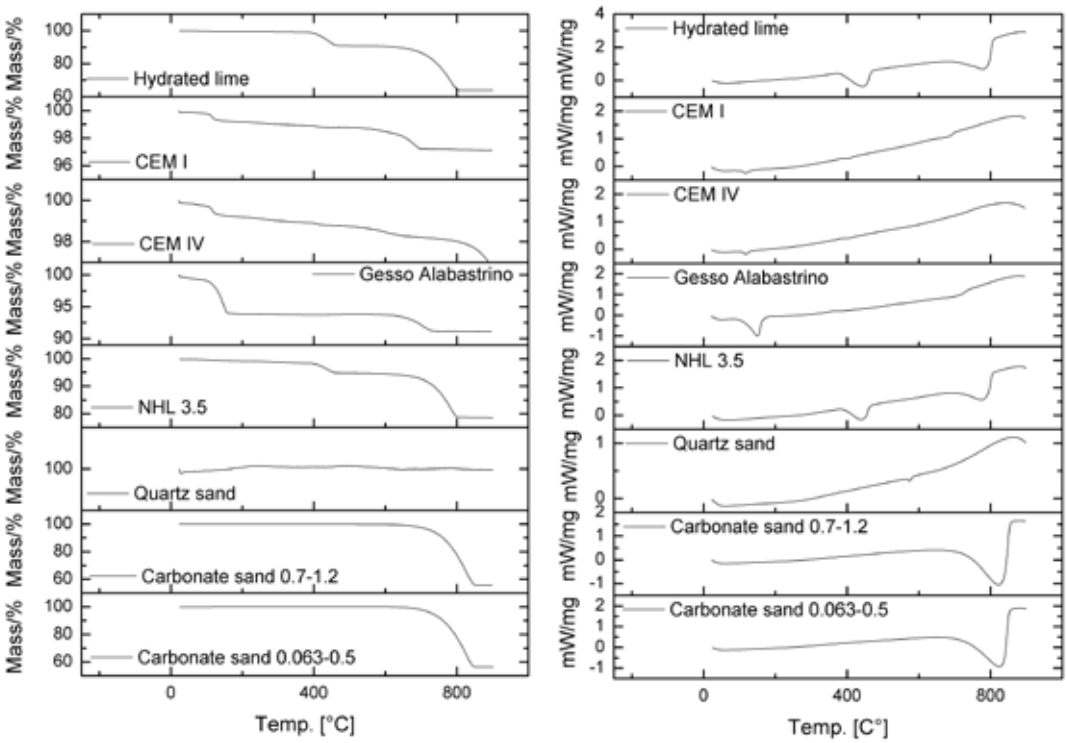

▲*Figure 11. The images show the TG (left) and DSC (right) graphs of the raw materials.*

The transition of quartz alpha into quartz beta is well visible at 573.8°C in the differential scanning calorimetry curve of quartz sand, while the TG curve is without a loss of weight, as it is expected in a phase transition (figure 11) [39]. Under 100°C there is only the loss of water due to surface water desorption [40]. The endothermic peak at 822°C allows us to identify the $CaCO_3$ in the carbonate aggregate (figure 11) [39,41–44]. Natural hydraulic lime 3.5 presents mainly the decomposition peaks of calcium carbonate and of calcium hydroxide at 774.7 and 439°C, respectively (figure 11) [39,41].

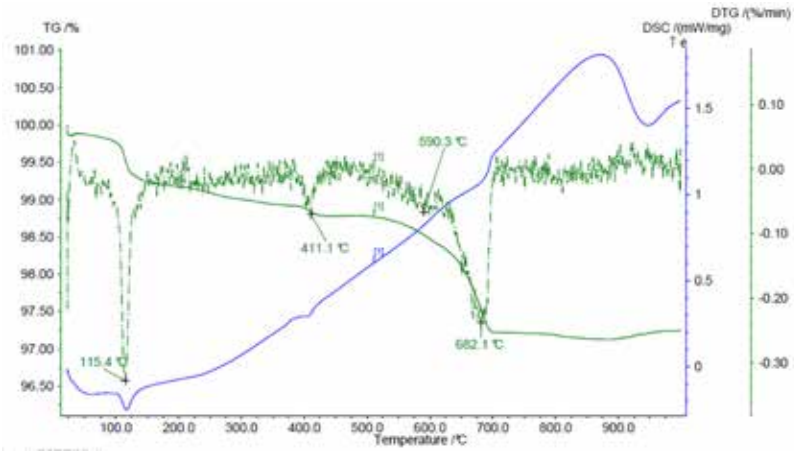

◀*Figure 12. DTG of cement I (Portland) raw material.*

The cement raw materials (figure 12) present a similar trend. Under 100°C, there is only the loss of water present in the sample as surface water desorption [40]. The peak at 115°C is due to the presence of gypsum and/or the hemihydrates (since only one peak is visible), that are contained in anhydrous cements [39–41,45]. The endothermic transition at 411°C is related to the presence of portlandite [39–41,46], while the double peaks at 590 and 682°C are due to the presence of carbonated phases [39–41,47] or could be present also C_2S transformations (beta to alpha form) according to Ramachandran et al. and Taylor et al. [45,48]. The peaks below 600°C could be also related to the C_3S transitions according to Taylor et al. [45]. Sample made by CEM IV (figure 13) present more attenuated peaks if compared to CEM I graph (figure 14).

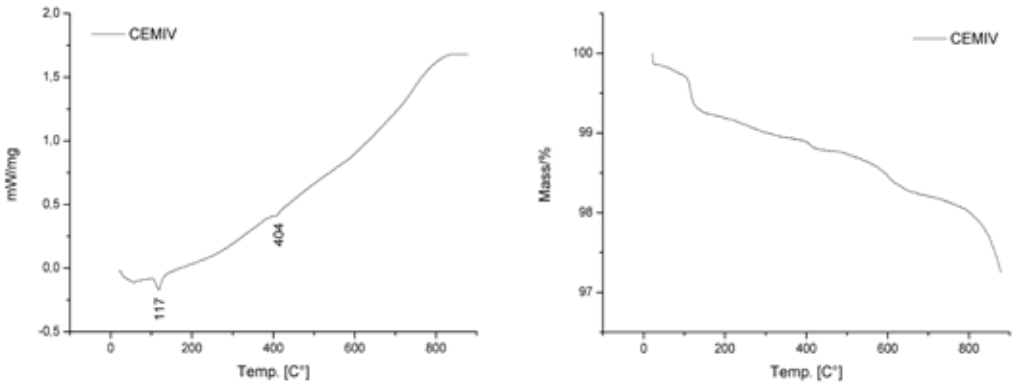

▲ *Figure 13. DSC (left) and TG (right) graphs of CEM IV Pozzolan cement.*

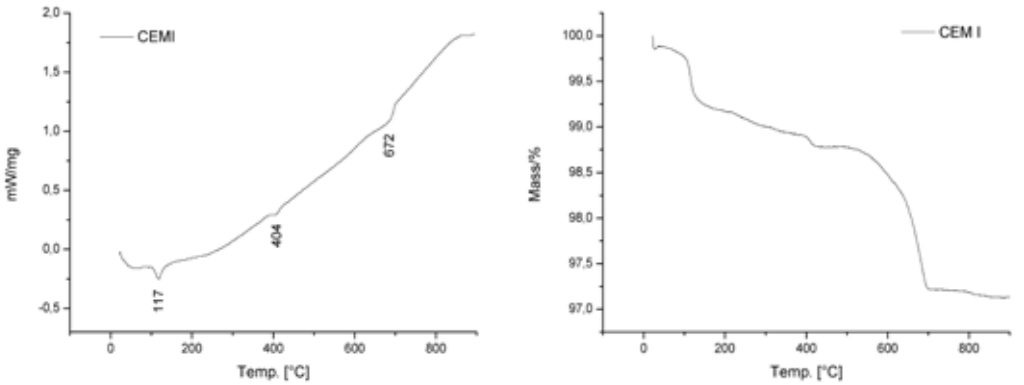

▲ *Figure 14. DSC (left) and TG (right) graphs of Portland cement (CEM I) raw material.*

The "gesso Alabastrino" raw material contains mainly bassanite, as suggested by the endothermic peak at 150°C (figure 15) [39,41]. It presents also an exothermic peak at 365°C that could be a transition between some organic impurities in the material [43] or to the conversion of soluble anhydrite γ (III) to insoluble anhydrite β (II) [48] or to the rearrangement in anhydrous $CaSO_4$ from hemihydrate to anhydrate structure [39] and the carbonate decomposition at about 700°C.

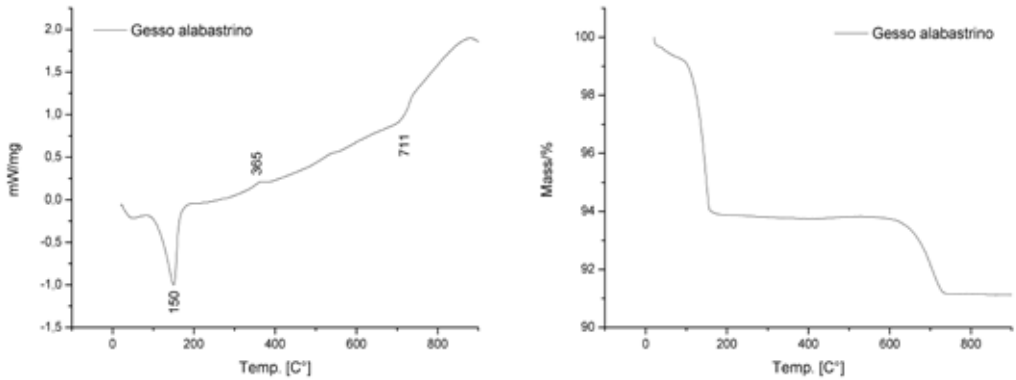

▲ *Figure 15. DSC (left) and TG (right) graphs of "gesso alabastrino" raw material.*

In table 12, the weight loss in percentage is shown. The percentage is calculated after the calculation of the weight loss in mg for each sample. The results are represented in percentage in order to compare the results. The range under 120°C has been considered as related to the presence of free water. The range between 120-200°C has been assigned to dehydration of sulphates while the range between 400-600°C to the dehydration of portlandite. The weight loss over 650°C has been assigned to to $CaCO_3$ decomposition. All the values found are in accordance with what is indicated in the norms with the exception of hydrated lime. NHL 3.5 is conform to the classification in UNI EN 459-1. CEM I and CEM IV are in accordance with EN 197-1. While "gesso alabastrino" is in accordance with EN 13279-2. Hydrated lime seems to be partly carbonated but we have to consider that the data reported in this thesis has been collected in a wide time span of the PhD thesis, during which time the hydrated lime inevitably carbonated. However, considering that by the compositional analysis there were not found impurities and non-compliant compounds, we are confident that the issue of hydrated lime partial carbonated should not affect the task, the analytical data and the goals achieved by this study. Moreover this type of hydrated lime that we used is classified as CL-70 that is that one that has the lower quantities of calcium hydroxide. In table 13 the results of the raw material analysis are summarized.

TG-DSC Results

	Values given as mass fraction in percent			
Material	<120°C	120-200°C	400-600°C	>650°C
Hydrated lime	0.45%	-	36.23%*	59.13%
NHL 3.5	0.53%	-	26.32%	31.84%
Gesso Alabastrino	0.75%	86.53%	-	4.55%
CEM I	0.27%	2.29%	3.54%	2.27%
CEM IV	0.27%	2.39%	6.82%	-
Carbonate sand 0.063-0.5mm	0.00%	-		98.27%
Carbonate sand 0.7-1.2mm	0.04%	-		99.20%
Quartz sand	0.04%	-	-	-

** the values are based on the product after subtraction of its free water and bound water content.*

Table 12. Weight loss % per temperature range after the calculation of the mg loss for each samples.

		Carbonate sand 0.7-1.2mm	Carbonate sand 0.063-0.5mm	Quartz sand	Bassanite (Gesso Alabastrino)	CEM I	CEM IV	Natural hydraulic lime 3.5	Hydrated lime
PXRD	calcite							•	•
	portlandite							•	•
	quartz	•	•	•	•		•	•	•
	bassanite				•				
	dolomite	•			•				
	anhydrite				•				
	gypsum					•	•		
	hatrurite/larnite/calcite					•	•	•	
	brownmillerite					•	•		
	feldspar			•					
	magnisian calcite/calcite	•	•						
	C_3A (?)					•	•		
	mullite (?)						•		
	micas (?)			•					
IR	$CaCO_3$	•	•			•	•	•	•
	SiO_2			•					
	feldspar (?)			•					
	$Ca(OH)_2$					•	•	•	•
	$CaSO_4$ $0.5H_2O$				•	•	•		
	$CaSO_4$ $2H_2O$ (?)				•	•	•	•	
	C_3A (?)					•	•	•	
	C_2S (?)					•	•	•	
	C_3S (?)					•		•	
TG-DSC	$CaCO_3$	•	•		•	•		•	•
	$Ca(OH)_2$					•	•	•	•
	quartz			•					
	C_2S (?)					•			
	C_3S (?)					•			
	$CaSO_4$ $2H_2O$ (?) / $CaSO_4$ $0.5H_2O$ (?)				•	•	•		
	$CaSO_4$				•				

Table 13. In this table the results of the analysis on the raw materials are summarized.

References

[1] Ente italiano di normazione, UNI EN 459-1:2015 Building lime - Part 1: Definitions, specifications and conformity criteria, (2015).

[2] N. Italiana, UNI EN 197 Composizione, specificazioni e criteri di conformità per cementi comuni, (2001).

[3] M.R. Derrick, D. Stulik, J.M. Landry, Infrared Spectroscopy in Conservation Science, Getty Conservation Institute, 2000. https://books.google.it/books?id=kpNQAgAAQBAJ.

[4] C.E. Weir, E.R. Lippincott, Infrared Studies of Aragonite, Calcite, and Vaterite Type Structures in the Borates, Carbonates, and Nitrates, J. Res. Natl. Bur. Stand. A. Phys. Chem. 65 (1961) 173–183. doi:10.6028/jres.065A.021.

[5] L. Fernández-Carrasco, D. Torrens-Martín, L.M. Morales, Sagrario Martínez-Ramírez, Infrared spectroscopy in the analysis of building and construction materials, Infrared Spectrosc. – Mater. Sci. Eng. 370 Technol. Technol. (2012) 369–382. doi:10.5772/36186.

[6] S. Gunasekaran, G. Anbalagan, S. Pandi, Raman and infrared spectra of carbonates of calcite structure, (2006) 892–899. doi:10.1002/jrs.1518.

[7] S. Gunasekaran, G. Anbalagan, Spectroscopic study of phase transitions in natural calcite mineral, Spectrochim. Acta - Part A Mol. Biomol. Spectrosc. 69 (2008) 1246–1251. doi:10.1016/j.saa.2007.06.036.

[8] R. Ylmén, U. Jäglid, Carbonation of Portland Cement Studied by Diffuse Reflection Fourier Transform Infrared Spectroscopy, Int. J. Concr. Struct. Mater. (2013). doi:10.1007/s40069-013-0039-y.

[9] I. Arrizabalaga, O. Gómez-Laserna, J.A. Carrero, J. Bustamante, A. Rodríguez, G. Arana, J.M. Madariaga, Diffuse reflectance FTIR database for the interpretation of the spectra obtained with a handheld device on built heritage materials, Anal. Methods. 7 (2015) 1061–1070. doi:10.1039/C4AY02189D.

[10] C. Ricci, C. Miliani, B.G. Brunetti, A. Sgamellotti, Non-invasive identification of surface materials on marble artifacts with fiber optic mid-FTIR reflectance spectroscopy, 69 (2006) 1221–1226. doi:10.1016/j.talanta.2005.12.054.

[11] V. Brunello, C. Corti, A. Sansonetti, C. Tedeschi, L. Rampazzi, Non-invasive FTIR study of mortar model samples: comparison among innovative and traditional techniques, Eur. Phys. J. Plus. 134 (2019) 270. doi:10.1140/epjp/i2019-12667-1.

[12] W. Vetter, M. Schreiner, Characterization of pigment-binding media systems comparison of non-invasive in-situ reflection FTIR with transmission FTIR microscopy, E-Preservationscience - Morana RTD. (2011) 10–22.

[13] C. Miliani, F. Rosi, A. Daveri, B.G. Brunetti, Reflection infrared spectroscopy for the non-invasive in situ study of artists' pigments, Appl. Phys. A Mater. Sci. Process. 106 (2012) 295–307. doi:10.1007/s00339-011-6708-2.

[14] A.H. Delgado, R.M. Paroli, J.J. Beaudoin, Comparison of IR techniques for the characterization of construction cement minerals and hydrated products, Appl. Spectrosc. (1996). doi:10.1366/0003702963905312.

[15] R. Ylmén, U. Jäglid, B.-M. Steenari, I. Panas, Early hydration and setting of Portland cement

monitored by IR, SEM and Vicat techniques, Cem. Concr. Res. 39 (2009) 433–439. doi:10.1016/j.cemconres.2009.01.017.

[16] T.L. Hughes, C.M. Methven, T.G.J. Jones, S.E. Pelham, P. Fletcher, C. Hall, Determining cement composition by Fourier transform infrared spectroscopy, Adv. Cem. Based Mater. 2 (1995) 91–104. doi:10.1016/1065-7355(94)00031-X.

[17] S.J. Gaffey, Spectral reflectance of carbonate minerals in the visible and near infrared (0.35-2.55 microns): calcite, aragonite, and dolomite, Am. Mineral. 71 (1986) 151–162. doi:10.1029/JB092iB02p01429.

[18] M. Vagnini, C. Miliani, L. Cartechini, P. Rocchi, B.G. Brunetti, A. Sgamellotti, FT-NIR spectroscopy for non-invasive identification of natural polymers and resins in easel paintings, in: Anal. Bioanal. Chem., 2009. doi:10.1007/s00216-009-3145-6.

[19] J.S. Gaffey, Spectral reflectance of carbonate minerals in the visible and near infrared (0.35-2.55 μm). Anhydrous carbonate minerals, J. Geophys. Res. 92 (1987) 1429–1440.

[20] G. Anbalagan, A.R. Prabakaran, S. Gunasekaran, Spectroscopic characterization of indian standard sand, J. Appl. Spectrosc. 77 (2010) 86–94. doi:10.1007/s10812-010-9297-5.

[21] M.J. Wilson, ed., Clay Mineralogy: Spectroscopic and Chemical Determinative Methods, Springer Netherlands, Dordrecht, 1994. doi:10.1007/978-94-011-0727-3.

[22] H.H.W. Moenke, Silica, the three dimensional silicates, borosilicates and beryllium silicates, in: Infrared Spectra Miner., 1974. doi:10.1180/mono-4.16.

[23] V.C. Farmer, ed., The Infrared Spectra of Minerals, Mineralogical Society of Great Britain and Ireland, Londan, 1974. doi:10.1180/mono-4.

[24] P. Yu, R.J. Kirkpatrick, B. Poe, P.F. McMillan, X. Cong, Structure of Calcium Silicate Hydrate (C-S-H): Near-, Mid-, and Far-Infrared Spectroscopy, J. Am. Ceram. Soc. 82 (2004) 742–748. doi:10.1111/j.1151-2916.1999.tb01826.x.

[25] K. Shinoda, T. Nagai, N. Aikawa, Pressure-dependent anharmonic coefficient of OH in portlandite by NIR-IR spectroscopy with DAC, J. Mineral. Petrol. Sci. 95 (2000) 65–70. doi:10.2465/jmps.95.65.

[26] F. Ridi, E. Fratini, S. Milani, P. Baglioni, Near-Infrared Spectroscopy Investigation of the Water Confined in Tricalcium Silicate Pastes, J. Phys. Chem. B. 110 (2006) 16326–16331. doi:10.1021/jp060026y.

[27] A. Peyvandi, D. Holmes, P. Soroushian, A.M. Balachandra, Monitoring of sulfate attack in concrete by Al^{27} and Si^{29} MAS NMR spectroscopy, J. Mater. Civ. Eng. 27 (2014) 04014226. doi:10.1061/(ASCE)MT.1943-5533.0001175.

[28] L. Fernández-Carrasco, D. Torrens-Martín, L.M. Morales, Sagrario Martínez-Ramírez, L. Fernández Carrasco, D. Torrens Martín, L.M. Morales, S. Martínez Ramírez, Infrared spectroscopy in the analysis of building and construction materials, InTech, 2012. doi:10.5772/36186.

[29] F. Rosi, A. Daveri, B. Doherty, S. Nazzareni, B.G. Brunetti, A. Sgamellotti, C. Miliani, On the Use of Overtone and Combination Bands for the Analysis of the $CaSO_4$ —H_2O System by Mid-Infrared Reflection Spectroscopy, Appl. Spectrosc. 64 (2010) 956–963. doi:10.1366/000370210792080975.

[30] S.N. Ghosh, S.K. Handoo, Infrared and Raman spectral studies in cement and concrete (review), Cem. Concr. Res. (1980). doi:10.1016/0008-8846(80)90005-8.

[31] G. Anbalagan, S. Mukundakumari, K.S. Murugesan, S. Gunasekaran, Infrared, optical absorption, and EPR spectroscopic studies on natural gypsum, Vib. Spectrosc. 50 (2009) 226–230. doi:10.1016/j.vibspec.2008.12.004.

[32] A. Mendes, W.P. Gates, J.G. Sanjayan, F. Collins, NMR, XRD, IR and synchrotron NEXAFS spectroscopic studies of OPC and OPC/slag cement paste hydrates, Mater. Struct. Constr. 44 (2011) 1773–1791. doi:10.1617/s11527-011-9737-6.

[33] X. Ren, W. Zhang, J. Ye, FTIR study on the polymorphic structure of tricalcium silicate, Cem. Concr. Res. (2017). doi:10.1016/j.cemconres.2016.11.021.

[34] L. Fernández-Carrasco, E. Vázquez, Reactions of fly ash with calcium aluminate cement and calcium sulphate, Fuel. 88 (2009) 1533–1538. doi:10.1016/j.fuel.2009.02.018.

[35] F. Rosi, A. Daveri, B. Doherty, S. Nazzareni, B.G. Brunetti, A. Sgamellotti, C. Miliani, On the Use of Overtone and Combination Bands for the Analysis of the CaSO 4 —H 2 O System by Mid-Infrared Reflection Spectroscopy, Appl. Spectrosc. 64 (2010) 956–963. doi:10.1366/000370210792080975.

[36] R.C. Mackenzie, Differential Thermal Analysis: Fundamental aspects, Acad. Press, 1978. https://books.google.it/books?id=-HoyvgAACAAJ.

[37] R. Gabrovšek, T. Vuk, V. Kaučič, Evaluation of the hydration of Portland cement containing various carbonates by means of thermal analysis, Acta Chim. Slov. 53 (2006) 159–165.

[38] R.C. Mackenzie, Differential Thermal Analysis: Applications, Academic Press, 1972. https://books.google.it/books?id=-rxpAAAAMAAJ.

[39] A. Moropoulou, A. Bakolas, K. Bisbikou, Thermal analysis as a method of characterizing ancient ceramic technologies, Thermochim. Acta. 269–270 (1995) 743–753. doi:10.1016/0040-6031(95)02570-7.

[40] A. Moropoulou, A. Bakolas, K. Bisbikou, Characterization of ancient, byzantine and later historic mortars by thermal and X-ray diffraction techniques, Thermochim. Acta. 269–270 (1995) 779–795. doi:10.1016/0040-6031(95)02571-5.

[41] L.M. Barcina, A. Espina, M. Sufirez, J.R. Garc, J. Rodr, Characterization of monumental carbonate stones by thermal analysis (TG, DTG and DSC), Science (80-.). 290 (1997) 181–189.

[42] H.F.W. Taylor, Cement chemistry. 2nd ed., 1997. doi:10.1016/S0958-9465(98)00023-7.

[43] J. Dweck, P.M. Buchler, A.C.V. Coelho, F.K. Cartledge, Hydration of a Portland cement blended with calcium carbonate, Thermochim. Acta. 346 (2000) 105–113. doi:10.1016/S0040-6031(99)00369-X.

[44] Z. Šauman, Carbonization of porous concrete and its main binding components, Cem. Concr. Res. 1 (1971) 645–662. doi:10.1016/0008-8846(71)90019-6.

[45] V.S. Ramachandran, R.F. Feldman, P.J. Sereda, Applications of Differential Thermal Analysis in Cement Chemistry, in: I. Chemical Publishing Company (Ed.), New York, 1969

Specimen analyses

Powder X-Ray diffraction (PXRD)

Specimens composed by one specific binder

Specimens made of one binder were analyzed to have reference data on hydrated pastes. In samples like G (lime putty) and C (hydrated lime) is evident how the carbonation process is still in progress because of the presence of portlandite (table 14).

In C (hydrated lime), G (lime putty), N (natural hydraulic lime), and Gs (gypsum) the presence of quartz has been identified but its diffraction peaks are very low. It is probably a residue from the rocks where the raw materials have been excavated. According to Ranjbar et al and Sun et al. [1,2] the presence of quartz and mullite in CIV is related to the crystalline components of fly ashes.

The identification of hydrated cement phases has not been easy since there is also a gel phase that it does not create scatter; obviously after a long curing time, the gel phase will convert into crystalline phases. For what concerns cement specimens CI (Portland cement) and CIV (pozzolanic cement) the ettringite has been identified. The recognition of larnite, hatrurite and tobermorite present the same problems already underlined in the paragraph of the raw materials: the main peaks of these phases are very close one to each other. Moreover these phases do not present intense scattering thus the differentiation and identification of the diffraction peaks is difficult. In the sample of natural hydraulic lime hydrated (N) only calcite, quartz and aragonite are detected while there are not signals of hydraulic phases.

In both cement samples the presence of calcite and vaterite is identified, as a product of carbonation [3–10]. The presence of vaterite could be due to a different crystallization of calcium carbonate in presence of cement material. As already seen in infrared spectroscopy chapter, the presence of aragonite or vaterite in lime-based and cement specimens could have been ascribed by the literature [3–5,7,8,11] for example to the interaction of lime with Mg atoms, as suggested by Duchi et al. and by Raymond and Clifford [7–10]. Elsewhere, the formation of aragonite is related to the use of raw materials which have been exposed to temperatures over 600°C [5], or to room temperature conditions with pH values close to 11 [8]. In this particular case, it is not possible to unambiguously explain the formation of aragonite or vaterite and further analysis beyond the scopes of this thesis should be designed.

An attempt to better identify these phases was done with the use of Bruker D8 instrument, with longer acquisition times (Materials and Methods). The results are shown in table 15, while the diffractogram of sample CI is visible in figure 16. These measures gave more intense peaks and helped allowing an easier identification of cement phases but always with some uncertain because of some overlapping of the peaks, as already discussed before. With regards to case studies, it is important to consider that this analysis is very time consuming. As it is possible to see, comparing tables 14-15, and figure 16-17, that the main phases are detected by both the diffractograms. There are some differences in the relative intensities that could be due to a preferential order, the scattering, casual different distribution of phases in the powder of the analysis. Anyway with both the instruments was possible to identify the same main minerals. With D8 the signals were clearer and some hypothesis on minor minerals could be done.

Label	Mineralogical phases						
G	Calcite	Portlandite	Quartz				
C	Calcite	Portlandite	Quartz				
CI	Calcite	Portlandite	Ettringite	Larnite/ Hatrurite/ Tobermorite (?)	Vaterite	Gypsum (?)	
CIV	Calcite	Portlandite	Ettringite	Larnite/ Hatrurite/ Tobermorite (?)	Quartz	Vaterite	Mullite (?)
Gs	Gypsum	Anhydrite	Dolomite	Quartz			
N	Calcite	Quartz	Aragonite				

Table 14. The results obtained by the analysis with the Miniflex instrument are shown. The mineralogical phases are written from the more intense to the weaker (key in table 6).

Label	Mineralogical phases							
CI	Calcite	Portlandite	Ettringite	Larnite/ Hatrurite/ Tobermorite	Vaterite	Gypsum (?)	Hydro-calumite (?)	CSHBrown-millerite (?)
CIV	Calcite	Portlandite	Ettringite	Larnite/ hatrurite/ Tobermorite	Quartz	Vaterite	Mullite	Brownmil-lerite (?)
N	Calcite	Quartz	Aragonite	Portlandite				

Table 15. The results obtained by the analysis with D8 instrument are shown. The mineralogical phases are written from the more intense to the weaker (key in table 6)..

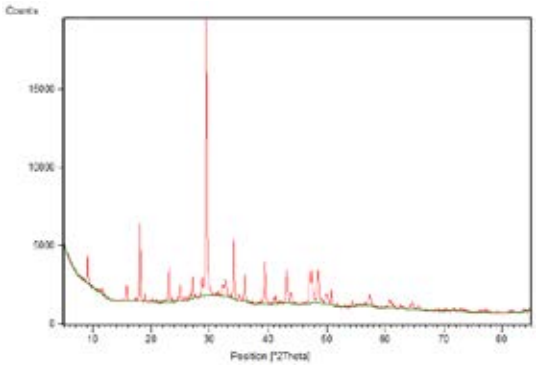

▲ *Figure 16. CI (Portland cement) sample analysed with Bruker D8 diffractometer.*

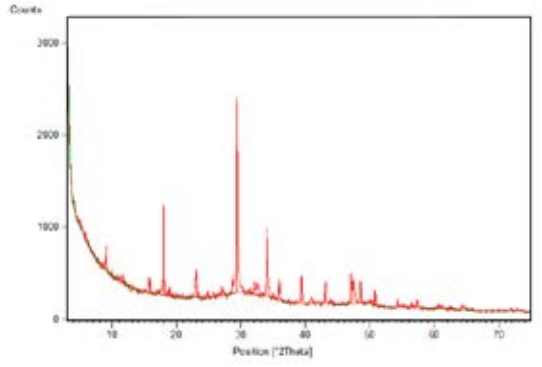

▲ *Figure 17. CI (Portland cement) sample analysed with Rigaku Miniflex diffractometer.*

Mortars composed by one specific binder and one specific aggregate

The mortars made with one binder and the aggregate were analyzed to evaluate the influence of the aggregate on the analysis. For samples with quartz sand, the presence of quartz is predominant in the pattern with the highest peaks. In addition, feldspars were detected in samples with quartz sand (Table 16). In GsQ and GsM, anhydrite coming from the raw material is still visible. In cement mortars (model samples CIQ, CIVQ, CIM and CIVM the presence of ettringite is always clear). In samples CIVM and CIQ vaterite is also present, probably due to a different carbonatation of $CaCO_3$ in cements probably caused by some ion interactions or pH influence during the carbonation process [3–5,7,8,10,11].

Moreover, in samples with carbonate sand dolomite is visible, coming from the aggregate (Raw materials characterization paragraph) while the signals of calcite and magnesian calcite are often overlapped and not distinguishable. It was not possible to detect hydraulic phases also in samples NQ and NM, as in sample N.

Label	Minerological phases						
GQ	Quartz	Calcite	Portlandite	Feldspar			
CQ	Quartz	Magnesian calcite/Calcite	Feldspar				
CIQ	Quartz	Vaterite	Portlandite	Calcite	Ettringite	Feldspar	Gypsum
CIVQ	Quartz	Calcite	Portlandite	Ettringite	Feldspar	Gypsum	
NQ	Quartz	Magnesian calcite/Calcite	Feldspar				
GsQ	Quartz	Gypsum	Anhydrite	Feldspar			
GM	Magnesian calcite/Calcite	Dolomite	Quartz	Portlandite			
CM	Magnesian calcite/Calcite	Dolomite	Quartz	Portlandite			
CIM	Magnesian calcite/Calcite	Dolomite	Portlandite	Ettringite	Quartz		
CIVM	Magnesian calcite/Calcite	Dolomite	Portlandite	Quartz	Ettringite		
NM	Calcite	Dolomite	Quartz	Portlandite			
GsM	Gypsum	Magnesian calcite/Calcite	Dolomite	Anhydrite	Quartz		

Table 16. The mineralogical phases of mortars are written from the more intense to the weaker (key in table 6).

Specimens composed by two binders

The analysis on specimens with two binders (table 16) was performed in order to have references for the interpretation of mixed mortars. In mixture like GN e CN the presence of calcite, portlandite and quartz is identified, while the hydraulic phases are not detected. The presence of cement in samples like GCI (figure 18) and CCI is mainly suggested by the occurrence of ettringite while the presence of hydrated silicates is hardly detected. In some cases, for example GCI, CCI, NCI and NCIV specimens some carbonate phases like vaterite or aragonite are detected concurrently with calcite. The presence of these phases is probably connected to the presence of cement phases that probably influence the crystallization of carbonates [10]. NCI have a very small peak at 7.7 d-spacing [Å] between 10° and 13°, where the peaks of some AFm phases peaks like hydrocalumite ($Ca_4Al_2(OH)_{12}[Cl(CO_3)_{0.5}]$ $4.8(H_2O)$) or *CSH* phase [12] could be found, thus it is not possible to have a reliable assignation. In samples like GCIV, GCI and CCI it is not possible to identify the diffraction peaks of ettringite (figure 18).

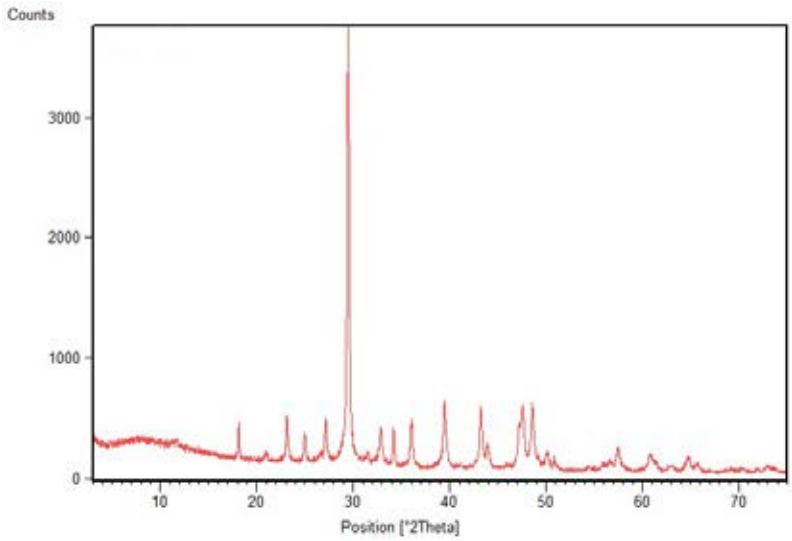

▲ *Figure 18. Diffraction pattern of sample GCI (lime putty and Portland cement)*

label	Minerological phases					
GN	Calcite	Quartz	Portlandite			
GCI	Calcite	Portlandite	Vaterite	Gypsum (?)		
GCIV	Calcite	Vaterite	Portlandite	Quartz	Mullite (?)	
GGs	Gypsum	Calcite	Portlandite	Anhydrite		
CN	Calcite	Portlandite	Quartz			
CCI	Calcite	Gypsum	Aragonite			
CCIV	Calcite	Quartz	Portlandite	Vaterite	Mullite	
CGs	Gypsum	Calcite	Portlandite	Anhydrite		
NCI	Calcite	Vaterite	Portlandite	Ettringite		
NCIV	Calcite	Portlandite	Vaterite	Quartz	Ettringite	Gypsum
NGs	Gypsum	Calcite	Quartz	Anhydrite		

Table 16. The mineralogical phases of mortars are written from the more intense to the weaker (key in table 6).

Mortars composed by a mix of two binders and a specific aggregate

The mixed mortars present all together the peaks observed in the single raw materials. When quartz sand is present, quartz usually has the most intense diffraction peak. The presence of magnesian calcite and/or calcite is usually detected in samples with carbonate aggregate with the highest intensities among the other mineralogical phases identified (the sand probably represents both the phases). Calcite usually presents the main diffraction peak at 3.03 d-spacing [Å], while magnesian calcite here identified has it at 3.02 d-spacing.

As is possible to observe in table 17, it is not always possible to distinguish the ettringite phase or other cement phases like tobermorite and *AFm* phases, when cement is present in the specimens (figure 19). In figure 20 an example of a blended mortar with natural hydraulic lime, gypsum and carbonate aggregate is shown.

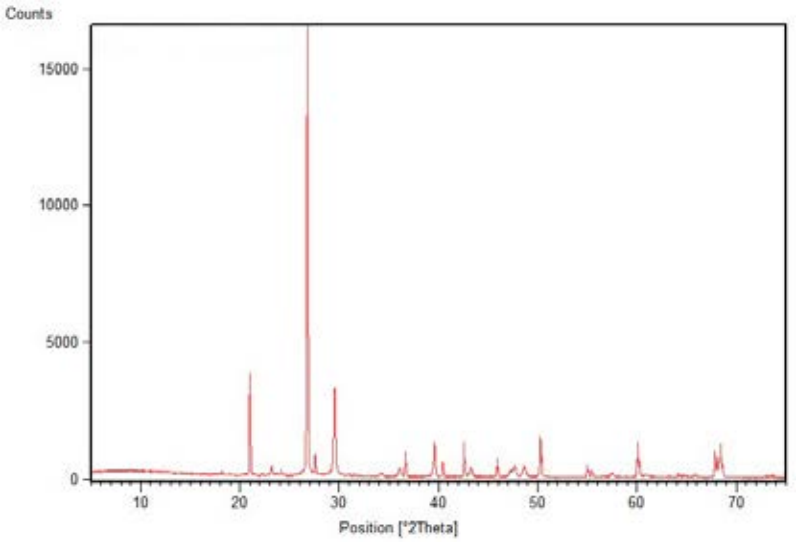

◀*Figure 19. Diffractogram of sample CCIQ, showing the signals of quartz, calcite, portlandite and feldspar.*

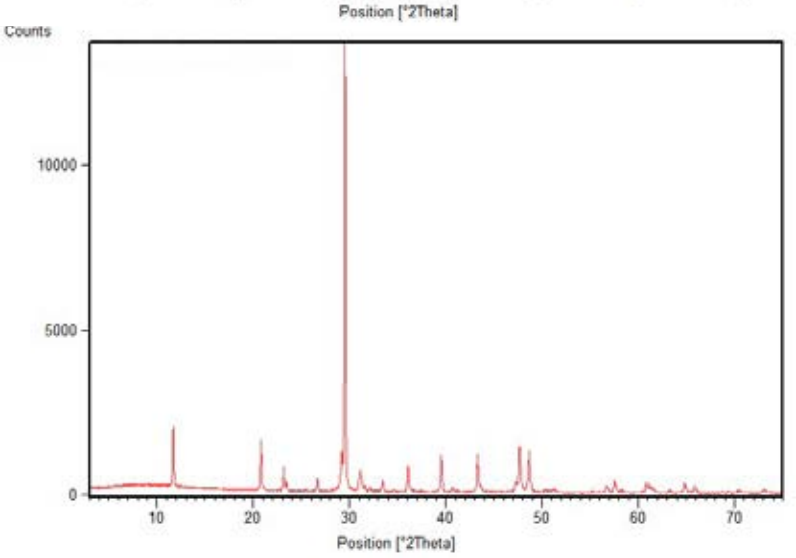

◀*Figure 20. Diffractogram of sample NGsM, showing the signals of magnesian calcite/calcite, gypsum, calcite, dolomite, anhydrite and quartz.*

label	Mineralogical phases						
GNQ	Quartz	Calcite	Feldspar				
GCIM	Magnesian calcite/Calcite	Dolomite	Quartz	Portlandite	Vaterite	Ettringite	
GCIQ	Calcite	Portlandite	Quartz	Ettringite	Feldspar		
GCIVM	Magnesian calcite	Dolomite	Quartz	Portlandite			
GCIVQ	Quartz	Calcite	Portlandite	Vaterite	Feldspar		
GGsM	Magnesian calcite/Calcite	Gypsum	Dolomite	Quartz	Anhydrite	Portlandite (?)	Micas (?)
GGsQ	Quartz	Gypsum	Magnesian calcite/Calcite	Portlandite	Anhydrite	Feldspar	Micas (?)
CNM	Magnesian calcite/Calcite	Quartz	Dolomite	Portlandite			
CNQ	Quartz	Calcite	Feldspar	Portlandite			
CCIM	Magnesian calcite/Calcite	Dolomite	Quartz	Portlandite			
CCIQ	Quartz	Calcite	Portlandite	Feldspar			
CCIVM	Magnesian calcite/Calcite	Quartz	Dolomite	Portlandite			
CCIVQ	Quartz	Calcite	Portlandite	Albite	Ettringite		
CGsM	Magnesian calcite/Calcite	Gypsum	Quartz	Portlandite	Dolomite	Micas (?)	
CGsQ	Quartz	Gypsum	Calcite	Portlandite	Feldspar	Micas (?)	
NCIM	Magnesian calcite/Calcite	Dolomite	Portlandite	Quartz	Ettringite		
NCIQ	Quartz	Magnesian calcite/Calcite	Portlandite	Feldspar	Ettringite		
NCIVM	Magnesian calcite/Calcite	Dolomite	Quartz	Ettringite			
NCIVQ	Quartz	Magnesian calcite/Calcite	Feldspar	Ettringite			
NGsM	Magnesian calcite/Calcite	Gypsum	Calcite	Dolomite	Anhydrite	Quartz	
NGsQ	Quartz	Gypsum	Calcite	Feldspar			
GNM	Magnesian calcite/Calcite	Dolomite	Quartz				

Table 17. The mineralogical phases of mixed mortars are written from the more intense to the weaker.

Discussion and conclusions

The drawbacks and advantages of X-ray diffraction analysis of model samples are summarized in table 18. Beside the well-known opportunity to detect the crystal the possibility of also distinguishing also the polymorph phases that are the product of the carbonation process could give some suggestion on the nature of the material. On the other hand, XRD presents a strong limitation in the identification of hydrated cement phases because they are usually not crystalline and because the patterns are hidden by other phases such as calcite, portlandite, gypsum or quartz. Notwithstanding this drawback, we have demonstrated that long acquisition time analyses could help in the identification of cement phases. With regards to routine analyses, this high quality acquisition mode is suggested when the presence of cements is supposed.

Advantages	**Drawbacks**
Identification of crystalline phases	No identification of gel phases
Identification of different $CaCO_3$ polymorphs.	No identification of C_2S and C_3S hydrated phases (gel).
Identification of ettringite in samples with cement and in mortars made by cement and aggregate.	Difficult identification of ettringite in samples with cement in mixed mortars and samples made by two binders.
In natural hydraulic lime 3.5, the identification of hydraulic compounds is possible in the raw material.	Impossibility of distinguishing between samples with natural hydraulic lime (N) and samples with lime (C, G).
Identification or lime and gypsum when mixed together.	

Table 18. Summary of advantages and drawbacks of powder XRD analysis applied on mortars model samples.

References

[1] N. Ranjbar, C. Kuenzel, Cenospheres: A review, Fuel. 207 (2017) 1–12. doi:10.1016/j.fuel.2017.06.059.

[2] J.M. Sun, Q. Yao, X.C. Xu, Classification of micro-particles in fly ash, Dev. Chem. Eng. Miner. Process. 9 (2001) 233–238.

[3] D. Ergenç, L.S. Gómez-Villalba, R. Fort, Crystal development during carbonation of lime-based mortars in different environmental conditions, Mater. Charact. 142 (2018) 276–288. doi:10.1016/j.matchar.2018.05.043.

[4] K. Zhang, C. Corti, A. Grimoldi, L. Rampazzi, A. Sansonetti, Application of Different Fourier Transform Infrared (FT-IR) Methods in the Characterization of Lime-Based Mortars with Oxblood, Appl. Spectrosc. (2018) 000370281881569. doi:10.1177/0003702818815693.

[5] M.B. Toffolo, E. Boaretto, Nucleation of aragonite upon carbonation of calcium oxide and calcium hydroxide at ambient temperatures and pressures: a new indicator of fire-related human activities, J. Archaeol. Sci. 49 (2014) 237–248. doi:10.1016/j.jas.2014.05.020.

[6] A. Burgos-Cara, C. V. Putnis, C. Rodriguez-Navarro, E. Ruiz-Agudo, Hydration effects on gypsum dissolution revealed by in situ nanoscale atomic force microscopy observations, Geochim. Cosmo chim. Acta. 179 (2016) 110–122. doi:10.1016/j.gca.2016.02.008.

[7] R.S.K. Lam, J.M. Charnock, A. Lennie, F.C. Meldrum, Synthesis-dependant structural variations in amorphous calcium carbonate, CrystEngComm. 9 (2007) 1226. doi:10.1039/b710895h.

[8] C.Y. Tai, F. Chen, Polymorphism of $CaCO_3$, precipitated in a constant-composition environment, AIChE J. 44 (1998) 1790–1798. doi:10.1002/aic.690440810.

[9] V. Duchi, M. V. Giordano, M. Martini, Riesame del problema della precipitazione di calcite od aragonite da soluzioni naturali, Rend. Soc. Ital. Di Mineral. e Petrol. 34 (1978) 605–618.

[10] E.T. Stepkowska, J.L. Perez-Rodriguez, M.J. Sayagues, J.M. Martinez-Blanes, Calcite, vaterite and aragonite forming on cement hydration from liquid and gaseous phase, J. Therm. Anal. Calorim. 73 (2003) 247–269.

[11] C. Rodriguez-Navarro, C. Jimenez-Lopez, A. Rodriguez-Navarro, M.T. Gonzalez-Muñoz, M. Rodriguez-Gallego, Bacterially mediated mineralization of vaterite, Geochim. Cosmochim. Acta. 71 (2007) 1197–1213. doi:10.1016/j.gca.2006.11.031.

[12] M.A.G. Aranda, A.G. De la Torre, L. Leon-Reina, Rietveld Quantitative Phase Analysis of OPC Clinkers, Cements and Hydration Products, Rev. Mineral. Geochemistry. 74 (2012) 169–209. doi:10.2138/rmg.2012.74.5.

Infrared spectroscopy

Application of Infrared spectroscopy on the set of specimens

Specimens composed by one specific binder

Hydrated lime (C)

Figure 21 shows that the main shift between ATR and transmission FTIR is related to the main band of the carbonate group, ascribable to υ_3 CO_3^{2-} antisymmetric stretching [1–3]. The peak at 1428cm^{-1} in the transmission spectrum is in fact shifted to 1397cm^{-1} in the ATR spectrum and inverted in the external reflection, as observed in the literature [4]. This band also splits in the transverse and longitudinal component of the vibration, at 1409 and 1507cm^{-1}. The peaks at 712cm^{-1} (υ_4 CO_3^{2-} symmetric in-plane bending) and 873cm^{-1} (υ_2 CO_3^{2-} out-of-plane asymmetric bending) are very similar in transmission and ATR spectra, but they appear as derivatives in the reflection mode spectrum [1,3,5]. The reflection is ruled by the Fresnel's law that explains the different behaviour of the inverted and derivatives peaks connected to the absorption index (k) and the refractive index (n). When k < 1, in fact, a derivative-like signal is observed; on the other hand, when k >> 1 inverted (restrahlen) peaks can be seen. The specimens are composed by a mixture of different components, thus it is not possible to know the specific reflection coefficients of the surfaces [2,6]. The peak of the υ_1 CO_3^{2-} symmetric stretching can be observed at 1075cm^{-1} (or slightly shifted) in all the spectra [2,3,5]. For the combination and overtone bands, the signal at 1797cm^{-1} (υ_1+υ_4 CO_3^{2-} and/or υ_2 overtone) is visible in all the spectra [2,7,8]. The band around 2512cm^{-1}, with its shoulder at 2594cm^{-1}, is generally assigned to υ_1+υ_3 and/or 2υ_2+υ_4 (CO_3^{-2}) [2,8]. Its results are particularly amplified in the reflection mode. The two peaks around 2981cm^{-1} and 2875cm^{-1} (overtone and combination bands of the υ_3 CO_3^{2-} antisymmetric stretching) are amplified in reflection mode, while they are not visible in the ATR spectrum [7,9–11]. The peak at 4269cm^{-1} (in reflection mode) is attributed to the second overtone mode of the asymmetric stretching of CO_3^{2-} (3υ_3) [2,12].

In all the spectra (figure 21), a peak around 3640cm^{-1}, due to the O-H stretching of $Ca(OH)_2$, is also visible [7]. In addition, a peak at 7082cm^{-1} is visible in the reflection spectrum: its assignment is still uncertain, but it should be the first overtone of $Ca(OH)_2$ stretching mode [13–16]. This peak was also found in the spectrum of reference hydrated lime, composed mainly of $Ca(OH)_2$, as evidenced by XRD analysis. The band at 5160cm^{-1} could be due to the presence of water, particularly to one of its overtones [14].

The results obtained by FTIR analysis are in accordance with those given by PXRD analysis, which identified the presence of calcite, portlandite and a very small amount of quartz [17].

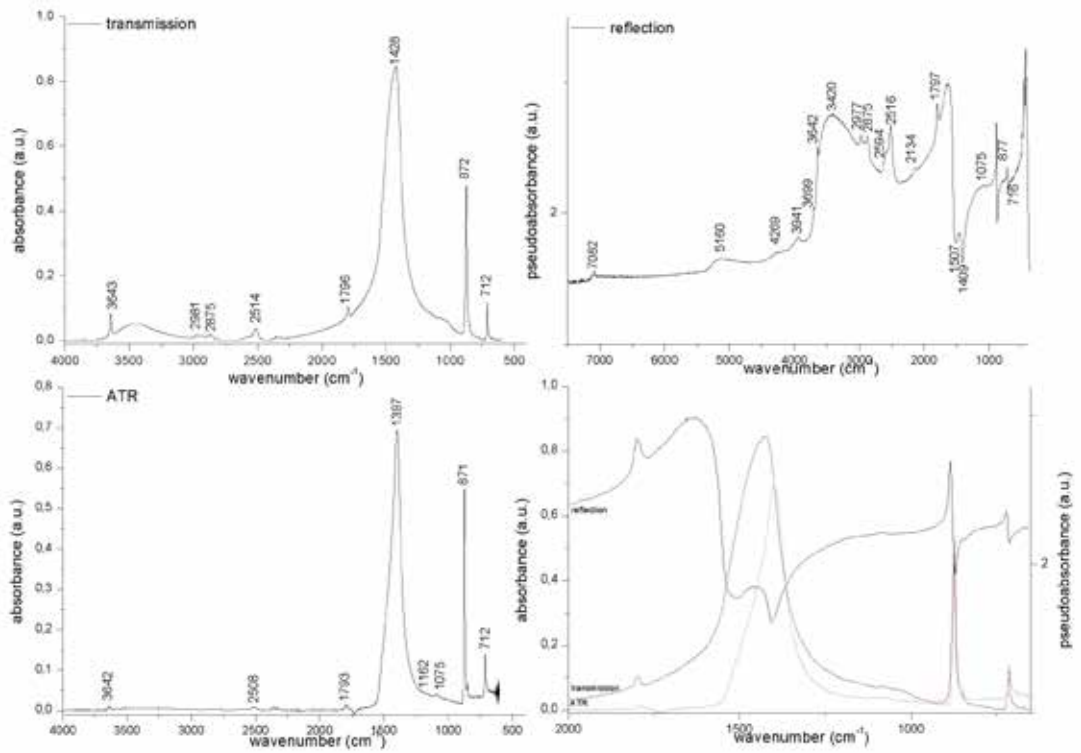

▲ *Figure 21. From the bottom left in clockwise order: ATR, Transmission, Reflection spectra, of a specimen of hydrated lime (C). The main peaks are shown. In the right bottom the overlapping of the three spectra underline the different shape of the main peak of carbonate (1428cm^{-1}).*

Natural hydraulic lime (N)

The main peaks and bands of $CaCO_3$ and $Ca(OH)_2$ were identified, as in the previous example (at about 713cm^{-1}, 875cm^{-1}, 1074cm^{-1}, 1397cm^{-1} and/or 1428cm^{-1}, 1797cm^{-1}, 2512cm^{-1}, 2594cm^{-1}, 2981cm^{-1}, 2874cm^{-1}, 4273cm^{-1}, 3640cm^{-1} and 7087cm^{-1}) (figure 22). The peak at 1796cm^{-1} attributed to $CaCO_3$ is particularly evident in the reflection mode. The peak of O-H stretching of $Ca(OH)_2$, around 3640cm^{-1}, has a very weak intensity and it cannot be seen in the ATR spectrum. The band at 5178cm^{-1} in reflection mode could be ascribed to the presence of water, particularly to one of its overtones [14]. One noteworthy result is that no portlandite was identified by PXRD analysis, and it was probably present under the limit of detection, while it can be observed using FTIR analysis. Another carbonate was found, which was aragonite (857cm^{-1} υ_2 CO_3^{2-}) [18], in agreement with the PXRD analysis.

Some peaks related to silicates, such those at about 470, 555, 780, 798, 1059, 1082 and 1161cm^{-1} are also visible, and they complicate the spectrum pattern particularly in the region at lower wavenumbers. Differences can be noted between the ATR and transmission spectra: for example, the peak at 1054cm^{-1}, clearly defined in the ATR spectrum, becomes a shoulder in the transmission spectrum. The characteristic doublet around 798 and 775cm^{-1}, visible in both the spectra, can be assigned to the Si-O symmetrical stretching vibrations of quartz [1,19]. Other peaks related to quartz and visible in the transmission and ATR spectra are around 470 and 520cm^{-1} (Si-O asymmetrical bending vibrations, obviously found only

in the transmission spectrum due to the shorter ATR range of analysis), 1163cm^{-1} (Si-O asymmetrical stretching vibrations) [19,20]. The peak at about 1083cm^{-1} is common to both silicates and aragonite (Si-O asymmetrical stretching vibrations and $v1$ symmetric CO_3 stretching respectively) [1,10,19–21]. In terms of the reflection mode, the region under 1300cm^{-1} is very complex, probably due to the presence of silicates, as identified by PXRD analysis that also determined quartz. The characteristic doublet of quartz is much less evident here and could only be hypothesised as inverted small peaks at 776 and 790cm^{-1}. The presence of quartz may also be supported by the presence of the band at 1990cm^{-1} [22]. PXRD analysis also confirms calcite as a main component, and the presence of aragonite.

The presence of aragonite in lime-based specimens has been ascribed by the literature [23–28] for example to the interaction of lime with Mg atoms, as suggested by Duchi et al. and by Raymond and Clifford [27–30]. Elsewhere, the formation of aragonite is related to the use of raw materials which have been exposed to temperatures over 600°C [25], or to room temperature conditions with pH values close to 11 [28]. In this particular case, it is not possible to unambiguously explain the formation of aragonite and further analysis beyond the scopes of this thesis should be designed [17].

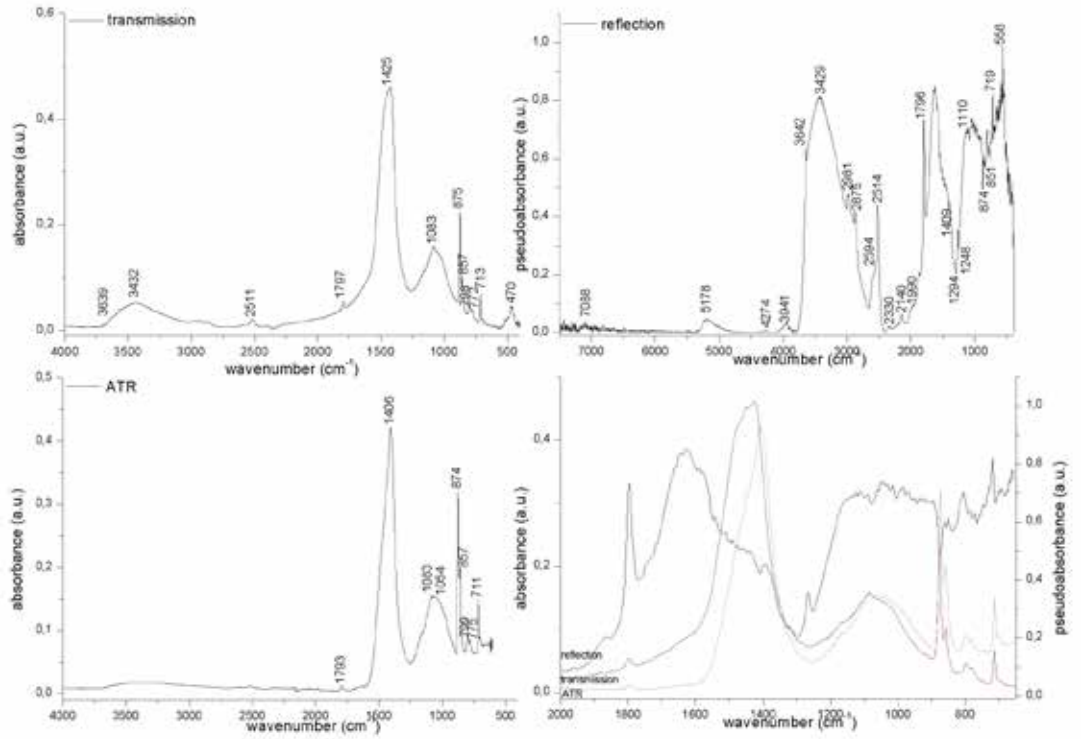

▲ *Figure 22. From the bottom left in clockwise order: ATR, transmission, reflection spectra, of a specimen of natural hydraulic lime (N). The main peaks are shown in the fourth graph (bottom right) the overlapping of the three spectra acquired in the three modes are shown (range 650-2000cm^{-1}).*

Portland Cement – Cement I (CI)

In figure 23, the transmission, ATR and reflection spectra of Portland cement are compared. The main peaks of $Ca(CO)_3$ and $Ca(OH)_2$ are visible at 713, 874, 1424, 1796, 2516, 2846, 2915, 3940cm^{-1} and 3643 and 7082cm^{-1}, respectively.

The signal peak at 459cm^{-1} could be related to the presence of different phases. According to Wilson and Fernandez-Carrasco et al. it could be a peak of quartz (antisymmetric bending of the O-Si-O bonds) [31,32], while in their recent work they assign this peak to C_3A phase (AlO^{6-}octahedral groups.) as Ghosh and Handoo in their work [5,33], Ren assigns the peak at about 460cm^{-1} to C_3S in-plane bending vibration υ_2 (indicating a dehydrated phase present) [34]. In this specimen, powder X-ray diffraction highlighted the presence of hydraulic silicates, but we could not identify C_3A not hydrated phase and quartz. It could show as the two techniques present different sensitiveness to these phases.
The absorbance at 976cm^{-1} in transmission spectrum is assigned to υ_3(Si-O) absorption band of *CSH* according to Ghosh [33], while Fernandez-Carrasco et Al. attributes it to Si-O vibrations [5], or elsewhere Si-O vibration of tobermorite is suggested [13]. In ATR mode this peak is shifted to 962cm^{-1}.
The peak at 1116cm^{-1} is due to υ_3 $[SO_4]^{2-}$ that could be connected to the presence of sulphates (gypsum or ettringite) [35–37]. This peak, in ATR mode, shifts to 1102cm^{-1}. It is ascribable to sulphates zone according to Ylmen et al. [11] and (1110cm^{-1}) Fernandez-Carrasco et al. to ettringite [31], while according to Arrizabalaga et al. to quartz [22], or to *CSH* zone 970-1100cm^{-1} according to Ylmen et al. [11].

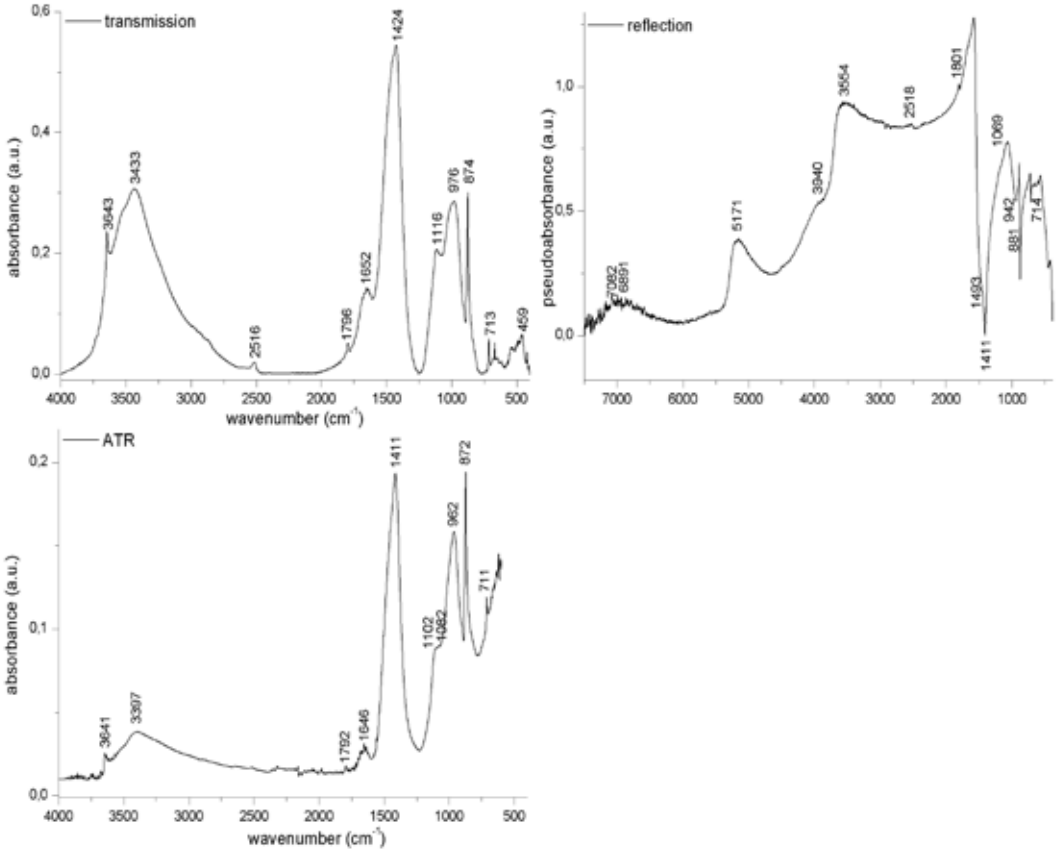

▲*Figure 23. From the bottom left in clockwise order: ATR, Transmission, Reflection spectra, of a specimen of Portland cement (CI). The main peaks are shown.*

The peak at 1082cm^{-1} could be due to the υ_1 CO_3^{2-} calcite symmetric stretching [1–3,5,10,21,32] or it could be the Si-O asymmetric stretching vibrations of quartz [20,21,31,32].
The band at 1652cm^{-1} is attributed to υ_2 H_2O bending vibration of ettringite [7,35,36] (1646cm^{-1} in ATR mode), or to CAH_{10} according to Fernandez-Carrasco et al., while according to Ylmén et al. this peak is caused by the bending vibration υ_2 of irregularly bound water [5,11]. Since the OH absorbance could have different origins, in this zone, it could be observed an overlapping of vibration of water present in different hydrated minerals that are present in cements. The presence of ettringite is confirmed by the peak at 5171cm^{-1} (OH combination band of water (υ_2+υ_3)), and the combination band of the OH and Al-OH stretching mode at 4491cm^{-1} [35].
The band at about 3433cm^{-1} is assigned to the stretching vibration υ_3 of H_2O and of υ_1 H_2O to ettringite [5,31,33,35]. This signal could also originate from the absorption of OH assigned to aluminum hydroxide $Al(OH)_3$ (bayerite) [5], which is confirmed also by the presence of the band at 3531cm^{-1} assigned to aluminum hydroxide [5,35].
The peak at 3643cm^{-1} (3641cm^{-1} in ATR mode) is assigned to OH stretching vibrations of $Ca(OH)_2$ but in the presence of *CSH* [13] and ettringite [33,35,36] it could represent an overlapping of the signals of all these phases. The peak at 7082cm^{-1} is the first O-H stretching overtone of $Ca(OH)_2$ [15]. In table 19 the main chemical compounds found in specimens made by one binder are listed.

label	**Chemical compound**						
G	$CaCO_3$	$Ca(OH)_2$	SiO_2 (?)				
C	$CaCO_3$	$Ca(OH)_2$	SiO_2 (?)				
CI	$CaCO_3$	$Ca(OH)_2$	Silicates/SiO_2	*CSH (?)*	*C_3S (?)*	*C_3A (?)*	ettringite
CIV	$CaCO_3$	$Ca(OH)_2$	Silicates/SiO_2	*CSH (?)*	*C_3S (?)*	*C_3A (?)*	ettringite
N	$CaCO_3$	$Ca(OH)_2$	Silicates/SiO_2				
Gs	$CaSO_4$ $2H_2O$	$CaCO_3$					

Table 19. List of the specimens and of the main chemical compound found in specimens made with one binder .

Mortars composed by one specific binder and one specific aggregate

Hydrated lime and quartz sand (CQ)

As shown in figure 24, the peaks previously ascribed to $CaCO_3$ and $Ca(OH)_2$ can be observed in spectra of sample CQ. The most interesting feature in reflection mode is the presence of two inverted peaks at 1093 and 1213cm^{-1}, apparently corresponding to the splitting of the band of quartz between 1000 and 1200cm^{-1}. Its characteristic shape is clearly identifiable in both CQ and CIQ reflection spectra (figures 24, 25) and also in the quartz reflection reference spectrum. Another proof can be found in the spectrum of Quartz GDS74 Sand Ottawa in the geological survey data book, series 1035 [38]. These peaks can be assigned to Si-O asymmetrical stretching vibration [1,19,20]. The region between 620cm^{-1} and 395cm^{-1} is very noisy in reflection mode, and only the peaks at 523 and 563cm^{-1} and the inverted doublet of quartz at 799 and 781cm^{-1} can be connected to the presence of silicates, whose reliable identification was not possible by using infrared spectroscopy. On the contrary, powder X-ray diffraction analyses determined the presence of quartz and feldspar [17].

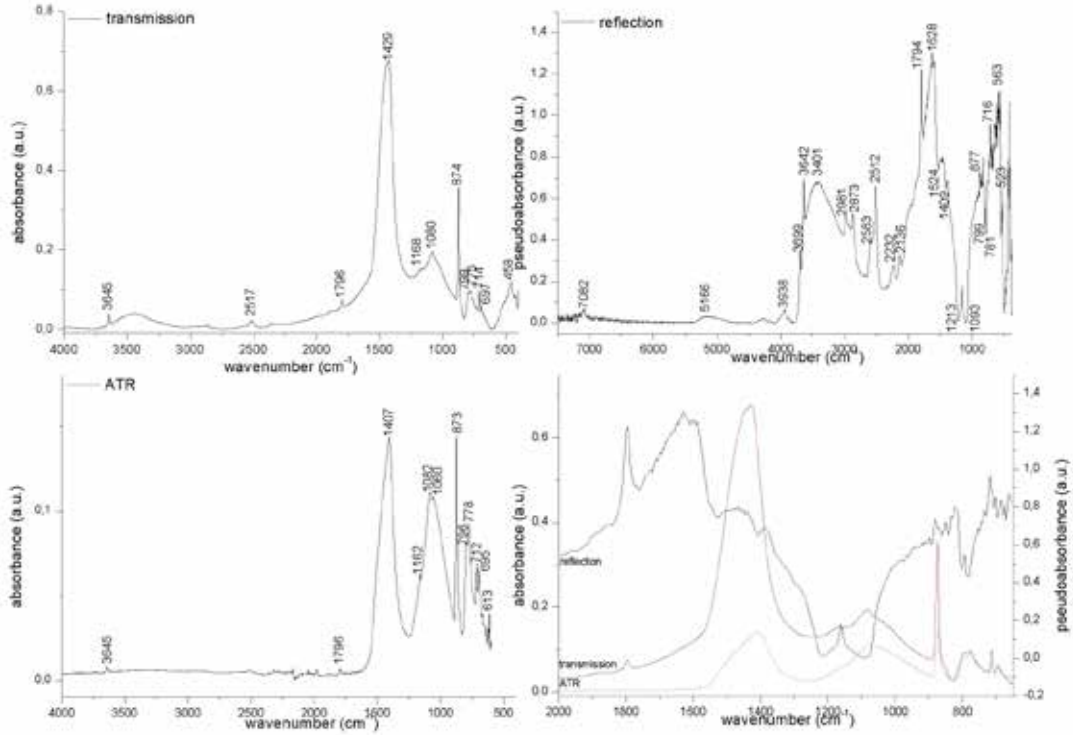

▲ *Figure 24. From the bottom left in clockwise order: ATR, Transmission, Reflection spectra, of a specimen of hydrated lime and quartz sand (CQ). The main peaks are shown. In the fourth graph (bottom right) the overlapping of the three spectra acquired in the three modes are shown (range 650-2000cm^{-1}).*

Portland cement and quartz sand (CIQ)

The transmission spectrum (figure 25) is very similar to the reference spectrum of Portland cement shown by Fernandez-Carrasco et al. [5]. The ATR and transmission spectra show the same peaks even if some differences in the relative intensities are detectable; as the peaks at 1083 and 978cm^{-1}. The peak at 978cm^{-1}, probably a Si–O stretching vibration of tobermorite [13], becomes a broad band in

the transmission mode. Below 1000cm^{-1} some peaks assigned to calcite and quartz are present, while the peaks between 400 and 1100cm^{-1} are ascribed to the bending and stretching vibrations of silicates, but infrared spectroscopy does not allow a reliable interpretation as the bands are common to several compounds with similar composition [32].

The peak of O-H stretching of portlandite at 3642cm^{-1} is visible only in the transmission and ATR spectra. In the reflection spectrum, only a very weak peak at 7077cm^{-1} can be identified. Furthermore, in the reflection spectrum a huge band from 1600 to 3600cm^{-1} is found. This band is not present in the other reflection spectra and hides some of the peaks linked to the presence of calcite. This broad band could be a particular aspect of the signals obtained from cement materials, probably ettringite and aluminum hydroxide, with reflection set up, but more specific studies are required to confirm this hypothesis [35].

In the reflection spectrum of this sample, as in CQ, the characteristic shape of the inverted peaks of Si-O asymmetrical stretching vibration at 1081 and 1219cm^{-1} and the inverted doublet of quartz at 799 and 781 cm^{-1} can be observed [38]. The infrared results are confirmed by PXRD, but with FTIR it was not possible to distinguish the characteristic cement silicates usually present [17,33]. The band at about 3436cm^{-1} is assigned to the stretching vibration υ_3 of H_2O with some character of υ_1 H_2O to ettringite [5,31,33,35] and/or to absorption of OH of the aluminum hydroxide $Al(OH)_3$ (bayerite) [5], while the band at 3529cm^{-1} is assigned to aluminum hydroxide [5,35].

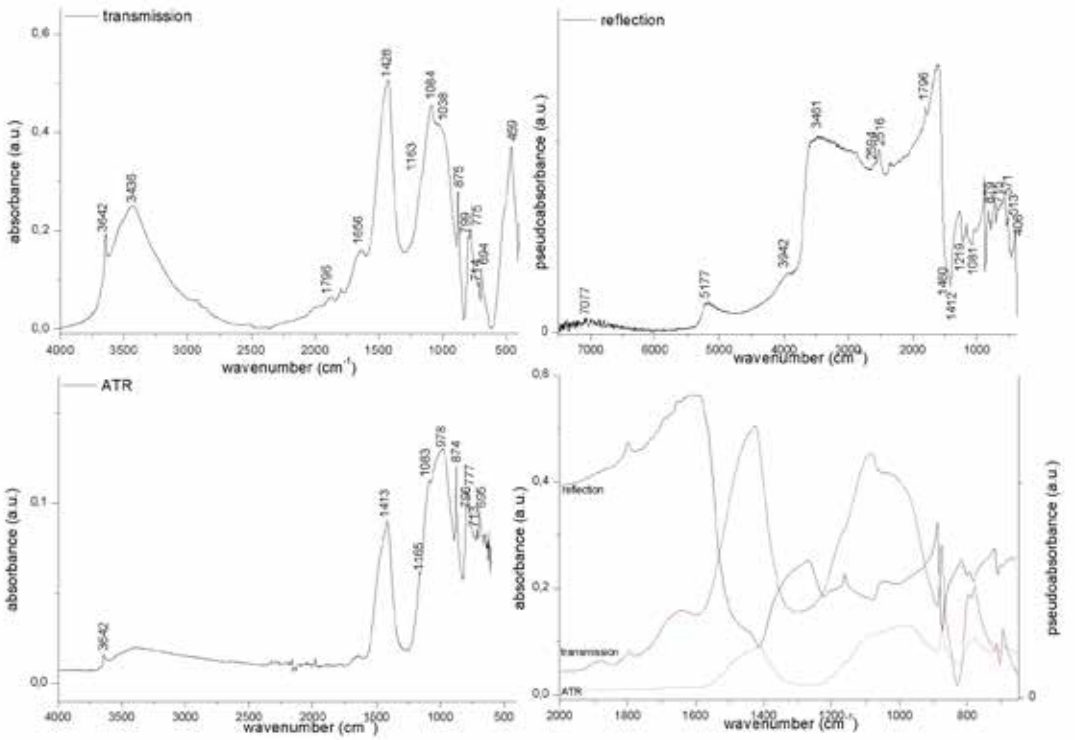

▲ *Figure 25. From the bottom left in clockwise order: ATR, transmission, Reflection spectra, and the overlapping of the three spectra between 650 to 2000 cm^{-1} of the specimen of Portland cement and quartz sand (CIQ). The main peaks are shown.*

Natural hydraulic lime and quartz sand (NQ)

In the sample NQ the characteristic peaks of calcite and portlandite are identified (714, 875, 1428-10, 1796 and 2512cm^{-1} and 3642 and 7077cm^{-1}) (figure 26). The peaks of silicate are more visible than in N specimen due to the presence of quartz in the aggregate. The doublet at 800 and 780cm^{-1} is visible in all the spectra. Furthermore the peaks at 1080 and 1184cm^{-1}, in transmission, and at 1080 and 1162cm^{-1}, in ATR mode, could be assigned to the presence of quartz (or carbonates (1080cm^{-1})) as already discussed in the previous paragraphs (hydrated lime and quartz sand, CQ).

The peak at 1046cm^{-1} visible only in ATR mode could be related to the presence of feldspar according to Farmer [21]. In reflection mode this sample presents the splitting of the quartz band to 1213 and 1091cm^{-1}. In N the presence of quartz was already visible but it was related to the presence of some impurities and some peaks were not clear. The peak at 5214cm^{-1} presents a shape similar to the one at about 5177cm^{-1} (O-H combination band of water ($\upsilon_2+\upsilon_3$)) in cements material assigned to OH of ettringite, but sulphates here are not present so it could be related to OH combination of other hydrated phases as silicates. The hydrated lime (composed by $Ca(CO)_3$) presents a band in this region (between 5000 and 5500cm^{-1}) but the shape and the intensity of the band in the material are different from those recorded in this sample, probably it is related to the different OH absorbance combination present.

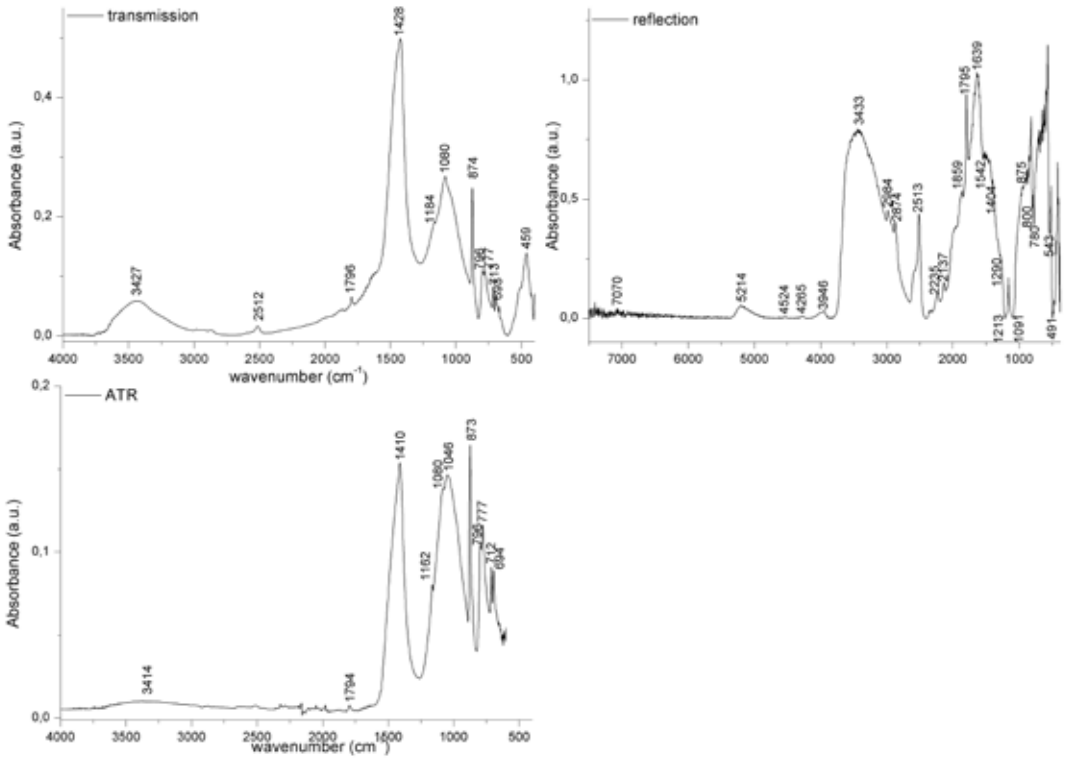

▲ *Figure 26. From the bottom left in clockwise order: ATR, Transmission, Reflection spectra of a specimen of natural hydraulic lime and quartz sand (NQ). The main peaks are shown.*

Gypsum and carbonate sand (GsM)

An example of a specimen with carbonate sand with a binder made of gypsum is discussed, so that the carbonate assignments are exclusively ascribable to the aggregate fraction.

The spectra, in figure 27, show very well-defined spectral patterns of the main components $CaCO_3$ and $CaSO_4$ $2H_2O$. The peaks related to $CaCO_3$ have been previously discussed. Both the binder and the aggregate fractions are clearly identifiable in all the spectra. As outlined, the ATR shift is always present and is particularly visible in the deformation and shift of peaks at 1143cm^{-1} and 1120cm^{-1} (υ_3 stretching vibrations SO_4^{-2}) [39], which are visible as a doublet in transmission and become a unique broad band in ATR at 1113cm^{-1}, while in reflection mode a single inverted peak at 1153cm^{-1} can be found. The peaks at 466cm^{-1} (υ_2 symmetric bending SO_4^{-2}) and 604cm^{-1} (υ_4 asymmetric bending SO_4^{-2}) are visible only in transmission mode. The peak at 669cm^{-1} (υ_4 asymmetric bending SO_4^{-2}) is well visible in both the ATR and transmission spectra [39]. For the reflection mode, a peak at 465cm^{-1} is present, together with two inverted peaks at 604 and 672cm^{-1}. The doublet centred at about 1620–1683cm^{-1} (υ_2 bending H_2O) is well identifiable in both ATR and transmission spectra, and it is only slightly shifted (1630–1685cm^{-1}) in the reflection mode [39].

Two strong peaks at 2138 ($\upsilon_1+\upsilon_3$ SO_4) and 2222cm^{-1} ($2\upsilon_3$ SO_4 and $\upsilon_2+\upsilon_L$ H_2O) are clearly visible only in reflection mode [2]. The characteristic peaks of $CaSO_4$ $2H_2O$ around 3400 and 3540cm^{-1} (υ_3 and υ_1 H_2O) become a unique broad band in reflection mode [39]. A peak at 5144cm^{-1} (υ_1 and/or υ_3 OH + υ_2 OH) can

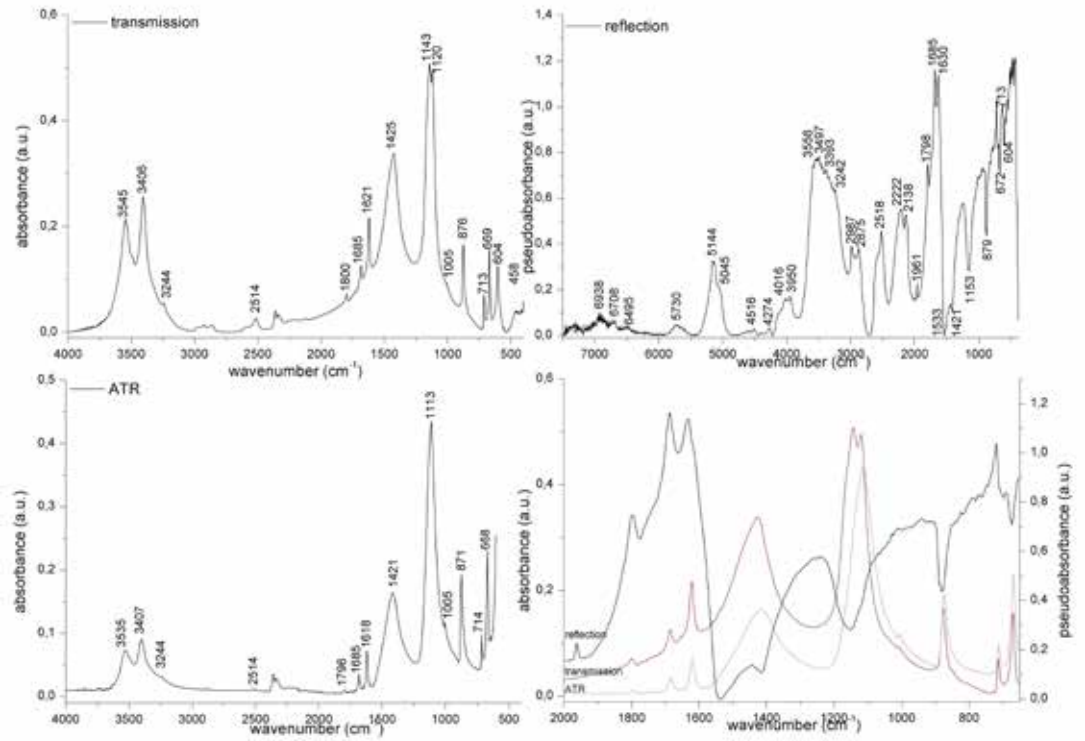

▲ *Figure 27. From the bottom left in clockwise order: ATR, transmission, Reflection spectra, and the overlapping of the three spectra between 650 to 2000 cm^{-1} of a specimen of gypsum and carbonate sand (GsM). The main peaks are shown.*

be found in the reflection spectrum [2,40]. At last, three overtones (ν(OH)) peaks are identified at 6495 cm^{-1}, 6708cm^{-1} and 6938cm^{-1} [12].

For what concerns the other samples with carbonate aggregate there are not difference in composition if we compare CM and GM samples with the samples C and G, since the chemical composition is the same. In the case of sample GsM, the bands connected to $Ca(CO)_3$ and $CaSO_4$ $2H_2O$ are clearly visible, as shown in figure 27. In the other samples (CIM, CIVM and NM) the signals of calcite are amplified if compared to the sample with the same binders. In table 20 the main chemical compounds found in specimens made by one binder are listed.

Mortars with quartz sand (Q)

Label	Chemical compound					
GQ	$Ca(CO)_3$	$Ca(OH)_2$	SiO_2	silicates (?)		
CQ	$Ca(CO)_3$	$Ca(OH)_2$	SiO_2	silicates (?)		
CIQ	$Ca(CO)_3$	$Ca(OH)_2$	SiO_2	ettringite	*CSH (?)*	$Al(OH)_3$ (?)
CIVQ	$Ca(CO)_3$	$Ca(OH)_2$	SiO_2	ettringite	*CSH (?)*	$Al(OH)_3$ (?)
NQ	$Ca(CO)_3$	$Ca(OH)_2$	SiO_2			
GsQ	$CaSO_4$ $2H_2O$	$Ca(OH)_2$	SiO_2			
Mortars with carbonate sand (M)						
Label	**Chemical compound**					
GM	$Ca(CO)_3$					
CM	$Ca(CO)_3$	$Ca(OH)_2$				
CIM	$Ca(CO)_3$	$Ca(OH)_2$	ettringite	$Al(OH)_3$ (?)	silicates (?)	*CSH (?)*
CIVM	$Ca(CO)_3$	$Ca(OH)_2$	ettringite	$Al(OH)_3$ (?)	silicates (?)	*CSH (?)*
NM	$Ca(CO)_3$	SiO_2 or silicates (?)				
GsM	$CaSO_4$ $2H_2O$	$Ca(OH)_2$				

Table 20. List of the samples made with one specific binder and one specific aggregate.

Specimens composed by a mix of two binders

Samples with a mix of two binders

Label	Chemical compounds					
GN	$Ca(CO)_3$	$Ca(OH)_2$	SiO_2			
GCI	$Ca(CO)_3$	$Ca(OH)_2$	*CSH (?)*	C_3S *(?)*	ettringite or gypsum	silicates (?)
GCIV	$Ca(CO)_3$	$Ca(OH)_2$	*CSH (?)*	ettringite or gypsum	$Al(OH)_3$ (?)	
GGs	$Ca(CO)_3$	$CaSO_4\ 2H_2O$	$Ca(OH)_2$			
CN	$Ca(CO)_3$	$Ca(OH)_2$	SiO_2	silicates (?)		
CCI	$Ca(CO)_3$	$Ca(OH)_2$	*CSH (?)*	C_3S *(?)*	ettringite or gypsum	silicates (?)
CCIV	$Ca(CO)_3$	$Ca(OH)_2$	*CSH (?)*	C_3S *(?)*	ettringite or gypsum	silicates (?)
CGs	$Ca(CO)_3$	$CaSO_4\ 2H_2O$	$Ca(OH)_2$			
NCI	$Ca(CO)_3$	$Ca(OH)_2$	ettringite	*CSH*	$Al(OH)_3$ (?)	silicates (?)
NCIV	$Ca(CO)_3$	$Ca(OH)_2$	ettringite			
NGs	$CaSO_4\ 2H_2O$	$Ca(CO)_3$	silicates (?)			

Table 21. List of the samples made with a mix of two binders.

In table 21 the specimens prepared by a mix of two binders and the chemical compounds found are listed. GCIV and CCIV present similar spectra both in transmission, in ATR and in reflection mode. The same similarities are visible also in GCI and CCI samples since the composition is comparable. CCI sample is reported as an example in the next paragraph. In general, both components of the mix of binders are visible in the samples, as calcite and gypsum, or silicates when cement is present. In reflection mode the peak at 5171cm^{-1} is sometimes slightly shifted but with the characteristic shape observed in cements.
Sometimes, especially on the so called "rough" surfaces, only peaks related to calcite are identified. This may be due to the surface roughness that enhances some peaks and to the presence of a surface layer with different composition from other surfaces. The formation of different layers is linked to the first steps of water evaporation from the specimens, carbonation and hardening. The presence of a layer different from the bulk in some samples is confirmed by ESEM analysis.

Hydrated lime and Portland cement (CCI)

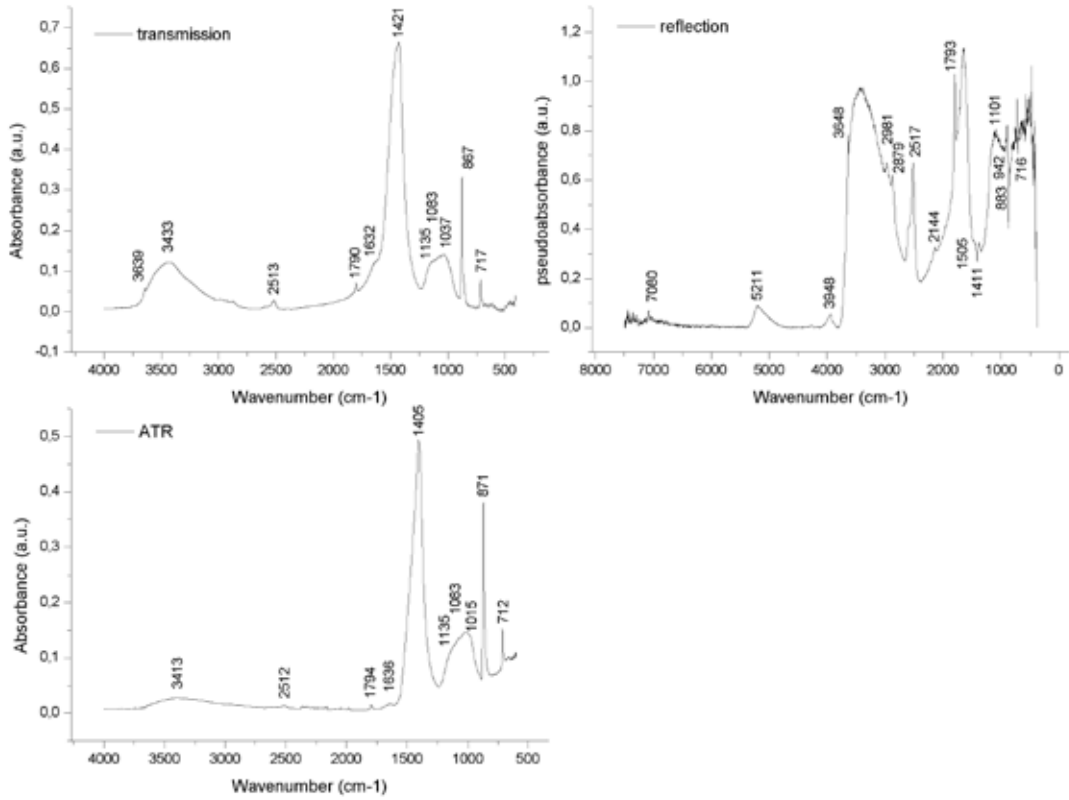

▲ *Figure 28. From the bottom left in clockwise order: ATR, Transmission, Reflection spectra of a specimen of hydrated lime and cement Portland (CCI). The main peaks are shown.*

The peaks of $Ca(CO)_3$ and $Ca(OH)_2$ are identifiable in all the spectra (figure 28). The peak at 1037cm^{-1} in transmission mode shifts to 1015cm^{-1} in ATR mode. If we consider the transmission mode, it could be a peak related to the presence of feldspars [32], that is not present in our sample since there is no aggregate. If we consider the ATR mode, the signal at 1015cm^{-1} could be a peak of sulphates (anhydrite) [37,40] or again a feldspar [32]. Therefore this peak, in this sample, is assigned to sulphates vibrations. Some peaks of *CSH* between 970 and 1100cm^{-1} could be present according to Ylmen et al. [11]. Considering the overlapping of different bands the single peaks are not clearly identifiable.

The peak at 1083-4cm^{-1} is assigned to quartz impurities (Si-O asymmetrical stretching vibrations) or to symmetric CO_3 stretching of $Ca(CO)_3$, or both. The shoulder at 1135cm^{-1} could be due to the presence of anhydrite or ettringite [5,33]. The peak at 1632-6cm^{-1} in transmission and ATR respectively is assigned to sulphates, like ettringite or gypsum [31,33,36,40,41], tobermorite according to Yu et al. [42] and to a peak of *CSH* according to Delgado et al [7]. In reflection mode the peaks at 1101cm^{-1} and 5211cm^{-1} are connected to the presence of sulphates and/or ettringite [11,33,35,40]. In the reflection spectra, between 900-1100cm^{-1}, there are two peaks: the first one in absorption (1101cm^{-1}), and the other inverted at 942cm^{-1}; this later was considered as a minimum between the two absorption peaks and it could be

connected to an unhydrated cement silicates phase as C_3S [7]. Its presence should be less frequent since the sample is made by hydrated cement, but in any case the presence of some unhydrated particle in the mixture could be possible.

Hydrated lime and gypsum (CGs)

In the spectra of this mixture the components of both the binders are identified. The peak at 602cm^{-1} ($\upsilon_4(SO_4)$ vibrations [39,43]) is visible in transmission and reflection but not in ATR mode because of the difference in the wavenumbers ranges between the two different instruments. The peak at 669cm^{-1} is well visible in all the spectra ($\upsilon_4(SO_4)$). The $\upsilon_1(SO_4)$ at 1005cm^{-1} is observable only in the spectrum in ATR mode [39,43]. The peak at 1119cm^{-1} (in transmission) and 1113cm^{-1} (in ATR mode) are assigned to $\upsilon_3(SO_4)$ [2]. This band appears as an inverted peak in reflection mode at 1146cm^{-1} $\upsilon_3(SO_4)$ according to Anbalagan et al [39]. The doublet at 1630 and 1685cm^{-1} (υ_2 bending H_2O) is present in all the spectra, although the peak at 1630cm^{-1} is slightly shift between transmission, ATR and reflectance mode [39,43]. The bands at about 2121cm^{-1} and 2224cm^{-1} are assigned to (υ_1+υ_3 SO_4) and (υ_2 + υ_L H_2O), respectively [2,40].

The peak at 2512-16cm^{-1} (υ_1 + υ_3 and/or $2\upsilon_2$ + υ_4 (CO_3^{-2})) is well visible in transmission and reflection modes, and the shoulder at 2583cm^{-1} is more intense/clearly identifiable in reflection mode. Also the main peaks of calcite are identified (715, 875, 1453, 1796cm^{-1}). The zone between 3000 and 4000cm^{-1} shows several differences in reflection mode, probably because the signals of gypsum are influenced by the surface roughness. These aspects will be discussed later. In the spectrum, in figure 29, the most intense peak is at 3496cm^{-1}, ($\upsilon_2(H_2O)$) [44], that is visible also in transmission presenting a lower intensity compared to the peaks at 3406 and 3547cm^{-1} assigned to $\upsilon_1(H_2O)$ and $\upsilon_3(H_2O)$ [39,45]. The combination bands about 5155cm^{-1} (υ_1 and/or υ_3 OH+υ_2 OH) [2,40] and the overtone bands over 6000cm^{-1} (6495cm^{-1} 1st overtone υ(OH), 6702cm^{-1} 1st overtone υ(OH), 6919cm^{-1} 1st overtone υ(OH)) are detectable in the reflectance spectrum [12].

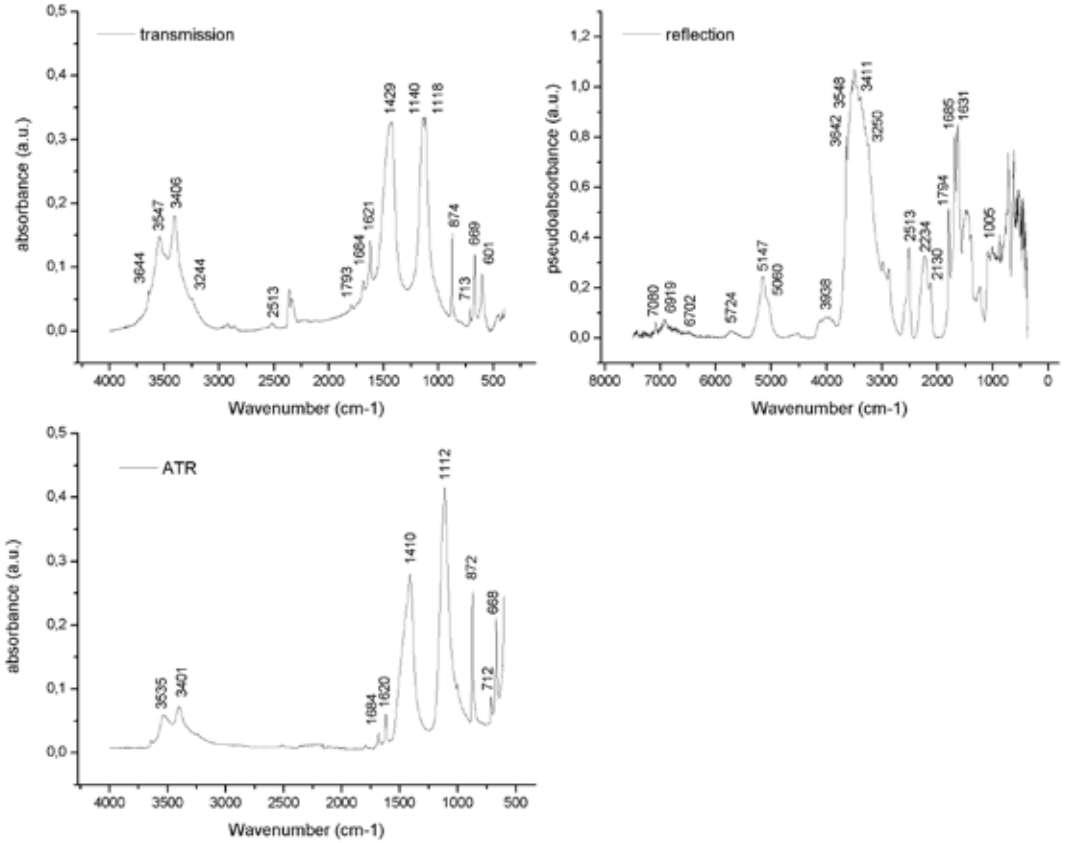

▲ *Figure 29. From the bottom left in clockwise order: ATR, Transmission, Reflection spectra of a specimen of hydrated lime and gypsum (CGs). The main peaks are shown.*

Mortars composed by a mix of two binders and a specific aggregate

Samples with 2 binders and carbonate and quartz sand					
Mortars with quartz sand (Q)					
Label	**Chemical compounds**				
GNQ	$CaCO_3$	$Ca(OH)_2$	SiO_2	silicates (?)	
GCIQ	$CaCO_3$	$Ca(OH)_2$	SiO_2	ettringite	$Al(OH)_3$ (?)
GCIVQ	$CaCO_3$	$Ca(OH)_2$	SiO_2	ettringite	silicates (?)
GGsQ	$CaSO_4$ $2H_2O$	$CaCO_3$	SiO_2		
CNQ	$CaCO_3$	$Ca(OH)_2$	SiO_2	silicates (?)	
CCIQ	$CaCO_3$	$Ca(OH)_2$	SiO_2	ettringite	silicates (?)
CCIVQ	$CaCO_3$	$Ca(OH)_2$	SiO_2	ettringite	silicates (?)
CGsQ	$CaSO_4$ $2H_2O$	$CaCO_3$	SiO_2		
NCIQ	$CaCO_3$	$Ca(OH)_2$	SiO_2	ettringite	*CSH (?)*
NCIVQ	$CaCO_3$	$Ca(OH)_2$	SiO_2	ettringite	
NGsQ	$CaSO_4$ $2H_2O$	$CaCO_3$	SiO_2		
Mortars with carbonate sand (M)					
Label	**Chemical compounds**				
GCIVM	$CaCO_3$	$Ca(OH)_2$	silicates (?)		
GCIM	$CaCO_3$	$Ca(OH)_2$	silicates (?)	ettringite (?)	
GGsM	$CaSO_4$ $2H_2O$	$CaCO_3$	$Ca(OH)_2$		
GNM	$CaCO_3$	$Ca(OH)_2$	SiO_2 (?)	silicates (?)	
CNM	$CaCO_3$	$Ca(OH)_2$	SiO_2 (?)	silicates (?)	
CCIM	$CaCO_3$	$Ca(OH)_2$	silicates (?)	ettringite (?)	
CCIVM	$CaCO_3$	$Ca(OH)_2$	ettringite	silicates (?)	
CGsM	$CaSO_4$ $2H_2O$	$CaCO_3$	SiO_2 (?)		
NCIM	$CaCO_3$	$Ca(OH)_2$	ettringite	*CSH (?)*	
NCIVM	$CaCO_3$	$Ca(OH)_2$	SiO_2 (?)	*CSH (?)*	ettringite
NGsM	$CaSO_4$ $2H_2O$	$CaCO_3$	SiO_2		

Table 22. List of the samples made with two binders and aggregates.

Hydrated lime, natural hydraulic lime and quartz sand (CNQ)

In GNQ and CNQ (figure 30, and table 22) the band between 900-1000cm^{-1} of hydrated hydraulic silicates is not visible; the peak at 1083cm^{-1} is assigned both to quartz or $CaCO_3$, while the doublet of 797cm^{-1} and 778cm^{-1} and the signals at 508 and 459cm^{-1} are assigned to quartz. In the same sample the peak at 1047cm^{-1} in ATR mode could due to a splitting of quartz or a feldspar component present in the sample.

The aggregate pattern sometimes covers the signals of other components. For example, the presence of quartz covers the signals of silicates. In all samples containing carbonate as aggregate the signals of calcite are amplified. In fact in the samples CNM and GNM only small peaks of silicates are visible, while the main peaks are assigned to calcite and portlandite. The peak at 5189cm^{-1} in the zone of OH overtone could indicate the presence of hydrated phases in the mixture.

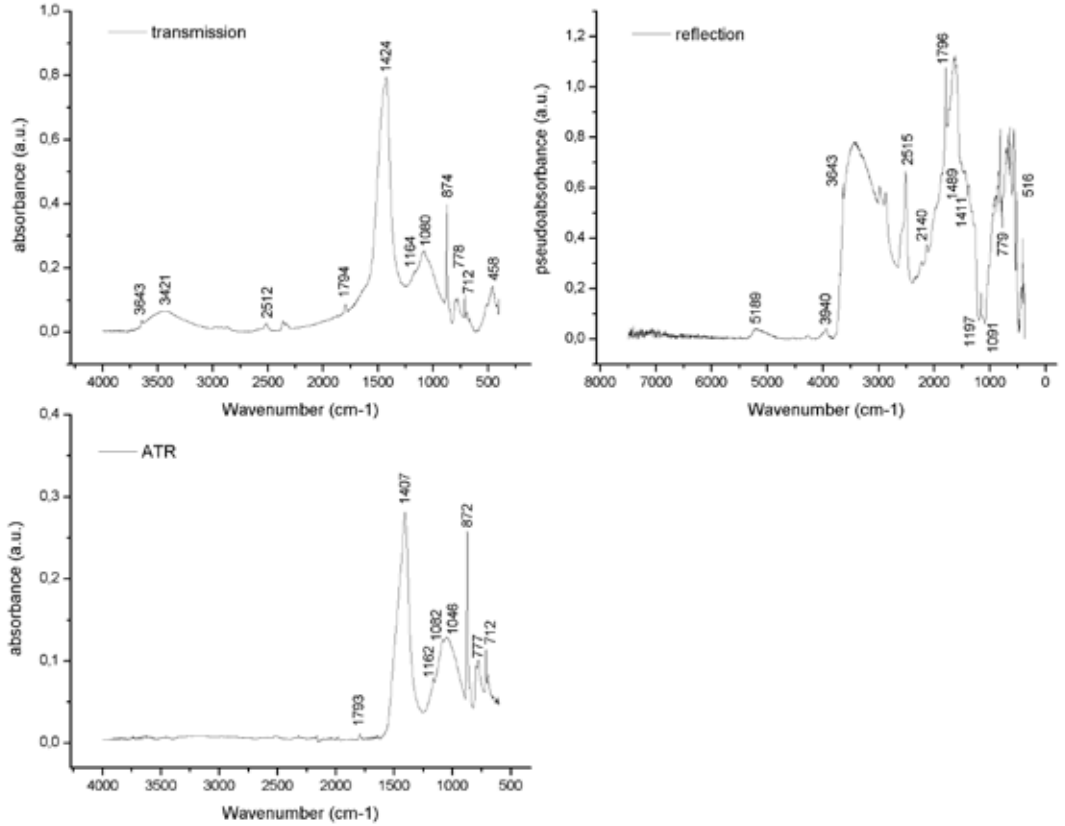

▲ *Figure 30. From the bottom left in clockwise order: ATR, Transmission, Reflection spectra of a hydrated lime, natural hydraulic lime and quartz sand (CNQ) specimen. The main peaks are shown.*

Hydrated lime, cement Portland and quartz sand (CCIQ)

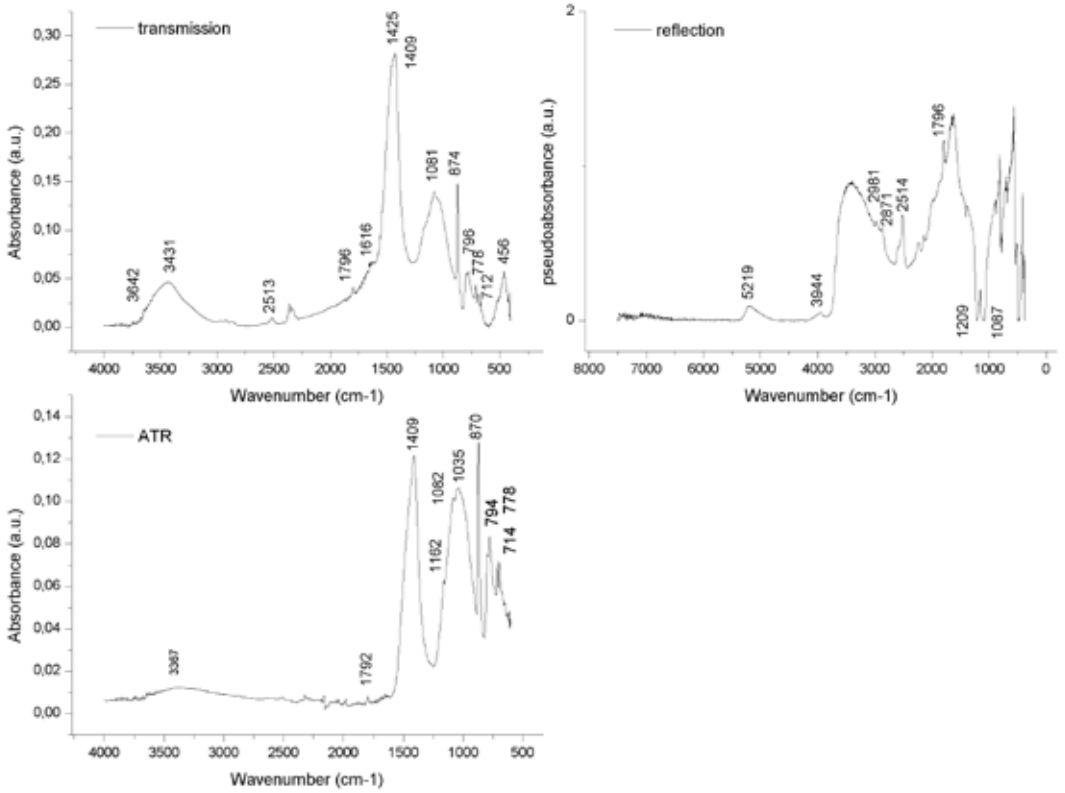

▲ *Figure 31. From the bottom left in clockwise order: ATR, transmission, reflection spectra of a hydrated lime, Portland cement and quartz sand (CCIQ) specimen. The main peaks are shown.*

The main peaks of calcite are present in all the spectra, while portlandite is visible only in transmission mode (figure 31). The prominent presence of 5219cm^{-1} that is assigned to OH of ettringite indicates the presence of cement in the mixture. The peak at 1616cm^{-1} (in transmission mode) confirms the presence of sulphates. In the reflection spectrum, at 1209 and 1087cm^{-1} there is the splitting of quartz that covers any other possible Si-O signals in this zone. A band at about 1000-980cm^{-1} is visible on infrared reflection spectra acquired on the smooth surface; in that case the components of quartz are less intense. This behaviour is seen also in samples like GCIQ, GCIVQ and CCIVQ. The dissimilar behaviour between the different surfaces will be discussed later. Moreover, the peak at 456cm^{-1} could be the overlay of quartz and hydraulic hydrated silicates vibrations, thus indicating the presence of silicates in the sample. The shoulder at 1025cm^{-1} (in transmission mode) could result by the overlapping of quartz and the silicates present in the cement. In ATR, a peak at 1035cm^{-1} is present, as in the ATR spectrum of quartz sand. In this case it could be considered a splitting of quartz or a feldspar component or both as already discussed in the paragraph of the specimen CCI.

Surface roughness

Hydrated lime C

The derivative peaks belonging to $CaCO_3$ at 712cm^{-1} υ_4, CO_3^{2-} and 873cm^{-1} υ_2, CO_3^{2-} [1,3,5] are visible only in the spectrum recorded on the "rough face" and scarcely recognizable on the other faces (figure 32). Conversely, the peaks related to $Ca(OH)_2$ (3640cm^{-1} O-H stretching [7] and 7087cm^{-1} 1st overtone of $Ca(OH)_2$ stretching modes [7,13,14]) are less intense on the "rough face" than those observed when analyzing the "smooth face" and the "180 face". In the same range, the weak peaks between 900 and 1300 cm^{-1} are visible only in the "smooth face" and the "180 face". In addition, the peak at about 1458cm^{-1}, which may suggest the presence of $CaCO_3$, presents the characteristic derivative shape also described in the literature only in the spectrum of the "rough face" [4]. The peak at 4185cm^{-1} could be a combination band of Ca-OH, as discussed in the literature [46], and it also appears in the spectrum of the reference commercial hydrated lime [17].

The shape of the double band at 4276cm^{-1} and 4268cm^{-1} (CO_3^{2-} ($3\upsilon_3$)) [2,12] is the same for "180" and "rough" faces, while the relative intensity is the opposite in the "smooth face" [17].

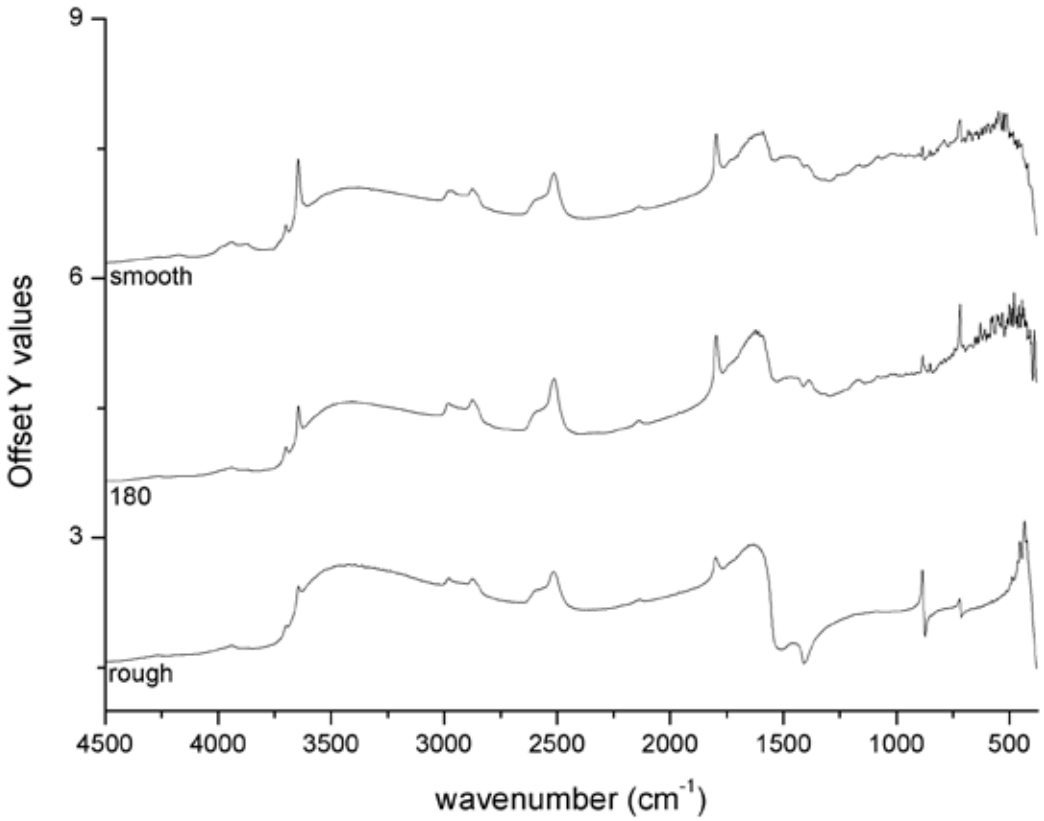

▲ *Figure 32. From the top: reflection spectra (4500–400 cm^{-1}) of smooth, 180 and rough faces of specimen C, the main peaks are at 712, 873, 1458, 1796, 2134, 2514, 2594, 2873, 2979, 3640, 3697, 4185, 4276, 4268cm^{-1}.*

Gypsum sample (Gs)

The doublet at 1633 and 1685cm^{-1} (υ_2 bending H_2O) is present in all the spectra but the relative intensities of the two peaks change [39] (figure 33). In the spectrum of the "180 face" the two peaks have almost the same intensity, while in the other two spectra the peak at 1634cm^{-1} is higher than the other one. The shape of the bands at about 2128cm^{-1} ($\upsilon_1+\upsilon_3$ SO_4) and 2220cm^{-1} ($\upsilon_2 + \upsilon_L$ H_2O) also depends on the roughness, becoming weaker from the "180 face" to the "smooth face", where the intensity is the same for the two peaks [2]. A more impressive difference emerges from the bands in the range 3000–4000cm^{-1} composed of the peaks 3245, 3388 and 3509cm^{-1} (υ_3 and υ_1 H_2O) [45]. In the spectrum of the "180 surface" a unique, large and intense band can be observed. Conversely, in the "rough face" the typical three peaks at 3497, 3443 and 3246cm^{-1} are more clearly distinguished, and in the "smooth face" they are well separated. The combination bands around 5155cm^{-1} (υ_1 and/or υ_3 OH+υ_2 OH) [2,40] and the overtone bands over 6000cm^{-1} (6495cm^{-1} 1st overtone υ(OH), 6702cm^{-1} 1st overtone υ(OH), 6910cm^{-1} 1st overtone υ(OH)) are detectable in all three spectra, but are much clearer in the "smooth face" [12].

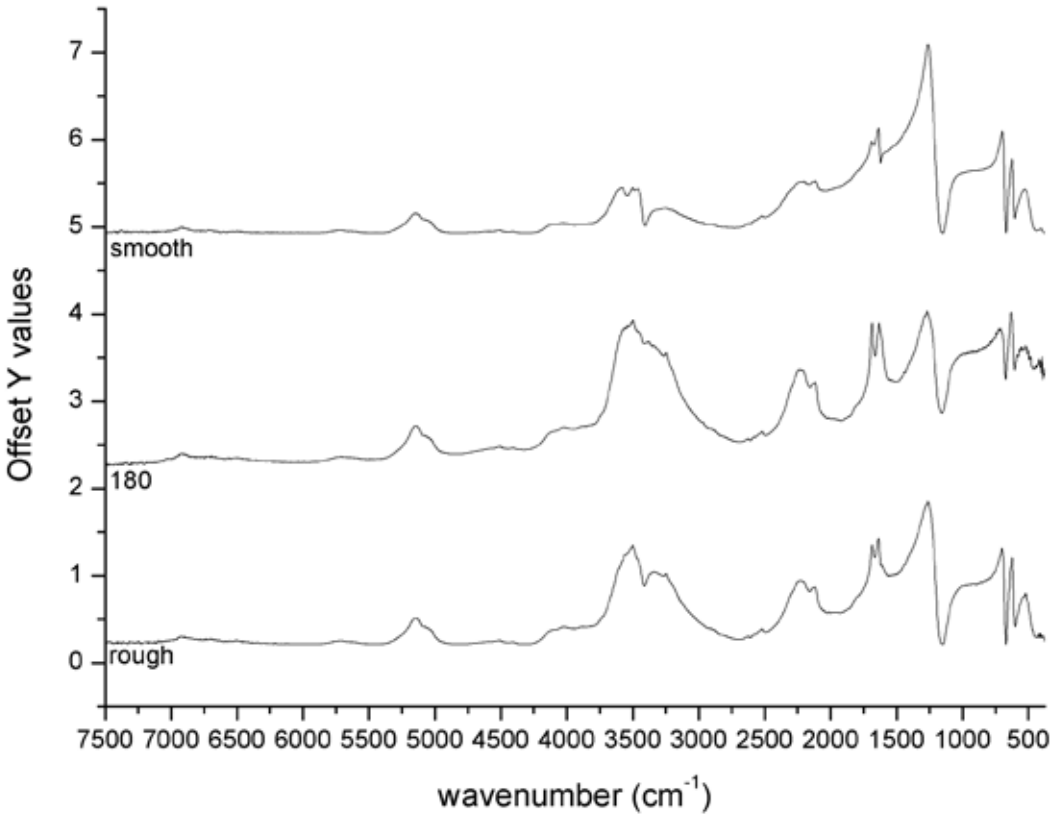

▲ *Figure 33. From the top: reflection spectra (7500–400 cm^{-1}) of 180, smooth and rough faces of specimen Gs, the main peaks are at: 604, 672, 1634, 1685, 2220, 3242, 3388, 3509, 5155, 6495, 6702, 6910cm^{-1}.*

Hydrated lime and quartz sand (CQ)

The analysis of the specimen made of hydrated lime and silicate sand shows better defined peaks around 2200 and 1100cm^{-1} for the "180 face" (figure 34). The derivative bands at 712 and 873cm^{-1} are clearer in the "rough faces". In addition, the main peak at 1424cm^{-1} (υ_3 CO_3^{-2}, the antisymmetric stretching) in some cases is inverted and split into two peaks at 1409 and 1507cm^{-1} and it is derivative in others [4].

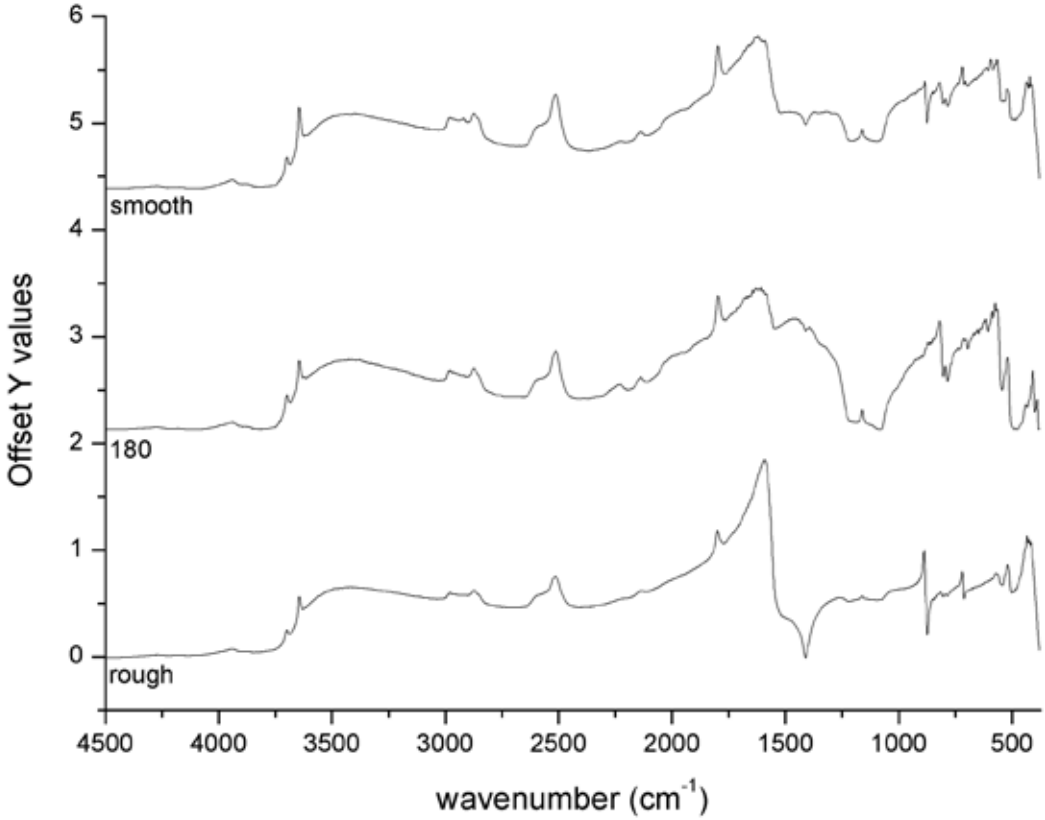

▲ *Figure 34. From the top: reflection spectra (7500–400 cm^{-1}) of 180, smooth and rough faces of specimen CQ, the main peaks are at 712, 873, 1409, 1507, 1796, 2514, 2594, 2873, 2979, 3640, 3697, 4185, 4276, 4268cm^{-1}.*

Portland cement and quartz sand (CIQ)

As it is possible to see, in figure 35, in the region under 2000cm^{-1} the peaks change a lot. For example in the spectrum of the rough surface only peaks of calcite are visible (712, 873, 1409 and 1796cm^{-1}). This phenomenon is observed also on other samples, in the rough surface. It could be due to a different division of the phases near the surface during the hardening. On the 180 surface both peaks of calcite (715, 879, 1412, 1460, 2516 and 3942cm^{-1}) and quartz (1081 and 1219cm^{-1}) are observable. The peak related to the splitting of quartz covers the peaks of cement silicates and sulphates. On the smooth face the peaks of quartz are not visible, while the peaks of calcite and of other silicates and sulphates are visible.

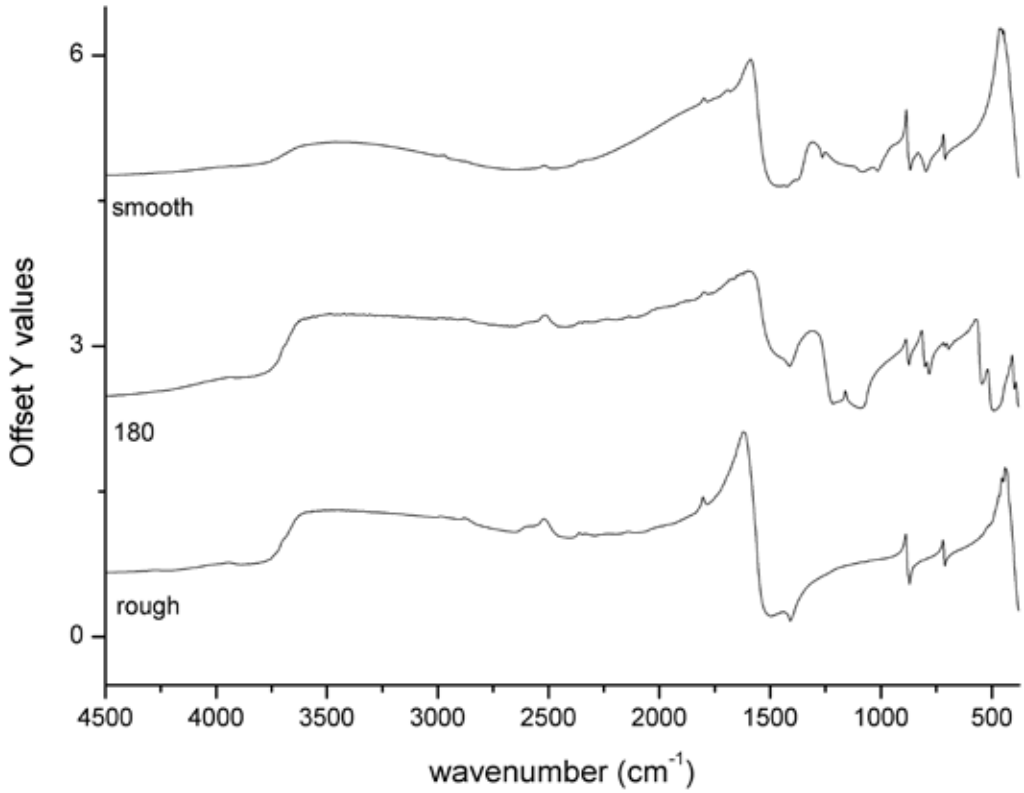

▲ *Figure 35. From the top: reflection spectra (7500–400 cm^{-1}) of 180, smooth and rough faces of specimen CIQ, the main peaks are at 712, 873, 1409, 1507, 1796, 2514, 2594, 2873, 2979, 3640, 3697, 4185, 4276, 4268 cm^{-1}.*

Natural hydraulic lime with Portland cement and quartz sand (NCIQ)

The main peaks of quartz, calcite and portlandite are clearly visible (460, 713, 778-6, 990-2, 1081, 1428-17, 1162, 1417, 1621, 3439, 3643cm^{-1}). In transmission and ATR mode the shoulder at 990cm^{-1} is probably due to the presence of hydrated silicates (figure 36). In ATR mode this band shifts to higher wavenumbers (992-1004cm^{-1}). In reflection mode (figure 37), a band in this zone is clearly visible only on the smooth surface; on the other surfaces the splitting of quartz covers the other peaks between 990 and 1200cm^{-1}.

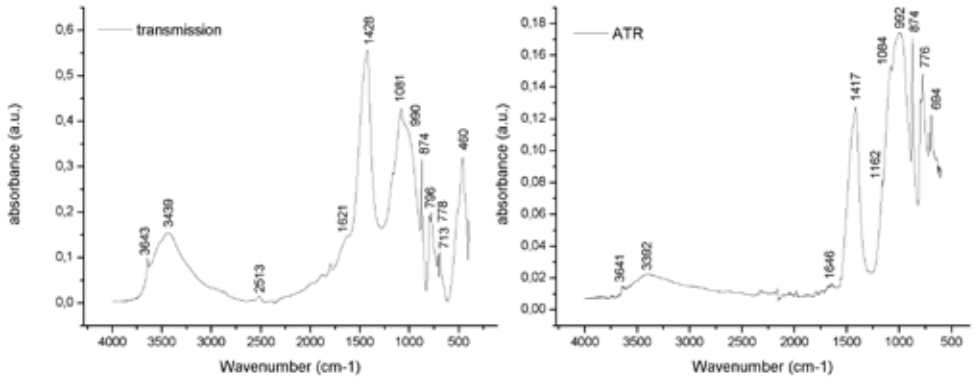

Figure 36. From the top: reflection spectra (7500–400 cm^{-1}) of 180, smooth and rough faces of specimen NCIQ, the main peaks are at 713, 874, 990-2, 1081-4, 1428-17, 1621-46, 2513, 3392, 3439 and 3643 cm^{-1}.

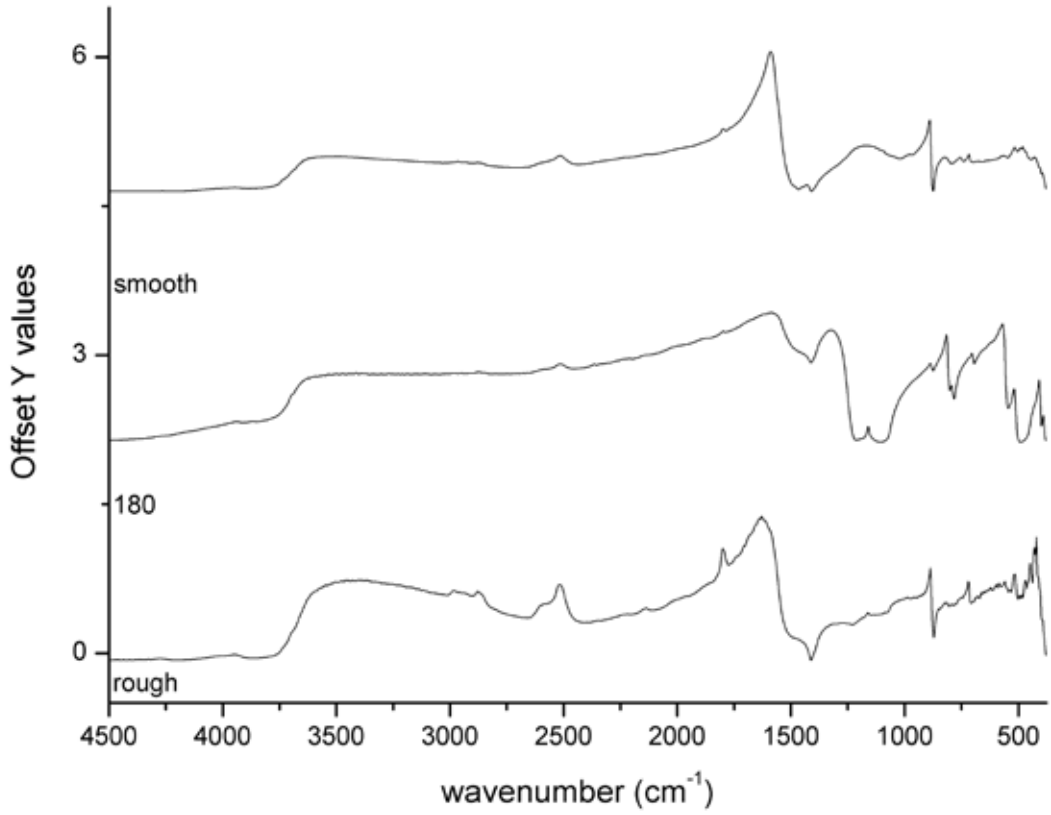

▲ *Figure 37. From the top: reflection spectra (7500–400 cm^{-1}) of 180, smooth and rough faces of specimen NCIQ, the main peaks are at 712, 873, 1409, 1507, 1796, 2514, 2594, 2873, 2979, 3640, 3697, 4185, 4276, 4268 cm^{-1}.*

Discussion and conclusions

The numerous data collected during this preliminary study allowed us to build a "database" of possible variations in the signals obtained with different FTIR techniques. The results show for the first time the potential of portable FTIR instrumentation, that could be used both during in-situ preliminary study of the building materials and when the removal of samples from the artworks is not allowed. The dependence of shape and intensity of signals on the surface roughness was studied as well, as a valuable tool for the interpretation of in situ analyses.

Summarizing the three techniques highlights, some important differences between transmission and ATR modes were found, particularly in the region around 1000cm^{-1}, where the relative intensities of the peaks change (figure 24) and also their shape, as could be seen in samples with gypsum (figure 27 and 33). Some interesting trends can also be noted in external reflection FTIR, such as the frequent splitting of the main band of the carbonate group (around 1430cm^{-1} υ_3 CO_3^{-2} antisymmetric stretching) into two inverted peaks, with a spacing of about 100cm^{-1}. Another similar feature is related to quartz, whose band around 1100cm^{-1} is generally inverted and clearly split in two peaks with a very particular and recognizable shape. Some signals (such as overtones of $CaCO_3$ at 2516 and 2594cm^{-1} and combination peaks at 2977 and 2875cm^{-1}) are strongly enhanced in their intensities in the reflection spectra; the characteristic peak of $Ca(OH)_2$ at 3642cm^{-1} is clearly detectable also in the reflection mode.

Some important shifts (around 20–25 cm^{-1} at most) have been detected at to $\upsilon 3$ CO_3^{-2} antisymmetric stretching peak. The broad band centred at 3436cm^{-1} and ascribable to O-H stretching is only evident in ATR mode. Furthermore, in samples bound with gypsum, an impressive change in shape and intensity of H_2O υ_3 and v_1 signals between 3244 and 3645cm^{-1} could be noticed in reflection mode, where they could even merge in a unique broad band. These changes are remarkable for the identification of gypsum in real samples, where its presence could either be due to its use in the binder or ascribed to a decay by-product.

This non-invasive study provides the first systematic application of external reflection FTIR on mortar materials, and also tests the response of the technique to differently roughed surfaces. The results show the high potential of portable FTIR in studying mortars; even if distortions, derivative and inverted signals could be present, the spectra are very informative and reliable for mixtures as well. In addition, the combination and overtones bands over 4500cm^{-1} can give further signals that are useful for the identification of the components of the mortars as the band at 5171 and 5219cm^{-1} (OH overtone). These presence of cement are amplified and suggest the presence of ettringite also thank to their characteristic shape.

The results of the response of differently surfaces roughness confirm the findings in the literature, and show how the intensity and the distortion of bands are influenced by the surface micro-morphology of the area analysed by the instrument. The experiments were designed expecting a better readability of the signals in the spectra of the smooth faces, as the appearance of the specimen surface was predicted to give less distorted signals, because of the less significance of the diffuse component. Conversely, no systematic correlation between roughness and legibility of peaks is evident from the data here presented, even if, generally speaking, spectra on smooth surfaces appear to be similar to traditional transmission spectra. Some specific peaks of the raw materials seem to be better defined in the rough faces. On the contrary, in the smooth faces other spectral ranges seem more informative. The derivative bands are thus always better defined in the rough face. Further systematic analyses of a larger set of specimens of various roughnesses would be of benefit. Moreover, in some cases as CIQ (figure 35), on the rough face the presence

of $CaCO_3$ is dominant. This behaviour could be explained by a selective formation of phase on the border during the setting, in fact a thick layer composed mainly by Ca and O is identified by ESEM EDX analysis. (Environmental scanning electron microscopy, ESEM paragraph).

This first set of data will allow to face real cases on unknown samples, where a mortar is present as rendering, plastering, bedding, stucco or as a support for painting layers. The use of the acquired spectral references will be of aid in case of studying calcium carbonate, present as binder, and gypsum, formed as by-products in decay processes, such as black crusts, encrustations and efflorescence, with the special improvement of monitoring their formation without sampling.

In mixed mortars is more difficult to distinguish the two components and the aggregate if compared to mortars composed by one binder. It is complex, especially when the cement is mixed with another binder, because it is not easy to separate the signals from one component to the other; some examples are CCIQ in figure 31 or CNQ in figure 30.

It is also difficult to distinguish the components when their composition is chemically the same but the sources of the raw materials are different, for example $CaCO_3$ could be present in the aggregate or/and in the binder. In figure 38 a comparison of three samples is shown

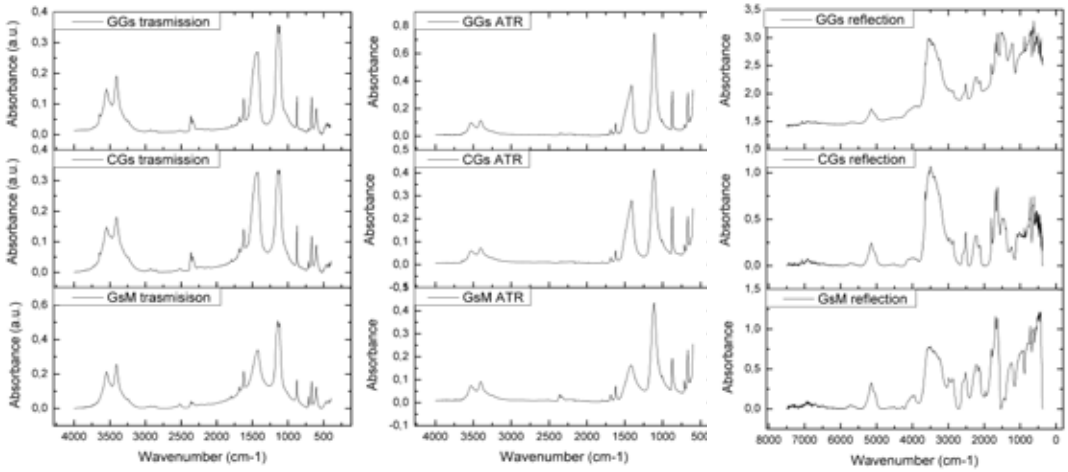

▲ *Figure 38. Comparison between samples GsM, CGs and GGs in transmission, ATR and reflection mode.*

The following table summarize the advantages and the drawbacks of transmission, ATR and reflection spectroscopy applied to the mortars investigated (table 23).

Transmission	
Advantages	**Drawbacks**
OH vibrations are more clearly shown than in ATR spectra	After sample is mixed with KBr no other analyses are possible
More references in literature.	
Cement identification, although if mixed it is more difficult.	
ATR	
Advantages	**Drawbacks**
The sample could be reused for other analyses.	Shift of some peaks.
Cement identification, although if mixed it is more difficult.	
Reflection	
Advantages	**Drawbacks**
No need to sample.	Splitting of some bands.
Portable.	Roughness influence into peak shape.
Two or more components of the mortars are identified, also the quartz of the aggregate.	Sensible to the composition of the first layer: problems if there is zonation.
Most of the peaks identified have the same wavenumbers as those of the peaks identified in transmission.	
Cement identification.	
The spectrum range is larger than the other two modes, so there is more information to identify the composition of the sample.	

Table 23. Summary of advantages and drawbacks of the three different infrared spectroscopies used.

References

[1] M.R. Derrick, D. Stulik, J.M. Landry, Infrared Spectroscopy in Conservation Science, The Getty Conservation Institute, Los Angeles, 1999.

[2] C. Miliani, F. Rosi, A. Daveri, B.G. Brunetti, Reflection infrared spectroscopy for the non-invasive in situ study of artists' pigments, Appl. Phys. A Mater. Sci. Process. 106 (2012) 295–307. doi:10.1007/s00339-011-6708-2.

[3] C.E. Weir, E.R. Lippincott, Infrared Studies of Aragonite, Calcite, and Vaterite Type Structures in the Borates, Carbonates, and Nitrates, J. Res. Natl. Bur. Stand. A. Phys. Chem. 65 (1961) 173–183. doi:10.6028/jres.065A.021.

[4] C. Ricci, C. Miliani, B.G. Brunetti, A. Sgamellotti, Non-invasive identification of surface materials on marble artifacts with fiber optic mid-FTIR reflectance spectroscopy, 69 (2006) 1221–1226. doi:10.1016/j.talanta.2005.12.054.

[5] L. Fernández-Carrasco, D. Torrens-Martín, L.M. Morales, Sagrario Martínez-Ramírez, Infrared spectroscopy in the analysis of building and construction materials, Infrared Spectrosc. – Mater. Sci. Eng. 370 Technol. Technol. (2012) 369–382. doi:10.5772/36186.

[6] L. Rampazzi, V. Brunello, C. Corti, E. Lissoni, Non-invasive techniques for revealing the palette of the Romantic painter Francesco Hayez, Spectrochim. Acta Part A Mol. Biomol. Spectrosc. 176 (2017) 142–154. doi:10.1016/j.saa.2017.01.011.

[7] A.H. Delgado, R.M. Paroli, J.J. Beaudoin, Comparison of IR techniques for the characterization of construction cement minerals and hydrated products, Appl. Spectrosc. (1996). doi:10.1366/0003702963905312.

[8] W. Vetter, M. Schreiner, Characterization of pigment-binding media systems - Comparison of non-invasive in-situ reflection FTIR with transmission FTIR microscopy, (2011) 10–22.

[9] P. Fletcher, C. Hall, Determining Cement Composition by Fourier Transform Infrared Spectroscopy, 7355 (1995).

[10] S. Gunasekaran, G. Anbalagan, S. Pandi, Raman and infrared spectra of carbonates of calcite structure, J. Raman Spectrosc. 37 (2006) 892–899. doi:10.1002/jrs.1518.

[11] R. Ylmén, U. Jäglid, B.-M. Steenari, I. Panas, Early hydration and setting of Portland cement monitored by IR, SEM and Vicat techniques, Cem. Concr. Res. 39 (2009) 433–439. doi:10.1016/j.cemconres.2009.01.017.

[12] M. Vagnini, C. Miliani, L. Cartechini, P. Rocchi, B.G. Brunetti, A. Sgamellotti, FT-NIR spectroscopy for non-invasive identification of natural polymers and resins in easel paintings, in: Anal. Bioanal. Chem., 2009. doi:10.1007/s00216-009-3145-6.

[13] P. Yu, R.J. Kirkpatrick, B. Poe, P.F. McMillan, X. Cong, Structure of Calcium Silicate Hydrate (C-S-H): Near-, Mid-, and Far-Infrared Spectroscopy, J. Am. Ceram. Soc. 82 (2004) 742–748. doi:10.1111/j.1151-2916.1999.tb01826.x.

[14] K. Shinoda, T. Nagai, N. Aikawa, Pressure-dependent anharmonic coefficient of OH in portlandite by NIR-IR spectroscopy with DAC, J. Mineral. Petrol. Sci. 95 (2000) 65–70. doi:10.2465/jmps.95.65.

[15] F. Ridi, E. Fratini, S. Milani, P. Baglioni, Near-Infrared Spectroscopy Investigation of the Water Confined in Tricalcium Silicate Pastes, J. Phys. Chem. B. 110 (2006) 16326–16331. doi:10.1021/jp060026y.

[16] A. Peyvandi, D. Holmes, P. Soroushian, A.M. Balachandra, Monitoring of sulfate attack in concrete by Al^{27} and Si^{29} MAS NMR spectroscopy, J. Mater. Civ. Eng. 27 (2014) 04014226. doi:10.1061/(ASCE)MT.1943-5533.0001175.

[17] V. Brunello, C. Corti, A. Sansonetti, C. Tedeschi, L. Rampazzi, Non-invasive FTIR study of mortar model samples: comparison among innovative and traditional techniques, Eur. Phys. J. Plus. 134 (2019) 270. doi:10.1140/epjp/i2019-12667-1.

[18] M. Sato, S. Matsuda, Structure of vaterite and infrared spectra, Zeitschrift Fur Krist. - New Cryst. Struct. 129 (1969) 405–410. doi:10.1524/zkri.1969.129.5-6.405.

[19] J. Hlavay, K. Jonas, S. Elek, J. Inczedy, Characterization of the Particle Size and the Crystallinity of Certain Minerals By Ir Spectrophotometry and Other Instrumental Methods - 2. Investigations on Quartz and Feldspar., Clays Clay Miner. 26 (1978) 139–143.

[20] G. Anbalagan, A.R. Prabakaran, S. Gunasekaran, Spectroscopic characterization of indian standard sand, J. Appl. Spectrosc. 77 (2010) 86–94. doi:10.1007/s10812-010-9297-5.

[21] V. C. Farmer, The Infrared Spectra of Minerals, 1974. doi:https://doi.org/10.1180/mono-4.

[22] I. Arrizabalaga, O. Gómez-Laserna, J.A. Carrero, J. Bustamante, A. Rodríguez, G. Arana, J.M. Madariaga, Diffuse reflectance FTIR database for the interpretation of the spectra obtained with a handheld device on built heritage materials, Anal. Methods. 7 (2015) 1061–1070. doi:10.1039/C4AY02189D.

[23] D. Ergenç, L.S. Gómez-Villalba, R. Fort, Crystal development during carbonation of lime-based mortars in different environmental conditions, Mater. Charact. 142 (2018) 276–288. doi:10.1016/j.matchar.2018.05.043.

[24] K. Zhang, C. Corti, A. Grimoldi, L. Rampazzi, A. Sansonetti, Application of Different Fourier Transform Infrared (FT-IR) Methods in the Characterization of Lime-Based Mortars with Oxblood, Appl. Spectrosc. (2018) 000370281881569. doi:10.1177/0003702818815693.

[25] M.B. Toffolo, E. Boaretto, Nucleation of aragonite upon carbonation of calcium oxide and calcium hydroxide at ambient temperatures and pressures: a new indicator of fire-related human activities, J. Archaeol. Sci. 49 (2014) 237–248. doi:10.1016/j.jas.2014.05.020.

[26] C. Rodriguez-Navarro, C. Jimenez-Lopez, A. Rodriguez-Navarro, M.T. Gonzalez-Muñoz, M. Rodriguez-Gallego, Bacterially mediated mineralization of vaterite, Geochim. Cosmochim. Acta. 71 (2007) 1197–1213. doi:10.1016/j.gca.2006.11.031.

[27] R.S.K. Lam, J.M. Charnock, A. Lennie, F.C. Meldrum, Synthesis-dependant structural variations in amorphous calcium carbonate, CrystEngComm. 9 (2007) 1226. doi:10.1039/b710895h.

[28] C.Y. Tai, F. Chen, Polymorphism of $CaCO_3$, precipitated in a constant-composition environment, AIChE J. 44 (1998) 1790–1798. doi:10.1002/aic.690440810.

[29] V. Duchi, M. V. Giordano, M. Martini, Riesame del problema della precipitazione di calcite od aragonite da soluzioni naturali, Rend. Soc. Ital. Di Mineral. e Petrol. 34 (1978) 605–618.

[30] E.T. Stepkowska, J.L. Perez-Rodriguez, M.J. Sayagues, J.M. Martinez-Blanes, Calcite, vaterite and aragonite forming on cement hydration from liquid and gaseous phase, J. Therm. Anal. Calorim. 73 (2003) 247–269.

[31] L. Fernández-Carrasco, E. Vázquez, Reactions of fly ash with calcium aluminate cement and calcium sulphate, Fuel. 88 (2009) 1533–1538. doi:10.1016/j.fuel.2009.02.018.

[32] M.J. Wilson, ed., Clay Mineralogy: Spectroscopic and Chemical Determinative Methods, Springer Netherlands, Dordrecht, 1994. doi:10.1007/978-94-011-0727-3.

[33] S.N. Ghosh, S.K. Handoo, Infrared and Raman spectral studies in cement and concrete (review), Cem. Concr. Res. (1980). doi:10.1016/0008-8846(80)90005-8.

[34] X. Ren, W. Zhang, J. Ye, FTIR study on the polymorphic structure of tricalcium silicate, Cem. Concr. Res. (2017). doi:10.1016/j.cemconres.2016.11.021.

[35] D. Gastaldi, F. Canonico, E. Boccaleri, Ettringite and calcium sulfoaluminate cement: Investigation of water content by near-infrared spectroscopy, J. Mater. Sci. 44 (2009) 5788–5794. doi:10.1007/s10853-009-3812-1.

[36] J. Bensted, S.P. Varma., Studies of ettringite and its derivatives, Cem. Technol. 2 (1971) 71–76.

[37] T.L. Hughes, C.M. Methven, T.G.J. Jones, S.E. Pelham, P. Fletcher, C. Hall, Determining cement composition by Fourier transform infrared spectroscopy, Adv. Cem. Based Mater. 2 (1995) 91–104. doi:10.1016/1065-7355(94)00031-X.

[38] R.F. Kokaly, R.N. Clark, G.A. Swayze, K.E. Livo, T.M. Hoefen, N.C. Pearson, R.A. Wise, W.M. Benzel, H.A. Lowers, R.L. Driscoll, A.J. Klein, USGS Spectral Library Version 7, Reston, VA, 2017. doi:10.3133/ds1035.

[39] G. Anbalagan, S. Mukundakumari, K.S. Murugesan, S. Gunasekaran, Infrared, optical absorption, and EPR spectroscopic studies on natural gypsum, Vib. Spectrosc. 50 (2009) 226–230. doi:10.1016/j.vibspec.2008.12.004.

[40] F. Rosi, A. Daveri, B. Doherty, S. Nazzareni, B.G. Brunetti, A. Sgamellotti, C. Miliani, On the Use of Overtone and Combination Bands for the Analysis of the CaSO 4 —H 2 O System by Mid-In frared Reflection Spectroscopy, Appl. Spectrosc. 64 (2010) 956–963. doi:10.1366/000370210792080975.

[41] L. Fernández-Carrasco, D. Torrens-Martín, L.M. Morales, Sagrario Martínez-Ramírez, L. Fer nández Carrasco, D. Torrens Martín, L.M. Morales, S. Martínez Ramírez, Infrared spectroscopy in the analysis of building and construction materials, InTech, 2012. doi:10.5772/36186.

[42] P. Yu, R.J. Kirkpatrick, B. Poe, P.F. McMillan, X.D. Cong, Structure of calcium silicate hydrate (C-S-H): Near-, mid-, and far-infrared spectroscopy, J. Am. Ceram. Soc. 82 (1999) 742–748. doi:10.1111/j.1151-2916.1999.tb01826.x.

[43] C. Kosztolanyi, J. Mullis, M. Weidmann, Measurements of the phase transformation temperature of gypsum-anhydrite, included in quartz, by microthermometry and Raman microprobe techniques, Chem. Geol. 61 (1987) 19–28. doi:10.1016/0009-2541(87)90022-2.

[44] M. Hass, G.B.B.M. Sutherland, The Infra-Red Spectrum and Crystal Structure of Gypsum, Proc. R. Soc. A Math. Phys. Eng. Sci. 236 (1956) 427–445. doi:10.1098/rspa.1956.0146.

[45] J.L. Post, S.M. Crawford, Uses of near-infared spectra for the identification of clay minerals, Appl. Clay Sci. 95 (2014) 383–387. doi:10.1016/j.clay.2014.02.010.

Thermal analysis

Specimens composed by one specific binder

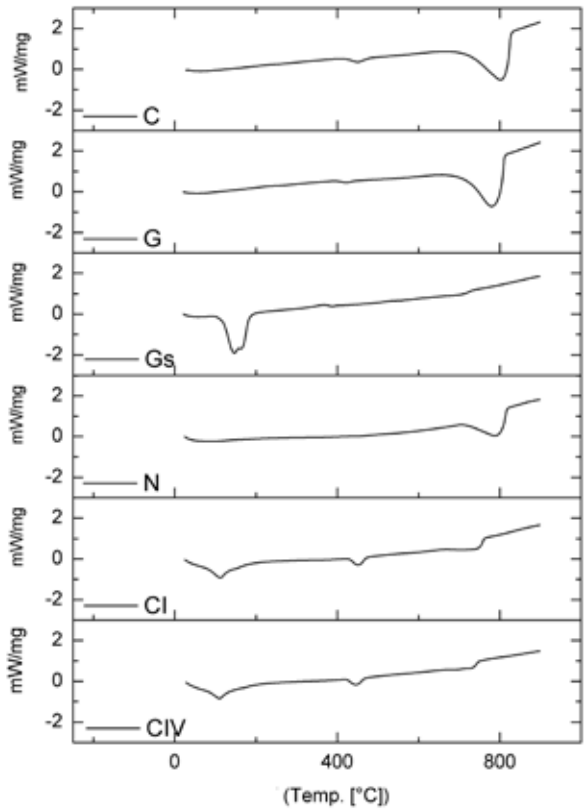

▲ *Figure 39. Differential scanning calorimetry curves of the reference sample made of one binder.*

Considering the differential scanning calorimetry curves (figure 39), the intense endothermic peak at 800°C in samples C (hydrated lime) and G (lime putty) is assigned to the decomposition of calcium carbonate [1–5] (Figure 38), while the smaller loss of weight between 420 and 450°C is assigned to calcium hydroxide decomposition [1,2,4,6–8]. The peak between 241 and 253°C could be due either to some hydroxide compounds like magnesium hydroxide, even if they usually present a degradation band at higher temperatures [1,2], or to hydromagnesite [4]. Samples C and G present also the highest weight loss - about 40% - due to the presence of carbonates (figure 40).

The sample made with natural hydraulic lime (N) shows also an endothermic peak (787°C) due to the decomposition of carbonate phases with a weight loss of about 30% (figure 39 and 40). The specimen presents also a very small endothermic peak at about 450°C that could be due either to the presence of not yet carbonated portlandite or to the OH group of some hydrated hydraulic phases.

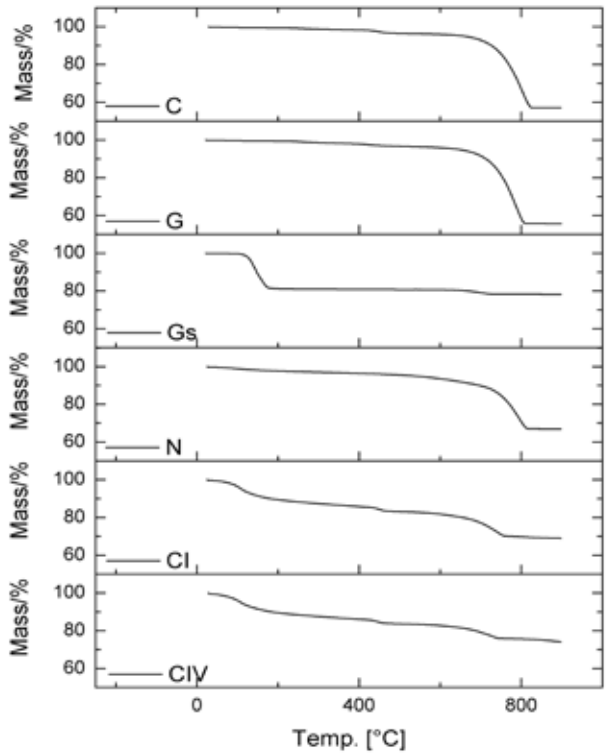

▲ *Figure 40. Thermogravimetric curves of the reference sample made of one binder.*

With regards to thermogravimetric curves, the specimen Gs composed by gypsum presents the expected characteristic peaks of dehydration at 149 and 165°C, due to the loss of 0.5 molecules of H_2O and then 1.50 molecule of H_2O per formula unit, respectively [1,2,4,9]:

$CaSO_4\ 2H_2O$ + heat -> $CaSO_4\ ½H_2O$ + 1 $½H_2O$

$CaSO_4\ ½H_2O$ -> $CaSO_4$ + $½H_2O$

Gs has also a small loss of weight and an endothermic peak at 750°C, given by the decomposition of calcium carbonate [1–5,10]. In this sample an exothermic peak at 366°C has been identified, that could derive either from some organic impurities in the material [2,4], or to the conversion of soluble to insoluble form of anhydrite [11], or to the rearrangement in anhydrous $CaSO_4$ from hemihydrate to anhydrate structure [1]. Since anhydrite is also found in PXRD analysis, this last interpretation could be the most plausible.

The DSC curves of CI and CIV present a similar trend, as shown in figure 41. The mass loss under 200°C is due both to free water and to the dehydration of *C-S-H* gel layers (110-112°C) and ettringite (152-165°C) [1,2,6–9,12–14]. The endothermic peaks at 445-450°C derive from the dehydration of calcium hydroxide [1,2,4,6–8]. Dicalcium silicate hydrate I, $Ca_2(HSiO_4)(OH)$, also gives an endothermic peak at 460-480°C, thus in this range an overlapping between portlandite and dicalcium silicate hydrate the dehydration could be observed. In the DSC graphs (figure 41), two endothermic peaks at 703 and 737°C for Portland cement and at 683 and 773°C for pozzolanic cement, are visible and explained by the presence of carbonates [1–5].

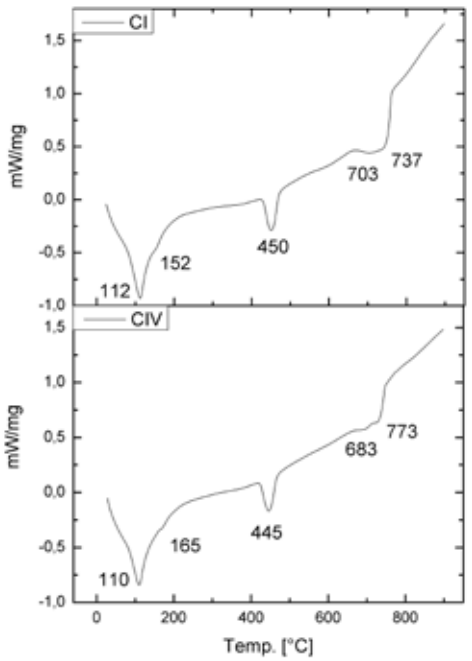

▲ *Figure 41. DSC curves of hydrated Portland cement (CI, above) and pozzolanic cement (CIV, bottom).*

In both cases, the occurrence of the lowest temperature peaks (683 and 703°C) could be due either to the presence of poorly crystallized calcium carbonate in the form of vaterite, calcite or aragonite and/or to the presence of finer particles of secondary calcite, that decompose at lower temperature [1,2,6,7,15]. The highest temperature peaks (737 and 773°C, respectively) probably originate from the decomposition of calcite in a more crystalline form (as can be a carbonate mineral contained in the rocks). In table 24 the main compounds found in sample made with one binder are summarized.

Name	**Chemical compound**			
G	$CaCO_3$	$Ca(OH)_2$		
C	$CaCO_3$	$Ca(OH)_2$		
CI	$CaCO_3$	$Ca(OH)_2$	*CSH (?)*	ettringite (?)
CIV	$CaCO_3$	$Ca(OH)_2$	*CSH (?)*	ettringite (?)
N	$CaCO_3$	$Ca(OH)_2$		
Gs	$CaSO_4\ 2H_2O$	$CaCO_3$	anhydrite (?)	

Table 24. List of the specimens and of the main chemical compounds found in specimens made with one binder.

Mortars composed by one specific binder and one specific aggregate

Specimens composed by one binder and carbonate sand

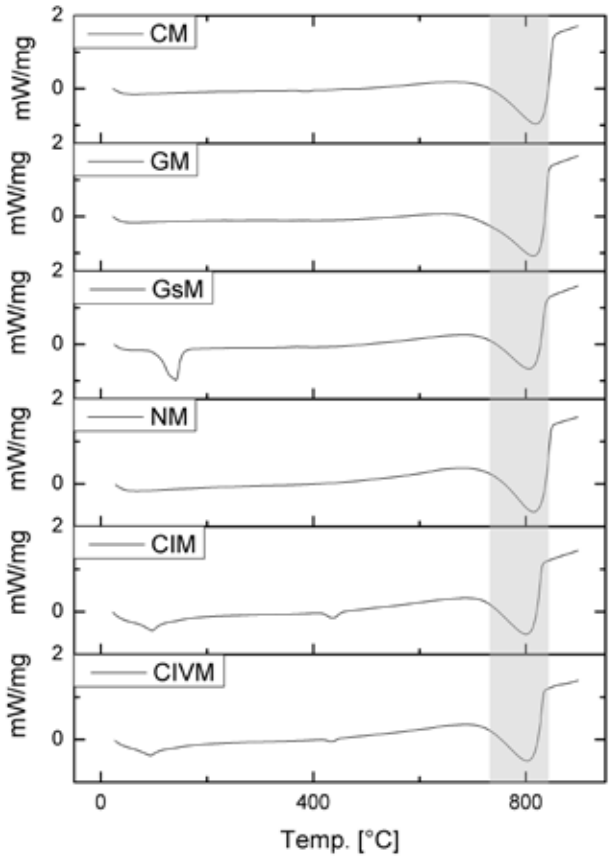

▲*Figure 42. Differential scanning calorimetry curves of the reference samples made of one binder and carbonate sand. The carbonate decomposition band is underlined in each graph.*

The DSC curves of CM and GM samples (figure 42) show the main endothermic peaks over 800°C, at 818.3°C and 813.8°C respectively. They present a total weight loss of about 43%, as calculated by the TG curves (figure 43). The peaks are assigned to the decomposition of calcium carbonate [1,3,4]. We cannot exclude the presence of other carbonates, as dolomite or magnesium carbonate, whose decomposition could coincide with the intense peak of calcium carbonate [1,2]. The small endothermic peak at 385.8°C indicates the occurrence of a small amount of uncarbonated calcium hydroxide. In the specimens containing carbonate sand, an endothermic peak of decomposition of calcium carbonate can be observed over 800°C. As previously hypothesized (Thermal analysis, Specimens composed by one specific binder), the high temperature is due to the presence of a better crystallized calcite, belonging to the aggregate fraction [2,6,7,15].

In the differential scanning calorimetry graphs of specimens CIM (peaks at 97, 137 and 436°C) and CIVM (93, 136 and 434°C), the presence of the binder phases is visible, even if overlapped with the loss of free water (at about 90°), the dehydration of *C-S-H* gel layers and the dehydration of sulphates (at about 137°) and portlandite (at about 434°). On the other hand, they are more attenuated; the decomposition

of carbonates is over 800°C and presents an intense weight loss. In specimen GsM the dehydration of gypsum is well visible at 132 and 141°C.

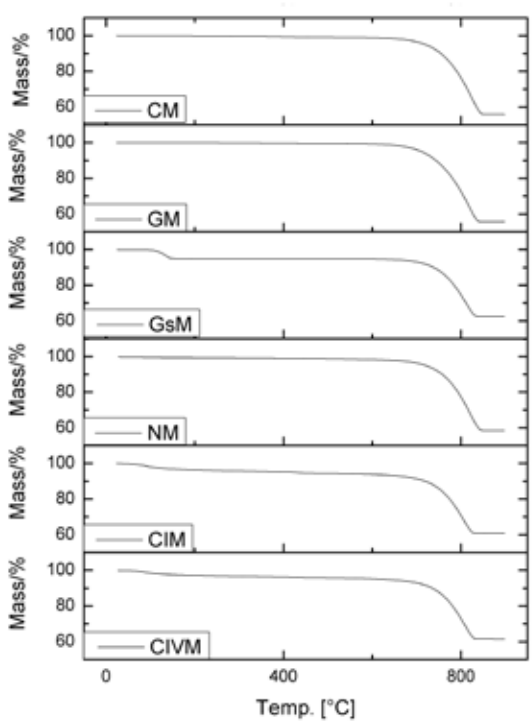

▲ *Figure 43. Thermogravimetric curves of the reference samples made of one binder and carbonate sand.*

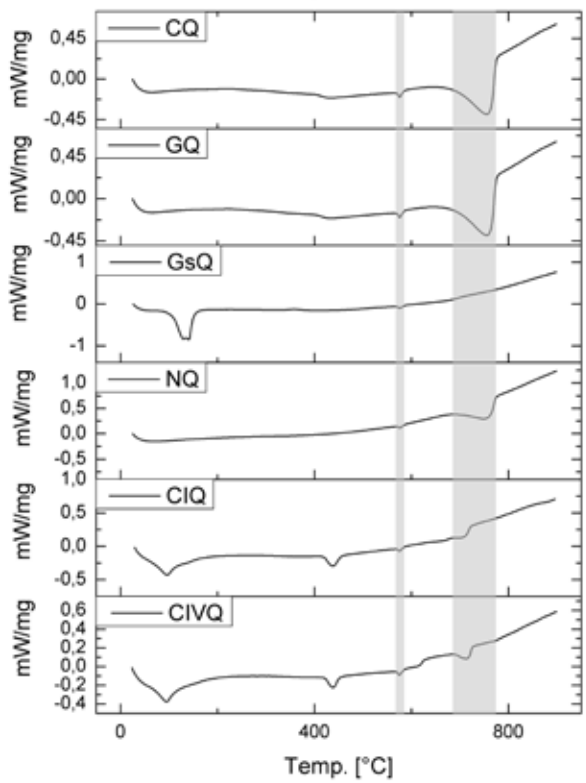

▲ *Figure 44. Differential scanning calorimetry curves of the reference samples made of one binder and quartz sand. The quartz transition from α into β phase and the carbonate decomposition are underlined in each graph.*

The endothermic peak at 575.5°C corresponds to the quartz phase change from alfa (α) into beta (β) form; this transition occurs without any loss of weight, and it is visible in each samples (figures 44 - 45). The endothermic peak at 755.2°C corresponds to the decomposition of calcium carbonate and it is clearly visible in specimens CQ, GQ and NQ, where only calcium carbonate is present. The peak of quartz is visible in all the samples where it is contained. Hydraulic phases should also be present in NQ (natural hydraulic lime 3.5 with quartz sand), but the peaks are not visible. Moreover, in these samples the carbonate bands appear under 800°C. This implies that here calcium carbonate is poorly crystallized, with small particle size, which is typical of a re-crystallized phase from calcium hydroxide [1,2,6,7,15]. An endothermic peak at 424°C is also present in GQ and CQ, due to the dehydration of uncarbonated calcium hydroxide. Feldspars are not visible in the curve, even if they were identified by powder X-ray diffraction analysis (Specimens analyses, Powder X-ray diffraction, PXRD) [1,4,16]. For what concerns the cement specimens, CIQ and CIVQ, the carbonate decomposition bands are shifted to 706 and 713°C, respectively. The lowering of these temperatures is due to the poorly crystallized carbonates with small particle size which decompose more quickly [1,2,6,7,15]. Under 200°C, the loss of free water and the dehydration of *CSH* and ettringite have been identified at 95 and 137°C in CIQ and at 95 and 148°C in CIVQ. In cement samples the peak of dehydration of portlandite (at 438°C in both the samples) is more intense than in the other specimens. At 616°C, CIVQ presents an endothermic slope that could be explained as the shift of the dehydration peak

of *C-S-H* gel structural OH^- groups after longer hydration, as suggested by Gabrovsek et al.; in alternative it could be due to the decomposition of a less crystalline carbonate [1,2,6,7,15]. In table 25 the main compounds identified in samples made by one binder and one type of aggregate are listed.

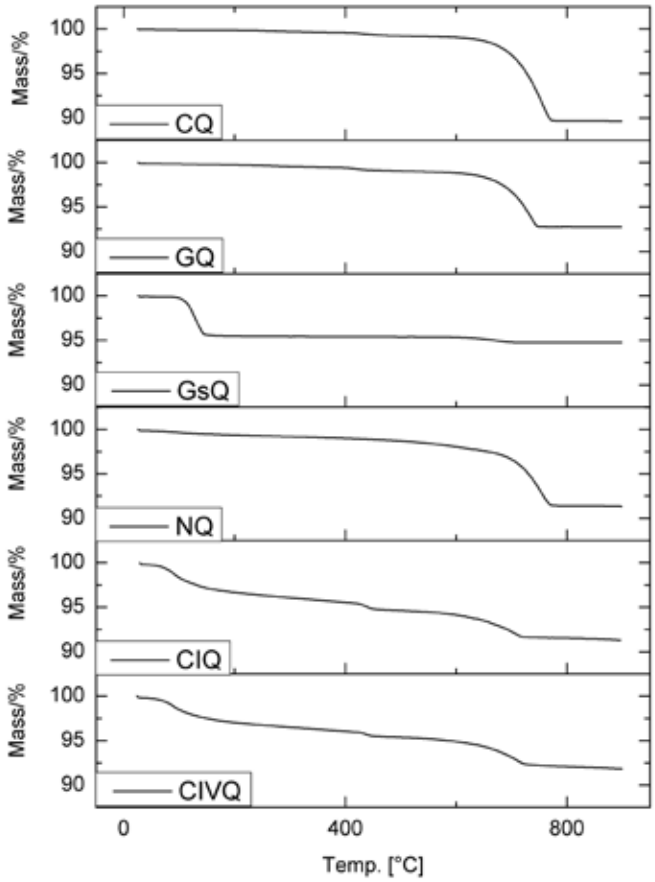

▲ *Figure 44. Thermogravimetric curves of the reference samples made of one binder and quartz sand.*

Mortars with quartz sand (Q)

Label	Chemical compound				
GQ	$CaCO_3$	SiO_2	$Ca(OH)_2$		
CQ	$CaCO_3$	SiO_2	$Ca(OH)_2$		
CIQ	$CaCO_3$	$Ca(OH)_2$	SiO_2	ettringite (?)	*CSH (?)*
CIVQ	$CaCO_3$	$Ca(OH)_2$	SiO_2	ettringite (?)	*CSH (?)*
NQ	$CaCO_3$	SiO_2	$Ca(OH)_2$		
GsQ	$CaSO_4\ 2H_2O$	SiO_2	$Ca(OH)_2$		
Mortars with carbonate sand (M)					
Name	**Chemical compound**				
GM	$CaCO_3$				
CM	$CaCO_3$				
CIM	$CaCO_3$	$Ca(OH)_2$	ettringite (?)	*CSH (?)*	
CIVM	$CaCO_3$	$Ca(OH)_2$	ettringite (?)	*CSH (?)*	
NM	$CaCO_3$				
GsM	$CaSO_4\ 2H_2O$	$CaCO_3$			

Table 25. List of the samples made with one specific binder and one specific aggregate

Specimens composed by a mix of two binders

Samples CN (figure 46) and GN present the same endothermic peaks (790 and 793°C, respectively, ascribed to the decomposition of carbonates) and the same weight losses (38.62% and 37%, respectively), as expected in similar specimens. No hydraulic phases have been found. The endothermic peak of portlandite is visible only in CN, probably because of a slower carbonation process.

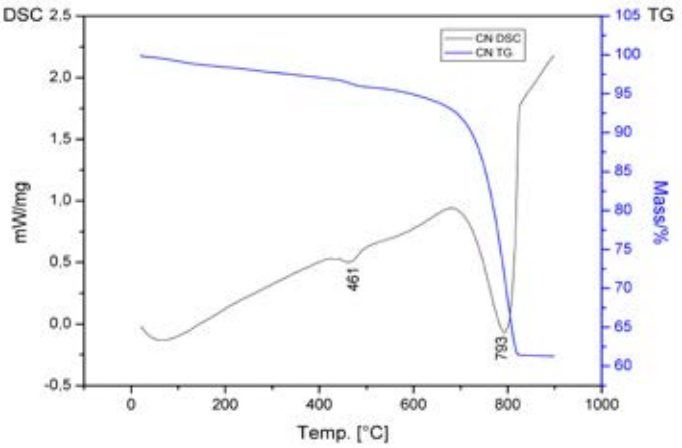

▲ *Figure 46. Differential scanning calorimetry and thermogravimetric curves of the reference sample made of two binders: hydrated lime and natural hydraulic lime (CN).*

In the specimen CGs (figure 47) and GGs the endothermic peaks of decomposition of gypsum have been identified at 155 and 158°C respectively. The dehydration of portlandite at 425 and 423°C and the decomposition of carbonates at 782 and 750°C can also be observed. In sample CGs there is also a small endothermic peak at 758°C, that could be related to the presence of a less crystalline carbonate decomposing at a lower temperature [1,2,6,7,15]. An exothermic peak at 441°C is shown in the sample GGs that could be related either to some organic impurities in the material [4], or to the conversion of soluble to insoluble anhydrite, or to the rearrangement in $CaSO_4$ from hemihydrate to anhydrate structure [1,11], as already observed in Gs sample (Thermal analysis, Specimens composed by one specific binder)

The samples CCI and CCIV (figure 48) present a similar trend and the same endothermic peaks. The carbonate decomposition maxima are recorded at 779 and 781°C in DSC graph, respectively. A small signal of portlandite dehydration is also visible at 463 and 454°C, respectively. An exothermic peak is found at 386°C, possibly due either to the decomposition of organic compounds [4], or to the conversion of soluble to insoluble anhydrite [11], or to the rearrangement in anhydrous $CaSO_4$ from hemihydrate to anhydrate structure [1].

In the DSC curves (figure 48) an intense band under 200°C was observed, corresponding to the loss of almost 4% of weight according to the TG data. In the DTG curve (figure 49) this region is clearer if compared to DSC curve and a peak at about 96°C has been identified. Most of the mass loss under 200°C is due to free water but we cannot exclude the dehydration of *CSH* gel layers and ettringite (152-165°C) [1,2,6–8,11] because the weight loss is higher compared to that observed in other samples showing a similar band, for example CN (figure 46). CN does not present any peak in DTG analysis, so the presence of *CSH* was excluded..

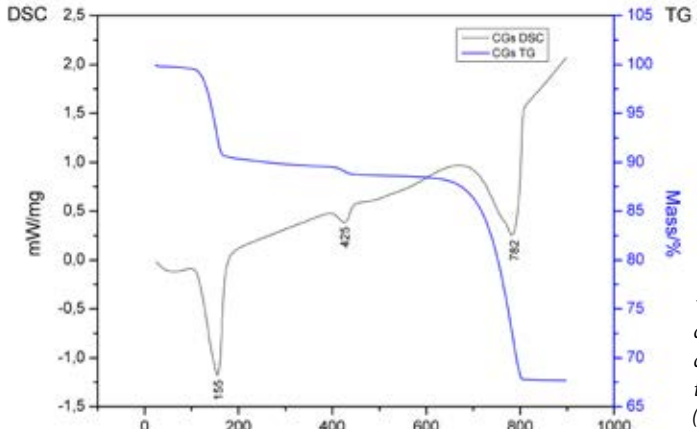

◀*Figure 47. Differential scanning calorimetry and thermogravimetric curves of the reference sample made of two binders: hydrated lime and gypsum (CGs).*

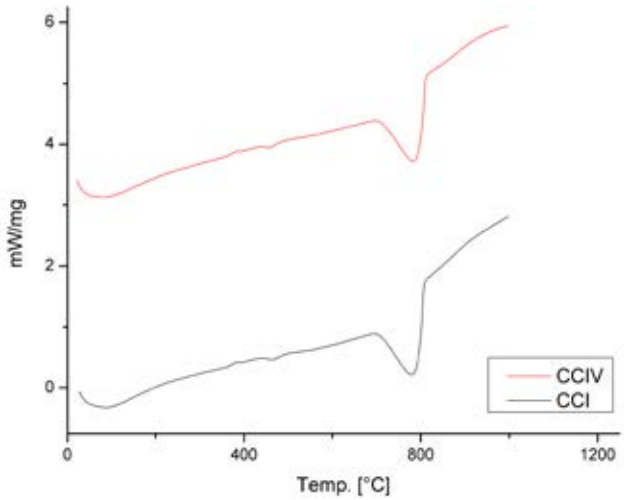

◀*Figure 48. DSC curves of CCI and CCIV specimens.*

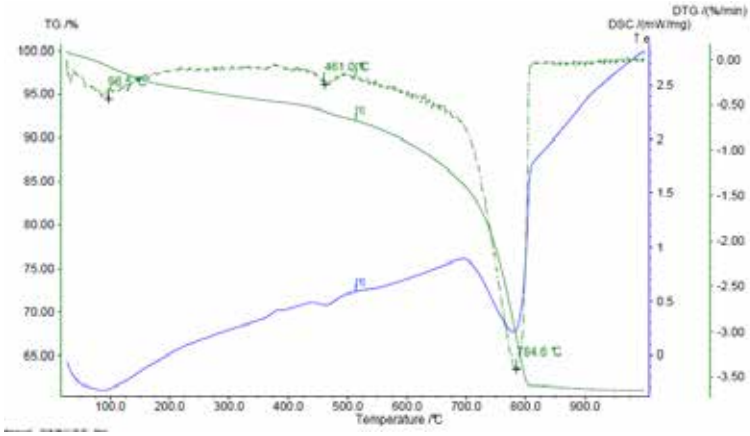

◀*Figure 49. DTG curve of CCI specimen.*

The specimens GCIV (figure 51) and GCI present a similar trend. As it is visible in the DSC curves, the main endothermic peaks are similar to those observed in CCI and CCIV specimens (figure 48). In the DTG curve of sample GCIV (figure 52), an endothermic transition at about 623°C is visible; its shape differs from that visible in the DTG curve of CI (shoulder shape) (figure 50). It is present also in the sample GCI and it could be due either to a less crystalline carbonate decomposition, or to the presence of finer particle size of secondary calcite [1,2,6,7,15] or to a shift of the dehydration peak of *CSH* gel structural OH- groups after longer hydration, as suggested by Gabrovsek et al. [7].

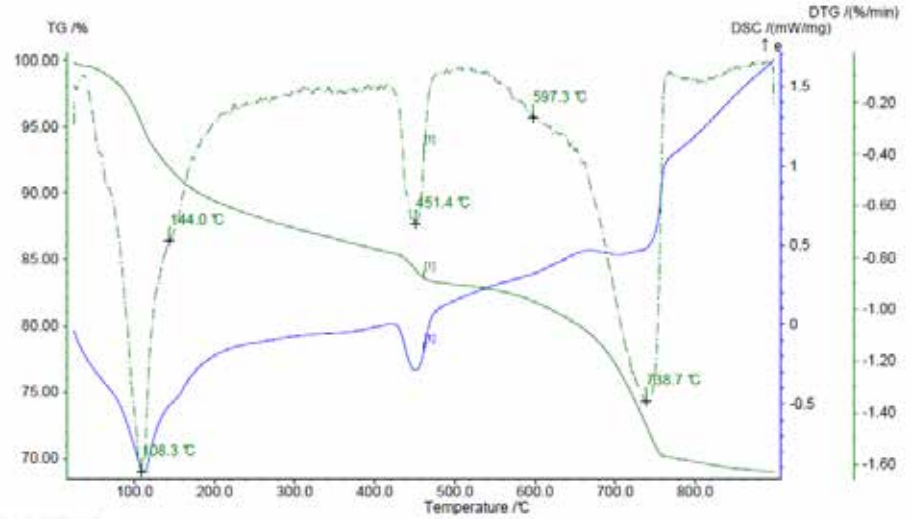

▲ *Figure 50. DTG curve of hydrated Portland cement.*

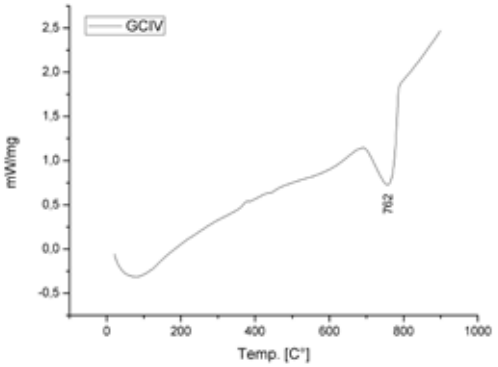

▲ *Figure 51. DSC curve of specimen GCIV.*

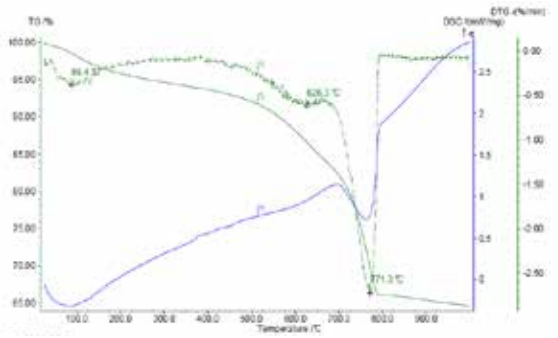

▲ *Figure 52. DTG of specimen GCIV.*

When the specimens are composed by natural hydraulic lime and cement I and IV (NCI and NCIV), they present amplified signals below 200°C which are more visible as displayed in figure 53. In fact, the endothermic peaks at 57, 97 and 141°C are more intense, if compared to sample CCI (figure 49). This behavior is probably due to the presence of calcium silicate hydrate also in natural hydraulic lime and to the lower quantity of calcium carbonate in the mixture. In table 26 the main compounds identified in samples made by two binders are listed.

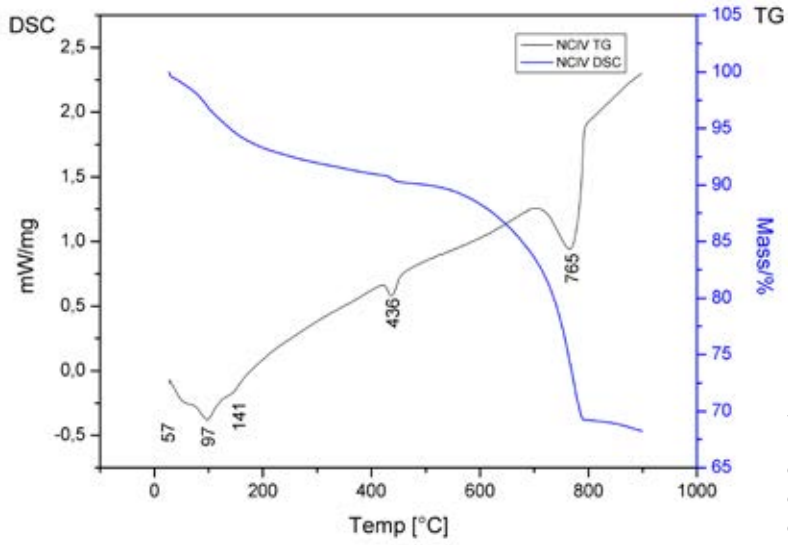

◀*Figure 53. Differential scanning calorimetry and thermogravimetric curves curve of sample NCIV as an example of natural hydraulic lime and cement mixed together.*

Samples with a mix of two binders

Label	Chemical compounds			
GN	$CaCO_3$			
GCI	$CaCO_3$	$Ca(OH)_2$	*CSH (?)*	ettringite (?)
GCIV	$CaCO_3$	*CSH (?)*	ettringite (?)	
GGs	$CaCO_3$	$CaSO_4$ $2H_2O$	$Ca(OH)_2$	$CaSO_4$ (?)
CN	$CaCO_3$	$Ca(OH)_2$		
CCI	$CaCO_3$	$Ca(OH)_2$	*CSH (?)*	ettringite (?)
CCIV	$CaCO_3$	$Ca(OH)_2$	*CSH (?)*	ettringite (?)
CGs	$CaCO_3$	$CaSO_4$ $2H_2O$	$Ca(OH)_2$	
NCI	$CaCO_3$	$Ca(OH)_2$	ettringite	*CSH (?)*
NCIV	$CaCO_3$	$Ca(OH)_2$	ettringite	*CSH (?)*
NGs	$CaSO_4$ $2H_2O$	$CaCO_3$	$CaSO_4$ (?)	

Table 26. List of the samples made with a mix of two binders.

Mortars composed by a mix of two binders and a specific aggregate

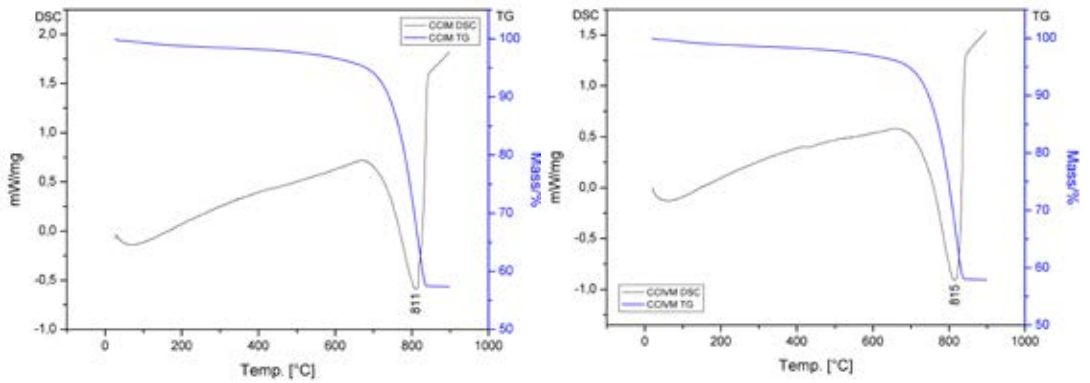

▲ *Figure 54. Differential scanning calorimetry and thermogravimetric curves of samples CCIM (left) and CCIVM (right).*

A small endothermic peak at 76.7°C is present in the specimen NCIM (figure 55). It is connected to the absorbed water, but since its shape seems to be similar to those found in CI, CIV, CCI and NCIV (figures 44, 49 and 53), it could also suggest the presence of some hydrated phase of cement pastes. However, the predominant phase is calcium carbonate. The endothermic peak of carbonate decomposition is over 800°C, as seen in carbonate sand and in specimens made with carbonate sand. As already explained for specimens with carbonate sand, the carbonate decomposition of the sand occurs at higher temperatures if compared to the $CaCO_3$ from the binder.

In samples where the carbonate component is predominant it is difficult to distinguish also the presence of cements, as in specimens CCIM and CCIVM containing carbonates both in the binder and in the aggregate (figure 54). In sample NCIVM it is difficult to distinguish the phases from carbonate and calcium hydroxide, as well.

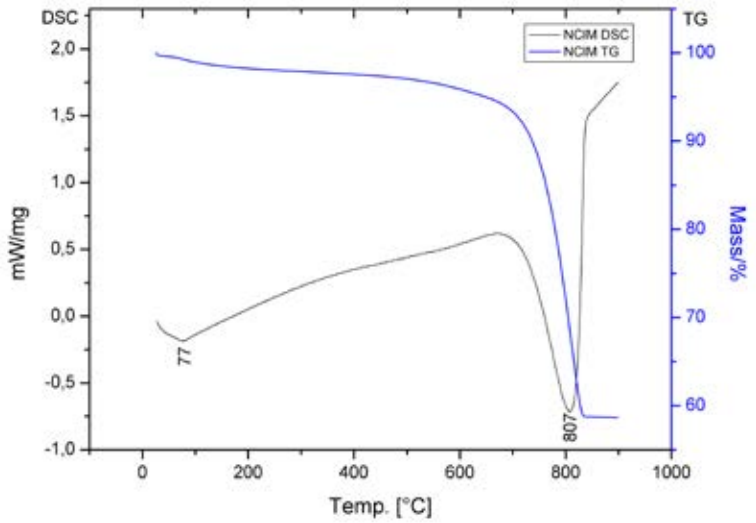

▲ *Figure 55. Differential scanning calorimetry and thermogravimetric curves of specimen NCIM.*

In all the samples with quartz sand it is possible to identify the transition from quartz alpha to quartz beta at 575°C. Moreover, also the endothermic peaks of calcite, calcium hydroxide and gypsum have been identified. Unlike the specimens with carbonate sand, these samples present the endothermic peaks of the decomposition of calcium carbonate under 800°C. This phenomenon occurs when the calcite comes from the carbonation of the binder and so is in a less crystalline phase, while the calcium carbonate present in the carbonate sand is more crystalline. This happens because the carbonate from the sand comes from ground rocks that are a naturally more crystalline source, thus it is characterized by a higher decomposition temperature.
In figure 56 an example of cement mixed with lime and quartz sand is presented. In this graph, that is very similar to those recorded for samples GCIVQ, GCIQ and CCIVQ, no clear evidence of the presence of cement is evidenced in the mixture.

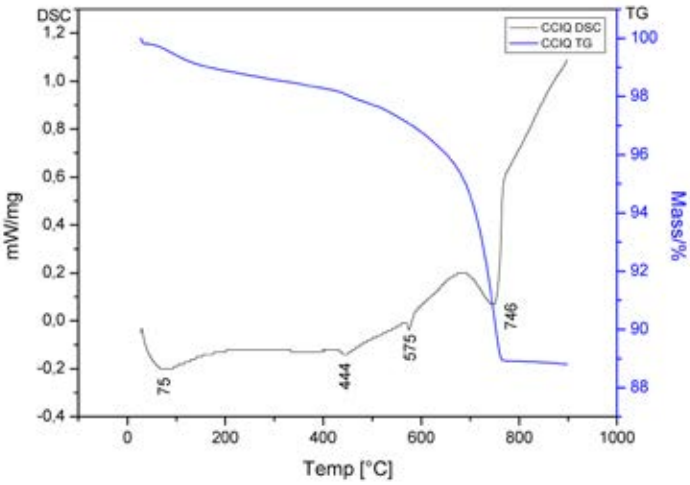

◀*Figure 56. Differential scanning calorimetry and thermogravimetric curves of CCIQ specimen.*

GCIQ presents the carbonate decomposition at 727°C, the quartz phase transition at 575°C, the dehydration of calcium hydroxide at 441°C and the water loss under 200°C. The shape of this last endothermic peak is similar to those found in cements and in cements mixed with natural hydraulic lime (figure 44 and 49). In the DTG curve an endothermic peak at 683°C is evident as well, that is connected to a lower crystalline calcium carbonate phase (figure 57). In table 27 the main compounds identified in samples made by two binders and one specific aggregate are listed.

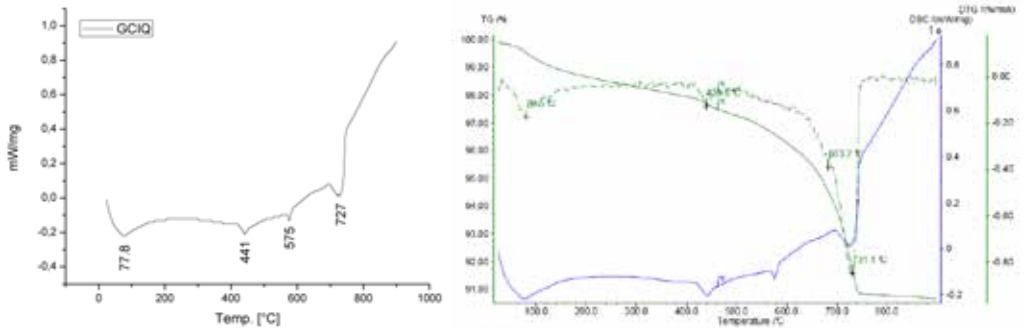

Figure 57 DSC curve of GCIQ on the left and DTG and TG curve on the right.

Samples with two binders and carbonate and quartz sand					
Mortars with quartz sand (Q)					
Label	**Chemical compounds**				
GNQ	$CaCO_3$	SiO_2			
GCIQ	$CaCO_3$	$Ca(OH)_2$	SiO_2	ettringite (?)	*CSH (?)*
GCIVQ	$CaCO_3$	$Ca(OH)_2$	SiO_2	ettringite (?)	*CSH (?)*
GGsQ	$CaSO_4$ $2H_2O$	$CaCO_3$	$Ca(OH)_2$	SiO_2	
CNQ	$CaCO_3$	$Ca(OH)_2$	SiO_2		
CCIQ	$CaCO_3$	$Ca(OH)_2$	SiO_2	ettringite (?)	*CSH (?)*
CCIVQ	$CaCO_3$	$Ca(OH)_2$	SiO_2	ettringite (?)	*CSH (?)*
CGsQ	$CaSO_4$ $2H_2O$	$CaCO_3$	SiO_2	$Ca(OH)_2$	
NCIQ	$CaCO_3$	$Ca(OH)_2$	SiO_2	ettringite(?)	*CSH (?)*
NCIVQ	$CaCO_3$	$Ca(OH)_2$	SiO_2	ettringite (?)	*CSH (?)*
NGsQ	$CaSO_4$ $2H_2O$	$CaCO_3$	SiO_2		
Mortars with carbonate sand (M)					
Label	**Chemical compounds**				
GCIVM	$CaCO_3$				
GCIM	$CaCO_3$				
GGsM	$CaSO_4$ $2H_2O$	$CaCO_3$	$Ca(OH)_2$		
GNM	$CaCO_3$				
CNM	$CaCO_3$	$Ca(OH)_2$			
CCIM	$CaCO_3$				
CCIVM	$CaCO_3$	$Ca(OH)_2$			
CGsM	$CaSO_4$ $2H_2O$	$CaCO_3$	$Ca(OH)_2$		
NCIM	$CaCO_3$	ettringite (?)	*CSH (?)*		
NCIVM	$CaCO_3$				
NGsM	$CaSO_4$ $2H_2O$	$CaCO_3$	SiO_2 (?)		

Table 27. List of the samples made with two binders and aggregates.

Discussion and conclusions

This technique has shown good results in the identification of the hydrated phases of mortars cement, but it fails when cement binders are mixed with different binders because it became harder to distinguish the components of the two binders. On the other hand, as expected, when hydrated lime and gypsum are mixed the signals of both are clearly visible.

The identification of hydraulic phases in natural hydraulic lime, as already seen in other techniques like infrared spectroscopy, is quite difficult because these phases are present in very low quantities. Usually only calcite is identified thanks to its very intense peak.

TG-DSC evidences the decomposition and dehydration of the phases and relative weight loss; in particular, a difference between different levels of crystallinity of calcium carbonate could help to evidence the presence of carbonate sand. In fact, carbonate sand is usually produced by grinding carbonate rocks that are more crystalline, due to their geological formation, compared to the calcium carbonate formed during the carbonation of hydrated lime in the binder. This technique has also underlined how, if the two carbonates are mixed together, the signal of the more crystalline phase is prominent. This implies that it is not possible to discern between two carbonate signals and identify the component of the aggregate and of the binder.

In samples with cement in the binder the quantification of the components has been attempted but, because of the overlap of the peaks of the phases present under 200°C, they could not be distinguished and quantified. Moreover, in most of the samples where calcite is found, it has different origins (from the binders and the aggregate) so it was not possible neither to distinguish between them nor to calculate the correct quantity for the samples with carbonate aggregate because the signals are overlapped. Anyway, in samples with carbonate aggregate the calcite decomposition usually occurs over 800°C. This factor can suggest the presence of this aggregate, to be checked with other techniques, like optical analysis.

The attempt to calculate the binder/aggregate ratio was performed on samples with quartz sand. It was possible to calculate it only on these samples because in the others the peak of decomposition of carbonate sand covers the peak of decomposition of calcium carbonate in the binder. To calculate the binder/aggregate ratio it was assumed that carbonate, calcium hydroxide, gypsum etc. came from the binder. Then the quantities of the phases before the dehydration were calculated and subtracted to the initial weight of the samples. The binder/aggregate ratios were obtained accordingly. As shown in table 28, the samples that present the correct binder/aggregate ratio used in the preparation of the specimens (1/3) are a few. These samples are those that use hydrated lime as binder. The samples containing cements in the binder present a calculated ratio probably lower than the effective one because it was not possible to quantify the hydrated phases, which are overlapped with sulphates phases. Also the samples with lime putty present lower values, explained by the proportion of the raw materials used. As the proportion was made by weight, so since lime putty contains also water, a lower content of hydrated lime was available in the specimens even compared to the other samples. These last results agree with thin section point counting results, in which the lack of binder is evident in samples made with lime putty (GM and GQ). For what concerns the other samples, the binder/aggregate ratio found by point counting is more similar to the 1:1 ratio while here the values vary from 0.3 to 0.1 (table 28). It is important to underline that in cement only the quantification of calcite was sure and, due to the overlapping of the peaks, quantification of other phases was not possible. It is important to remark that TG-DSC provide a b/a ratio in weight more comparable with the method

we used to prepare the samples, while μCT tomography and point counting give results in volume/volume. For this reason there is not direct correspondence between the results obtained.
To summarize, TG-DSC could be useful in the quantitative analysis especially in lime mortars, while in cement mortars, due to the heterogeneity and the overlapping of the peaks, the calculations are more difficult or not possible to be done. In table 29 the main advantages and drawbacks of thermic analyses are shown.

Specimens	Binder/aggregate ratio
CQ	0.3
GQ	0.2
NQ	0.2
CIVQ	0.1
CIQ	0.1
GsQ	0.2
NGsQ	0.4
NCIVQ	0.2
NCIQ	0.2
GNQ	0.4
CNQ	0.3
GGsQ	0.2
CGsQ	0.3
GCIVQ	0.2
GCIQ	0.2
CCIVQ	0.3
CCIQ	0.3

Table 28. Binder/aggregate ratio calculated by TG analysis of specimens with quartz-sand.

Advantages	Drawbacks
Quantitative analysis.	Difficult identification of cement phases in mixed mortars.
Identification of the main compounds like $CaCO_3$, $CaSO_4$ $2H_2O$, $Ca(OH)_2$.	In mixed mortars is difficult the identification of cement compouns.
Identification of cement phases in samples in one binder mortars.	

Table 29. Summary of the advantages and drawbacks of thermal analysis applied to all the specimens made in this study.

References

[1] R.C. Mackenzie, Differential Thermal Analysis: Fundamental aspects, Acad. Press, 1978. https://books.google.it/books?id=-HoyvgAACAAJ.

[2] R.C. Mackenzie, Differential Thermal Analysis: Applications, Academic Press, 1972. https://books.google.it/books?id=-rxpAAAAMAAJ.

[3] A. Moropoulou, A. Bakolas, K. Bisbikou, Thermal analysis as a method of characterizing ancient ceramic technologies, Thermochim. Acta. 269–270 (1995) 743–753. doi:10.1016/0040-6031(95)02570-7.

[4] A. Moropoulou, A. Bakolas, K. Bisbikou, Characterization of ancient, byzantine and later historic mortars by thermal and X-ray diffraction techniques, Thermochim. Acta. 269–270 (1995) 779–795. doi:10.1016/0040-6031(95)02571-5.

[5] S. Gunasekaran, G. Anbalagan, Spectroscopic study of phase transitions in natural calcite mineral, Spectrochim. Acta - Part A Mol. Biomol. Spectrosc. 69 (2008) 1246–1251. doi:10.1016/j.saa.2007.06.036.

[6] J. Dweck, P.M. Buchler, A.C.V. Coelho, F.K. Cartledge, Hydration of a Portland cement blended with calcium carbonate, Thermochim. Acta. 346 (2000) 105–113. doi:10.1016/S0040-6031(99)00369-X.

[7] R. Gabrovšek, T. Vuk, V. Kaučič, Evaluation of the hydration of Portland cement containing various carbonates by means of thermal analysis, Acta Chim. Slov. 53 (2006) 159–165.

[8] H.F.W. Taylor, Cement chemistry. 2nd ed., 1997. doi:10.1016/S0958-9465(98)00023-7.

[9] D.L. Hudson-Lamb, C.A. Strydom, J.H. Potgieter, The thermal dehydration of natural gypsum and pure calcium sulphate dihydrate (gypsum), Thermochim. Acta. 282–283 (1996) 483–492. doi:10.1016/0040-6031(95)02819-6.

[10] L.M. Barcina, A. Espina, M. Sufirez, J.R. Garc, J. Rodr, Characterization of monumental carbonate stones by thermal analysis (TG, DTG and DSC), Science (80-.). 290 (1997) 181–189.

[11] V.S. Ramachandran, R.F. Feldman, P.J. Sereda, Applications of Differential Thermal Analysis in Cement Chemistry, in: I. Chemical Publishing Company (Ed.), New York, 1969.

[12] X. Guo, F. Meng, H. Shi, Microstructure and characterization of hydrothermal synthesis of Al-substituted tobermorite, Constr. Build. Mater. 133 (2017) 253–260. doi:10.1016/j.conbuildmat.2016.12.059.

[13] C.A. Strydom, D.L. Hudson-Lamb, J.H. Potgieter, E. Dagg, The thermal dehydration of synthetic gypsum, Thermochim. Acta. 269–270 (1995) 631–638. doi:10.1016/0040-6031(95)02521-9.

[14] C. Biagioni, E. Bonaccorsi, M. Lezzerini, S. Merlino, Thermal behaviour of Al-rich tobermorite, Eur. J. Mineral. 28 (2016) 23–32. doi:10.1127/ejm/2015/0027-2499.

[15] Z. Šauman, Carbonization of porous concrete and its main binding components, Cem. Concr. Res. 1 (1971) 645–662. doi:10.1016/0008-8846(71)90019-6.

[16] A. Bakolas, G. Biscontin, A. Moropoulou, E. Zendri, Characterization of structural byzantine mortars by thermogravimetric analysis, Thermochim. Acta. 321 (1998) 151–160. doi:10.1016/S0040-6031(98)00454-7.

Raman spectroscopy and micro infrared reflection spectroscopy (μ-FTIR)

Raman spectroscopy and micro infrared reflection spectroscopy (μ-FTIR) were performed on raw materials, mixes and hydraulic mortars to evaluate the potentiality of these techniques in the identification of hydraulic phases. For instrumental reasons the micro infrared reflection spectroscopy (μ-FTIR) was used only on the cross sections of hydrated pastes because this technique requires a very reflective surface.

Raman spectroscopy

Raw materials (powder)

The raw materials characterization was obtained on powders. In table 30 the main phases identified are listed for each sample. The presence of calcite is highlighted in CEM IV and CEM I, whereas it is uncertain for NHL 3.5 due to the overlapping of the main peak of calcite (1087cm^{-1}) with portlandite which shows two main peaks at 1085cm^{-1} ($\upsilon_1[CO_3^{2-}]$) and 3620cm^{-1} (OH stretching vibration) [1–6]. The peak at 3620cm^{-1} allows unequivocally identifying the presence of portlandite. The other peaks of calcite (713cm^{-1}, 283cm^{-1}, 156cm^{-1}) were not always visible because of their lower intensity and the noise of the spectra.

Raw materials	Calcite	Portlandite	C_3S	C_2S	Gypsum	C_4AF	Carbon	Quartz	C_3A	Anatase	Hematite
CEM IV	•		•		•	•	•	•			
CEM I	•		•	•	•	•					
NHL 3.5	?	•		•	•	?	•			•	•

Table 30. Results of Raman spectroscopy analysis of hydraulic raw materials.

The presence of C_3S was detected in CEM IV and CEM I, as reported in figures 58 and 59. The peak at 836cm^{-1} has been assigned to C_3S υ_1 SiO_4 vibration (figure 58) [2,3,7]. In figure 59 a spectrum collected on NHL 3.5 raw material shows the C_2S signal at 856cm^{-1} (υ_1 SiO_4 vibration) [2,8] and a possible presence of calcite (713cm^{-1} In-plane bending (υ_4) of CO_3^{2-} and 1085cm^{-1} symmetric stretching (υ_1) of CO_3^{2-}) [2–4,6,8,9].

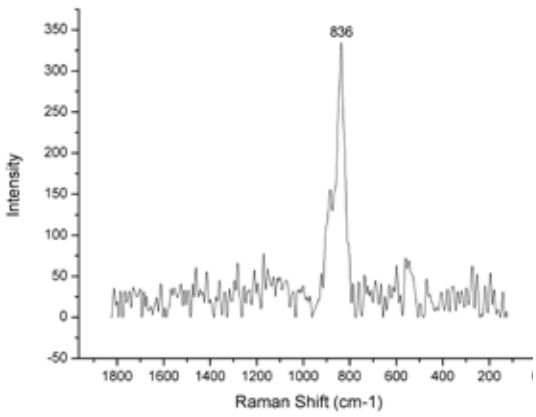

▲ *Figure 58. C_3S peak at 836cm^{-1} in Portland cement raw material (CEM I).*

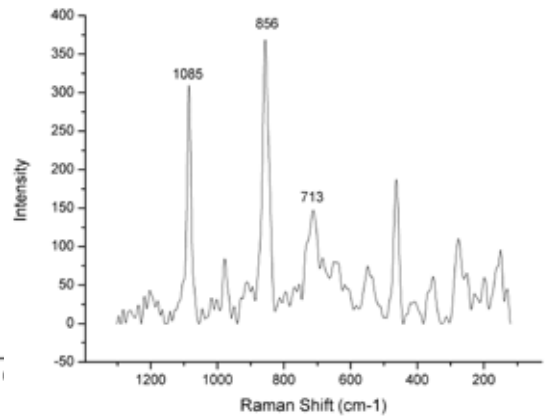

▲ *Figure 59. C_2S peak at 856cm^{-1} and possible presence of calcite (713cm^{-1} and 1085cm^{-1}) acquired on NHL 3.5 raw materials.*

In figure 60 the broad band of brownmillerite (C_4AF) around 726cm^{-1} (υ_1 [(Fe, Al)O_4^{5-}]) [6,10,11] is reported. This characteristic broad band, detected in CEM IV and CEM I, has been identified according to Schmid et al. [6], whereas the maximum intensity presents a shift of about 10cm^{-1} if compared to the results obtained by Deng et al. [4]. However, due to the broad shape of this peak, the position of the maximum intensity could significantly change. In samples with natural hydraulic lime (NHL 3.5) the presence of hematite, anatase, carbon and gypsum has been identified. The presence of gypsum in this material it is not usual and it could be present because of some impurities of the material, moreover it has been identified only with this technique.

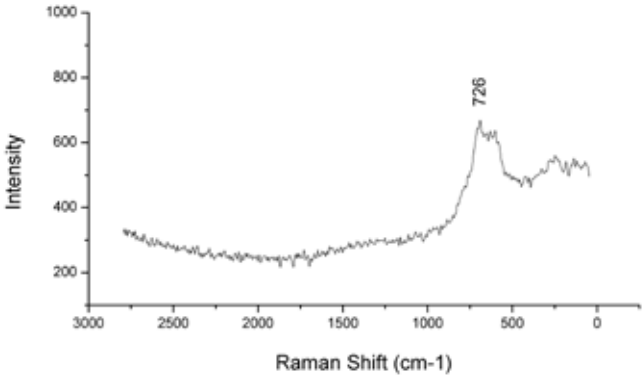

◀*Figure 60. Spectra of brownmillerite (peak at 726cm^{-1}) collected on CEM IV raw material.*

Hydrated pastes (without aggregate)

The analysis was performed on hydrated powders and on bulk samples. The results from both the mode used are in accordance. The mineralogical phases identified are reported in table 31. An example of characteristic hydrated phase tobermorite, detected both in each of the hydrated cements without aggregate and in some of the mortars samples (in the next paragraph), is shown in figure 61. It is the signal of Si-O-Si bending according to Kirkpatrick et al. [12].

	calcite	portlandite	ettringite	quartz	tobermorite *CSH*	C_2S	C_3S	C_4AF	carbon	gypsum/ sulphates	hematite	anatase
CIV	**?**	•	•	•	•	•		•	•	•		
CI	•	•	•		•	•	•	•		**sulphates**		
N	•	•			•	•		•		**gypsum**	•	•

Table 31. Results of Raman spectroscopy analysis of hydraulic specimens without the aggregate.

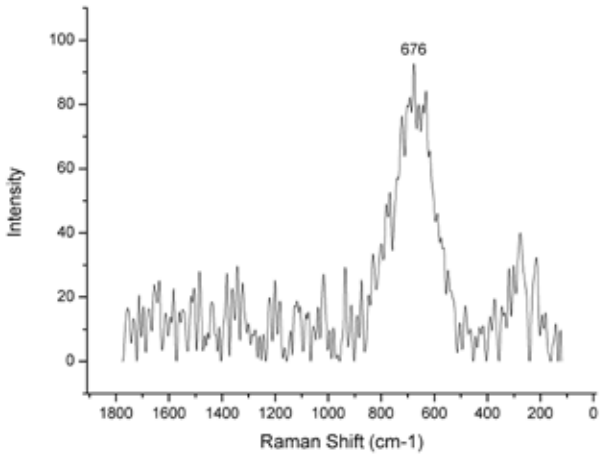

▲*Figure 61. Peak at 676cm^{-1} assigned to Si-O-Si bending of tobermorite collected on CI sample (Portland cement).*

In figure 62 and 63, the ambiguity between gypsum and other generic sulphates is due to the fluctuation of the position of the main peak. For a more precise discrimination among the different sulphate phases other bands are required. In figure 62 the peak at 1007cm^{-1} has been assigned to υ_1 [SO_4^{2-}] of gypsum, while the peak at 836cm^{-1} has been assigned to C_3S (υ_1 SiO_4 vibration of C_3S) [2–4,6,7,13].

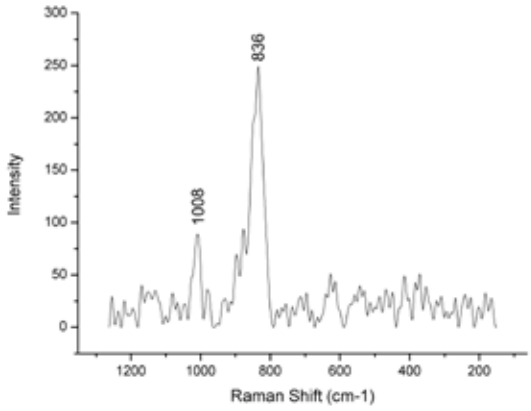

▲ *Figure 62. Spectrum acquired on hydrated pozzolanic cement (CIV) where C_3S and gypsum are present.*

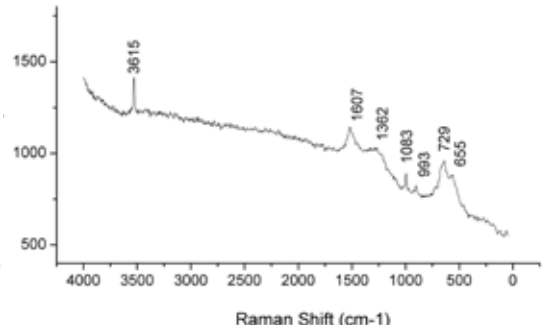

▲ *Figure 63. Spectra collected on hydrated pozzolanic cement (CIV) paste.*

The spectrum in figure 63 is collected on hydrated pozzolanic cement (CIV). The peaks at 3615 and 1083cm^{-1} have been assigned to OH stretching vibration and $v_1[CO_3^{2-}]$ of portlandite [1,8]. The two peaks at 1607 and 1362cm^{-1} are assigned to carbon [14]. The peak at 993cm^{-1} is assigned to v_1 sulphate vibration of the ettringite structure [13,15]. In the lower part of the spectrum the peaks at 729 and 655cm^{-1} are assigned to the broad band of C_4AF (brownmillerite) [6,10,11]. It is interesting to see the presence of gypsum in the sample N (natural hydrated lime) since with no other techniques used in this study gypsum was identified in this sample. It could be present due to some impurities of the raw materials.

Hydrated hydraulic mortars

On the mortar samples the analyses were carried out selecting the areas that microscopically show only the binder contribution. Tobermorite and brownmillerite (C_4AF) were identified, even if in some cases the peaks are very close one to each other and overlapped (figure 64). In sample CIVM (figure 64), the Si-O-Si bending of tobermorite has been identified at 667cm^{-1} while the peak of brownmillerite has been recognized at 731cm^{-1} [1,6,10–12]. In this last spectrum also the peak of a sulphate is visible at 1002cm^{-1} but its assignation is still uncertain. In the same spectrum the peak of $v_1[CO_3^{2-}]$ at 1088cm^{-1} have been identified [6,8,16]. It is interesting to underline that in the sample NQ also ettringite has been identified in one measurement. This phase usually is found in cement, but since with Raman spectroscopy gypsum was identified in the raw materials, during the hydration it could have reacted with some aluminates present in the mortar to crystallize ettringite.

Portlandite and calcite have been identified. Some impurities phases, as already identified in the raw materials, like hematite, anatase and carbon have been identified in hydrated mortars (table 32). As it is possible to observe in figure 65, calcite (1086cm^{-1}) and anatase are identified by the clear presence of peaks at 146 (v_6), 401 (v_4), 516 (v_3) and 641cm^{-1} (v_1) vibrations, as reported in the RRUFF database (RRUFF ID:R060277.2) and in literature [17,18].

	calcite	portlandite	ettringite	tobermorite *CSH*	C_4AF	carbon	gypsum	anatase
CIVQ	?	•		•	•			
CIQ	?	•	•		•			
NQ	•	•	•	•	•			
CIVM	?	•	•	•	•		•	
CIM	?	•	•		?		•	
NM	•	?		?	•	•		•

Table 32. Results of Raman analysis on hydraulic mortars.

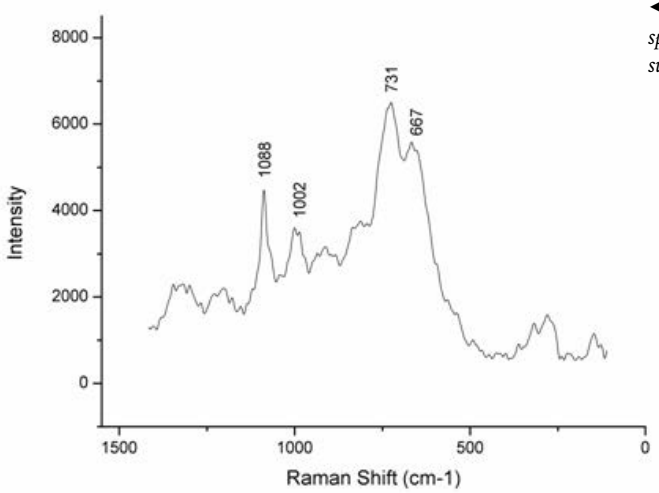

◀*Figure 64. Spectrum collected on CIVM specimen where tobermorite, brownmillerite, sulphate and calcite or portlandite are detected.*

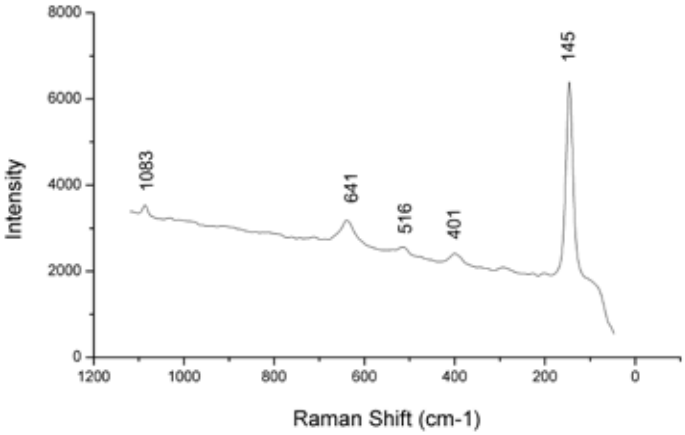

◀*Figure 65. Spectrum collected on NM specimen where anatase and calcite are detected.*

Discussion

Mineralogical phases	**Band**
C_3S: Hatrurite/Alite (Ca_3SiO_5):	835cm^{-1}
C_2S: Larnite/Belite (Ca_2SiO_4):	855-860cm^{-1}
C_4AF: Brownmillerite (4CaO Al_2O_3 Fe_2O_3) presents two broad bands between:	620-640 e 720-730cm^{-1}
Tobermorite: hydrate phase of C_3S and C_2S:	665-680cm^{-1}
Portlandite:	3620cm^{-1}, 1085cm^{-1}
Ettringite:	985-990cm^{-1}
Anatase:	143cm^{-1}
Ematite:	296cm^{-1}
Gypsum:	1008cm^{-1}

Table 33. In the table the main peaks found in this study are listed.

In table 33 the main diagnostic peaks identified in this study are summarized. Raman spectroscopy proved to be a particularly effective technique for the identification of C_2S (Belite), C_3S (Alite), C_4AF (Brownmillerite), tobermorite (*CSH*), ettringite, portlandite.

The raw materials have not yet undergone a complete hydration process, as demonstrated by the presence of C_2S, C_3S and C_4AF in reacted powders or samples. The C_4AF phase is characterized by two broad bands whose position varies, from 620-640cm^{-1} and 720-730cm^{-1}. Tobermorite can be hidden under the two bands of C_4AF, in the hydrated cement. It may depend on its low Raman scattering and its low amount in the samples. When portlandite is present in the spectrum (identifiable as the peak at 3620cm^{-1}) it is not possible to unequivocally identify calcite if only the peak at 1083cm^{-1} is present, due to the overlapping with the main band of portlandite. Moreover it is possible to identify generic sulphates, gypsum and ettringite whose bands vary from 970 to 1000cm^{-1}, but in some cases more than one peak is required for a better assignation of the type of sulphates. Surprisingly, the C_3A phase was never found by Raman spectroscopy. It is important to underline that, if a phase is not found, it does not necessarily mean that it is not present. In fact the lateral resolution of the Raman is only a few microns thus the area analyzed in each measure is strictly connected to the laser's spot dimensions. For this reason is defined as a punctual technique. Furthermore, some difficulties in the identification of the phases could be due to a low Raman scattering or they could cause fluorescence that covers all the other signals (this phenomenon takes place when a substance absorbs an electromagnetic radiation and emits light). The main advantages and drawbacks are summarized in table 34. It is also important to be aware that Raman spectroscopy has been the only analysis, among those considered in this study that allowed the identification of some phases like hematite, anatase and gypsum in natural hydraulic samples. The other limitations of Raman analysis are the following: The final and relevant achievement of Raman analyses deals with the presence of hydraulic phases, which can be easily recognized through the presence of peaks in the range of 620-640cm^{-1} and 720-740cm^{-1} and 835cm^{-1} and 855-860cm^{-1}, independently by their assignment to a specific phase. This could be the first information that could be acquired during the analysis, and then a more in depth study of the vibrational signals could lead to the identification of the different phases.

Advantages	Drawbacks
Identification of hydraulic phases, especially if there are bands in the range: 620-740cm^{-1}.	Fluorescence.
Identification of oxides like hematite and anatase that usually are not identified by the other techniques.	Punctual analysis (a few microns); in case of inhomogeneous samples some phases could not be identified even if they are present.
Identification of unhydrated hydraulic phase also in hardened pastes.	Substances without or with a low Raman scattering are not detected.

Table 34. Summary of advantages and drawbacks of Raman spectroscopy applied to cements and natural hydraulic lime pastes and mortars.

Micro-infrared reflection spectroscopy (μ-FTIR)

μ-FTIR was carried out on the polished cross sections of specimens with hydraulic binders previously analyzed by Raman spectroscopy. The instrument selected 100x100μm areas of analysis, thanks to the use of the microscope. μ-FTIR was performed only on the polished cross sections of hydrated pastes because this technique requires a very reflective surface. The analysis was mainly performed where an abundance of binder appeared at the optical microscope. All the spectra showed a similar trend to that obtained by infrared in external reflection mode (ER-FTIR). Unfortunately, this modality of analysis produces noise, especially in the spectral ranges above 3500cm^{-1} and around 1650cm^{-1}. In the following paragraphs some spectra are discussed. In table 35 the results of the μ-FTIR on hydraulic binders are summarized.

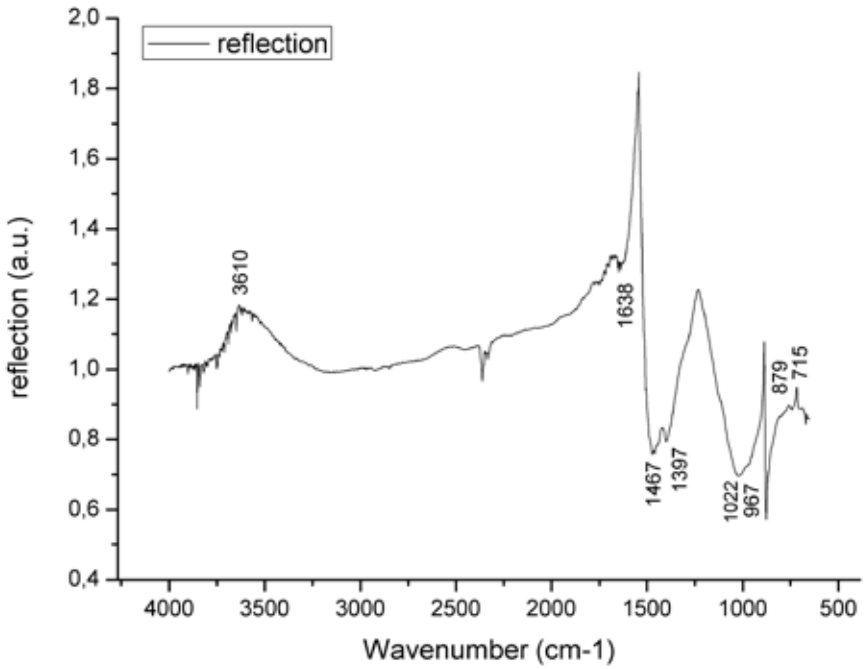

Figure 66. Portland cement polished cross section (CI) analyzed by μ-FTIR.

In the specimen (CI) containing Portland cement in the binder fraction (figure 66), the presence of the main peaks of $CaCO_3$ (715, 879, 1397 and 1467cm^{-1}) was observed [19–22]. The same splitting of the bands of calcite already observed in external reflection mode (1397 and 1467cm^{-1}) is present. In this spectrum the presence of calcium silicate hydrate has been suggested too by the band at 967cm^{-1} (υ_3 of $[SiO_4]^{4-}$) [23,24]. The peak at 1022cm^{-1} is connected the presence of C_2AS, CAH_{10}, gibbsite according to Fernandez-Carrasco [25], while the signal at 1638cm^{-1} has been assigned to sulphate, possibly ettringite [23,25,26].

With regards to sample CIV, the analysis was focused on a particle that has the appearance of a fly ash (figure 67). The main peaks of calcite (878cm^{-1} and the splitting at 1397 and 1457cm^{-1}) and quartz (the doublet at 776 and 797cm^{-1}) were identified [19–22,26–29]. The peak at 966cm^{-1} is assigned to the presence of a hydrated calcium silicate (for example *CSH* or tobermorite), an unhydrated calcium silicate, such as C_2S [23,30,31], or gibbsite [25]. The peak at 1024cm^{-1} is assigned to bayerite ($Al(OH)_3$) or to CAH_{10}, according to Fernandez-Carrasco et al. [25], while the signal at 1068cm^{-1} could be related to the presence of fly ash, as suggested by Fernandez-Jimenez et al. [32].

	calcite	tobermorite	ettringite	quartz	aluminates $Al(OH)_3$ or CAH_{10}
CI	•	•	•	?	**?**
CIV	•	•	•	•	**?**
N	•	**?**		•	

Table 35. Results of μ-FTIR analysis on hydraulic specimens made with one binder.

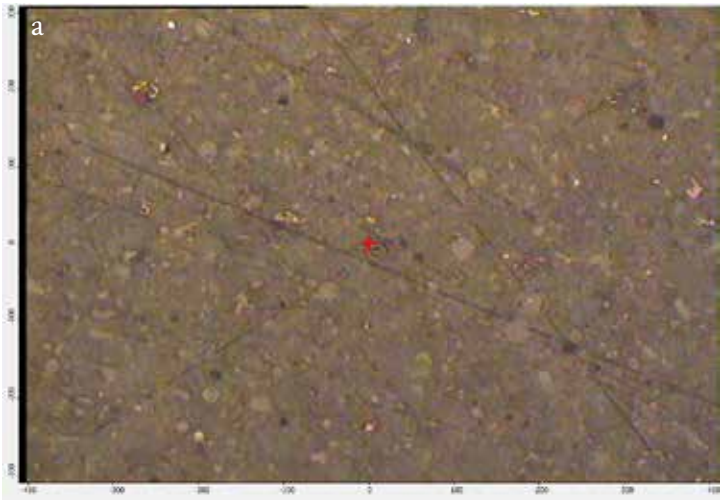

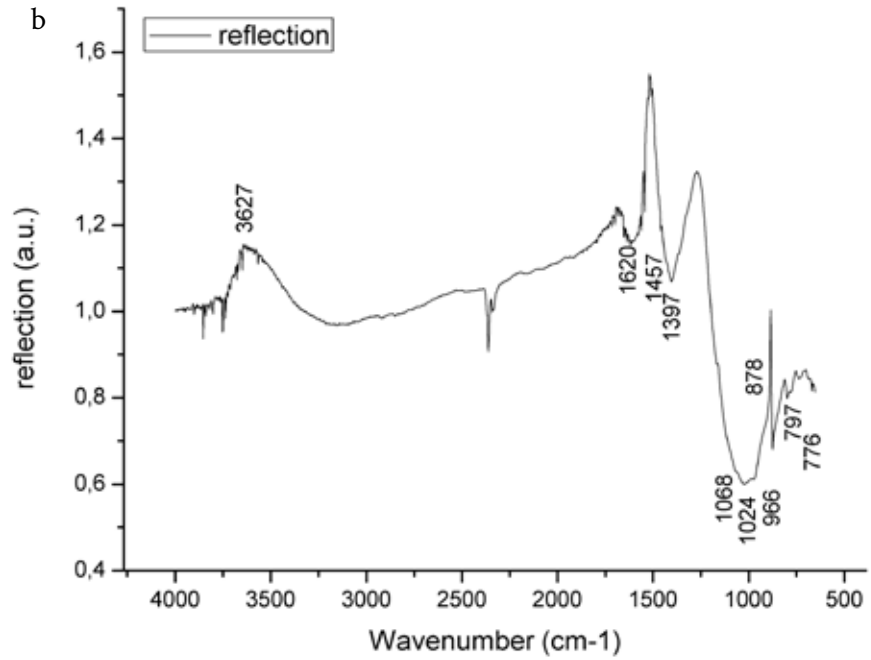

◀*Figure 67. Pozzolanic cement cross section (CIV) analyzed by μ-FTIR. The image of the analysed area (a) and the spectrum (b) are shown.*

The samples with natural hydraulic lime were rough, so in some cases it was difficult to perform the analysis since μ-FTIR requires a very smooth surface to favor the reflection. Moreover, in some cases the resin was embedded in the sample pores altering the analysis.
In samples mortars, it was also possible to select the areas with a minor amount of aggregate to perform the analysis.

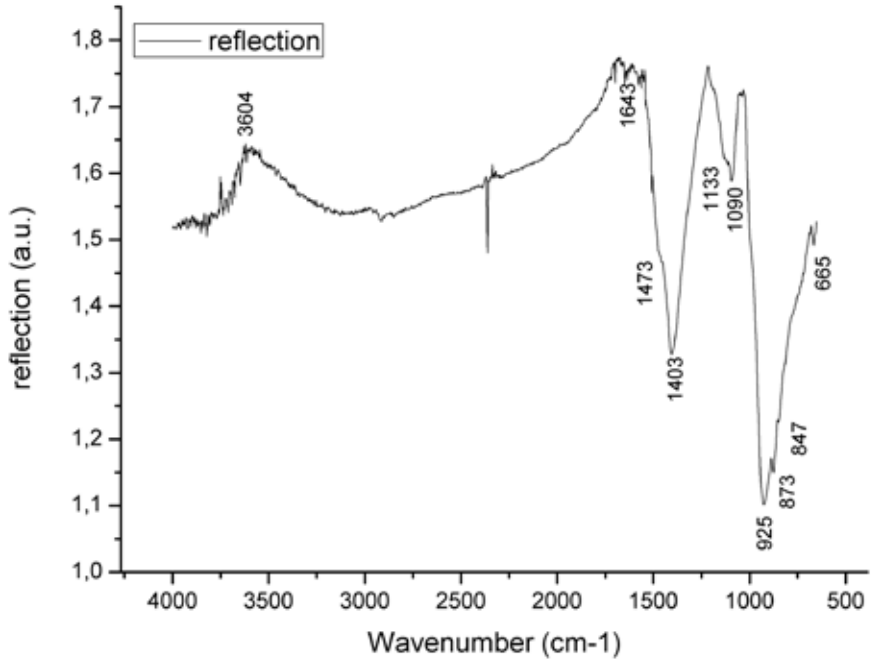

Figure 68. Portland cement with quartz aggregate polished cross section (CIQ) analyzed by μ-FTIR.

In the sample containing quartz aggregate (CIQ) the spectrum (figure 68) presented the main peaks of calcite splitted to 1402 and 1452cm^{-1} and the signal at 873cm^{-1} [19–22]. The peaks at 847 and 925cm^{-1} could be assigned to C_2S, C_3S or CA_2 or C_2AS. The band at 1090cm^{-1} could be a shifting of that ascribed to tobermorite, while the peaks at 1133cm^{-1} and 1643cm^{-1} have been assigned to ettringite. The signal at 665cm^{-1} could suggested several phases: gypsum, according to Arrizabalaga, Hughes and Ghosh [23,24,33]; *CSH*, as discussed by Delgado et al. [34]; tobermorite, as suggested by Guo et al. [30]; gibbsite, according to Wilson [28]; anorthite, as determined by Farmer [27].
In the cross section of the samples containing natural hydraulic lime, no clear evidence of the presence of hydraulic phases was visible. In sample NM (natural hydraulic lime and carbonate aggregate) (figure 69), the main peaks of calcite (873, 1415 and 2516cm^{-1}) were identified [19–22]. The peak at 698cm^{-1} is assigned to quartz, according to Wilson [28], while the peaks at 1037 and 1072cm^{-1} could be due to the presence of silicates in the sample.

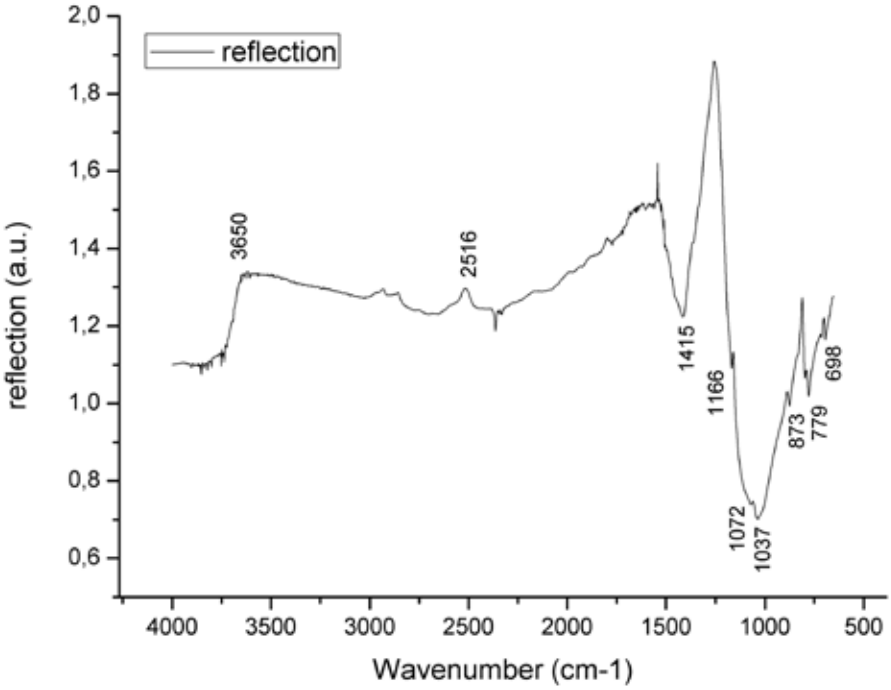

Figure 69. μ-FTIR spectrum of natural hydraulic lime with carbonate aggregate specimen (NM)..

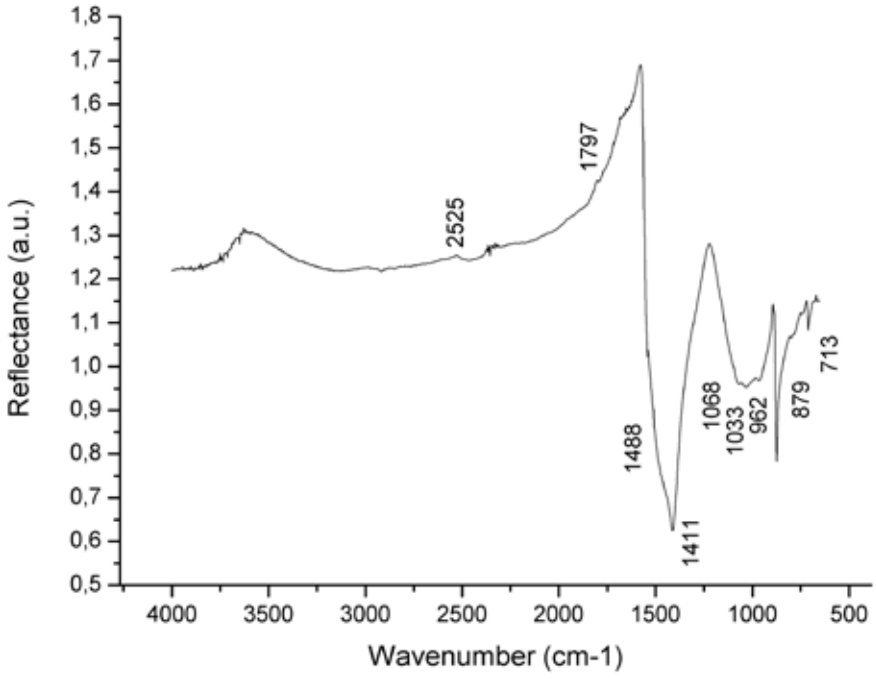

Figure 70. μ-FTIR spectrum of sample CIVM (pozzolanic cement and carbonate sand).

The main peaks of calcite were identified in the spectra of sample CIVM (713, 879, 1411 and 1488, 1797, 2525cm^{-1}) (figure 70). The peak at 962cm^{-1} is assigned to the presence of a calcium silicate hydrate (for example *CSH* or tobermorite), unhydrated calcium silicate, as C_2S [23,30,31], or gibbsite [25]. The peak at 1033cm^{-1} and 1068cm^{-1} could be related to the presence of $Al(OH)_3$ according to Fernadez-Carrasco et al. [25]. The signal at 1068cm^{-1} could be related to the presence of fly ash too, as suggested by Fernandez-Jimenez et al. [32]. The sample NQ was difficult to analyze and no reliable results were found because it was not cohesive after the polishing of the cross section. In table 36 the main μ-FTIR results are summarized.

	calcite	**tobermorite**	**ettringite**	**quartz**	***C_2S* or *C_3S***	**aluminates**
CIQ	•	•	•	•	**?**	**?**
CIVQ	•	•	• sulphates	•	**?**	
NQ						
CIM	•		•	•	•	
CIVM	•	•	•	**?**		**?**
NM	•	silicates		•		

Table 36. Results of μ-FTIR analysis on hydraulic mortars.

Discussion

In table 37 the main advantages and drawbacks of the application of μ-FTIR to hydraulic mortars and mixes are summarized. In all the mixes, except for the samples with natural hydraulic lime, the hydrated or not hydrated hydraulic phases were identified. The most important issue to take into account is that the samples need to be accurately polished, thus it is better if they are embedded into epoxy resin. μ-FTIR requires in fact a very smooth surface, in order to obtain a good reflection signal. Moreover, in the cement samples both hydrated and unhydrated calcium silicates were determined. Ettringite was identified in samples with cement binder too. Portlandite was not identified by μ-FTIR, probably for the high level of noise affecting the spectral region where its main peaks appear. Some derivative or split peaks were observed in the spectra, as for portable reflection spectroscopy, for example the splitting of carbonate main peak (Specimens analyses, Infrared spectroscopy) .

Advantages	**Drawbacks**
Identification of hydraulic phases.	It requires a carefully polished cross section, difficult to obtain for some samples.
Identification of unhydrated hydraulic phase also in hardened pastes.	Small areas of analysis: some phases could not be identified even if present.
	The spectra often present noise, especially in the spectral range over 3500cm^{-1} and around 1650cm^{-1}.

Table 37 Summary of advantages and drawbacks of μFTIR spectroscopy applied to cements and natural hydraulic lime pastes and mortars.

Conclusions

Both techniques have shown their potentiality in the identification of hydraulic phases. One of main differences is the area of analysis: Raman is in fact a punctual analysis (a few microns), while μ-FTIR analyzes an area of 100μm^2. Any way both techniques could focus the source radiation on the area where apparently no grains of the aggregate appeared, recording the signal coming from the binder. The presence of C_3A and its hydrated phases was difficult to be identified with both techniques. μ-FTIR could suggest them only in some cases only. On the other hand, Raman spectroscopy identified hydraulic phases also in natural hydraulic lime specimens.

Raman spectroscopy does not necessarily require a cross section, as powders could also be analysed.

Both techniques highlighted the presence of unhydrated hydraulic cement phases in reacted powders or samples. This feature has been identified only by SEM and petrographical/optical analyses, while the other techniques used in this study proved to be ineffective.

The next step of the research deals with the evaluation of the analytical capability of these techniques in the identification of the hydraulic phases also in mixed mortars.

References

[1] J. Higl, M. Köhler, M. Lindén, Confocal Raman microscopy as a non-destructive tool to study microstructure of hydrating cementitious materials, Cem. Concr. Res. 88 (2016) 136–143. doi:10.1016/j.cemconres.2016.07.005.

[2] S.S. Potgieter-Vermaak, J.H. Potgieter, R. Van Grieken, The application of Raman spectrometry to investigate and characterize cement, Part I: A review, Cem. Concr. Res. 36 (2006) 656–662. doi:10.1016/j.cemconres.2005.09.008.

[3] C. García-Florentino, M. Maguregui, H. Morillas, U. Balziskueta, A. Azcarate, G. Arana, J.M. Madariaga, Portable and Raman imaging usefulness to detect decaying on mortars from Punta Begoña Galleries (Getxo, North of Spain), J. Raman Spectrosc. 47 (2016) 1458–1466. doi:10.1002/jrs.4949.

[4] C.-S. Deng, C. Breen, J. Yarwood, S. Habesch, J. Phipps, B. Craster, G. Maitland, Ageing of oilfield cement at high humidity: a combined FEG-ESEM and Raman microscopic investigation, J. Mater. Chem. 12 (2002) 3105–3112. doi:10.1039/b203127m.

[5] J. Sun, Z. Wu, H. Cheng, Z. Zhang, R.L. Frost, A Raman spectroscopic comparison of calcite and dolomite, Spectrochim. Acta - Part A Mol. Biomol. Spectrosc. 117 (2014) 158–162. doi:10.1016/j.saa.2013.08.014.

[6] T. Schmid, P. Dariz, Chemical imaging of historical mortars by Raman microscopy, Constr. Build. Mater. 114 (2016) 506–516. doi:10.1016/j.conbuildmat.2016.03.153.

[7] M. Torres-Carrasco, A. del Campo, M.A. de la Rubia, E. Reyes, A. Moragues, J.F. Fernández, New insights in weathering analysis of anhydrous cements by using high spectral and spatial resolution Confocal Raman Microscopy, Cem. Concr. Res. 100 (2017) 119–128. doi:10.1016/j.cemconres.2017.06.003.

[8] J. Ibáñez, L. Artús, R. Cuscó, Á. López, E. Menéndez, M.C. Andrade, Hydration and carbonation of monoclinic C_2S and C_3S studied by Raman spectroscopy, J. Raman Spectrosc. 38 (2007) 61–67. doi:10.1002/jrs.1599.

[9] Y. Yue, J. Jing, P.A.M. Basheer, J.J. Boland, Y. Bai, Characterisation of carbonated Portland cement paste with optical fibre excitation Raman spectroscopy, Constr. Build. Mater. 135 (2017) 369–376. doi:10.1016/j.conbuildmat.2017.01.008.

[10] P. Dariz, J. Neubauer, F. Goetz-Neunhoeffer, T. Schmid, Calcium aluminates in clinker remnants as marker phases for various types of 19th-century cement studied by Raman microspectroscopy, Eur. J. Mineral. 28 (2016) 907–914. doi:10.1127/ejm/2016/0028-2577.

[11] M. Conjeaud, H. Boyer, Some possibilities of Raman microprobe in cement chemistry, Cem. Concr. Res. 10 (1980) 61–70. doi:10.1016/0008-8846(80)90052-6.

[12] R.J. Kirkpartick, J.L. Yarger, P.F. McMillan, P. Yu, X. Cong, Raman spectroscopy of C-S-H, tobermorite, and jennite, Adv. Cem. Based Mater. 5 (1997) 93–99. doi:10.1016/S1065-7355(97)00001-1.

[13] D. Gastaldi, E. Boccaleri, F. Canonico, M. Bianchi, The use of Raman spectroscopy as a versatile characterization tool for calcium sulphoaluminate cements: A compositional and hydration study, J. Mater. Sci. 42 (2007) 8426–8432. doi:10.1007/s10853-007-1790-8.

[14] S.S. Potgieter-Vermaak, J.H. Potgieter, M. Belleil, F. Deweerdt, R. Van Grieken, The application of Raman spectrometry to the investigation of cement: Part II: A micro-Raman study of OPC, slag

and fly ash, Cem. Concr. Res. 36 (2006) 663–670. doi:10.1016/j.cemconres.2005.09.010.

[15] S. Sahu, D.L. Exline, M.P. Nelson, Identification of thaumasite in concrete by Raman chemical imaging, Cem. Concr. Compos. 24 (2002) 347–350. doi:10.1016/S0958-9465(01)00086-5.

[16] C. Deng, C. Breen, J. Yarwood, S. Habesch, J. Phipps, B. Craster, Ageing of oilfield cement at high humidity : a combined FEG-ESEM and Raman microscopic investigation, (2002) 3105–3112. doi:10.1039/b203127m.

[17] T. Ohsaka, F. Izumi, Y. Fujiki, Raman spectrum of anatase, TiO_2, J. Raman Spectrosc. 7 (1978) 321–324. doi:10.1002/jrs.1250070606.

[18] W.F. Zhang, Y.L. He, M.S. Zhang, Z. Yin, Q. Chen, Raman scattering study on anatase TiO_2 nanocrystals, J. Phys. D. Appl. Phys. 33 (2000) 912–916. doi:10.1088/0022-3727/33/8/305.

[19] M.R. Derrick, D. Stulik, J.M. Landry, Infrared Spectroscopy in Conservation Science, The Getty Conservation Institute, Los Angeles, 1999.

[20] C. Miliani, F. Rosi, A. Daveri, B.G. Brunetti, Reflection infrared spectroscopy for the non-invasive in situ study of artists' pigments, Appl. Phys. A Mater. Sci. Process. 106 (2012) 295–307. doi:10.1007/s00339-011-6708-2.

[21] C.E. Weir, E.R. Lippincott, Infrared Studies of Aragonite, Calcite, and Vaterite Type Structures in the Borates, Carbonates, and Nitrates, J. Res. Natl. Bur. Stand. A. Phys. Chem. 65 (1961) 173–183. doi:10.6028/jres.065A.021.

[22] C. Ricci, C. Miliani, B.G. Brunetti, A. Sgamellotti, Non-invasive identification of surface materials on marble artifacts with fiber optic mid-FTIR reflectance spectroscopy, 69 (2006) 1221–1226. doi:10.1016/j.talanta.2005.12.054.

[23] S.N. Ghosh, S.K. Handoo, Infrared and Raman spectral studies in cement and concrete (review), Cem. Concr. Res. (1980). doi:10.1016/0008-8846(80)90005-8.

[24] T.L. Hughes, C.M. Methven, T.G.J. Jones, S.E. Pelham, P. Fletcher, C. Hall, Determining cement composition by Fourier transform infrared spectroscopy, Adv. Cem. Based Mater. 2 (1995) 91–104. doi:10.1016/1065-7355(94)00031-X.

[25] L. Fernández-Carrasco, D. Torrens-Martín, L.M. Morales, Sagrario Martínez-Ramírez, L. Fernández Carrasco, D. Torrens Martín, L.M. Morales, S. Martínez Ramírez, Infrared spectroscopy in the analysis of building and construction materials, InTech, 2012. doi:10.5772/36186.

[26] L. Fernández-Carrasco, E. Vázquez, Reactions of fly ash with calcium aluminate cement and calcium sulphate, Fuel. 88 (2009) 1533–1538. doi:10.1016/j.fuel.2009.02.018.

[27] V. C. Farmer, The Infrared Spectra of Minerals, 1974. doi:https://doi.org/10.1180/mono-4.

[28] M.J. Wilson, ed., Clay Mineralogy: Spectroscopic and Chemical Determinative Methods, Springer Netherlands, Dordrecht, 1994. doi:10.1007/978-94-011-0727-3.

[29] G. Anbalagan, A.R. Prabakaran, S. Gunasekaran, Spectroscopic characterization of indian standard sand, J. Appl. Spectrosc. 77 (2010) 86–94. doi:10.1007/s10812-010-9297-5.

[30] X. Guo, F. Meng, H. Shi, Microstructure and characterization of hydrothermal synthesis of Al-substituted tobermorite, Constr. Build. Mater. 133 (2017) 253–260. doi:10.1016/j.conbuildmat.2016.12.059.

[31] P. Yu, R.J. Kirkpatrick, B. Poe, P.F. McMillan, X. Cong, Structure of Calcium Silicate Hydrate (C-S-H): Near-, Mid-, and Far-Infrared Spectroscopy, J. Am. Ceram. Soc. 82 (2004) 742–748. doi:10.1111/j.1151-2916.1999.tb01826.x.

[32] A. Fernández-Jiménez, A. Palomo, Mid-infrared spectroscopic studies of alkali-activated fly ash structure, Microporous Mesoporous Mater. 86 (2005) 207–214. doi:10.1016/j.micromeso.2005.05.057.

[33] I. Arrizabalaga, O. Gómez-Laserna, J.A. Carrero, J. Bustamante, A. Rodríguez, G. Arana, J.M. Madariaga, Diffuse reflectance FTIR database for the interpretation of the spectra obtained with a handheld device on built heritage materials, Anal. Methods. 7 (2015) 1061–1070. doi:10.1039/C4AY02189D.

[34] A.H. Delgado, R.M. Paroli, J.J. Beaudoin, Comparison of IR techniques for the characterization of construction cement minerals and hydrated products, Appl. Spectrosc. (1996). doi:10.1366/0003702963905312.

Microstructural analysis

The main focus of this work is the characterization of the pore network properties of historical mortars to evaluate the advantages and the drawbacks of mercury intrusion porosimetry and micro-computed X-ray tomography, which are discussed in this chapter. These techniques have been applied to building materials with a particular attention to the benefit that these analyses bring in the study of historical mortars. In order to reach our purposes, twelve mixtures of mortars were prepared. The choice of the composition was decided on restoration practice and based on the most diffused mortars used in the past and currently. In the selected mixtures, two different cement mortars were included in order to evaluate modern mixtures.

Mercury intrusion porosimetry is a well-known technique and the most used one for the characterization of pore size distribution in building materials [1,2,11,12,3–10]. MIP is based on the Washburn equation which relates the contact angle (θ) of a non-wetting liquid (Hg) with a surface of a solid material and with the surface tension (γ) of the liquid itself, connected to the pressure (P) applied in order to obtain the measure of the equivalent pore radii (r) [13–15]:

$$r = -2\gamma\cos\theta/P$$

Several studies have shown that the results should be interpreted with care [4,8,9,13,16–21]. This technique is affected by the so-called "ink bottle effect" that could overestimate or underestimate the pore radii [13]. In fact, this technique, due to the Washburn equation, measures the pore throat size at the beginning of the intrusion: so, if there is a larger volume inside, the analysis will measure it with a small radius. Hence it is supposed pores are cylindrical. Another drawback of this technique is that once the analysis is done, the sample cannot be studied with other techniques because it is totally saturated with Hg. Another restriction is that the MIP can only measure the porosity under 90μm. Moreover, MIP analysis, due to the high pressure applied, could alter the sample forming cracks inside sample that could modify the results of the analysis without being identified [4].

On the other hand X-ray μCT [3,4,28,29,6,14,22–27] is a powerful non-destructive analysis: it is important for a variety of topics over the porosity analysis; in fact, it also gives information on volume structure, aggregate, and cracks inside the samples. Another remarkable advantage in the use of μCT is that, contrary to MIP, it is possible to perform other analysis on the same sample after a μCT analysis. One of the drawbacks of this technique is that it cannot measure all the smaller pore sizes as MIP: in fact, μCT pore radii measures are recorded above 10μm (with the parameter used in this study) (figure 71). Furthermore, some choices during the data analysis could influence the results such as the threshold, the resolution, the dimension of the voxels and the segmentation, hence it is user dependent. The voxels are the three-dimensional equivalent of a pixel in a 2D image. It is the lower boundary on pore sizes that can be measured. In other words objects smaller than a voxel size cannot be distinguished with standard μCT and image analysis.

The combination of mercury intrusion porosimetry and computed X-ray tomography has been reported in different works [4,13,14,18,23] but not on the large and various set of mortars considered in this work, with interest for building and conservation science. A comparison between the two techniques was performed in order to evaluate their limits on these materials with a particular attention to the advantages of the application on cultural heritage material. The possibility to study the material with a non-destructive

approach (μCT) allows several advantages: for example, different analysis could be performed on the same sample, it could provide more complete information and a deeper characterisation also from the inner part of the sample, where it is usually not allowed a direct observation. The main advantage of μCT is that it can identify large pores that are connected by very small pores and which are considered as ink-bottle in MIP. Moreover μCT porosity allows also to study and to visualize the microstructure, the cohesion and eventually identify some damages not visible from the outside part.

Mercury Intrusion Porosimetry (MIP)

Mercury intrusion porosimetry (MIP) was carried out using a Thermo Scientific PASCAL 140 and PASCAL 240. The measuring range (pressure) is 0.1-200 Mpa, the resolution (pressure) is from 0.01 Mpa to 100 Mpa and from 100 to 200 Mpa. The accuracy >0.2% while the resolution in volume is 0.1 mm^3. The measuring range radius is between 7.5 and 3.7 X 10^{-3} microns. For each specimen two samples were analysed with this technique.

The different mortars mixed design investigated are shown in table 38. Their composition was already discussed in a previous work [30]. The binder/aggregate ratio was 1:3 (weight/weight).

The specimens were prepared mixing the binders with the aggregates together with a measured amount of water, and then the mix was poured in silicone molds. The set was prepared in a steady environment room at 20°C and 65% of RH. Then the specimens with aerial binders were removed from the mold and cured in the same environmental conditions for 6 months. Cements and natural hydraulic mortars were stored in an environmental chamber with 90% of RU and 20°C according to EN196 [31].

At the end of the analysis the porous system data obtained by the two techniques were compared.

Sample with quartz sand	
CIQ	CEM I
CIVQ	CEM IV
CQ	hydrated lime
GsQ	gypsum
GQ	lime putty
NQ	natural hydraulic lime 3.5
Sample with carbonate sand	
CIM	CEM I
CIVM	CEM IV
CM	hydrated lime
GM	lime putty
NM	natural hydraulic lime 3.5
GsM	gypsum

Table 38. Mix designs of the mortars prepared for this study.

Computed microtomography analysis

X-ray computed micro-tomography (μCT) images were measured on the custom-built HECTOR scanner at the Centre for X-ray Tomography of Ghent University (UGCT). This scanner rotates the sample 360° during the analysis, and geometric settings resulted in a voxel size of 10 micron. Images were obtained with an X-ray tube operated at 160kV and 10W, equipped with a 1mm Al filter and by taking 1401 frames. Beam hardening was reduced by the presence of a 1mm Al filter between the X-ray source and the sample. Octopus Reconstruction and Octopus Analysis were used for reconstruction and image analysis respectively. VGStudio was used for 3D visualizationn [32–35]. The dimension of the samples analysed are $1cm^3$.

For the calculation of the sphericity only voids with at least 3 voxels of equivalent diameter were considered in order to exclude the smallest volumes that could produce error in the calculation. The program Octopus analysis calculates the equivalent diameter as "the diameter of a sphere with the same number of voxels as the object" and the maximum opening as "the diameter of the largest inscribed sphere in the object (only possible if the Distance transform is determined)".

Due to the amount of data analysed and in order to perform the CT image analysis with a reasonable timing, the volume analysed for each sample was divided in two, and then the results were averaged. This factor, with others that will be discussed later, has to be taken into account in the interpretation of the results. In fact, it can lead to a partial over- or underestimation of the data due to the fact that there could be some pores between the two volumes that, during the software analysis, could be considered as part of different pores related to smaller or bigger volumes, as hypothesized by the software.

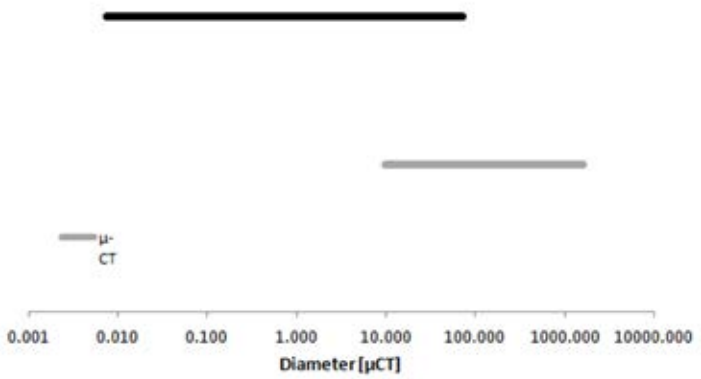

◀Figure 71. Comparison between μ-CT and MIP pore size distribution.

Results

Mercury Intrusion Porosity (MIP)

In table 39, the porosity results obtained by MIP analysis are summarized. As it is visible in table 39, the average pore radius and the total % porosity are very small for specimens made by cement (CIQ, CIM, CIVQ, and CIVM). This behaviour is probably related to the composition of these materials. In fact, these samples are made of two types of cement (CEM I and CEM IV). Always considering this set of four samples, it is evident that sample CIVM has slightly higher values than the other cement-based samples.

This sample recorded a larger average pore radius, a total cumulative volume and also a higher total porosity. This behaviour could be due to different causes, like some difference in the blending process, but it could depend also on the different aggregate used in CIVM from CIVQ. In CIVM the carbonate sand was used, while in CIVQ quartz sand was used. For what concerns the cumulative volume (%) distribution, figure 72 (a, b, c and d) shows its values in relation to the pore size distribution and the relative and the specific volume. As it is visible (figure 72) all the four cement samples present a high pore distribution between 0.1 and 0.01μm pore (throat) diameter. Samples (CIM, CIVQ and CIVM) also appear as trimodal; in fact, they present two other peaks of the distribution of pore (throat) diameter distribution between 0.1-1μm and between 1-10μm. Also the sample with natural hydraulic lime shows a trimodal pore size distribution. This behaviour could be related to multiple factors that could influence this parameter, for example the composition of the binder, or the way used to stir the mixture.
As regards the other samples analysed, a total porosity of generally than 20% was measured. All the other samples present a higher average pore radius compared to the values obtained for samples made with cement. Samples NM and NQ show an average pore radius lower than the samples not made of cement. It could be related to the more similar composition with the cementitious material although they present a higher porosity than the one obtained with cements. They present a higher pore radius compared to cementitious material and accordingly they present a higher total cumulative volume.
The samples made with gypseous binder present a very narrow pore size distribution at about 1μm. This particular feature was recorded only in this type of material and this appears to be characteristic of this blend (figure 73).
Lime mortars (lime putty and hydrated lime) show a bi-modal pore size distribution. Both the mixtures made with lime putty and hydrated lime show a similar behaviour, except for GM that appears more similar to a trimodal distribution.

Samples	Total cumulative volume (mm^3/g)	Bulk density (g/cm^3)	Average pore radius (μm)	Total specific surface area (m^2/g)	Total porosity (%)
CIQ	49.3	1.8	0.02	5.4	8.8%
CIM	46.1	2.0	0.03	5.2	9.4%
CIVQ	45.5	1.9	0.02	6.3	8.7%
CIVM	60.7	1.9	0.09	6.1	12%
CQ	133.3	1.6	0.58	1.3	21.7%
CM	133.2	1.9	0.44	1.5	24.8%
GsQ	146.5	1.7	0.65	0.8	25.5%
GsM	109.9	1.8	0.92	0.5	19.4%
GQ	126.4	1.7	4.35	1.4	21.8%
GM	134.0	1.9	2.42	1.2	25%
NQ	121.0	1.8	0.34	2.9	21.9%
NM	125.5	1.8	0.13	5.35	22.1%

Table 39. Results average of the MIP analysis

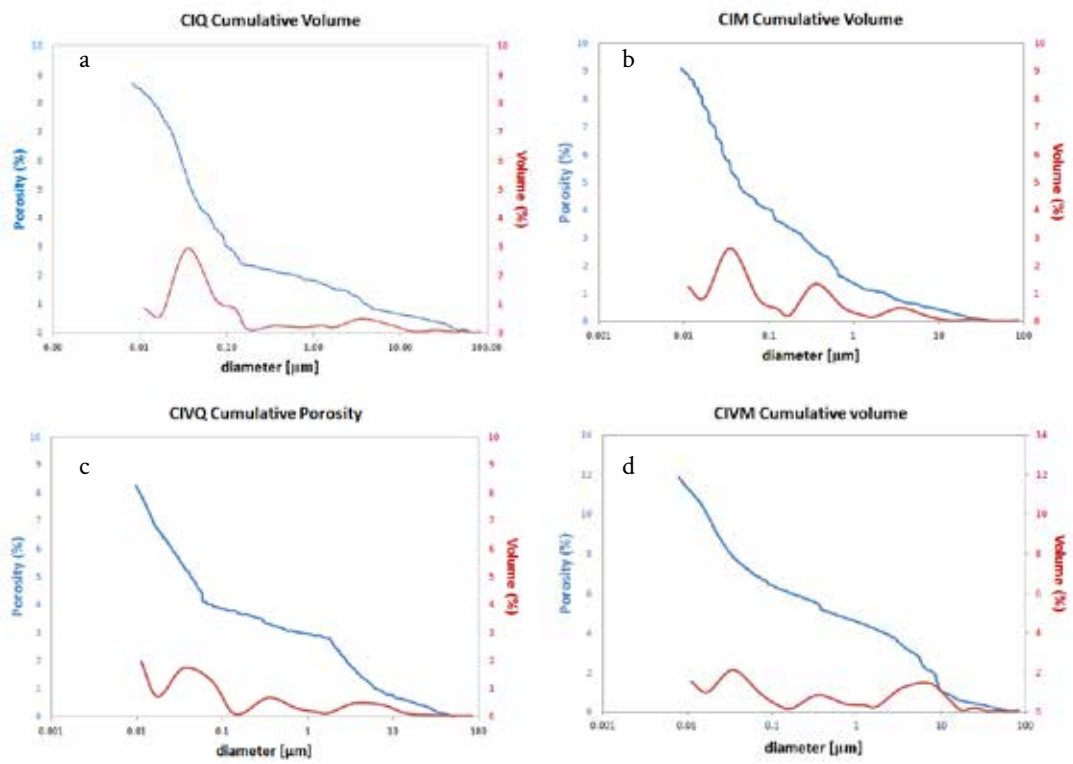

▲*Figure 72 a, b, c, d. MIP Cumulative volume distribution of samples CIQ, CIM, CIVQ and CIVM.*

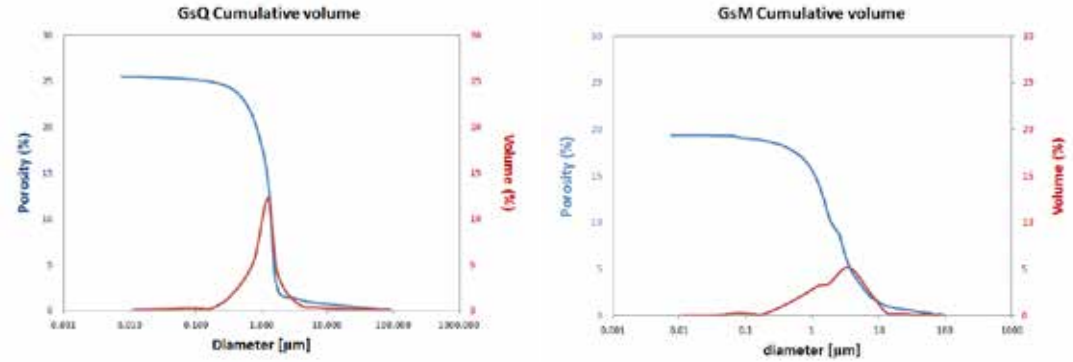

▲*Figure 73. The pore size distribution of samples with gypsum, note that the scale in the Y axis of these samples is different from the previous CIM, CIQ, CIVM and CIVQ.*

X-ray Computed Tomography porosity

The μCT allowed evaluating porosity of air voids over 10 μm^3. In table 40, the porosity, the maximum opening, the equivalent diameter and the sphericity are showed.

As it is possible to see (table 40), pores (> 10μm) in cement and NHL samples have the highest sphericity (sphericity closer to 1, correspond to spherical measured object), and it is also confirmed by the images in figures 74 and 75. Among these samples, it is possible to distinguish between the most spherical pores of CIQ, CIVQ and NQ (0.67, 0.59 and 0.63 respectively) and the least spherical CIM, CIVM and NM (0.57, 0.46 and 0.47 respectively). This feature is probably related to the different aggregate used in the samples. In fact, half of the samples are made of quartz sand and the others of carbonate sand. Probably the composition and the shape of the aggregate grain influence the air voids distribution inside the samples. The samples with the highest sphericity seem to have quartz sand (rounded grains) and the others carbonate sand (rough and irregular grains). This trend is also visible in the other samples with hydraulic lime, lime putty and gypsum.

The composition of the binder is similar to the aggregate in samples CIQ and CIVQ and for this reason, in these two cases, it is impossible to distinguish all the grain of the aggregate from the binder (figure 75 a, c).

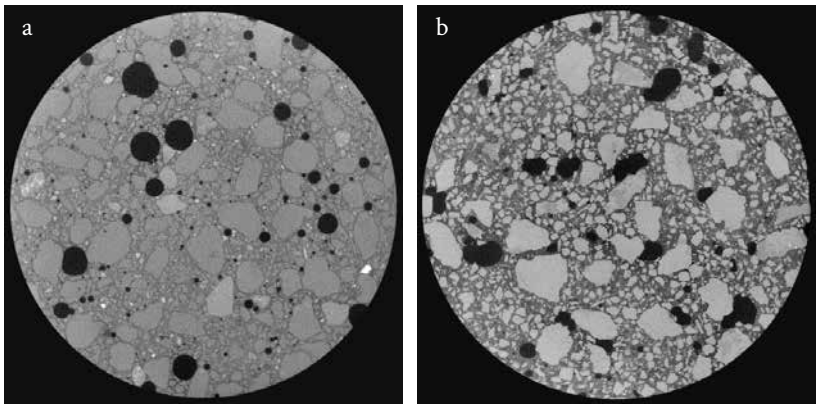

▲ *Figure 74. Slices of X-ray tomography for samples NQ (a) and NM (b).*

Porosity	µCT			
Sample	Porosity Total Volume (%):	Equivalent Diameter [µm]	Maximum Opening [µm]	Sphericity
CIQ	7.1%	46	32.2	0.67
CIVQ	3.5%	90.5	65.7	0.59
CQ	5.5%	43.7	25	0.54
GsQ	2,2%	45.9	28.1	0.56
GQ	18.24%	50.6	28.8	0.52
NQ	6%	62.4	46.7	0.63
CIM	7.45%	93.4	58.5	0.57
CIVM	5.9%	33.9	19.5	0.46
CM	6.0%	37.1	20	0.49
GsM	12.8%	26	14.5	0.48
GM	14.2%	59.8	28	0.47
NM	7.5 %	21.7	13.95	0.47

Table 40. Porosity of the micro-computed tomography results.

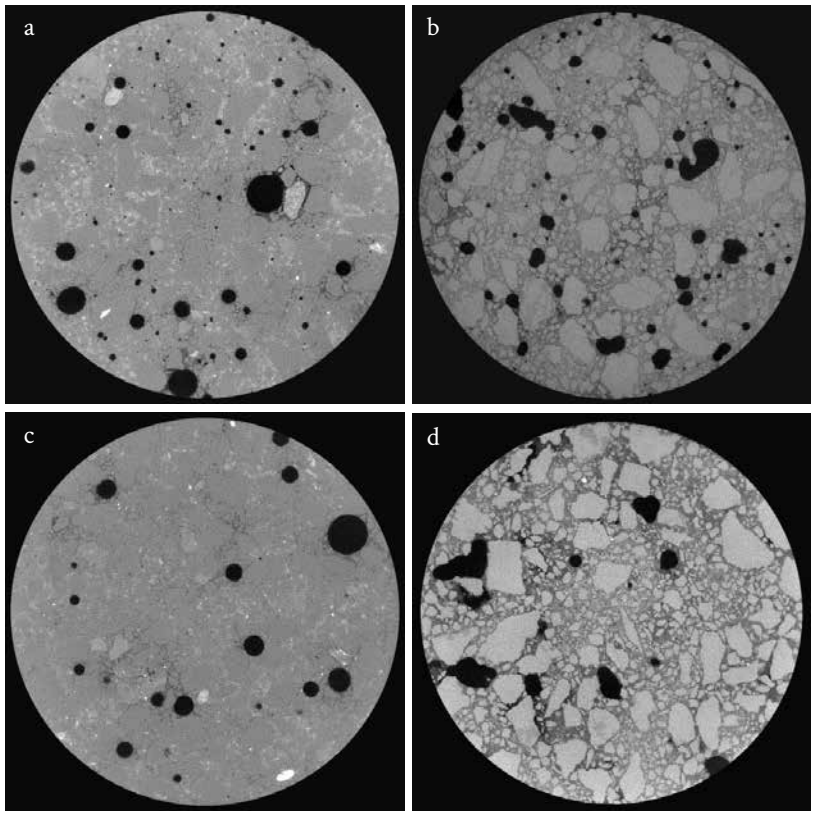

▲ *Figure 75. Slices of X-ray tomography for samples CIQ (a), CIM (b), CIVQ (c), CIVM (d).*

Comparison between MIP and μCT porosity results

	MIP	μCT
Sample	**Total porosity (%):**	**Total porosity (%):**
CIQ	8.8%	7%
CIVQ	8.7%	3.5%
CQ	21.7%	5.5%
GsQ	25.5%	2.2%
GQ	21.8%	18.24%
NQ	21.9%	6%
CIM	9.4%	7.45%
CIVM	12%	5.9%
CM	24.8%	6.0%
GsM	19.4%	12.8%
GM	25%	14.2%
NM	22%	7.5 %

Table 41. Porosity results of MIP and X-ray tomography.

μCT allowed evaluating the total porosity. The most representative is the total porosity, since the open porosity measured with μCT is not comparable with the one measured with MIP because of instrumental differences. In any case, considerations on the total porosity of both techniques can be proposed.
In table 41 the porosity measured with mercury intrusion porosity and computed tomography are compared. With the two techniques, in samples with the same binder's compositions, and different aggregate the porosity values seems to follow the same trend. It is important to consider that the porosity of both refers to two different pores/air voids diameters distributions. Only a small region in the measuring range overlaps (between 10μm to 90μm). In the case of sample GsQ, for example, there is a huge difference between the porosity measured with MIP (25.5%) – where the porosity's value is similar to non-hydraulic samples – and the porosity measured with μCT (2.2%). As it is visible in figure 73, the MIP's pore diameter is centered at around 1μm, under the limit of detection of μCT, while the centred value of the maximum opening measured with μCT is 28.1μm. This difference in the diameter measured shows the limits of the two techniques. This means that only the biggest air voids are detected with μCT. In case of MIP, results are affected by the ink-bottle effect, measuring some big pores by the size of their pore throat (hence assigning a large volume to this underestimated pore size).
GQ and GM are two samples that recorded a high porosity both in μCT and MIP analysis. μCT porosity is 18.2% for GQ and 14.2% for GM, while with MIP the values are: 21.8% and 25% respectively (figure 76 and table 41). An explanation to the high porosity obtained with both techniques is that the sample has a wide pore size distribution, including pores well visible with MIP (under 100μm) and μCT (over 10μm). This hypothesis seems to be confirmed by the pore size distributions obtained from the two techniques (figure 76). In fact, in MIP both samples present a good pore size distribution between 10 and 100μm, 1 and 10μm and 0.1 and 1μm, while in μCT they present the highest pore size distribution between 49 and 150μm.

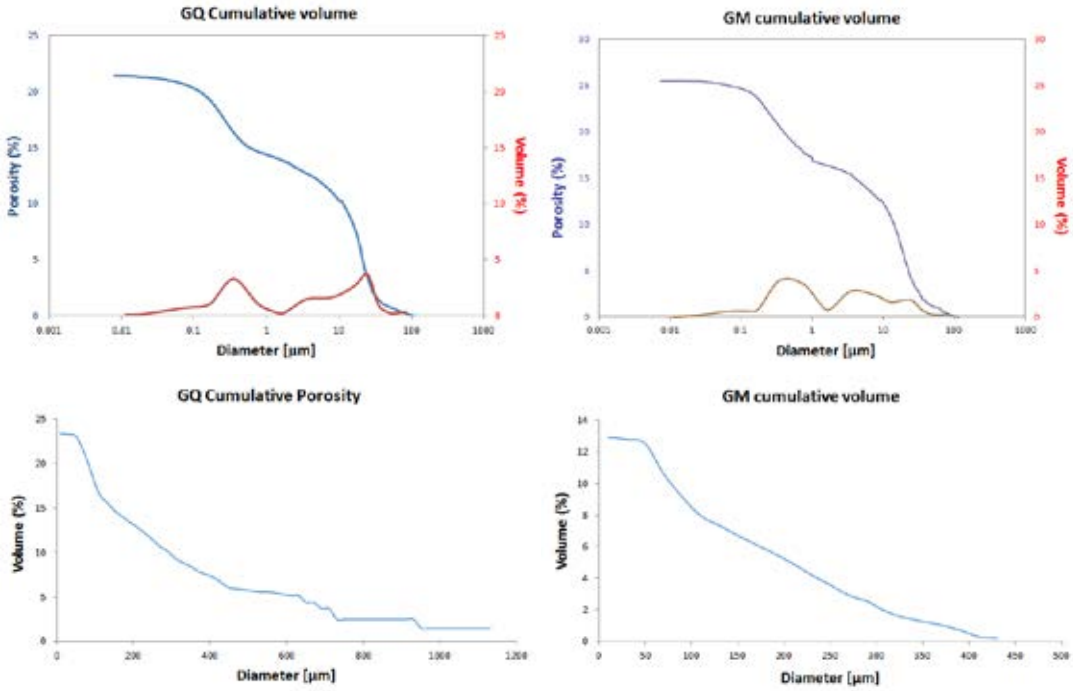

▲*Figure 76. GQ (left) and GM (right) cumulative volume and pore size distribution of MIP and CT pore size distributions.*

Comparable observations could be done for samples CIQ and CIM. It is important to underline that even if the values of porosity are similar, only a small range is in common between the two techniques, so the values of porosity refer to different ranges.

	MIP	CT	Point counting
Samples	**Total porosity (%):**	**Total porosity (%):**	**Total porosity (%):**
CIQ	8.8%	7%	7.4%
CIVQ	8.7%	3.5%	5.2%
CQ	21.7%	5.5%	13.4%
GsQ	25.5%	2,2%	3%
GQ	21.8%	18.24%	21.8%
NQ	21.9%	6%	3%
CIM	9.4%	7.45%	5.8%
CIVM	12%	5.9%	4.4%
CM	24.8%	6.0%	8.6%
GsM	19.4%	12.8%	8.4%
GM	25%	14.2%	17%
NM	22%	7.5 %	17.6%

Table 42. Comparison between MIP, µCT and point counting porosity results.

In addition to MIP and μCT porosity, also point counting on the images collected by optical microscopy has been performed. The point counting analysis was performed with JMicroVision software using 200 points and a random grind. Before performing point counting, the classes of selection were created. In table 42 the results of porosity obtained with MIP, μCT and point counting are compared. In some samples (GsQ, CIVM, CM, GM and NQ) the porosity percentages obtained by the point counting are similar to the ones measured with the CT images. This is due to the similar scale of resolution of the two images techniques. In fact, the point counting is performed on thin sections with optical analysis. In other samples the porosity values measured with point counting are higher than those measured with μCT. This may occur because of irregularities of the samples and differences in air voids shape and dimensions, which could be more visible in one or in the other technique. In other samples, like GQ and CIQ, the porosity percentages are similar in all the three techniques: this could be due because the pores are equally distributed in all the range of detection of all the three techniques.

μCT Aggregate analysis

μCT – Aggregate analysis

Samples	Aggregate Total Volume (%):	Equivalent Diameter Average [μm]	Maximum Opening Average [μm]	Sphericity
CIQ	-	-	-	-
CIVQ	-	-	-	-
CQ	62.1	61.9	32.8	0.51
GsQ	52.1	115.5	65.7	0.56
GQ	-	-	-	-
NQ	52.6	34.3	18.8	0.52
GsM	50.8	75.2	42.7	0.53
CIM	51.2	60.9	34.3	0.52
CIVM	49.6	99.9	48.3	0.49
CM	53.3	85.7	49.9	0.56
GM	53.3	119.7	68.5	0.56
NM	55.7	85.6	46.8	0.52

Table 43. μCT aggregate analysis results.

μCT in this study was also applied to evaluate aggregate distribution in the sample and its quantification in volume (table 43 and figure 77).

The samples with quartz aggregate (GQ, CIQ and CIVQ), only on 3 out 6 samples it could be possible to clearly identify the aggregate grains. This problem occurs because of the low grey scale contrast between the aggregate grains and the binders, which depends on the material composition, the scan itself and on the morphology inside the samples. On the contrary, in the samples with carbonate aggregate there was no problem in evaluating the aggregate fraction.

In samples with carbonate aggregate, it was possible to distinguish the aggregate from the binder in all the samples. The volume % obtained from the μCT software analysis was almost constant from about 50 until

about 55%, while for the samples with quartz aggregate there are more differences (from 52 until 62). The equivalent diameter and the maximum opening also change between one sample to another, while sphericity values remain more constant from 0.49 to 0.56 for all the analysed samples. These differences (also in the set of samples with the same aggregate) could be explained with some observations: since every binder has a different composition in every reconstruction of the scans, the grey scale histogram of the samples changes and so every time new threshold levels have to be defined. In samples with less contrast between binder and aggregate, it is therefore possible that the thresholding process becomes more complex and it does not select all the grains or binders. Moreover, even if the beam hardening corrections were applied, in some samples – because of their morphology – a lighter, just visible rim, was still present and it influences the selection of the threshold levels. Furthermore, the aggregate grains with a diameter less than 10μm could not be identified and visualized with computed tomography analysis.

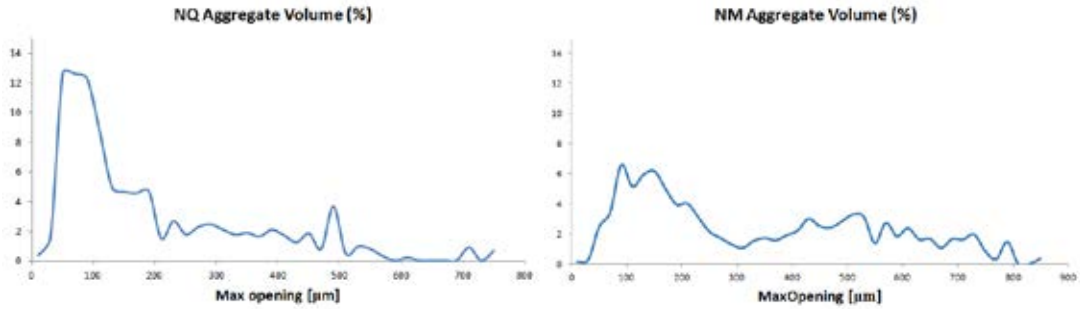

▲ *Figure 77 Aggregate volume distribution calculated with μCT analysis on NQ (left) and NM (right) samples.*

	Aggregate %	Binder %
CIQ	-	-
CIVQ	-	-
CQ	62.1	37.9
GsQ	52.1	47.9
GQ	-	-
NQ	52.6	47.4
GsM	50.8	49.2
CIM	51.2	48.8
CIVM	49.6	50.4
CM	53.3	46.7
GM	53.3	46.7
NM	55.7	44.3

Table 44. CT volume % aggregate and binder values.

Samples	Binder	Aggregate	Porosity	Other
CIQ	44.6%	48%	7.4%	-
CIVQ	44.4%	50.4%	5.2%	-
CQ	41.4%	45.2%	13.4%	-
GsQ	44%	50.8%	3%	2.2%
GQ	23.2%	55%	21.8%	-
NQ	41.4%	55.6%	3%	-
CIM	46%	48.2%	5.8%	-
CIVM	38%	57.6%	4.4%	
CM	39.8%	51.6%	8.6%	-
GsM	41.2%	48.4%	8.4%	2%
GM	20.6%	62.2%	17%	-
NM	34.2%	48.2%	17.6%	-

Table 45 Point counting results.

From the μCT analysis (table 44) the ratio between the binder and the aggregate does not appear constant throughout the sample, even if during the mixture process a ratio in weight of 1/3 binder/aggregate was used. Here the volumes are analysed with μCT analysis, so it is not easy to find a relation between the proportions. The proportion in volumes is more similar to a 1:1 ratio (volume/volume). This is probably due to the difference between the volume ratio and the weight of the materials and because of the detection limit of the technique that could not select all the aggregate components. But for specimens belonging to the samples with one type of aggregate, the binder/aggregate ratio is the same. This is important because it proves that, even if there are differences in attenuation, reconstruction parameters etc., the technique could identify the aggregate from the binder. This last concept could also be applied to the point counting analysis (table 45).

As it is possible to observe in table 42, the % of the aggregate is higher if compared to the binder's more similar to the proportion used. In samples where the gypsum's binder is present, some black particles were identified too and were sorted in the "other" category. By point counting they correspond to 2% inside the binder. The samples with lime putty present the lowest quantity of binder: this could be explained by the fact that the components of the mortar were weighted and because lime putty contains also water so the calcium hydroxide weighed was less than the other samples.

μCT	
Advantages	**Drawbacks**
It can analyze the samples without destroying it.	Problem in the identification of the two binders in mixed mortars.
It measure porosity over 10μm.	The instruments are not diffused as MIP.
3D visualization of open and closed porosity.	It does not measure porosity under 10μm.
It allow the analysis of the aggregate volume.	
3D visualization of the aggregate and of the binder.	
MIP	
Advantages	**Drawbacks**
It measure open porosity under 100μm.	It is invasive and destructive (sample full of Hg).
The instruments are more diffused if compared to μCT.	The samples could not be analyzed with other technique after MIP analysis.
It measure porosity under 90μm.	It can damage the sample and alter the measure of porosity.
	It does not measure porosity over 90μm.
	It does not measure the aggregate.

Table 46. Summary of advantages and drawbacks of μCT and MIP analysis applied to mortars model.

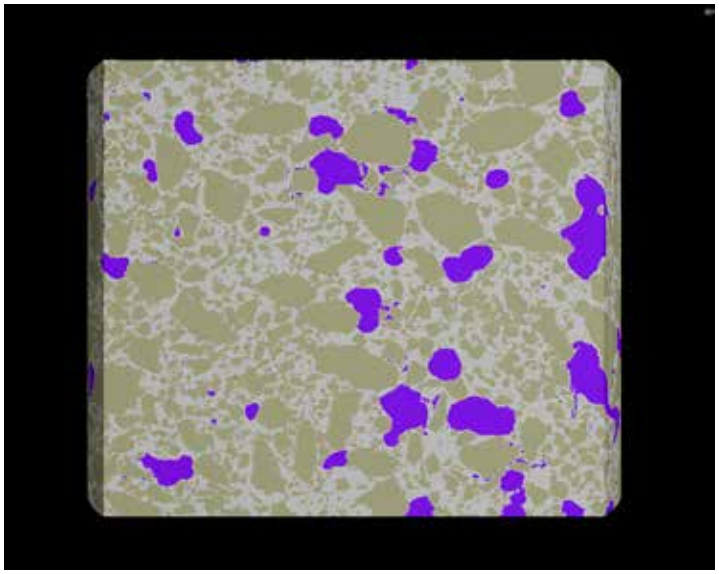

▲ *Figure 78. Example of the visualization of pores (violet), aggregate (light brown) and the binder (white) of NM sample.*

Discussion and conclusions

The data acquired with mercury intrusion porosimetry for aerial lime samples (CM, CQ, GM, GQ) present a pore size distribution comparable to those found by Mosquera et al. for the same type of binder with the same proportion binder/aggregate [5]. Also the porosity % and the bulk density (g/cm^3) are comparable.

The cement total porosity (%) of our samples are similar to those found by Cnudde et al. 2009 [4] and also the micro CT results are similar to those found in our research for samples CIQ, CIVQ, CIM and CIVM. The difference between the cement samples analyzed in this research and those in Cnudde research is the pore size distribution: in fact, their samples do not present a trimodal trend like CIQ, CIVQ, CIM and CIVM. On the contrary, Arandigoyen et al. found a higher porosity (about 20%) compared to our results (8-12%) [1], as it is shown in his study (2007) regarding samples composed by a cement mortar, with the same binder/proportion used in this work. In a previous work of Arandigoyen et al. [36] for specimens made with lime they measured a MIP porosity between 49.9 and 58.8 with the increase of water/binder ratio. On the other hand, Arandigoyen's results for lime mortars are similar to the data recorded by this research. In another article of 2006 Arandigoyen measured high values for MIP porosity both for lime and cement mortars [37]. In Wan et al. work [23] also it was evidenced a trimodal in μCT analysis, that is a trend that we found only in MIP analysis and not in μCT. It is important to underline that even if the values of porosity are similar, only a small range is in common between the two techniques, so the porosity values refer to different ranges. The comparison with the literature helped us to see that our results are similar to those found by the other authors. Cook et al. [12] compared the porosimetric results on model cement sample with different water/binder ratio in order to study the difference in the pore size distribution. They obtained a pore size distribution unimodal and centered between 0.1 and 0.01μm, very different from what we have observed in our samples. In some cases a bimodal pore size distribution in observed in their sample related to the increase in the amount of water and aging time.

Moreover, thanks to this research, it was possible to evaluate the application of two porosimetric techniques on a set of reference specimens for artificial building materials, a comparison that has never been done before. From the comparison of the results obtained with the two techniques, we proved the complementarity nature of these two techniques. As already discussed in advance, mercury intrusion porosimetry provides information on the porosity under 90μm diameter, while computed tomography gives information over 10μm. In addition, while interpreting the results it is important to bear in mind the limits and the drawbacks of each technique in order to correctly interpret the results. For example, the mercury intrusion porosimetry tends to overestimate the micro-porosity while, on the contrary, the computed tomography analysis could underestimate the micro-porosity. Computed tomography has the advantage of providing information about the whole sample like the aggregate distribution or/and the presence of cracks. It can also give a 3D visualization (figure 78) of the results and it could be used for further investigations without destroying the samples. In table 46 the summary of the advantages and drawbacks of the two techniques is shown.

So, the use of one or both techniques depends on the type of the sample, on the aim of the research, which information is needed and what the analytical plan is. Both could give more information than just one of them alone: in fact, using both it is possible to provide a better characterisation of the sample than with only one of the two. Furthermore, the μCT could give more information about the whole sample structure.

For what concerns future developments, the porosity of these sets of samples could be compared to the results of other techniques such as BET (Brunauer–Emmett–Teller theory), water immersion porosimetry, NMR imaging and different resolution of μCT analysis etc, in order to improve the comparison between different porosimetric techniques.

References

[1] M. Arandigoyen, J.I. Alvarez, Pore structure and mechanical properties of cement–lime mortars, Cem. Concr. Res. 37 (2007) 767–775.

[2] G.F. Andriani, N. Walsh, Physical properties and textural parameters of calcarenitic rocks: Qualitative and quantitative evaluations, Eng. Geol. 67 (2002) 5–15. doi:10.1016/S0013-7952(02)00106-0.

[3] L. Korat, V. Ducman, A. Legat, B. Mirtič, Characterisation of the pore-forming process in lightweight aggregate based on silica sludge by means of X-ray micro-tomography (micro-CT) and mercury intrusion porosimetry (MIP), Ceram. Int. 39 (2013) 6997–7005. doi:10.1016/j.ceramint.2013.02.037.

[4] V. Cnudde, A. Cwirzen, B. Masschaele, P.J.S. Jacobs, Porosity and microstructure characterization of building stones and concretes, Eng. Geol. 103 (2009) 76–83. doi:10.1016/j.enggeo.2008.06.014.

[5] M.J. Mosquera, B. Silva, B. Prieto, E. Ruiz-herrera, Addition of cement to lime-based mortars: Effect on pore structure and vapor transport, 36 (2006) 1635–1642. doi:10.1016/j.cemconres.2004.10.041.

[6] J.J. Beaudoin, Porosity measurement of some hydrated cementitious systems by high pressure mercury intrusion-microstructural limitations, Cem. Concr. Res. 9 (1979) 771–781. doi:10.1016/0008-8846(79)90073-5.

[7] H. Cheng-yi, R.F. Feldman, Influence of silica fume on the microstructural development in cement mortars, Cem. Concr. Res. 15 (1985) 285–294. doi:10.1016/0008-8846(85)90040-7.

[8] D. Shi, D.N. Winslow, Contact angle and damage during mercury intrusion into cement paste, Cem. Concr. Res. 15 (1985) 645–654. doi:10.1016/0008-8846(85)90064-X.

[9] R.A. Olson, C.M. Neubauer, H.M. Jennings, Damage to the Pore Structure of Hardened Portland Cement Paste by Mercury Intrusion, J. Am. Ceram. Soc. 80 (2005) 2454–2458. doi:10.1111/j.1151-2916.1997.tb03144.x.

[10] I. Odler, H. Köster, Investigations on the structure of fully hydrated portland cement and tricalcium silicate pastes. II. Total porosity and pore size distribution, Cem. Concr. Res. 16 (1986) 893–901. doi:10.1016/0008-8846(86)90013-X.

[11] D.A. Lange, Image analysis techniques for characterization of pore structure of cement-based materials, 24 (1994) 841–853.

[12] R.A. Cook, K.C. Hover, Mercury porosimetry of hardened cement pastes, 29 (1999) 933–943.

[13] F. Moro, H. Böhni, Ink-Bottle Effect in Mercury Intrusion Porosimetry of Cement-Based Materials, J. Colloid Interface Sci. 246 (2002) 135–149. doi:10.1006/jcis.2001.7962.

[14] P. Klobes, H. Riesemeier, K. Meyer, J. Goebbels, K.-H. Hellmuth, Rock porosity determination by combination of X-ray computerized tomography with mercury porosimetry, Fresenius. J. Anal. Chem. 357 (1997) 543–547. doi:10.1007/s002160050210.

[15] A.B. Abell, K.L. Willis, D.A. Lange, Mercury intrusion porosimetry and image analysis of cement-based materials, J. Colloid Interface Sci. 211 (1999) 39–44. doi:10.1006/jcis.1998.5986.

[16] S. Diamond, A critical comparison of mercury porosimetry and capillary condensation pore size distributions of portland cement pastes, Cem. Concr. Res. 1 (1971) 531–545. doi:10.1016/0008-

8846(71)90058-5.

[17] S. Diamond, Mercury porosimetry An inappropriate method for the measurement of pore size distributions in cement-based materials, 30 (2000) 1517–1525.

[18] F. Tariq, R. Haswell, P.D. Lee, D.W. Mccomb, Characterization of hierarchical pore structures in ceramics using multiscale tomography, Acta Mater. 59 (2011) 2109–2120. doi:10.1016/j.actamat.2010.12.012.

[19] D. Winslow, S. Diamond, A mercury porosimetry study of the evolution of porosity in portland cement, ASTM J. Mater. (1970). doi:10.5703/1288284314510.This.

[20] S. Diamond, D. Bonen, Microstructure of Hardened Cement Paste—A New Interpretation, J. Am. Ceram. Soc. (1993). doi:10.1111/j.1151-2916.1993.tb06600.x.

[21] S. Diamond, Aspects of concrete porosity revisited, 29 (1999) 1181–1188.

[22] S. Lu, E.N. Landis, D.T. Keane, X-ray microtomographic studies of pore structure and permeability in Portland cement concrete, Mater. Struct. 39 (2007) 611–620. doi:10.1617/s11527-006-9099-7.

[23] K. Wan, Q. Xu, Local porosity distribution of cement paste characterized by X-ray micro-tomography, Sci. China Technol. Sci. 57 (2014) 953–961. doi:10.1007/s11431-014-5513-5.

[24] A. du Plessis, B.J. Olawuyi, W.P. Boshoff, S.G. le Roux, Simple and fast porosity analysis of concrete using X-ray computed tomography, Mater. Struct. 49 (2016) 553–562. doi:10.1617/s11527-014-0519-9.

[25] M. Lanzón, V. Cnudde, T. de Kock, J. Dewanckele, X-ray microtomography (μ-CT) to evaluate microstructure of mortars containing low density additions, Cem. Concr. Compos. 34 (2012) 993–1000. doi:10.1016/j.cemconcomp.2012.06.011.

[26] V. Cnudde, J.A.N. Dewanckele, M. Boone, T. De Kock, M. Boone, L. Brabant, M. Dusar, M.D.E. Ceukelaire, H.D.E. Clercq, R. Hayen, P. Jacobs, High-Resolution X-Ray CT for 3D Petrography of Ferruginous Sandstone for an Investigation of Building Stone Decay, 1017 (2011) 1006–1017. doi:10.1002/jemt.20987.

[27] M. Lanzón, V. Cnudde, T. De Kock, J. Dewanckele, A. Piñero, X-ray tomography and chemical-physical study of a calcarenite extracted from a Roman quarry in Cartagena (Spain), Eng. Geol. 171 (2014) 21–30. doi:10.1016/j.enggeo.2013.12.007.

[28] S. Hemes, G. Desbois, J.L. Urai, B. Schröppel, J.-O. Schwarz, Multi-scale characterization of porosity in Boom Clay (HADES-level, Mol, Belgium) using a combination of X-ray μ-CT, 2D BIB-SEM and FIB-SEM tomography, Microporous Mesoporous Mater. 208 (2015) 1–20. doi:10.1016/j.micromeso.2015.01.022.

[29] S. Peng, Q. Hu, S. Dultz, M. Zhang, Using X-ray computed tomography in pore structure characterization for a Berea sandstone : Resolution effect, J. Hydrol. 472–473 (2012) 254–261. doi:10.1016/j.jhydrol.2012.09.034.

[30] V. Brunello, C. Corti, A. Sansonetti, C. Tedeschi, L. Rampazzi, Non-invasive FTIR study of mortar model samples: comparison among innovative and traditional techniques, Eur. Phys. J. Plus. 134 (2019) 270. doi:10.1140/epjp/i2019-12667-1.

[31] Ente italiano di normazione, UNI EN 196-1 Determinazione delle resistenze meccaniche, (1996).

[32] J. Vlassenbroeck, M. Dierick, B. Masschaele, V. Cnudde, L. Van Hoorebeke, P. Jacobs, Software tools for quantification of X-ray microtomography at the UGCT, 580 (2007) 442–445.

doi:10.1016/j.nima.2007.05.073.

[33] L. Brabant, J. Vlassenbroeck, Y. De Witte, V. Cnudde, M.N. Boone, J. Dewanckele, L. Van Hoorebeke, Three-Dimensional Analysis of High-Resolution X-Ray Computed Tomography Data with Morpho+, Microsc. Microanal. 17 (2011) 252–263. doi:10.1017/S1431927610094389.

[34] B.C. Masschaele, V. Cnudde, M. Dierick, P. Jacobs, UGCT : New X-ray radiography and tomography facility, 580 (2007) 266–269. doi:10.1016/j.nima.2007.05.099.

[35] B. Masschaele, M. Dierick, D. Van Loo, M.N. Boone, HECTOR : A 240kV micro-CT setup optimized for HECTOR : A 240kV micro-CT setup optimized for research, (2013). doi:10.1088/1742-6596/463/1/012012.

[36] M. Arandigoyen, B. Bicer-Simsir, J.I. Alvarez, D.A. Lange, Variation of microstructure with carbonation in lime and blended pastes, Appl. Surf. Sci. 252 (2006) 7562–7571. doi:10.1016/j.apsusc.2005.09.007.

[37] M. Arandigoyen, J.I. Alvarez, Blended pastes of cement and lime: Pore structure and capillary porosity, Appl. Surf. Sci. 252 (2006) 8077–8085. doi:10.1016/j.apsusc.2005.10.019.

Thin section analysis

Mortars composed by one specific binder and aggregate

The thin sections of samples containing one binder with the aggregate were used as reference, to help the identification of the mineralogical phases in blended mortars. In the following paragraph the most significant results are shown and discussed.

The mortars made with lime binder (hydrated lime and lime putty GM and GQ) present a brownish binder both in ppl (plane polarized light) and xpl (cross polarized light) images (figures 78, 79, 80 and 81).

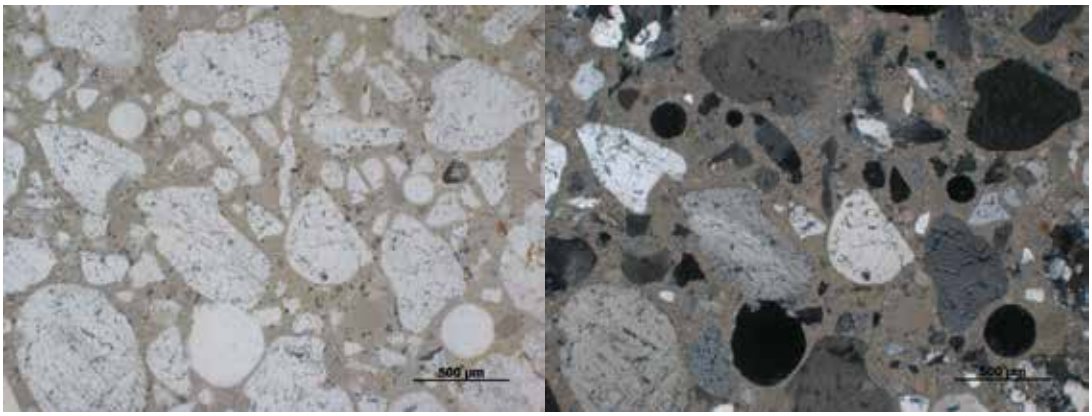

▲ *Figure 79. Images ppl and xpl of hydrated lime and quartz sand (CQ), scale bar 500µm.*

Moreover, the quartz sand size is medium to coarse and poor moderately sorted, the grains are rounded, and equant to elongated. In some cases, metamorphic quartz is visible (polycrystalline metamorphic quartz) (right bottom corner in figure 79). The pores are almost spherical (air voids). Also some lumps are identified in the binder matrix (figure 80). Lumps are a mass of binder that is not well mixed with the mix.

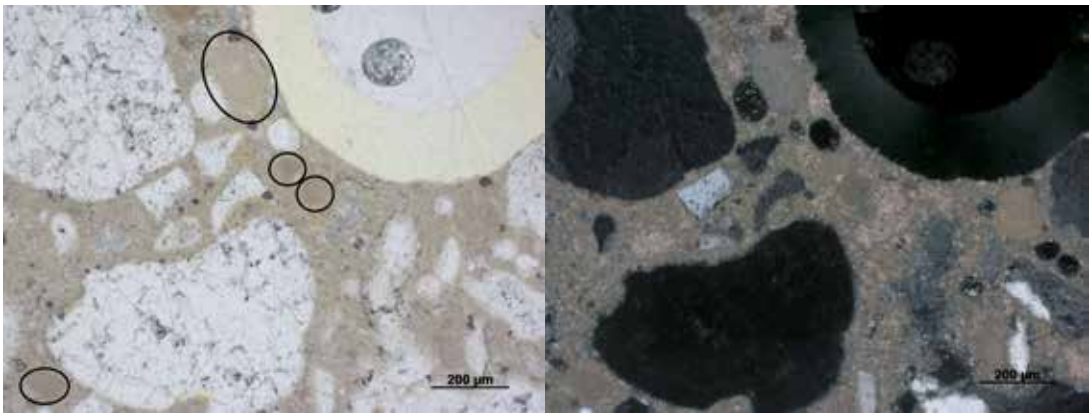

▲ *Figure 80. Images in ppl and xpl. Some lumps (highlighted by the circles) are present in the binder in sample CQ (hydrated lime and quartz sand), scale bar 200µm.*

The carbonate sand is poorly sorted and some calcite crystals are twined, as it is visible in xpl images (figures 81, 82 and 83). The carbonate sand grains have a heterogeneous texture, showing sub-angular, equant, irregular and elongate shapes.
Pores are rounded and irregular, also occasionally sub-angular. Some lumps are clearly visible in the binder matrix also in CM specimens (figure 82).

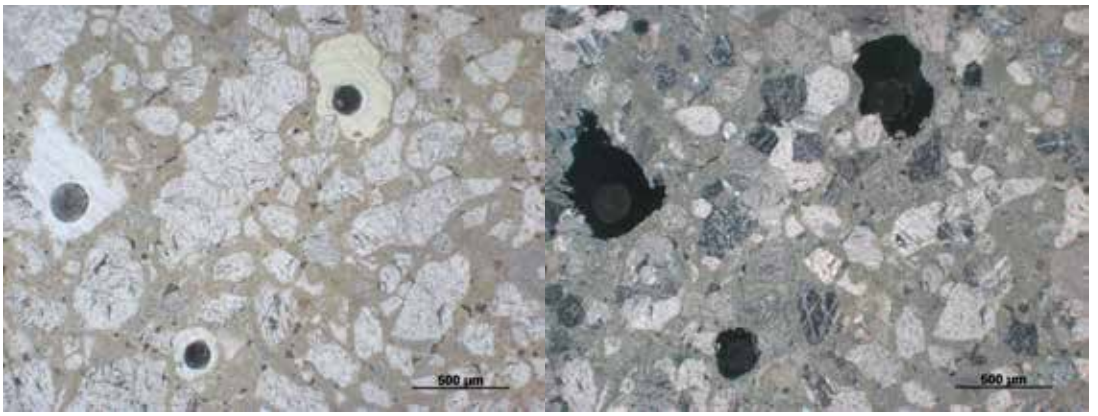

▲ *Figure 81. Images in ppl and xpl modes of sample CM (hydrated lime and carbonate sand), scale bar 500µm.*

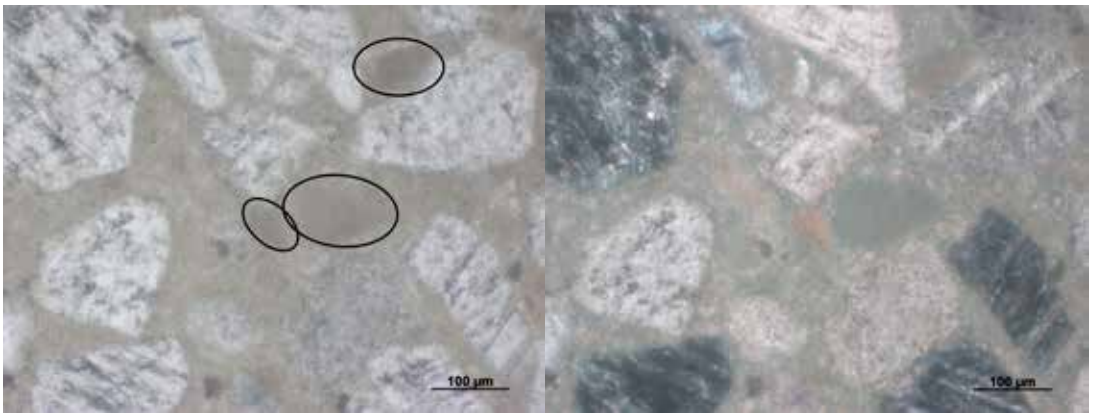

▲ *Figure 82. Images in ppl and xpl. Some lumps (highlighted by the circles) are present in the binder of sample CM (hydrated lime and carbonate sand), scale bar 100µm.*

The specimens with only lime putty with quartz or carbonate sand (GM and GQ) present several cracks in the lime binder (figures 83 and 84). The quartz sand presents rounded, moderately sorted aggregate with equant and elongate grains. Probably a feldspar grain (pink in xpl) is visible too in figure 83. The carbonate sand is moderately sorted and some calcite crystals are twined, as it is visible in xpl images. Pores are irregular.

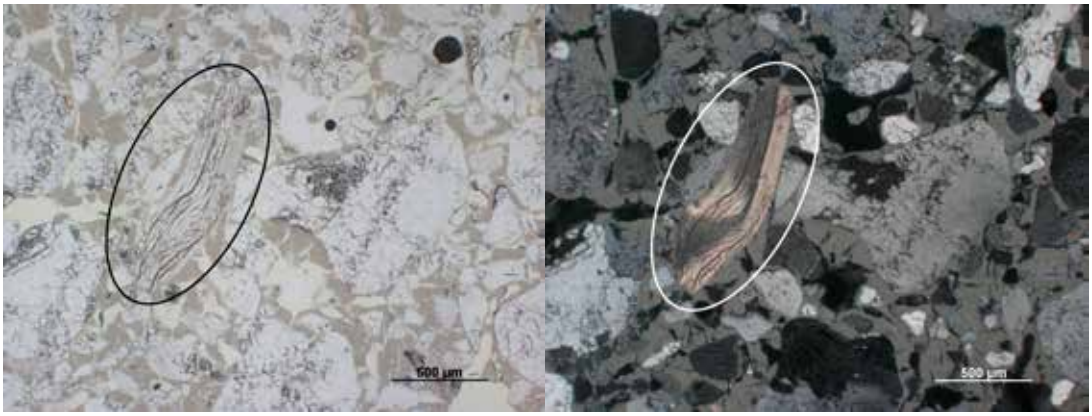

▲ *Figure 83. Ppl and xpl images of specimen GQ (lime putty and quartz sand), the feldspar grain is highlighted by the circles, scale bar 500µm.*

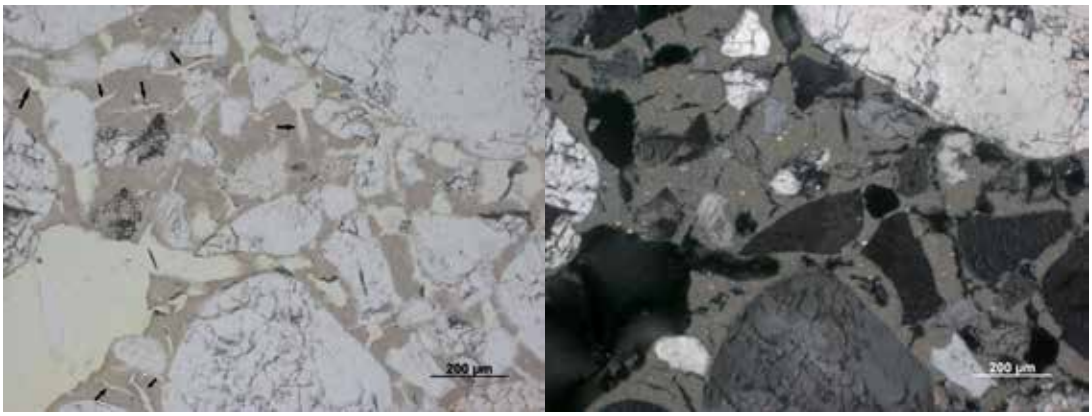

▲ *Figure 84. Ppl and xpl images of specimen GQ (lime putty and quartz sand) scale bar 200µm.*

Details of the sample where some shrinkage cracks are clearly visible in the binder are shown in figures 83, 83 (arrows) and 85. The cracks are present also in the other sample made with lime putty, GM (figure 85). The phenomenon is probably due to a rapid hardening, to the lack of binder and due to shrinkage during drying. This phenomenon could happen in lime putty mortars because lime putty contains a big amount of free water, especially if compared to hydrated lime. As the proportions were made on weight and lime putty is already wet weighing more than a powder, the volumetric amount of lime putty is probably lower compared to other binders.

The aerial mortars made with gypsum (GsQ and GsM) appear darker and grayish in xpl images, if compared to lime binders (figure 86-87). The binder appears so darker probably because it is composed by very small crystals of gypsum (figure 87). Anhydrite crystals are visible in the gypsum binder, for example in the right bottom angle of figure 87. In figure 88, 89 and 90 thermo-anhydrite is visible (it is usually found in modern high temperature gypsum). Anhydrite is easily distinguishable because of the high interference colors in cross polarized light [1].

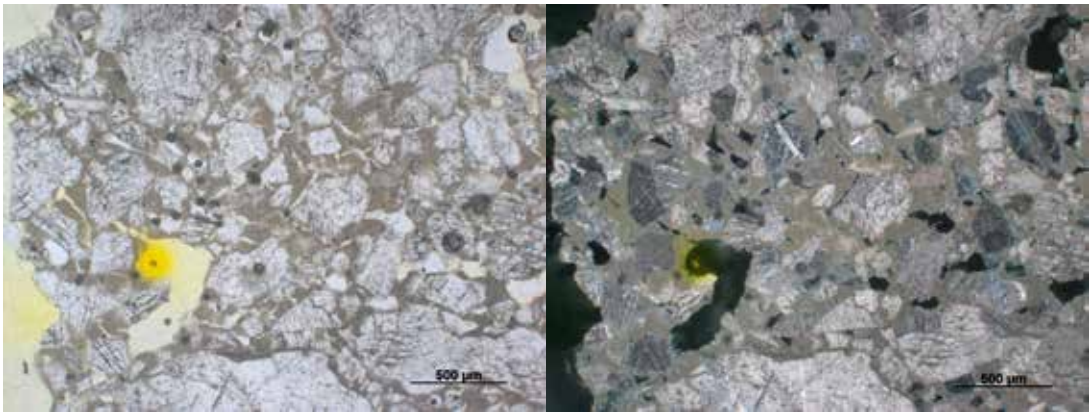

▲ *Figure 85. Images in ppl and xpl mode of sample GM (lime putty and carbonate sand), scale bar 500µm.*

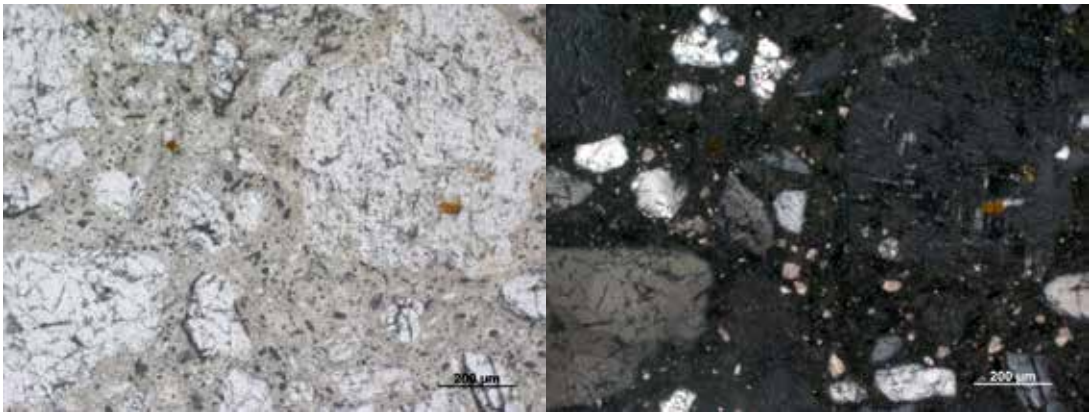

▲ *Figure 86. Images in ppl and xpl mode of sample GsQ (gypsum and quartz sand), scale bar 200µm.*

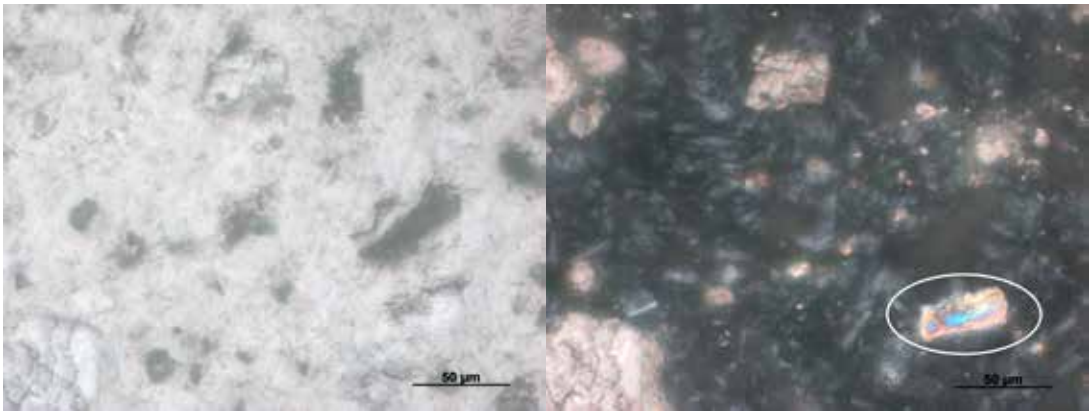

▲ *Figure 87. Images of sample GsM (gypsum and carbonate sand) in ppl and xpl of gypsum binder where are visible gypsum crystals and anhydrite crystals (bottom right circle), scale bar 50µm.*

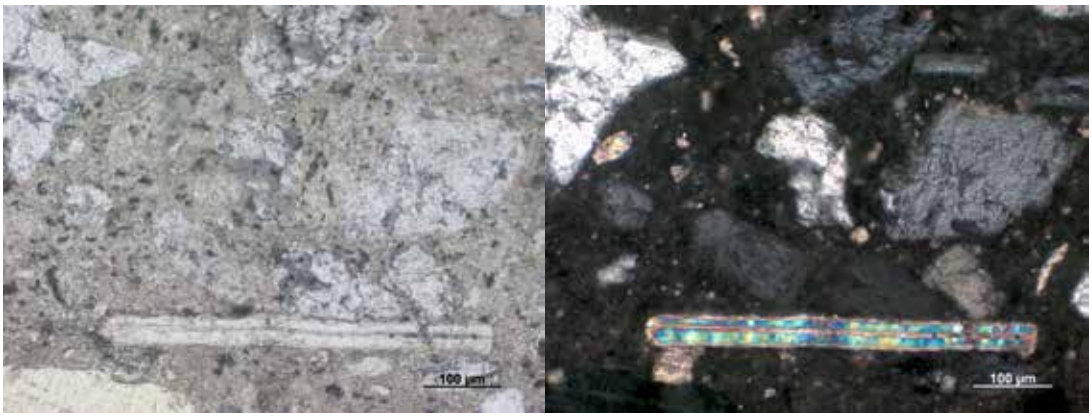

▲ *Figure 88. Images (ppl and xpl) of sample GsQ. On the bottom a crystal of thermo-anhydrite is well visible, scale bar 100µm.*

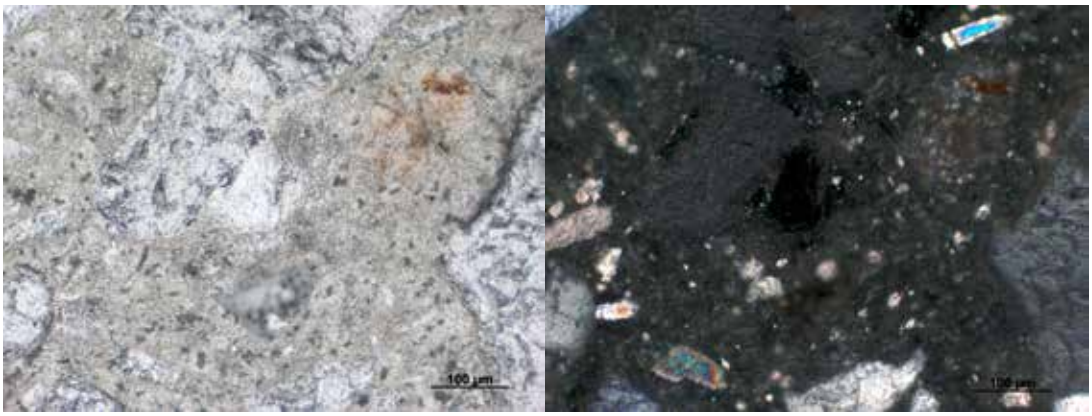

▲ *Figure 89. Images (ppl and xpl) of sample GsQ (gypsum and quartz sand). On the top and on the bottom some crystals of anhydrite are well visible, scale bar 100µm.*

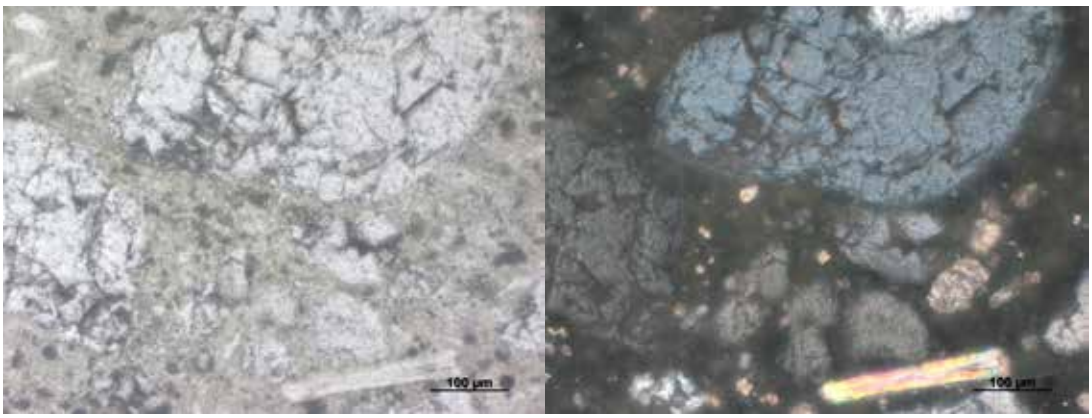

▲ *Figure 90. Images (ppl and xpl) of sample GsQ (gypsum and quartz sand). On the bottom a crystal of thermo-anhydrite is well visible, scale bar 100µm.*

Concerning the cement mortars (CIQ, CIM, CIVQ and CIVM), cement binders (dark brown) are darker than lime binder. A carbonation rim is well visible near the border in xpl images (figures 91 - 95), and near the air voids in figure 93. It is lighter than the other part of the binder. Some examples are the following images where the rims appear clearer and brownish if compared to the bulk of the samples. The quartz aggregate size is medium to coarse, poorly sorted, equant to elongate, and also polycrystalline metamorphic quartz is present. Pores are almost spherical.
Carbonate sand aggregate is sub-angular, from equant to irregular. Pores are sub-rounded and irregular. The aggregate is poorly sorted and some crystals are twined (figure 95). Dark small crystals are probably part of unhydrated clinker particles and they are visible in all the samples with cement (figures 96 and 97). In mortars with pozzolanic cement (CEM IV) also the presences of fly ashes have been evidenced as it is visible in figures 98 and 99.

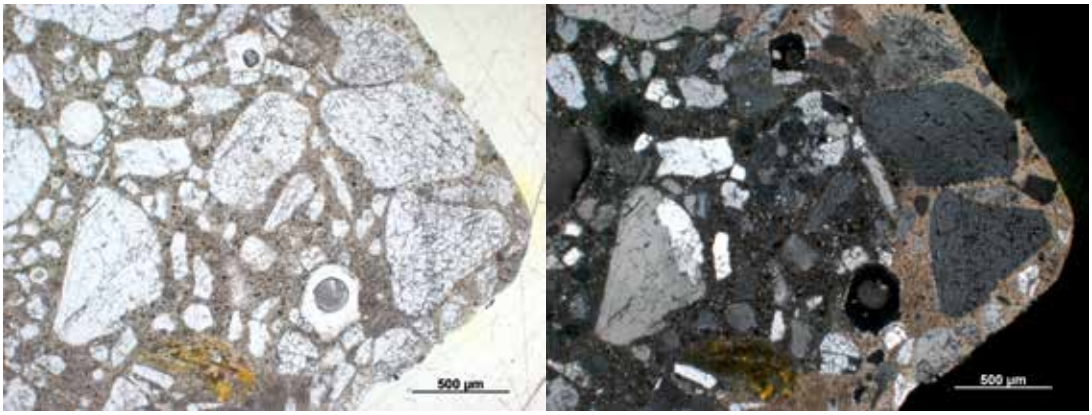

▲ *Figure 91. Images (ppl and xpl) of sample CIQ (CEM I and quartz sand), scale bar 500µm.*

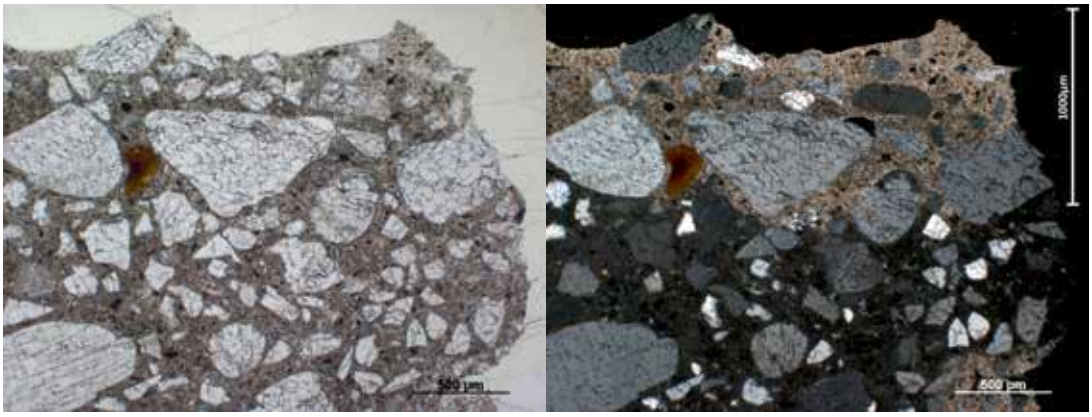

▲ *Figure 92. Images (ppl and xpl) of specimen CIVQ (CEM IV and quartz sand), scale bar 500µm.*

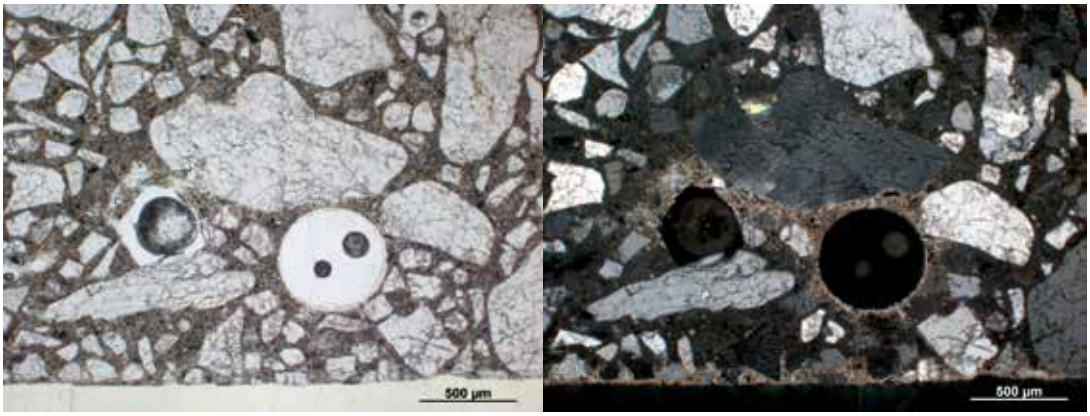

▲ *Figure 93. Images (ppl and xpl) of specimen CIVQ (CEM IV and quartz sand), scale bar 500µm.*

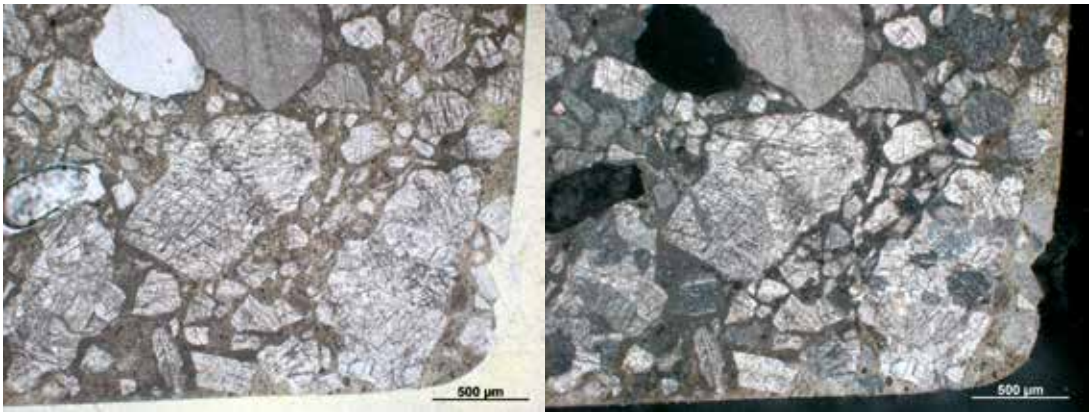

▲ *Figure 94. Images (ppl and xpl) of specimen CIM (CEM I and carbonate sand), scale bar 500µm.*

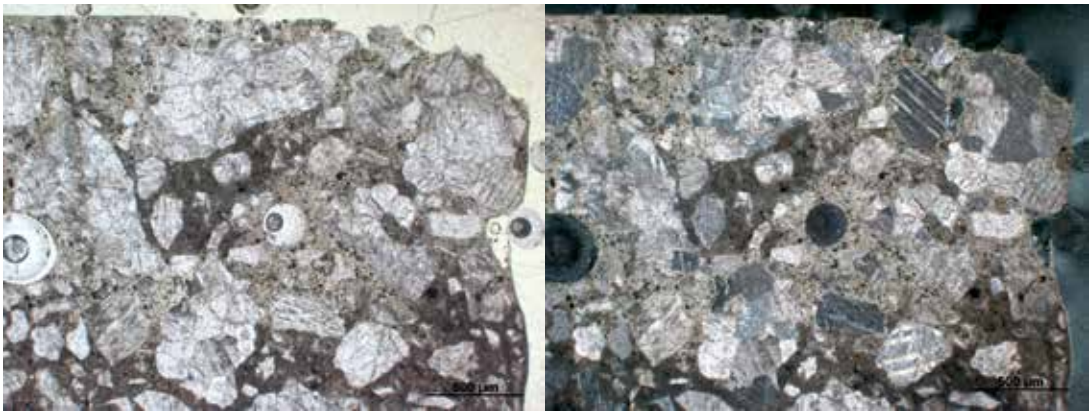

▲ *Figure 95. Images (ppl and xpl) of specimen CIVM (CEM IV and carbonate sand), scale bar 500µm.*

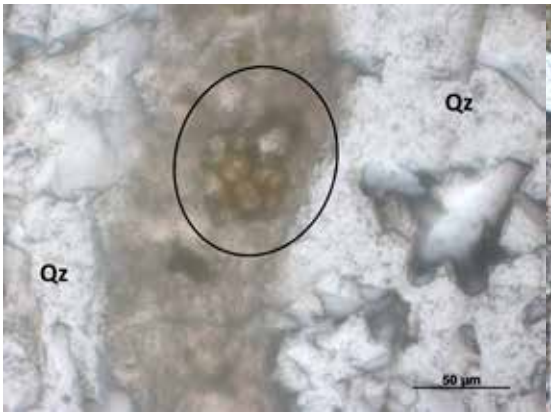

▲ *Figure 96. Image of clinker relict (in the circle), unhydrated in sample CIQ (CEM I and quartz sand), scale bar 50µm.*

▲ *Figure 97. Image of gray particles of unhydrated cement in sample CIM (CEM I and carbonate sand), scale bar 100µm.*

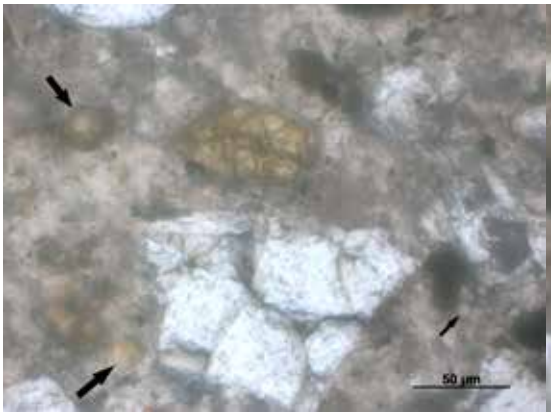

▲ *Figure 98. Ppl image of sample CIVQ where some fly ashes (arrows) and clinker particles unhydrated are visible in the binder, scale bar 50µm.*

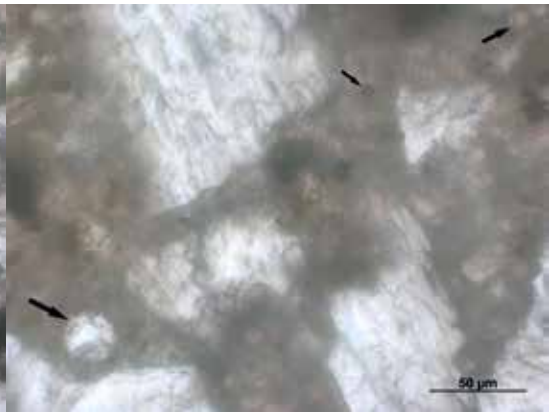

▲ *Figure 99. Ppl image of sample CIVM where some fly ashes (arrows) are visible in the binder, scale bar 50µm.*

The natural hydraulic lime (NQ and NM) shows a reddish binder probably due to the presence some Fe-oxide components like hematite as confirmed by Raman analysis of the raw materials paragraph (Raman spectroscopy and micro infrared reflection spectroscopy (µ-FTIR) paragraph). Some red particles were observed in the binder fraction, that could be residues contained in the raw materials (figure 100). Moreover, some gray crystals were observed, that could be some unhydrated calcium silicates present in the material (figures 101 and 102).

The aggregate is composed by a quartz sand which is poorly sorted and by carbonate sand that is sub-angular from equant to irregular, with some elongated carbonate grains. Pores are sub-rounded and irregular. The samples with carbonate sand were less cohesive, so it was more difficult to obtain a reliable thin section (figure 103).

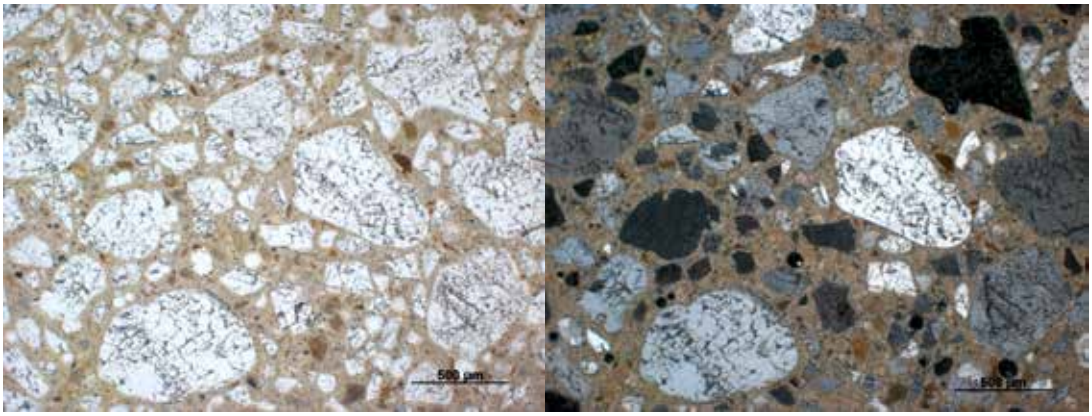

▲ *Figure 100. Images (ppl and xpl) of natural hydraulic lime mortars samples with quartz sand (NQ), scale bar 500µm.*

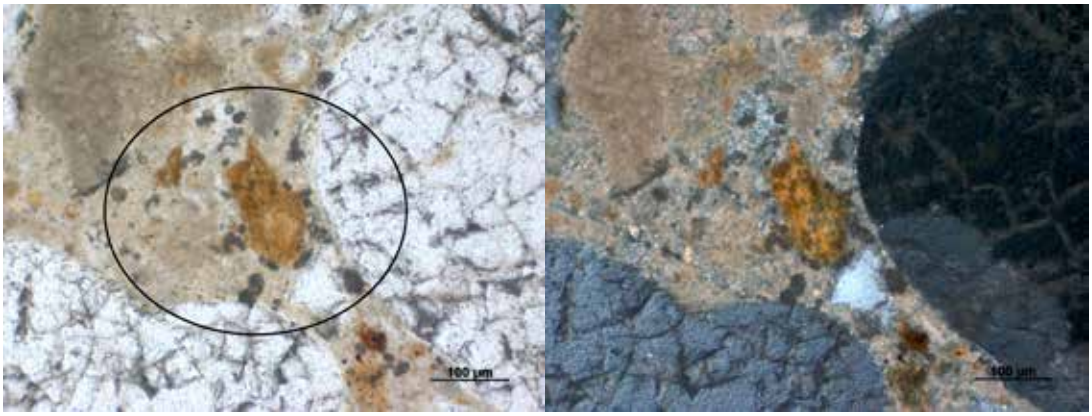

▲ *Figure 101. Images (ppl and xpl) of reddish particles with some gray crystals, probably a part of hydraulic grains in (NQ), scale bar 100µm.*

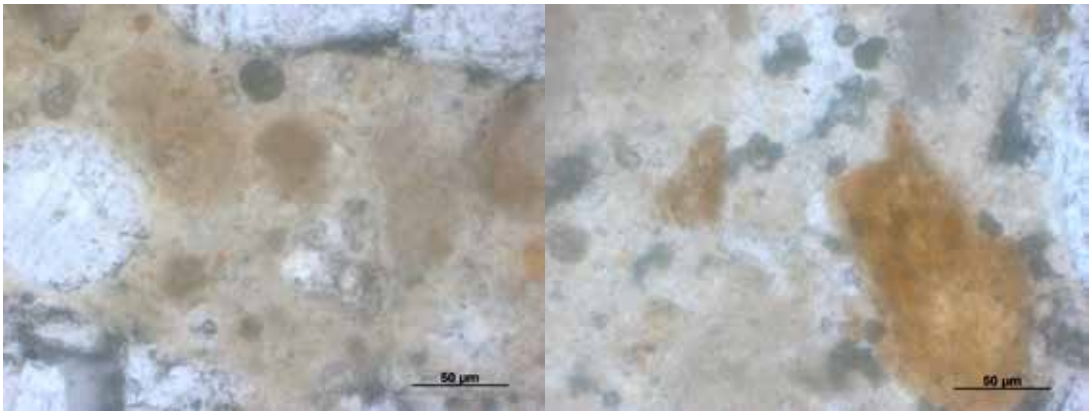

▲ *Figure 102. Images (ppl) of natural hydraulic lime samples. Red particles and gray particles are visible in the images (NQ), scale bar 50µm.*

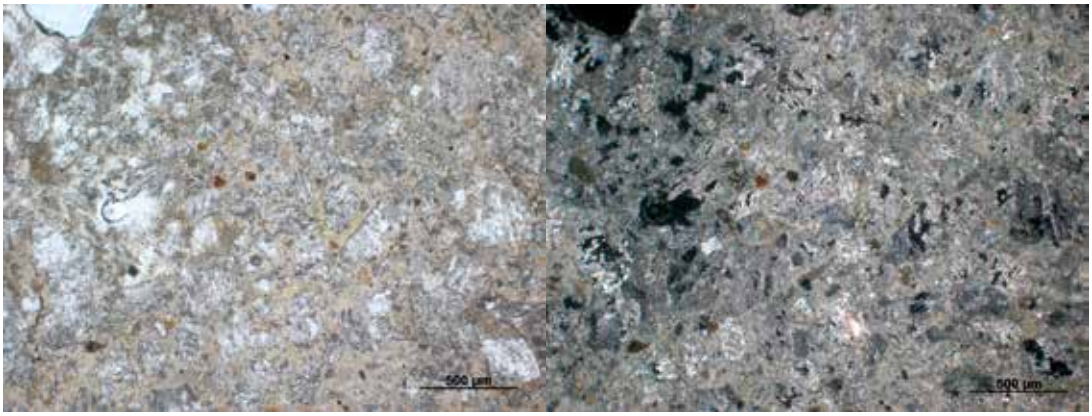

▲ *Figure 103. Ppl and xpl images of the specimen made by natural hydraulic lime 3.5 and carbonate sand (NM), scale bar 500µm.*

Mortars composed by two specific binders and one specifc aggregate

Mortars made by lime (hydrated lime or lime putty) and gypsum (CGsM, CGsQ, GGsM and GGsQ) as binder present a brownish color in ppl images, with some of the black particles already seen in gypsum binder which nature is not identified. Moreover, in xpl mode the binder becomes dark, similarly to what observed for gypsum binders (Thin section analysis of mortars composed by one specific binder and aggregate paragraph). Anhydrite is present too, for the interference colors in xpl images (figure 104-5). In addition, some lumps of lime are visible in the binder matrix (figures 106-7). In figure 104, near the border it is possible to observe a thick lighter layer (about 15μm) that could be due the presence of calcium carbonate. The carbonate aggregate shows some sub-angular from equant to irregular and some elongate twined carbonate grains, while the quartz sand is rounded and poorly sorted from equant to elongate (figure 108). The aggregate sand features just discussed have been observed in all the samples (figures 104-108) [1–4].

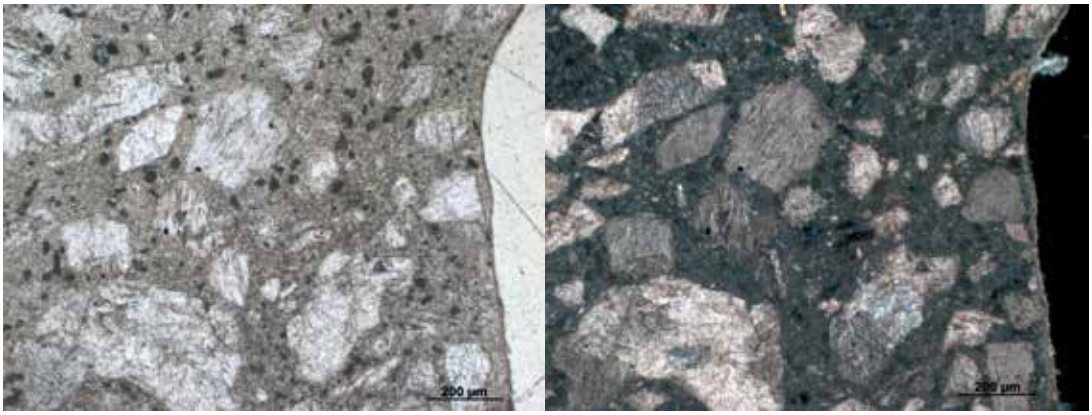

▲*Figure 104. Images in ppl and xpl mode of sample CGsM (hydrated lime, gypsum and carbonate sand), scale bar 200μm.*

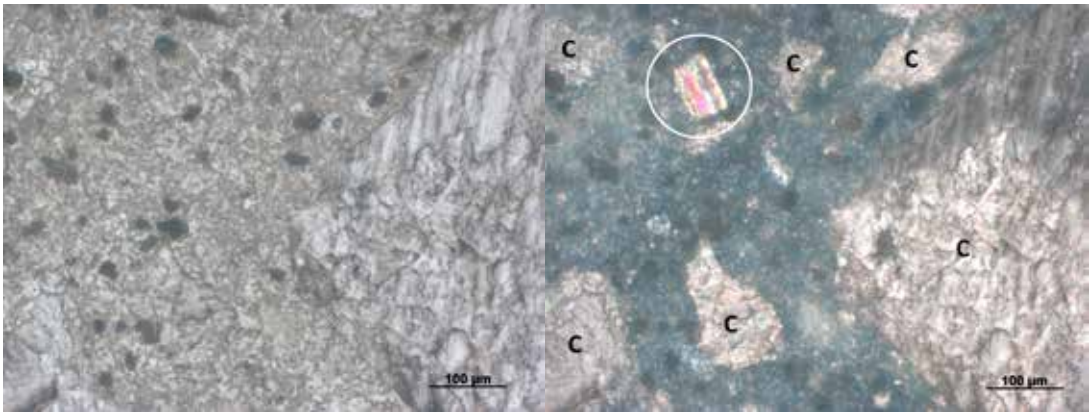

▲*Figure 105. Images ppl and xpl mode of sample CGsM (hydrated lime, gypsum and carbonate sand (C in the photo)), scale bar 100μm.*

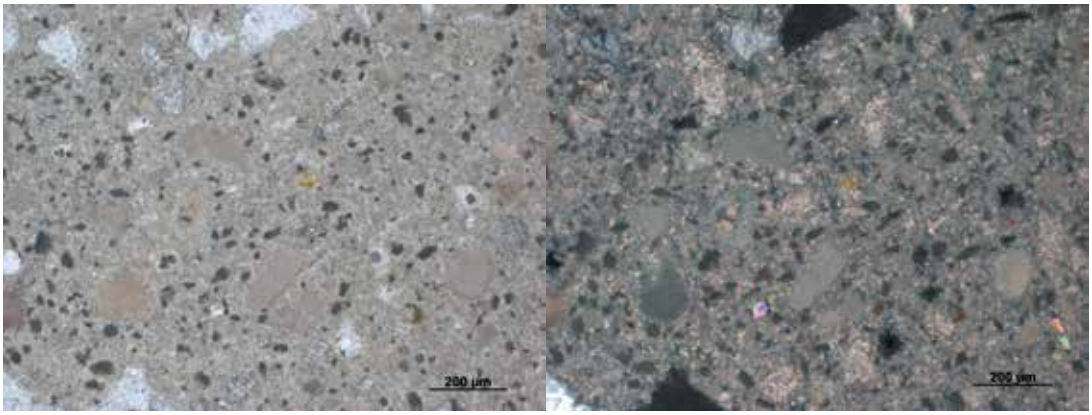

▲ *Figure 106. Images in ppl and xpl mode of sample CGsQ (hydrated lime, gypsum and quartz sand), scale bar 200µm.*

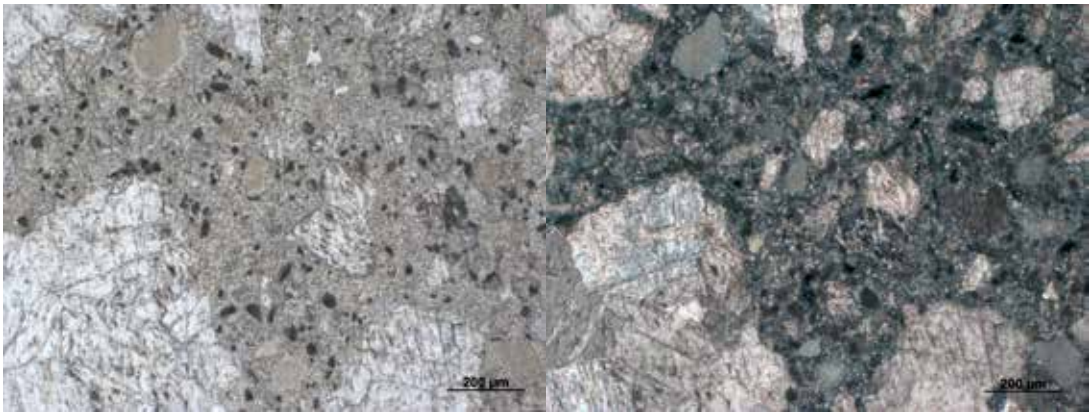

▲ *Figure 107. Images in ppl and xpl mode of sample GGsM (lime putty, gypsum and carbonate sand), scale bar 200µm.*

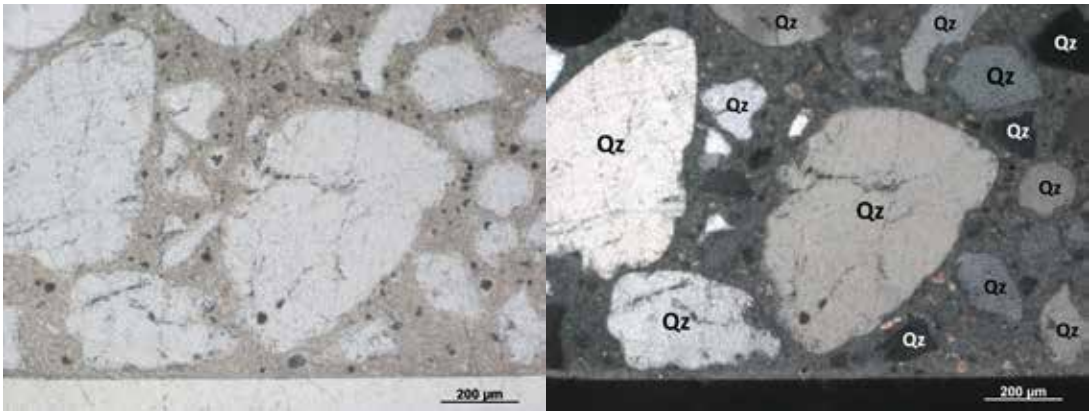

▲ *Figure 108. Ppl and xpl images of sample GGsQ (lime putty, gypsum and quartz sand (Qz in the photo)), scale bar 200µm.*

In mixed mortars prepared with cement, unhydrated cement clinker relicts were identified in each sample (figures 109-12, and figures 113 and 115) helping the identification of cement binder. Some fly ash spheres have been observed in mortars with pozzolanic cement (figure 111, 114 and 116). In some cases the carbonation rim near the border of the mortars was clearly visible (figure 117).

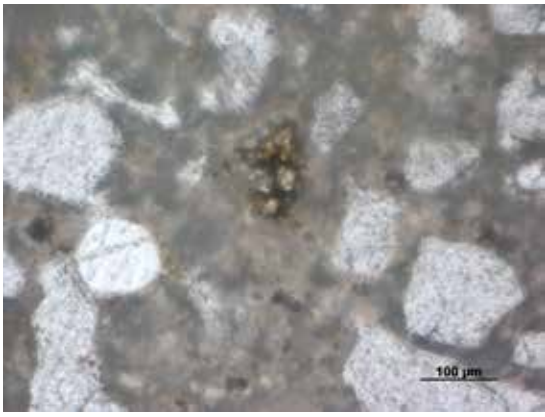

▲*Figure 109. Ppl image of unhydrated clinker in mortar CCIQ (hydrated lime, CEM I and quartz sand), scale bar 100µm.*

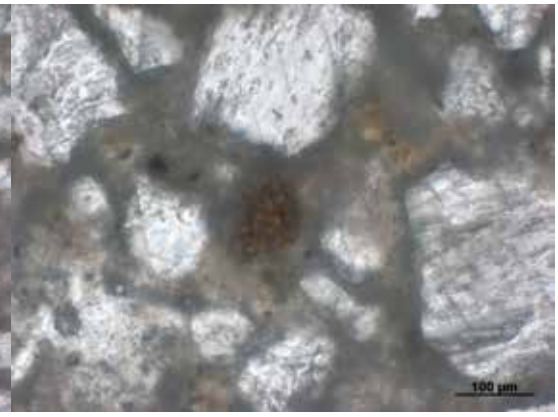

▲*Figure 110. Ppl image of unhydrated clinker in mortar CCIVM (hydrated lime, CEM IV and carbonate sand), scale bar 100µm.*

▲*Figure 111. Ppl image of unhydrated clinker (circle) and fly ash (arrows) in mortar CCIVQ (hydrated lime, CEM IV and quartz sand), scale bar 50µm.*

▲*Figure 112. Ppl image of unhydrated clinker in mortar GCIM (lime putty, CEM I and carbonate sand), scale bar 50µm*

▲ *Figure 113. Ppl image of unhydrated clinker (circle) in mortar GCIVM (lime putty, CEM IV and carbonate sand), scale bar 100µm.*

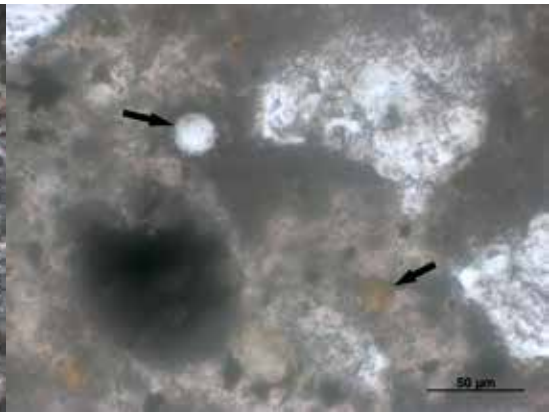

▲ *Figure 114. Ppl image of a fly ashes white and red (arrows) in mortar GCIVM (lime putty, CEM IV and carbonate sand), scale bar 50µm.*

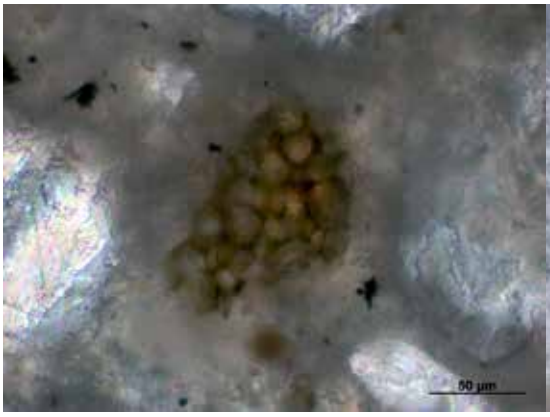

▲ *Figure 115. Ppl image of unhydrated clinker in mortar CCIVM (hydrated lime, CEM IV and carbonate sand), scale bar 50µm (zoom of figure 112).*

▲ *Figure 116. Ppl image of a red fly ash (arrow) in mortar CCIVM (hydrated lime, CEM IV and carbonate sand), scale bar 50µm.*

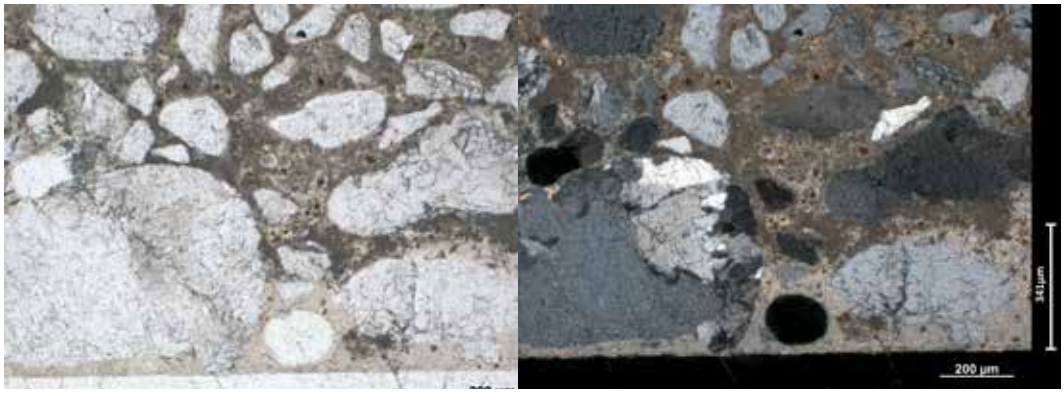

▲ *Figure 117. Ppl and xpl image of the carbonation rim in cross sections of mortar GCIQ (lime putty, CEM I and quartz sand), scale bar 200µm.*

The samples taken from the mixed mortars with hydraulic lime, lime putty and natural hydraulic lime show reddish particles in the binder matrix. The pores are almost spherical, as in the mortars made with cement. In some cases, some cracks are visible in the binder (figures 118-19). The presence of some unhydrated hydraulic particles was not visualized during the analysis , except in the area shown in figure 120, where the grain in the center could be appear as unhydrated hydraulic particles but it is still uncertain [1–3].

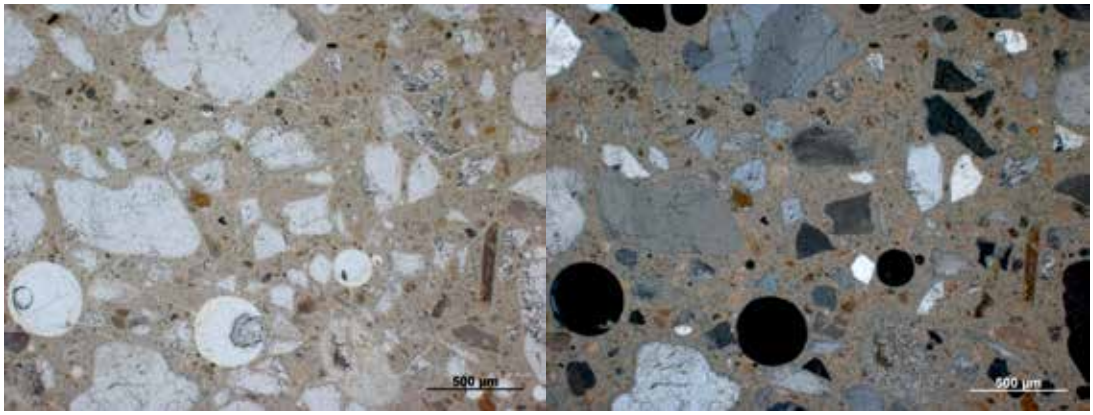

▲ *Figure 118. Images at 5x in ppl and xpl mode of GNQ (lime putty, natural hydraulic lime 3.5 and quartz sand), scale bar 500µm.*

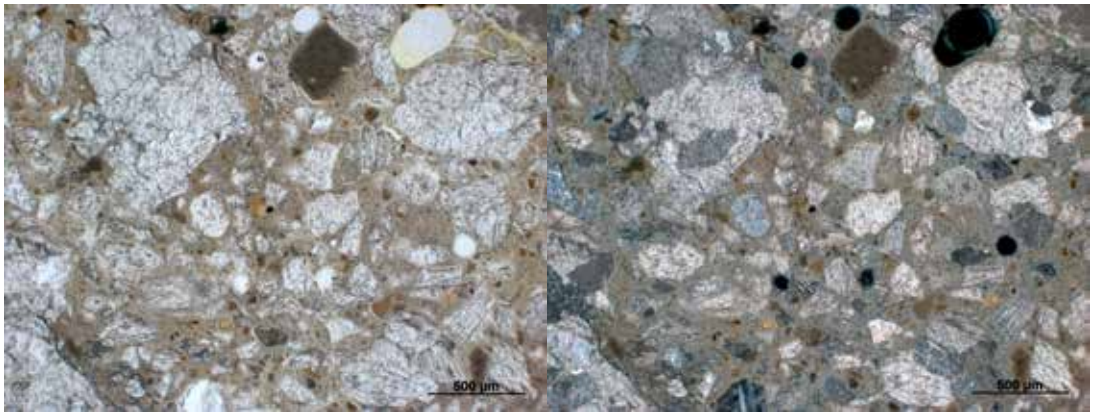

▲ *Figure 119. Images in ppl and xpl mode of GNM (lime putty, natural hydraulic lime 3.5 and carbonate sand, scale bar 500µm.*

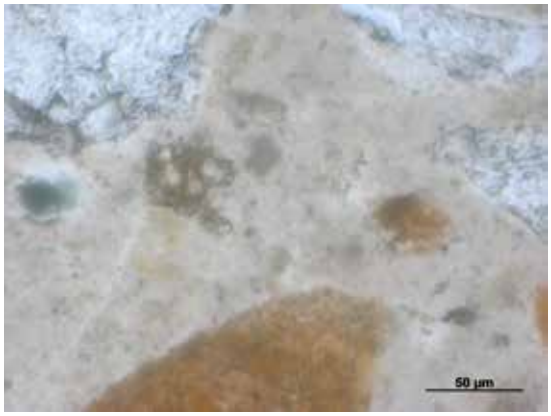

◀ *Figure 120. Image in ppl mode of GNQ (lime putty, natural hydraulic lime 3.5 and quartz sand), scale bar 50µm.*

Discussion and conclusions

Summarizing the results of thin section analysis, we can underline some advantages and drawbacks (table 47). When possible, the technique allows a good characterization of the aggregate, with the identification of the main mineralogical phases, shape and dimensions. The identification of binders in samples with one specific binder was easier than in the mortars with two specific binders, where the single components were not distinguished. In some cases, the identification of the unhydrated crystals could suggest the presence of cement, although quantification was not possible. Moreover, unhydrated cement crystals were identified in all the samples with cements, also when cements mixed with another binder.
The observation of thin sections allowed the identification of the carbonation rims near the border of the specimens that is of major concern when studying the hydration of the mortars.

Advantages	**Drawbacks**
Identification of cement unhydrated crystals, gypsum and fly ashes.	In the mortars with two specific binders, where the single components were not distinguished.
Aggregate characterization.	
It gives colour visualization of the sample.	

Table 47. Summary of the advantages and drawbacks of thin sections analysis applied to all the specimens made in this study.

References

[1] E. Pecchioni, F. Fratini, E. Cantisani, Atlas of the Ancient Mortars in thin section under optical microscope, 2014.

[2] J. Weber, F. Pintér, K. Thomas, Atlas of thin sections of minerals materials in cultural heritage, (2018).

[3] J.P. Ingham, Geomaterials under the microscope A colour guide building stone, roofing slate, aggregate, concrete, mortar, plaster, bricks, ceramics, and bituminous mixtures, Manson Publishing Ltd, 2013.

[4] P. Walker, Hollis, Lane, Stephan, Stutzman, Petrographic Methods of Examining Hardened Concrete : A Petrographic Manual, (2006) 353.

Environmental scanning electron microscopy (ESEM)

The environmental scanning electron microscopy has been applied to polished cross sections of mortars with quartz and carbonate sand made with one or two binders. It has been applied also to samples made only with hydraulic binders, because despite being widespread materials in historical mortars, the literature of reference is scarce.

Specimens composed by hydraulic binders

In figure 121, a grain of cement, from specimen CI (Portland cement), with his hydration rim, is shown. As it is possible to observe by the EDX spectra in point 1 and 2, in the rim there is a lower concentration of Ca in relation to the core of the particle. This happens because during the hydration the Ca tend to diffuse in the matrix and the EDX spectrum shows the decalcification effect of Ca-silicate grains [1]. Probably in point 1 the EDX signals are originated by different components. In fact, in figure 121 it is possible to glimpse the interstitial phase between the bright grains of Ca-silicate. It explains the presence of Fe and Al in the EDX point analysis in point 1 due the fact that the interstitial phase could be C_3A or C_4AF. In figure 122 the schematic visualization of the unhydrated/hydrate zones of the cement particle are shown.

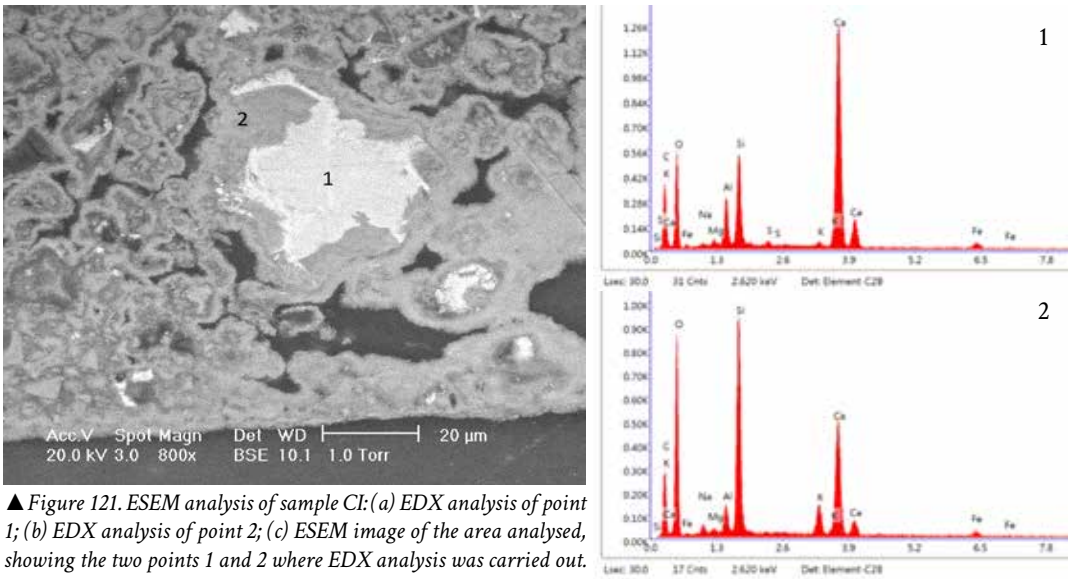

▲ *Figure 121. ESEM analysis of sample CI: (a) EDX analysis of point 1; (b) EDX analysis of point 2; (c) ESEM image of the area analysed, showing the two points 1 and 2 where EDX analysis was carried out.*

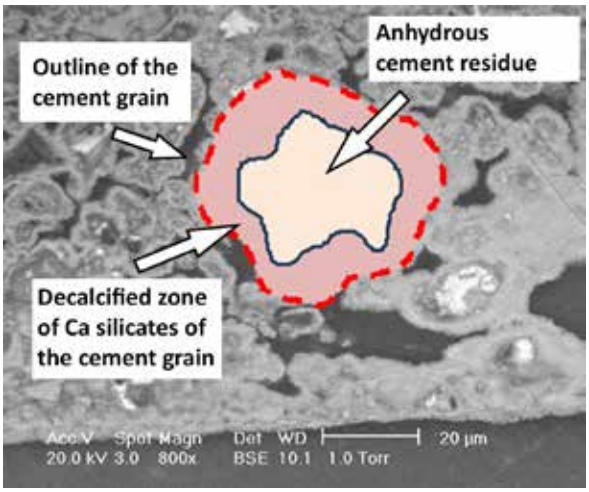

◀*Figure 122. The schematic visualization of the unhydrate/hydrate zones of the cement particle are shown, (figure 120).*

In the analysis of pozzolanic cement model sample (CIV), the fly ash particles are clearly recognizable (figure 123 a-b). The particles identified have a mixed iron/alumino-silicate composition, as it is visible in the EDX spectra, and present a dendritic pattern [1–3].

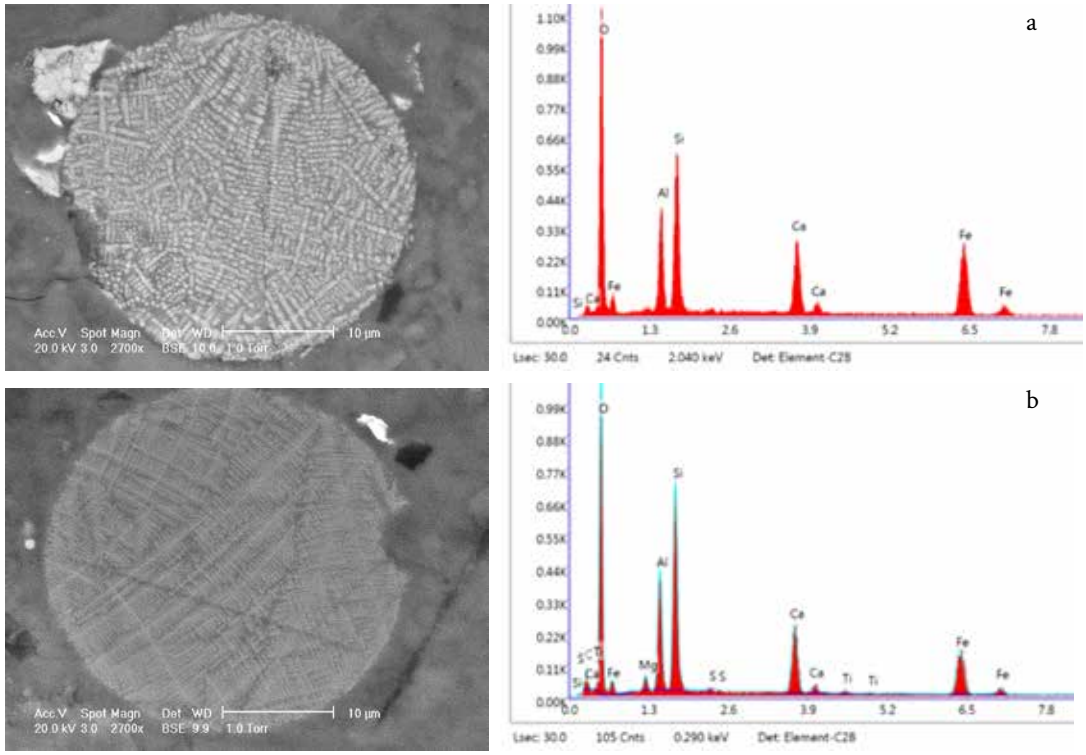

▲*Figure 123. a) and b). Iron and alumino-silicate mixed fly ash grains with dendritic pattern in the polished cross section of specimen CIV.*

In sample CIV the hydration rim that is visible around some cement particles was identified (figure 124). Probably, it is composed by hydration product such as *C-S-H* (figure 125 point 2), as suggested by EDX analysis. In fact, the brighter zone in the middle of the grain is richer in calcium (figure 125 point 1) than the rim. That means that there is a diffusion of calcium in the binder due to hydration of cement particles [1]. The relative intensities of the elements shown in figure 125 point 1, and the characteristic globular and ovoid shape of the particles suggest the presence of C_2S (Ca_2 SiO_4) crystals [1,4–10].

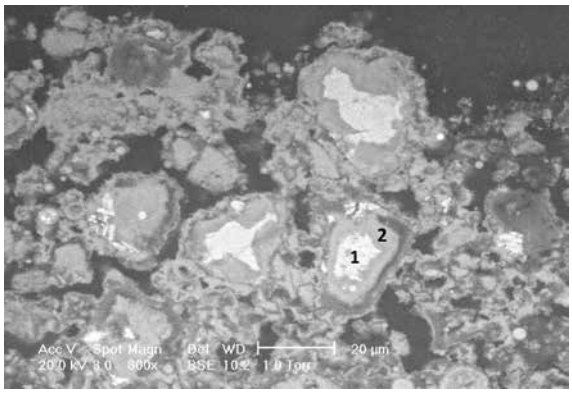

◀*Figure 124. CIV surface with cement particles partially hydrated with the hydration rim is shown.*

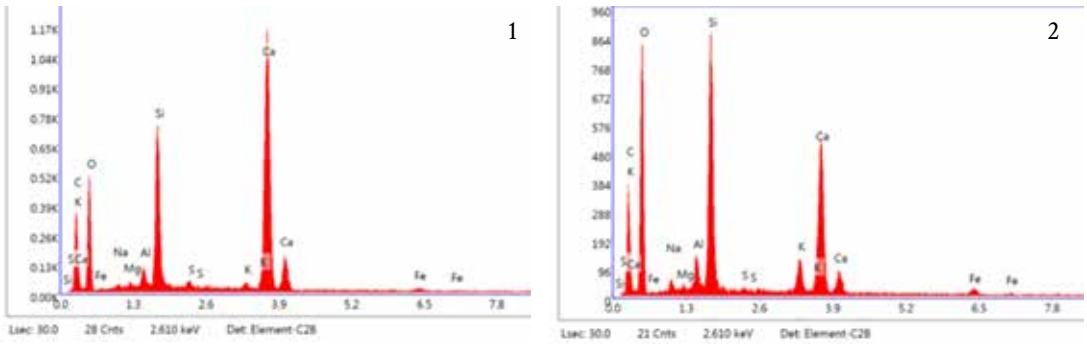

▲*Figure 125. EDX spectra collected in figure 118, in point 1 the EDX spectrum of the anhydrous cement residue is shown, while in point 2 the EDX spectrum of the decalcified zone around the Ca silicate is presented.*

The natural hydrated lime (N) specimens present a heterogeneous binder with several particles (figure 126), where Ca, Si, Al, Mg and Fe are almost equally distributed; and only in some zones a major concentration of some elements is observed (figure 127). The binder of this model sample is very heterogeneous, as shown in figure 121, considering that the image is collected on a sample without the aggregate. The Ca map distribution shows that calcium is abundant in the external layer of the sample, probably due to the carbonation of the sample (figure 127). The EDX maps of calcium, silicium and aluminum show the distribution of these elements in the matrix of the sample, that could be connected to the presence of silicate and aluminates of hydraulic phases (figure 127).

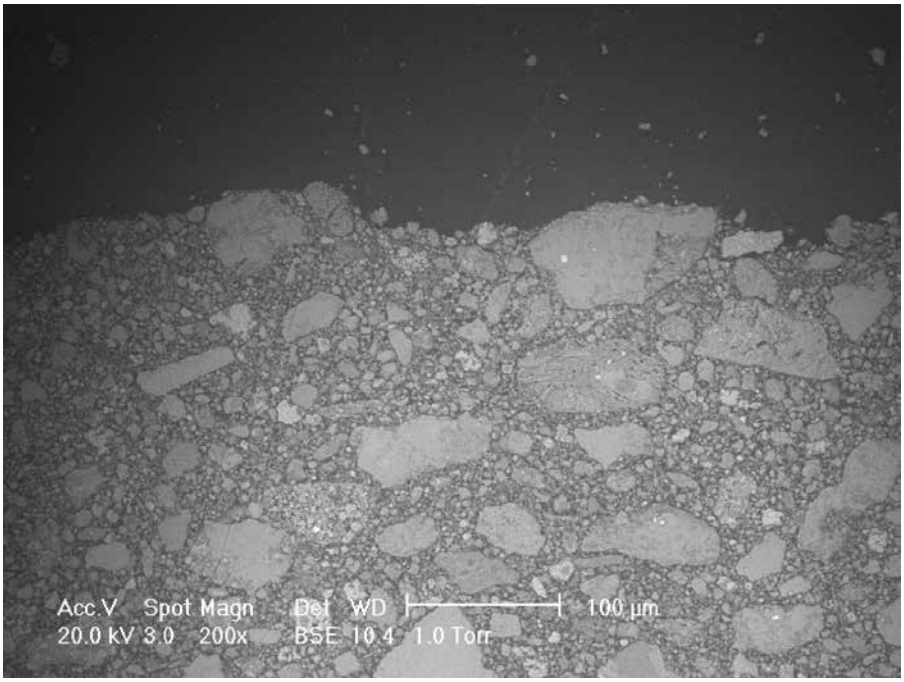

▲ *Figure 126. N (natural hydraulic lime) specimen polished cross section observed in BSE.*

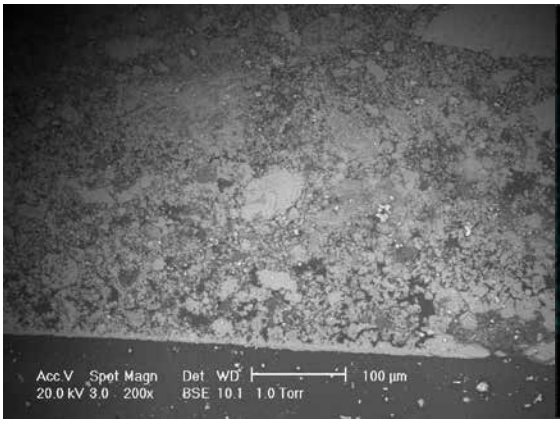

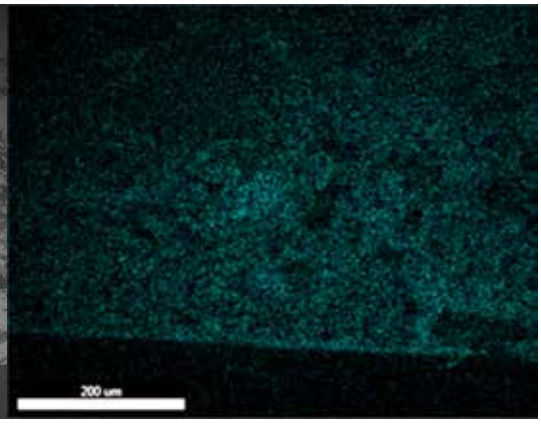

▲Ca

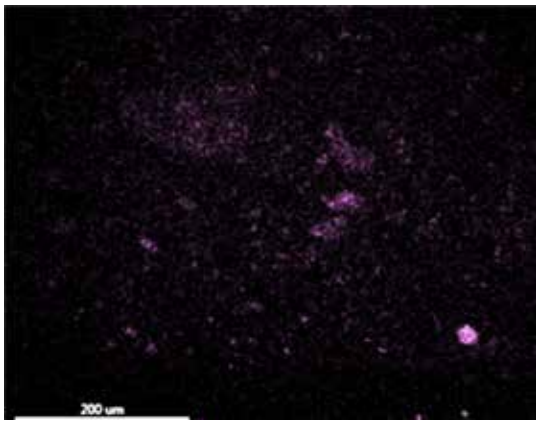

▲Si

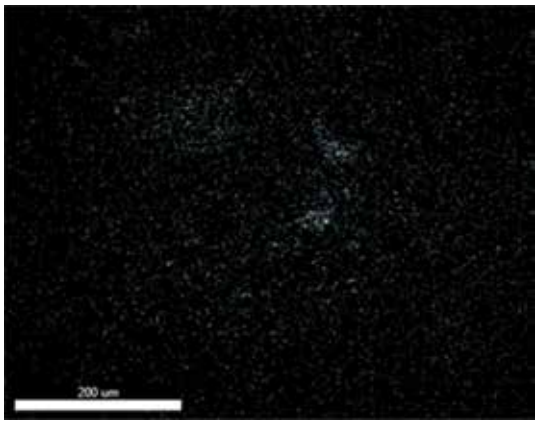

▲Al

▲*Figure 127. EDX maps of Ca, Si and Al of sample N (natural hydraulic lime figure 120) are shown.*

Mortars of mortars composed by one binder and one aggregate

In figure 128 two BSE images of the specimen containing lime putty and quartz sand (GQ) are shown. The carbonation rim near the border of the sample is visible in figure 128 (a) and (b). Furthermore, in figure 128 (b) some shrinkage cracks are well visible in the binder between the aggregate grains too; this feature was observed also in the tomography images and thin section analysis (Microstructural analysis paragraph).

In the specimens made with gypsum (GsQ and GsM) the identification easily occurs by the presence of the characteristic needles crystals (figure 129 and 130). In figure 130, the EDX point analysis shows the elemental composition of the binder (S, Ca and O) (spot 1) and also the composition of the aggregate: in spot 2 Ca, O and C are prevalent, while in spot 3 also Mg is present (as already seen in PXRD results table 16). It confirms the XRD analysis where also some phases with Mg were identified in the aggregate.

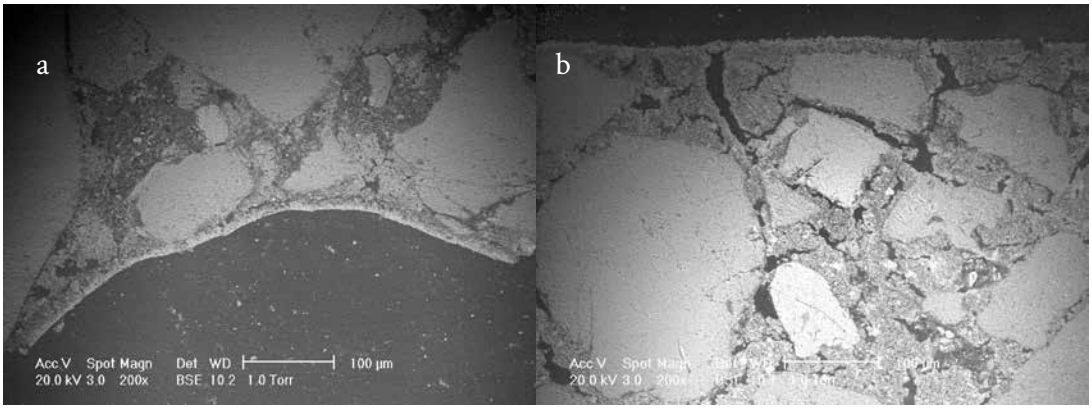

▲ *Figure 128. GQ polished cross section in BSE images. The carbonation rims (a) and some cracks (b) are visible the binder.*

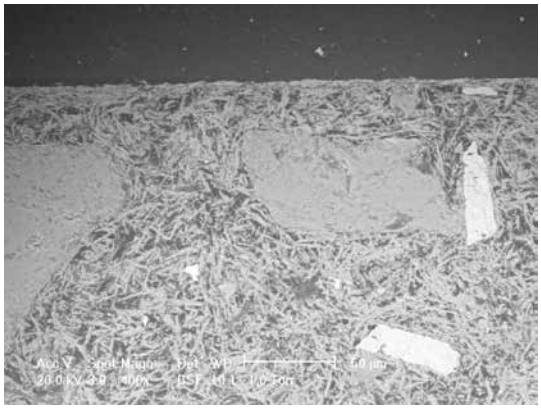

◀ *Figure 129. GsQ (gypsum and quartz sand) BSE image, the gypsum crystals needles are well visible in the binder.*

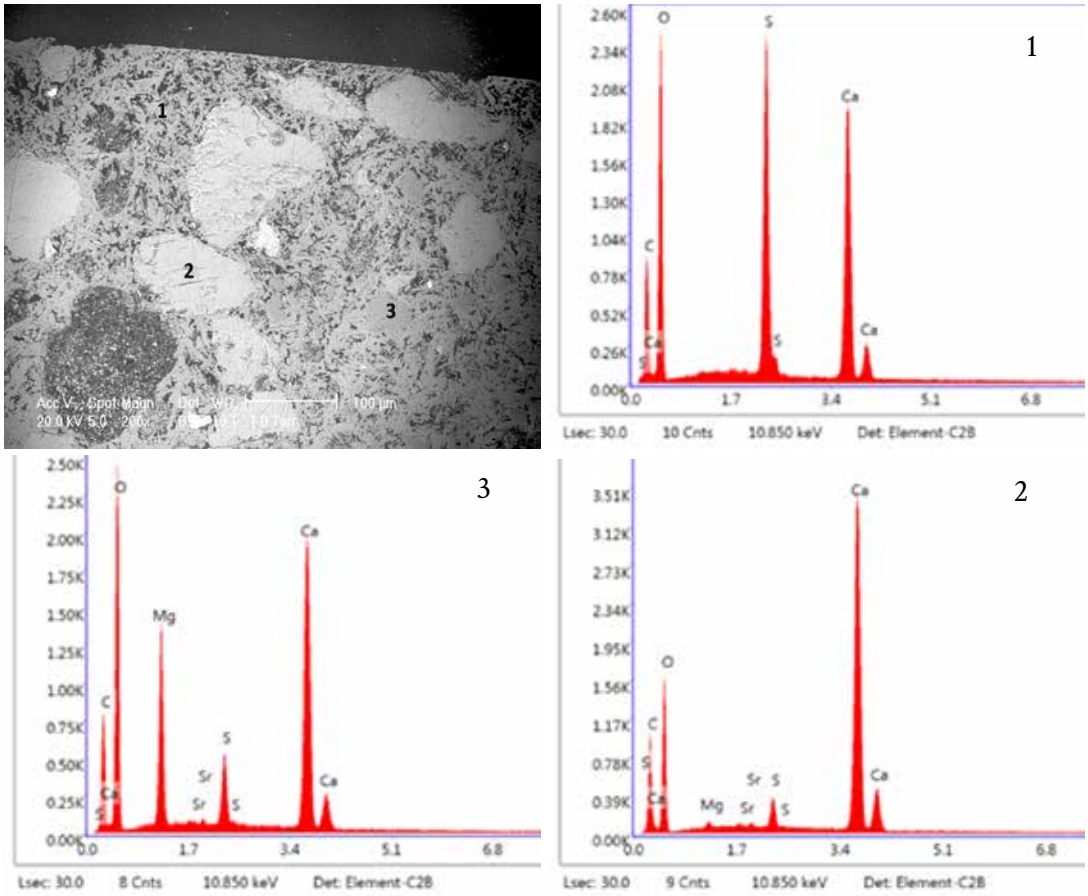

▲ *Figure 130. GsM (gypsum and carbonate sand) BSE images and EDX analysis, Mg in the aggregate is identified: 1) EDX spectrum of point 1; 2) EDX spectrum of point 2; 3) EDX spectrum of point 3.*

The aggregate grains are more clearly visible in sample NM (figure 131). Some darker zones can be observed (figure 131 point 1 and 3), in the grains that correspond to higher intensities of signals of Mg, compared to the lighter part of the grain. This is confirmed by the EDS analysis on the aggregate grain and confirm the Mg phases found in the PXRD analysis.

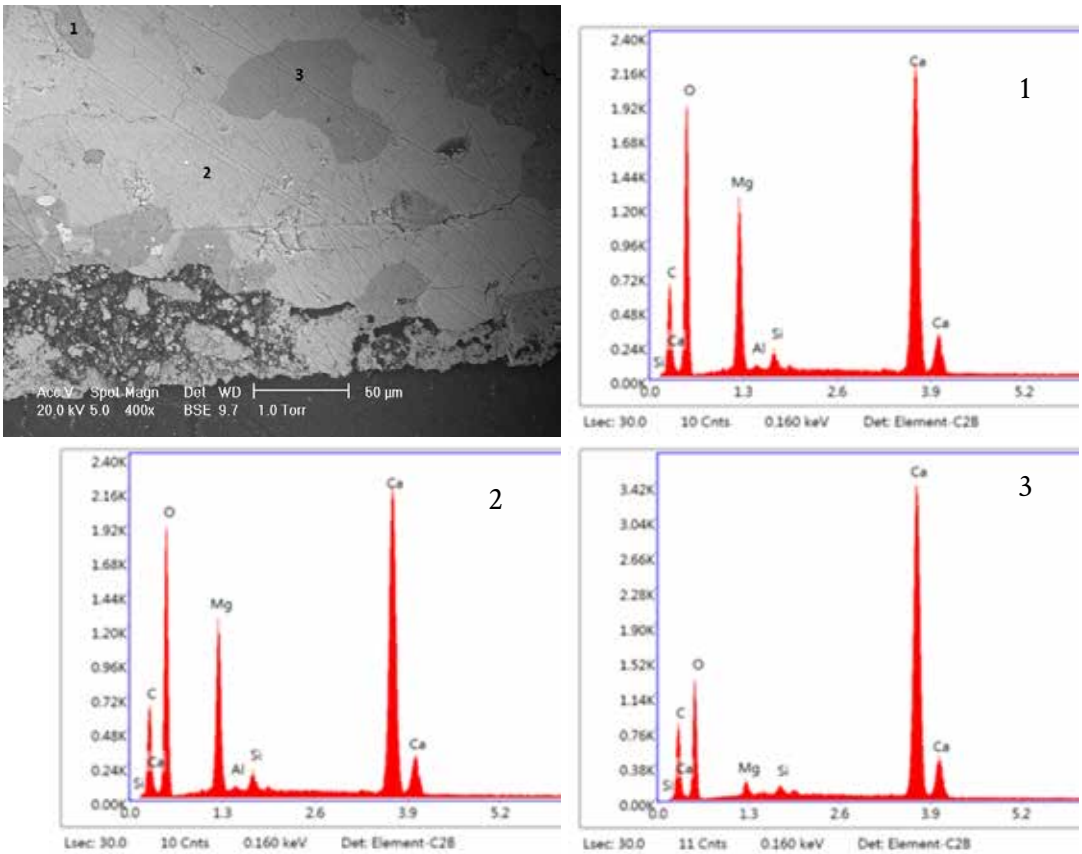

▲ *Figure 131. NM (natural hydraulic lime 3.5 and carbonate sand) BSE image and EDX spectra of the aggregate grain, 1) EDX analysis of point 1; 2) EDX analysis of point 2; 3) EDX analysis of point 3.*

In figure 132 the BSE image and the elemental distribution of CIM mortar are shown. The two grains indicated by the arrows present a hydration rim. In the core, a higher concentration of Ca was determined compared to the rim. The shape of the crystal and the composition are consistent with a crystal of partially hydrated cement mineral identified as alite, that usually presents a hexagonal shape [1].

In the samples with the aggregate and pozzolanic cement, the fly ash particles are clearly visible (figure 133) as in all the other specimens made with CEM IV. Figure 134 shows a particle of carbon observed in the CIVQ sample.

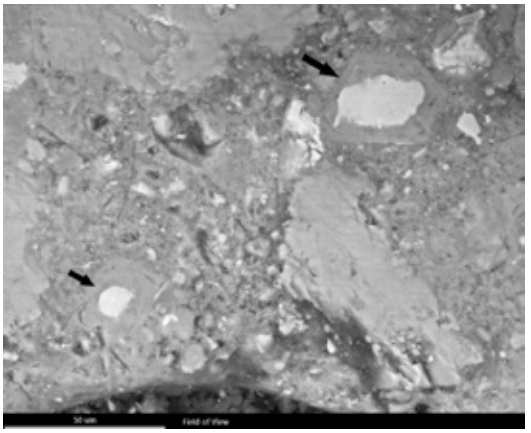

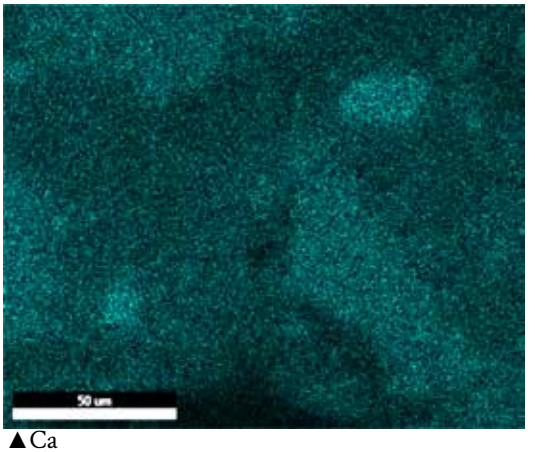

▲Ca

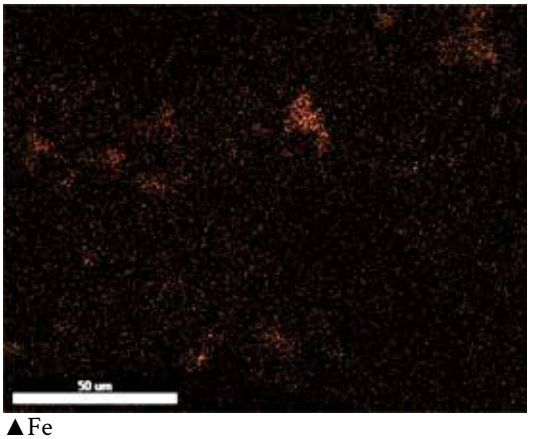

▲Fe

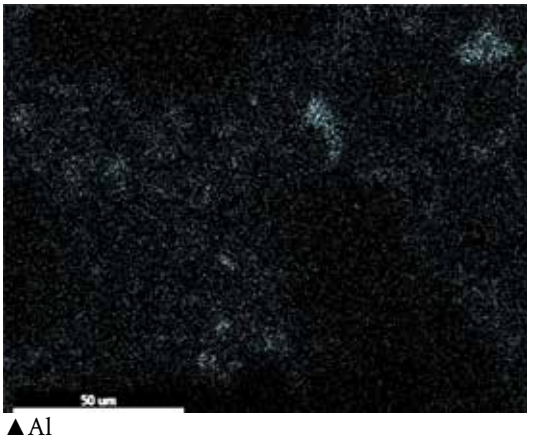

▲Al

▲*Figure 132. Image of sample CIM in BSE and EDX elemental maps.*

Figure 133. Cenosphere fly ash in CIVQ sample polished cross section.

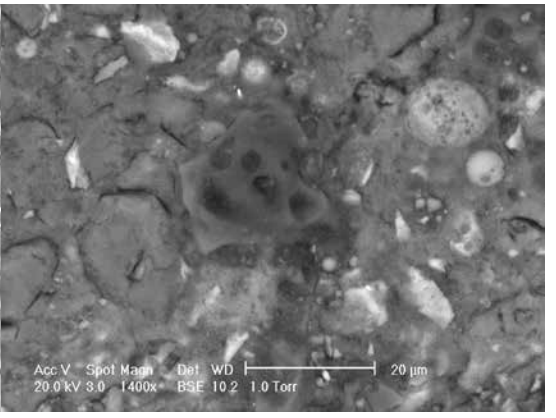

Figure 134. Carbon particle in the CIVQ's polished cross section in BSE image.

Mortars composed by two binders and one specific aggregate

From a morphological point of view the gypsum needles are clearly visible in SEM BSE images if compared to calcium carbonate phase, and are predominant. Thus, in mixed mortars the carbonate and the gypsum components are not easily discriminated by the morphological analysis and by the EDX analysis. Moreover, the EDX analysis does not give always a help, since calcium is present also in gypsum, and so if the two phases are uniformly mixed together both S and Ca are identified. Otherwise, if the two different binders are not well mixed together some lumps of one of the two will be found allowing the identification of the components. An example of a sample where calcium carbonate and gypsum are mixed together is CGsM, which is shown in figure 135. The aggregate grains are embedded in a needle matrix and near the border a thin layer with less porosity is visible and the EDX analysis suggests that here a high concentration of Ca is present, probably due to a layer of $CaCO_3$. In figure 136 a detail is shown. As it is possible to observe between the gypsum needles there is the presence of other small crystals that could be $CaCO_3$ phase. This hypothesis is also suggested by the EDX point analysis. In fact, if we compare spot 1 and spot 2, the signals of Ca are more intense than those of S.

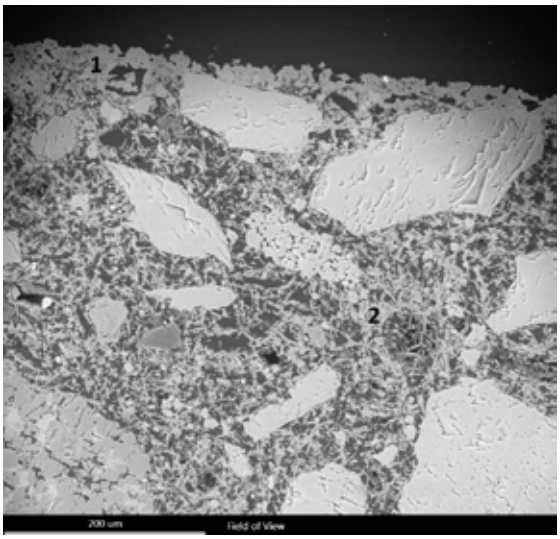

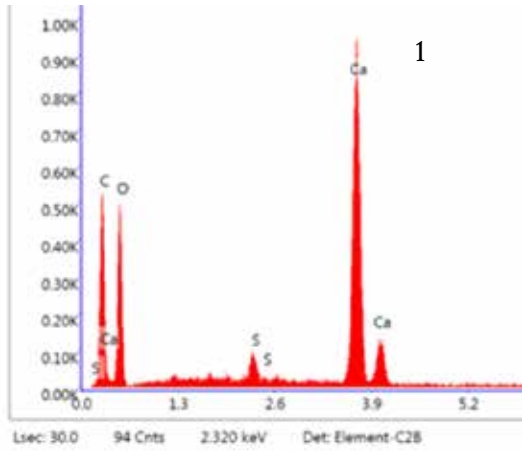

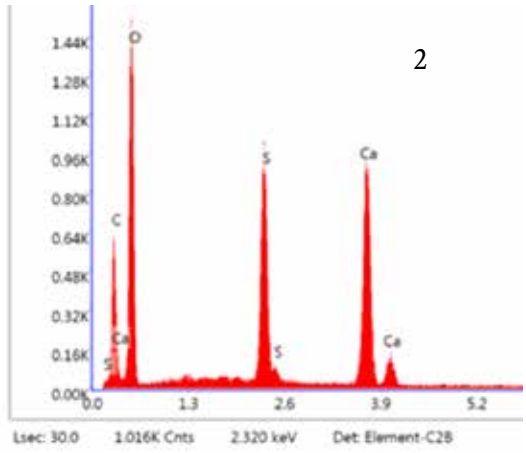

▲*Figure 135. CGsM (hydrated lime, gypsum and carbonate sand) BSE image with EDX point analysis spectra. 1) EDX spectrum of point 1; 2) EDX spectrum of point 2.*

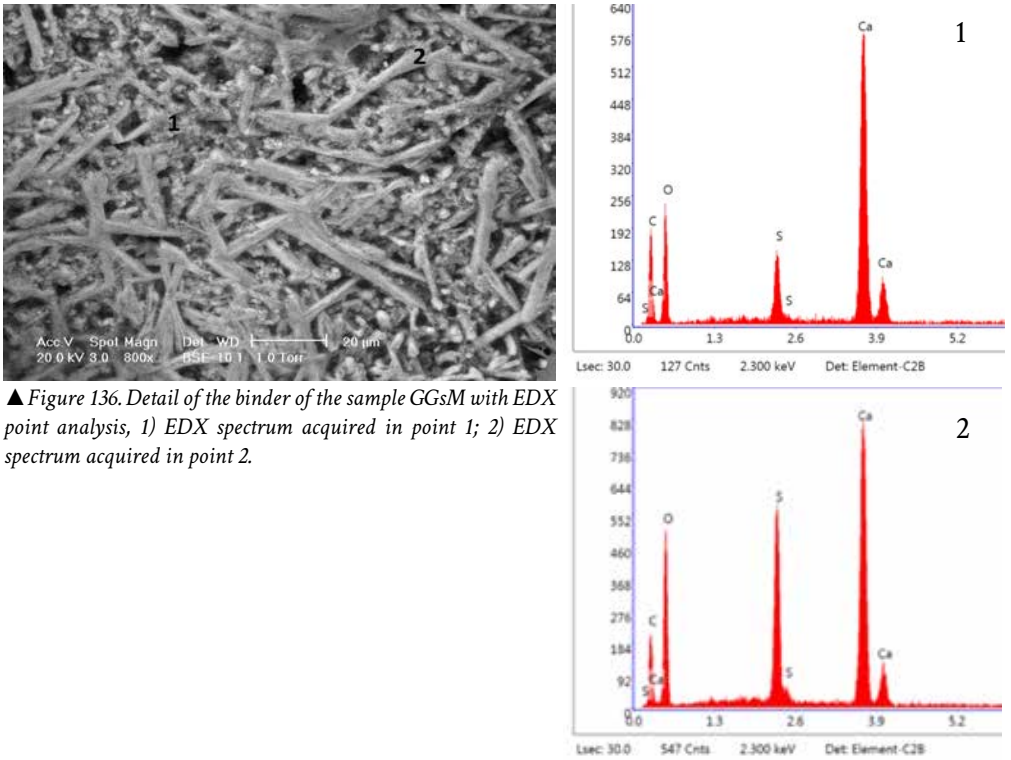

▲ *Figure 136. Detail of the binder of the sample GGsM with EDX point analysis, 1) EDX spectrum acquired in point 1; 2) EDX spectrum acquired in point 2.*

For what concerns mixed mortars with cements binders, it was possible to recognize some phases that could lead to identify cement presence. For example, unhydrated relict crystals of the clinker and the interstitial phases formed in between them (figures 137 and 138). The presence of fly ashes was the marker of mortars with pozzolanic cement (figure 138). It is part of this type of cement according to norms of the cement classification [11].

Furthermore also a thin layer with abundance of Ca was observed on the borders of almost every sample. This could explain the presence of almost only $CaCO_3$ in most of the external reflection infrared spectroscopy spectra performed on the surfaces "rough" and "smooth".

The particle in figure 137 represents some not hydrated crystals of cement. The analysis in spot 1 represents probably a calcium silicate phase C_2S or more probably C_3S by the shape of the crystals. In fact the EDX spectrum of spot 2 presents Al, Fe and Ca that could be associated with C_4AF or C_3A [1,6,10,12–13].

In figure 138 a crystal of partially unhydrated cement particle is visible. In the center of the crystal, in the brighter zone there are more intense signals of Ca (poin 1) compared to the external rim (dark gray, point 2). Moreover, Ca, Al and S suggest the presence of some sulphates phases in this zone.

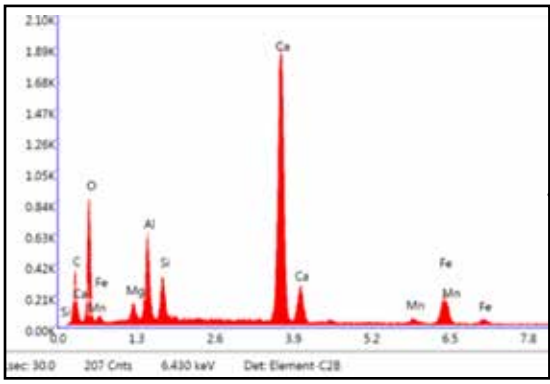

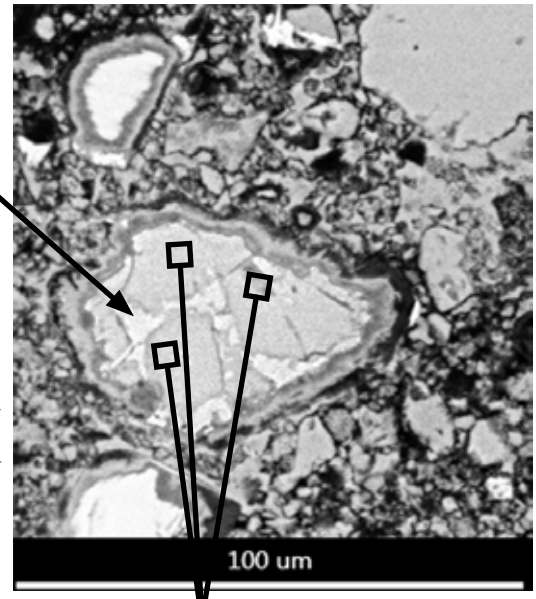

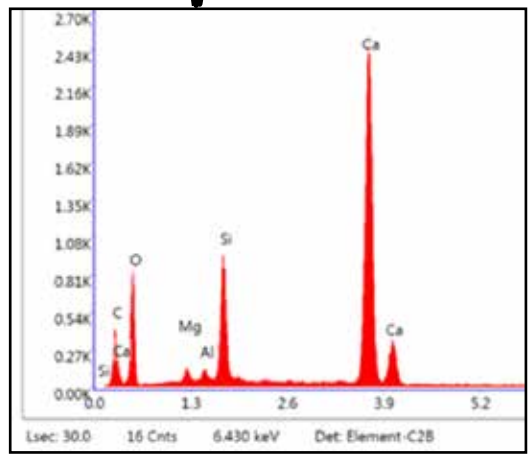

▲*Figure 137. Image of CCIM (hydrated lime, Portland cement and carbonate sand) where the not hydrated cement crystals are visible; 1) EDX spectrum of probably C_3A or C_4AF phase; 2) EDX spectrum of probably C_3S phase.*

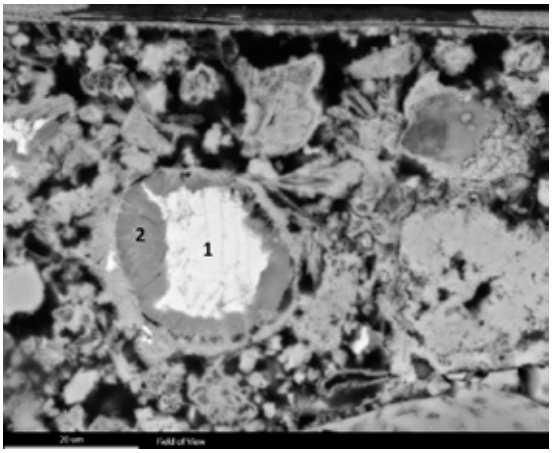

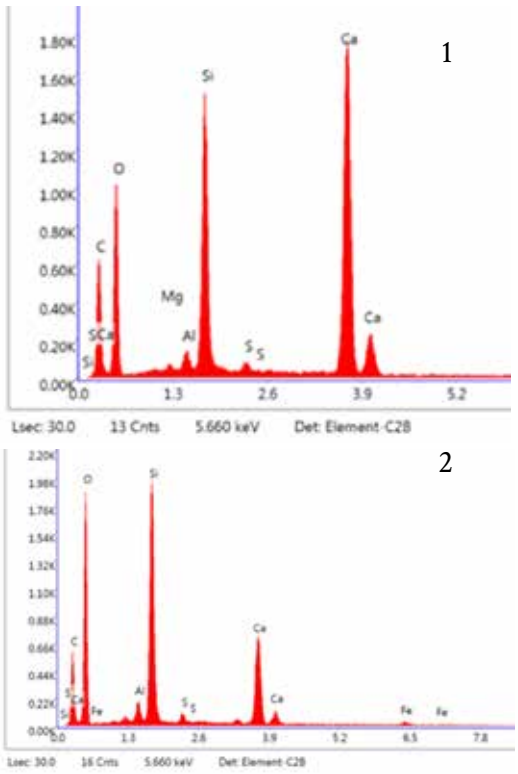

▲*Figure 138. SEM BSE image of mortar CCIQ (hydrated lime, Portland cement and quartz sand) the points of analysis are indicated in figure: 1) EDX spectrum of point 1; 2) EDX spectrum of point 2.*

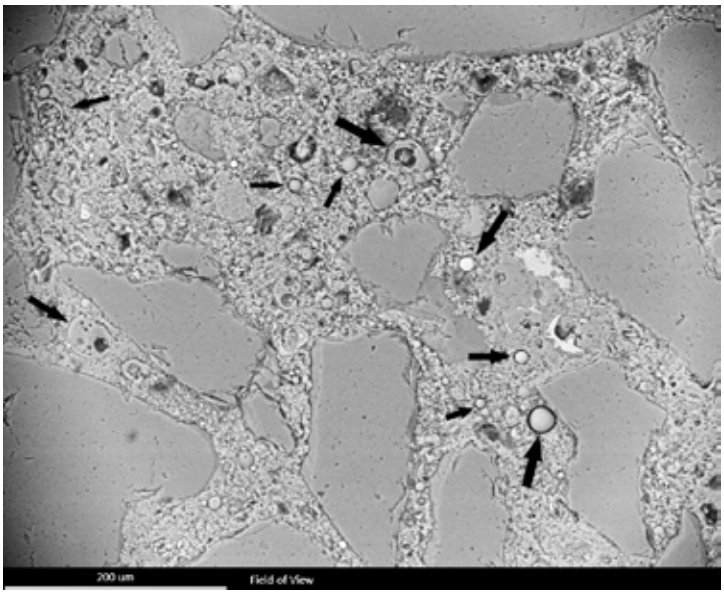

◀*Figure 139. 200x BSE image of GCIVQ (lime putty, pozzolanic cement and quartz sand), fly ashes are well visible in the matrix (arrows).*

In mortars NCIVQ (natural hydraulic lime 3.5 with CEM IV and quartz sand), NCIM (natural hydraulic lime with Portland cement (CEM I) and carbonate sand) and NCIVM (natural hydraulic lime with pozzolanic cement (CEM IV) and carbonate sand) some decalcified cements grains (figure 140, 141, 143 and 144) are clearly visible. The mortar shown in figure 140 and 141 contains ovoid grains which are probably unhydrated clinker crystals, while the dark particles are decalcified C_2S phase [1]. It is also confirmed by the low Ca/Si ratio present in EDX spectra, where the counts of Ca are very low. An example of spectrum collected in the rounded dark crystals is shown in figure 141. The EDX spectrum of the brighter zone (point 2) suggests the presence of C_4AF or C_3A [1,6,10,12–13] (figure 142).

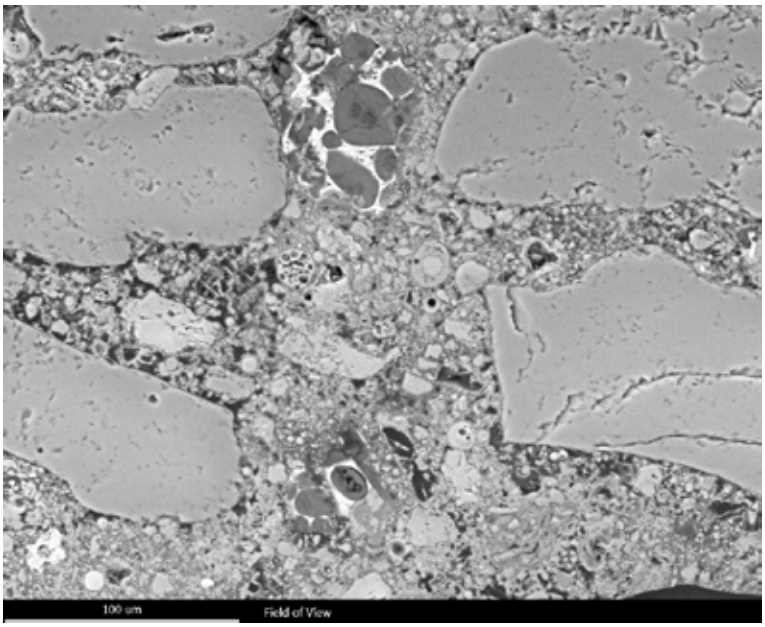

◀*Figure 140. SEM BSE image of a region of a sample taken from NCIVQ mortar where ovoid grains in the top and bottom center are unhydrated clinker crystals, the dark particles are decalcified C_2S.*

In figure 141, 143 and 144 some decalcified cement crystals are visible. In figure 145 the EDX spectra acquired on NCIVM specimen are shown. Spot 1 shows the spectrum of a decalcified Ca-silicate crystal with low Ca, while spot 2 shows the spectrum of the brighter phase around the Ca-silicate crystals, that is probably composed by C_4AF or C_3A [1,6,10,12–13].

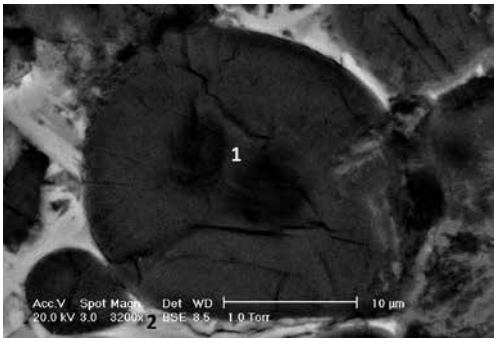

◀*Figure 141. Detail of figure 139, it shows a decalcified crystal of belite in mortar NCIVQ.*

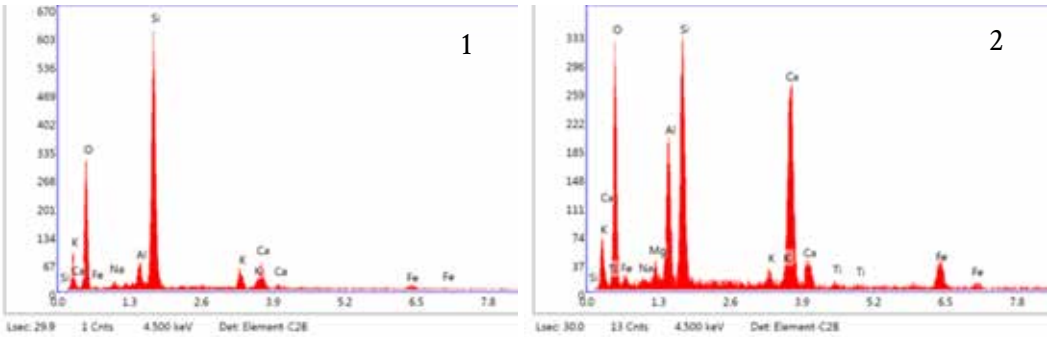

▲*Figure 142. EDX spectra collected on NCIVQ in figure 140.*

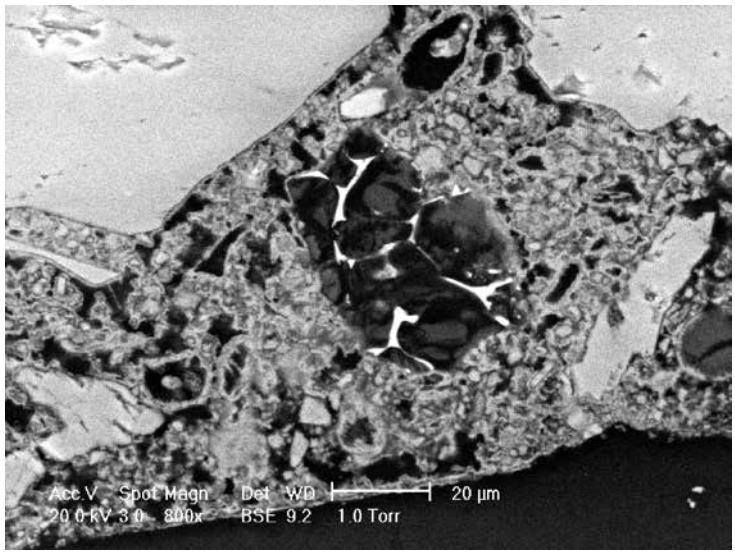

▲*Figure 143. NCIM (natural hydraulic lime, Portland cement and carbonate sand) BSE image of decalcified crystals (black) and interstitial phase (the brighter area).*

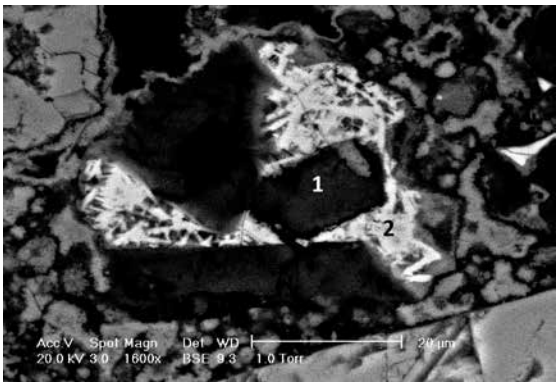

◀*Figure 144. NCIVM (natural hydraulic lime, pozzolanic cement and carbonate sand) BSE image with de-calcified cement crystals (black) and C_3A or C_4AF phases (white), 1) point of EDX analysis number 1; 2) point of EDX analysis number 2.*

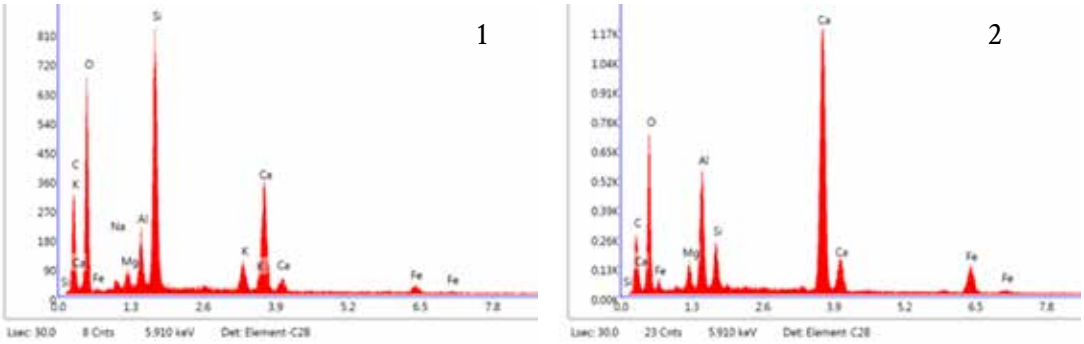

▲*Figure 1445 NCIVM (natural hydraulic lime, pozzolanic cement and carbonate sand) spectra of EDX analysis (point 1 and 2) acquired on figure 143.*

In samples with natural hydraulic lime it was more difficult to identify the unhydrated hydraulic phase in the samples. In figure 146 an example of hydraulic phase, in sample CNM, is shown. The picture shows the partial hydration of calcium silicate particle: in spot 1 the signals of calcium are more intense than in the hydration rim (spot 2), where also S is present. The presence of some sulphates is also identified by Raman spectroscopy and infrared spectroscopy in raw materials (Raman spectroscopy and micro infrared reflection spectroscopy (μ-FTIR) paragraph) even if it is not expected in this type of samples. In figure 146 also a layer near the border is well visible. The EDX analysis shows a high intensity of the signals of Ca, O and C (spot 3), suggesting the presence of a $CaCO_3$ layer.

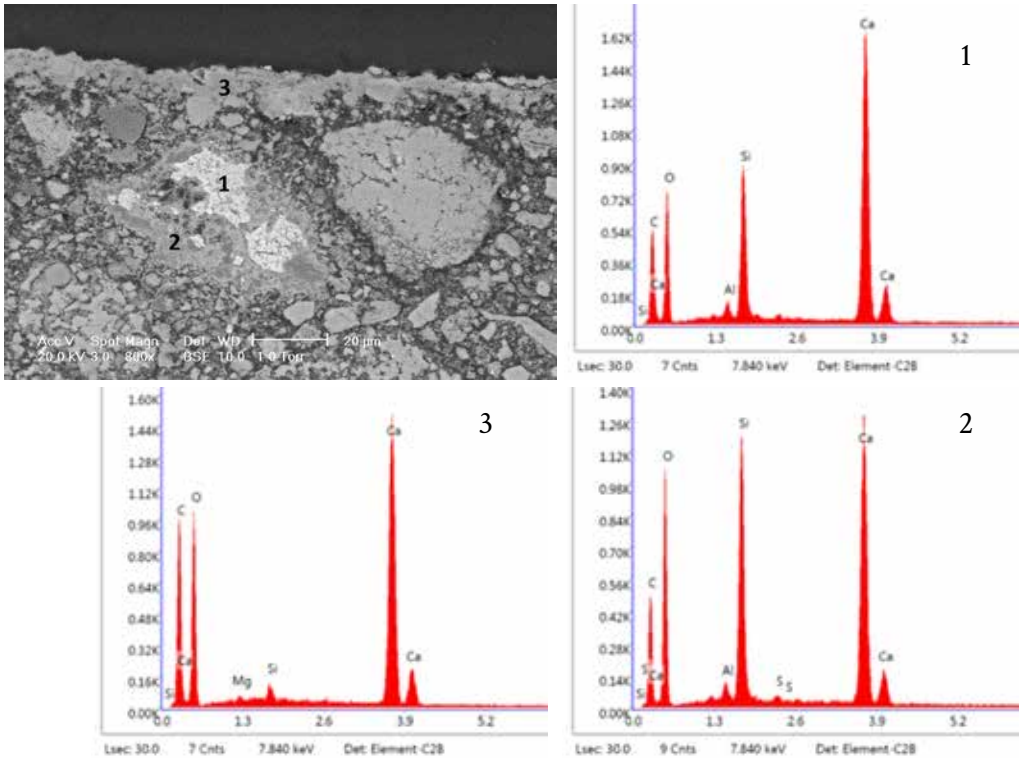

▲*Figure 146. CNM BSE image and EDX spectra are shown. 1) spectrum of EDX point analysis 1; 2) spectrum of EDX point analysis 2; 3) spectrum of EDX point analysis 3.*

Discussion and conclusions

The scanning electron microscope allows the characterization of the mortars' microstructure as it allows to visualize the morphology of crystals, aggregate and pores. Moreover, it is possible also to see the presence of carbonation rims. Then the EDX analysis could add information on the elemental composition by point or map analysis. The BSE images could also identify the presence of possible stratigraphy in the sample.

For what concerns the mortars made using one binder the identification of the type of mortar is relatively easy. Obviously, there are no differences between lime putty mortars and hydrated lime samples apart from the presence of cracks in specimens made with lime putty, probably connected to a too rapid carbonation process or a lack of binder in the mortars or to the shrinkage process connected to the presence of too much water.

Focusing on the mixed mortars, the possibility of distinguishing the different components of the two binders became harder. For example, in the mixes made by lime putty and gypsum (as binders) the presence of gypsum is clearly visible by the presence of needle crystals, while the presence of calcium carbonate is more difficult to detect, as it is shown in sample GGsM (lime putty, gypsum and carbonate sand) (figure 136).

In mixed mortars where one of the two binders is cement, the identification of clinker as unhydrated crystal relicts helps to recognize the presence of a cement component in the mortar. The clinker particles present in fact a characteristic shape and morphology that is informative. Furthermore, BSE coupled with EDX analysis helps in the identification of cement unhydrated phase; the relative intensities of the EDX spectra, collected on the same area of the sample, could provide suggestions of the mineralogical phases analysed by calculating the ratio intensities (Ca/Si) for Ca-silicate phases.

If the recognition of the presence of cements is almost straightforward, the presence of other binders mixed together (lime putty, hydrated lime or natural hydraulic lime) is not so clear. In fact, $CaCO_3$ is present in aerial binders, but it is also present both in cements and in natural hydraulic lime, so the possibility of distinguishing the different binders mixed together is hard. In the mortars made with natural hydraulic lime, the binder appears very heterogeneous as it is visible in figure 126, but the identification of crystals that could suggest the presence of an hydraulic phase was very difficult because only a few of them were found. In some cases like in figure 146 the unhydrated calcium silicate phase was identified in a mixed mortar (CNM, hydrated lime, natural hydraulic lime and carbonate sand). In table 48 the main advantages and drawbacks of environmental scanning electron microscope are listed.

Advantages	**Drawbacks**
Identification of gypsum phase.	Problem in the identification of the two binders in mixed mortars.
Identification of unhydrated cement crystals in all the mortars with cements binders.	The samples have to be embedded in polished cross sections for a better identification of the components (it is a restriction for historical mortars, if there is only low quantity of sample).
Elemental map distribution.	
Identification of C_3A and/or C_4AF.	
No coating is required.	

Table 48. Summary of advantages and drawbacks of ESEM analysis applied to mortars model

References

[1] H.F.W. Taylor, Cement chemistry. 2nd ed., 1997. doi:10.1016/S0958-9465(98)00023-7.

[2] B.G. Kutchko, A.G. Kim, Fly ash characterization by SEM – EDS, 85 (2006) 2537–2544. doi:10.1016/j.fuel.2006.05.016.

[3] N. Ranjbar, C. Kuenzel, Cenospheres: A review, Fuel. 207 (2017) 1–12. doi:10.1016/j.fuel.2017.06.059.

[4] L. Black, A. Brooker, SEM–SCA: combined SEM – Raman spectrometer for analysis of OPC clinker, Adv. Appl. Ceram. 106 (2007) 327–334. doi:10.1179/174367607X228052.

[5] M. Benmohamed, R. Alouani, A. Jmayai, A. Ben Haj Amara, H. Ben Rhaiem, Morphological Analysis of White Cement Clinker Minerals: Discussion on the Crystallization-Related Defects, Int. J. Anal. Chem. 2016 (2016) 1–10. doi:10.1155/2016/1259094.

[6] I. Vidovszky, F. Pintér, An Investigation of the Application and Material Characteristics of Early 20 th -Century Portland Cement-Based Structures from the Historical Campus of the Budapest University of Technology and Economics, Int. J. Archit. Herit. (2018) 1–18. doi:10.1080/15583058.2018.1545059.

[7] J. Weber, K. Bayer, F. Pintér, Nineteenth Century "Novel" Building Materials: Examples of Various Historic Mortars Under the Microscope, in: 2012: pp. 89–103. doi:10.1007/978-94-007-4635-0_7.

[8] G. Moir, Cements, in: Adv. Concr. Technol., Elsevier, 2003: pp. 3–45.

[9] S. Yousuf, P. Shafigh, Z. Ibrahim, H. Hashim, M. Panjehpour, Crossover Effect in Cement-Based Materials: A Review, Appl. Sci. 9 (2019) 2776. doi:10.3390/app9142776.

[10] F. Pintér, C. Gosselin, The origin, composition and early age hydration mechanisms of Austrian natural Portland cement, Cem. Concr. Res. 110 (2018) 1–12. doi:10.1016/j.cemconres.2018.04.020.

[11] Ente Italiano di normazione, UNI EN 197 Composizione, specificazioni e criteri di conformità per cementi comuni, (2001).

[12] J. Weber, K. Bayer, F. Pintér, Nineteenth Century "Novel" Building Materials: Examples of Various Historic Mortars Under the Microscope, in: 2012: pp. 89–103. doi:10.1007/978-94-007-4635-0_7.

[13] R. Bookseries, Historic Mortars, Springer Netherlands, Dordrecht, 2012. doi:10.1007/978-94-007-4635-0.

CHAPTER 4

Discussion

Before starting the discussion of the results, it is important to remember that the core idea of this project was inspired by the need of robust and reliable analytical methods for the characterisation of mortars. In particular, the main concern was to collect information on how to build up the analytical procedure in order to get results able to specify the mortar typology, balancing time and costs. In addition, several new techniques have been recently introduced in conservation science; consequently the improvement induced by the knowledge of mortars has been considered. In order to test the chosen analytical techniques, designing an analytical protocol a series of model samples were prepared. The evaluation of the application of different techniques to mortar model samples has been done. The analytical protocol was focused in particular to distinguish the obtained results in those coming from the binder from those coming from the aggregate. Summarising, the protocol considered:

- the response of each technique to the different compounds present;
- the analytical problems involved in each technique;
- the balance of advantages and drawbacks;
- the complementarities of the techniques;
- the total amount of samples needed;
- the time used to perform the analysis;
- budget factors.

The analyses performed on specimens prepared with one specific binder (G, C, CI, CIV, Gs and N), without the aggregate, were considered as references. Without the presence of the aggregate the signals of the binder were better characterized and the main components have been identified. The knowledge of the composition of the binder is important to define the typology of the mortars (lime mortars, hydraulic mortars, cement mortars mixed mortar, etc…). With infrared spectroscopy we have seen a good characterisation of the main compounds like $CaCO_3$, $Ca(OH)_2$, $CaSO_4$ $2H_2O$, the presence of silicates and SiO2. In the specimens made with a cement binder the hydrated hydraulic phases as tobermorite have been identified and also the presence of ettringite, which is a characteristic occurrence of cements. This phase presents peaks clearly visible in transmission and ATR mode and also in reflection mode, where the combinations bands are intense and well visible over $4000cm^{-1}$ [1–11] (Micro-infrared reflection spectroscopy (μ-FTIR) paragraph). Powder X-ray diffraction presents its main restriction in the identification of hydrated silicate phases that are poorly crystallized, usually in gel phases. Furthermore the diffraction peaks of tobermorite are overlapped by those of larnite and hatrurite, which are the anhydrous hydraulic silicate phases present in cements. X-ray diffraction also has shown the presence of different polymorph of $CaCO_3$ (aragonite or vaterite) in specimens with cement or natural hydraulic lime, that could indicate

a different carbonation mechanism in presence of hydraulic compounds [12–19]. SEM-EDX analysis on these types of samples underlined the presence of unhydrated clinker particles, with interstitial phases as C_3A and C_4AF in the matrix of the specimens (as in CCIM, NCIVQ, NCIM or NCIVM) and fly ashes in those made with pozzolanic cement [20–27]. Also Raman spectroscopy identified the presence of hydraulic unhydrated and hydrated cement phases [28–36]. DSC-TG identified the occurrence of carbonates, gypsum, portlandite, and cement hydrated phases. In DSC curves the cement hydrated phases were present, but they overlapped each-other (under 200°C), thus is harder to quantify the singles phases. On the other hand, in natural hydraulic lime no hydraulic phases were identified with TG-DSC analysis [37–44]. The results found in the specimens with a single binder are confirmed, but when introducing the aggregate, this could create interference with the identification of cement hydrated phases.

In infrared spectroscopy spectra the bands of quartz fall very close to those diagnostic for the identification of hydrated hydraulic silicates in cements. For mortars without cement binder, the presence of carbonate in the aggregate is added to that present in the binder, without any possibility to distinguish the two different origins. Powder X-ray diffraction allows the identification of ettringite in samples with cements but no determination of calcium silicate hydrate in hydraulic mortars. TG-DSC led to the identification of the main phases, including the cement hydrated phases. When the carbonate sand is added, there is the shift of the decomposition peak of carbonates to higher temperatures, which accounts also for the decomposition of binder carbonate. It could suggest the presence of the carbonate aggregate but, in the presence of a mortar blended with a carbonate phase, it is not possible to distinguish between their origins. On the contrary, scanning electron microscopy and thin section analysis on the samples with cement easily allowed the identification of clinker relicts, fly ashes, C_3A and/or C_4AF, and the nature of the aggregate. The two techniques also permitted the visualization of carbonation rims in the samples, if present. Raman spectroscopy proved to be able in the identification of hydraulic phases in hydraulic mortars.

The analyses on specimens made by two different types of binders were done to evaluate the influence of the two binders without the aggregate. Also in these specimens the presences of the main compounds have been identified with infrared spectroscopy. Cements have been identified by the presence of ettringite, even if ettringite was not individuated in each of the cement specimens. Moreover, in X-ray diffraction the main phases are highlighted but, when cements are mixed with another binder, it was not possible to identify ettringite in all cases. Also TG-DSC technique presents some difficulties in the identification of the different phases in mixed mortars. SEM-EDX and thin sections analysis allowed to clearly observe clinker relicts in the specimens, but these two techniques could not distinguish the components from one binder to the other.

The presence of two binders mixed with the aggregate in order to produce the mixed mortars, increases the difficulties in the identification of the compounds and of the origins of the phases. In samples with quartz aggregate, the presence of quartz could cover some infrared spectroscopy signals of hydrated silicates. Moreover, the carbonate aggregate increases the signals of carbonates in the specimens, lowering and covering other peaks. On the contrary, SEM-EDX analysis and thin section analysis allowed the identification of cement clinker relicts, C_3A and/or C_4AF or fly ashes in all the samples where they were present. In these samples the presence of quartz from the aggregate is visible in the TG-DSC and the carbonate decomposition in the aggregate shifts at higher temperatures. Moreover, it was possible to

calculate the binder/aggregate ratio (B/A) in mortars with quartz aggregate (assuming that the aggregate is only composed by quartz and the total amount of decomposed $CaCO_3$ comes from the binder). The TG-DSC results provide a B/A ratio which is more similar to the proportions used to prepare the specimens, while CT tomography and point counting give results as volume/volume ratio which is difficult to convert in weight with such heterogeneous materials.

In the following paragraphs different analytical approaches are suggested, on the basis of the objectives of the analysis and the type of the samples. The sequence is elaborated considering the practical and analytical advantages and drawbacks which emerged in this study. First of all, thanks to the good results obtained with ER-FTIR spectroscopy, this technique is suggested as the first step before sampling. In fact, it can give suggestions of the main composition of the analysed area. It is important to remember that infrared spectroscopy in external reflection gave different results in relation to the surface roughness and the presence of a carbonation rim nears the surface. These factors have to be considered when portable infrared is used. On the basis of the analytical questions, which change case by case, it can suggest the best sampling points. In the interpretation of this first result the characteristic of this type of measure has to be taken into account.

After the choice of the sampling area, if the samples are powders or we have enough to grind a part of it, a fine grinding is suggested. In order to perform powder X-ray diffraction usually almost 1g of sample is needed (with a minor amount of sample in some sample-holder the powder could move and deform the diffractograms). After this analysis, if it is possible to perform infrared spectroscopy with bench-top instruments (in transmission or ATR mode) using the same powder from the XRD analysis it should be done to implement the results. FTIR could give more information on the hydrated phases, especially in the case of hydraulic hydrated phases of hydraulic mortars, such cements and natural hydraulic lime. Moreover, ettringite in some cases is not detected in PXRD. After these analyses if there still are some uncertainties about the presence of hydraulic compounds, Raman spectroscopy is suggested. It gives the possibility to detect these phases even if the instrumental setting usually has to be adjusted from case to case, to avoid heating, burning the sample or fluorescence generation. Furthermore it is a point analysis, hence the search of these phases could take several time. In order to have quantitative values of the main phases TG-DSC could be performed; it can also give the binder/aggregate ratio in mortars with silicate aggregate. In case of carbonate aggregate, we have observed that the decomposition band of carbonate shifts to over 800°C, probably because of well-ordered crystals from the aggregate. An attempt to create a logical and methodological order in the multi analytical sequence procedure could be observed in figure 147. The flow charts have been created according to the international standards [45].

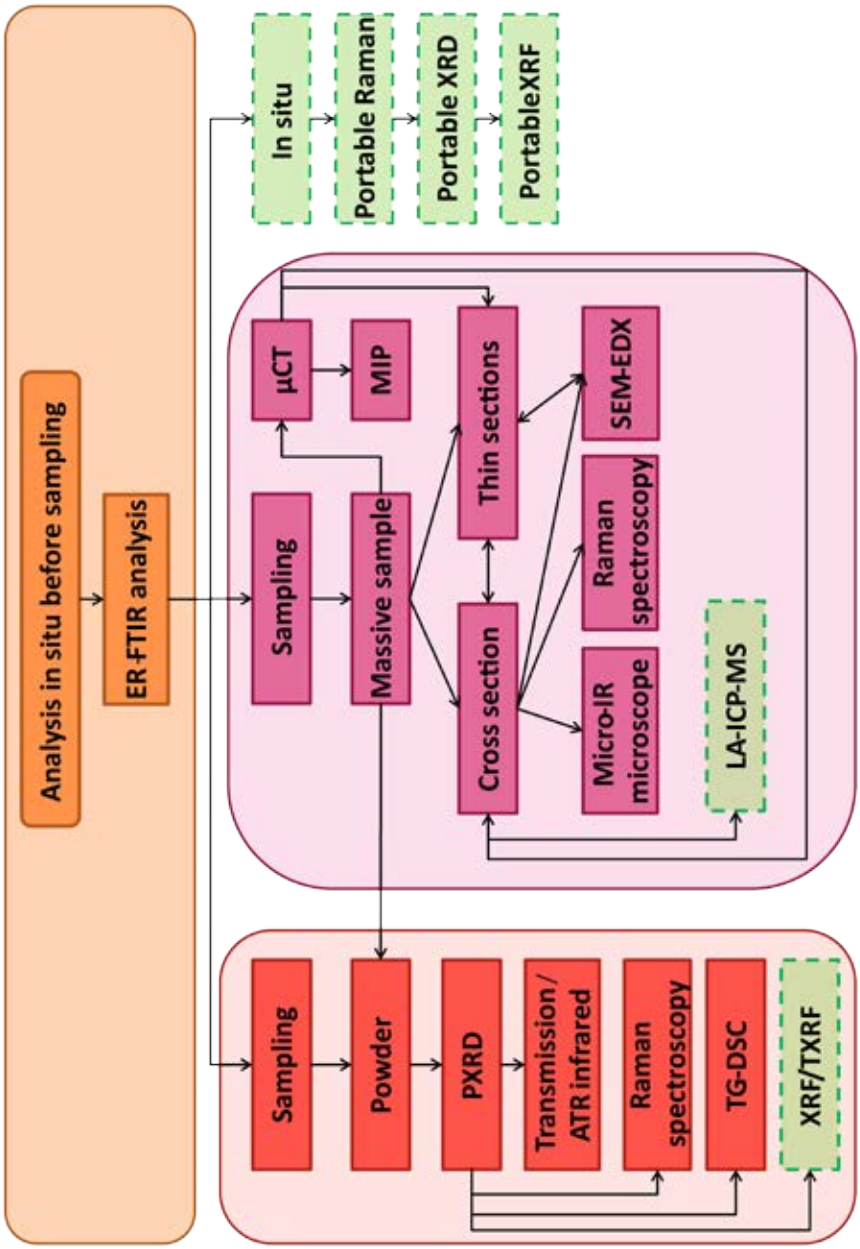
Analysis in situ before sampling
ER-FTIR analysis
In situ
Portable Raman
Portable XRD
PortableXRF
Sampling
µCT
MIP
Massive sample
Thin sections
SEM-EDX
Cross section
Raman spectroscopy
Micro-IR microscope
LA-ICP-MS
Sampling
Powder
PXRD
Transmission / ATR infrared
Raman spectroscopy
TG-DSC
XRF/TXRF

As shown in figure 147, a preliminary analysis with portable infrared spectroscopy is suggested, in order to evaluate the main components of the sampling surfaces and plan the sampling, prior to the analysis of the powder and massive samples. Then two procedures are suggested in relation to the kind of sample (powder or massive fragment). Powder X-ray diffraction is followed by the use of the same powder for the infrared, Raman and TG-DSC analysis. PXRD is the first step, because it requires a greater amount of powder compared to the other analysis. In the powder analysis we suggest also XRF/TXRF analysis that could give information on elemental composition, trace elements and it can help in the provenance studies. Regarding the analysis of the massive sample as it is, the μCT could be performed if we are interested in microstructure analysis. Then, on the basis of the initial analytical question, if we are interested in the composition, the cross sections or thin sections could be prepared to perform microscope observations and chemical analyses. On the other hand, if we are interested in the pore size distribution, also the mercury intrusion porosimetry could be performed. We have to consider that after the MIP analysis the sample could not be used anymore because of the intrusion of Hg. On the contrary, after μCT the samples could be re-used because their composition does not change.
The green boxes figure 147 lists some techniques that could be used to improve the in situ analysis. These are already used in mortar studies but they are not widely diffused and an in depth study of their application to mortar materials is required. On the in situ analysis, portable Raman spectroscopy, portable X-ray diffraction and portable X-ray fluorescence have been suggested. Due to the good results obtained with bench-top Raman spectroscopy in would be interesting to test the portable instrument on these materials even if the problems underlined in this study, especially in the acquisition of the spectra. Portable X-ray diffraction is a relatively new instrument that is still not widely diffused but has great potentialities. The ability to carry out mineralogical analysis in situ could help in the sampling choice and in the study of the materials when sampling is not possible. Moreover, also portable X-ray fluorescence could help in the in situ analysis by giving the elemental composition of the materials analysed and maybe suggest the sampling points. This technique in its bench-top modalities could be used in the analysis of the powder samples, especially, if raw materials or other comparison samples are present provenance studies could be carried out. Also LA-ICP-MS is suggested in the study of cross sections for elemental analyses: in fact, it can also give the spatial distribution of the elements or the trace elemental analysis. Moreover, on the cross sections also Raman spectroscopy imaging could be used to connect the spatial position with the compositional data. The choice between cross sections and thin sections depends on the analytical questions and also on the cost, time and ability of the operator. In fact, to create a thin section specific instruments and a certain ability of the technician who prepares it, is required, since the sample has to be polished, stacked on a glass and then its thickness reduced to 30μm. If the thickness is not correct, there will be a change in the interference colors that are very important in the interpretation of the analysis. A cross section in this case is usually obtained from the emended sample cut off from the thin section. On the other hand, the preparation of a cross section is quicker and cheaper. These are the reasons why there is a double arrow in the flow chart. In fact, the remains left from the thin section preparation are usually a cross section that could be polished and used. While to prepare a thin section a cross section not too much polished is required. Both types of sections could be put inside the electron microscope. In the SEM-EDX microscope it

◀*Figure 147. Schematic procedure for the sampling and the analysis of a powder and massive sample.*

is possible to perform elemental analysis on the binder and on the aggregate in order to have the elemental composition of the point or the area analyzed. It does not give the mineralogical composition as the thin section or PXRD analysis but only the chemical composition. For example, with the thin sections it is also possible to obtain the mineralogical composition, since it gives information on the origins of minerals (for example: polymorph quartz, the presence of feldspar that could not be distinguished with SEM-EDX etc.). In figure 148 the scheme of the powder sample analysis is expanded to show the main diagnostic point and sequence. For each technique the main diagnostic peaks or phases that could lead to the identification of the binder or aggregate compounds are specified. In the scheme the most significant peaks are reported. The flow chart follows the idea that if the indicated phases are not found in our sample, it can be deduced that it is composed by other binders which are not mentioned (lime binder etc). In figure 149 the flow chart for the analysis of the massive samples is explained. It describes the main characteristic features for the identification of the mortar typology. Also in this case the choice of the analysis is influenced by the analytical question at the beginning of the single case studies.

Figure 148. Schematic sequence of analysis of a powder sample. ►

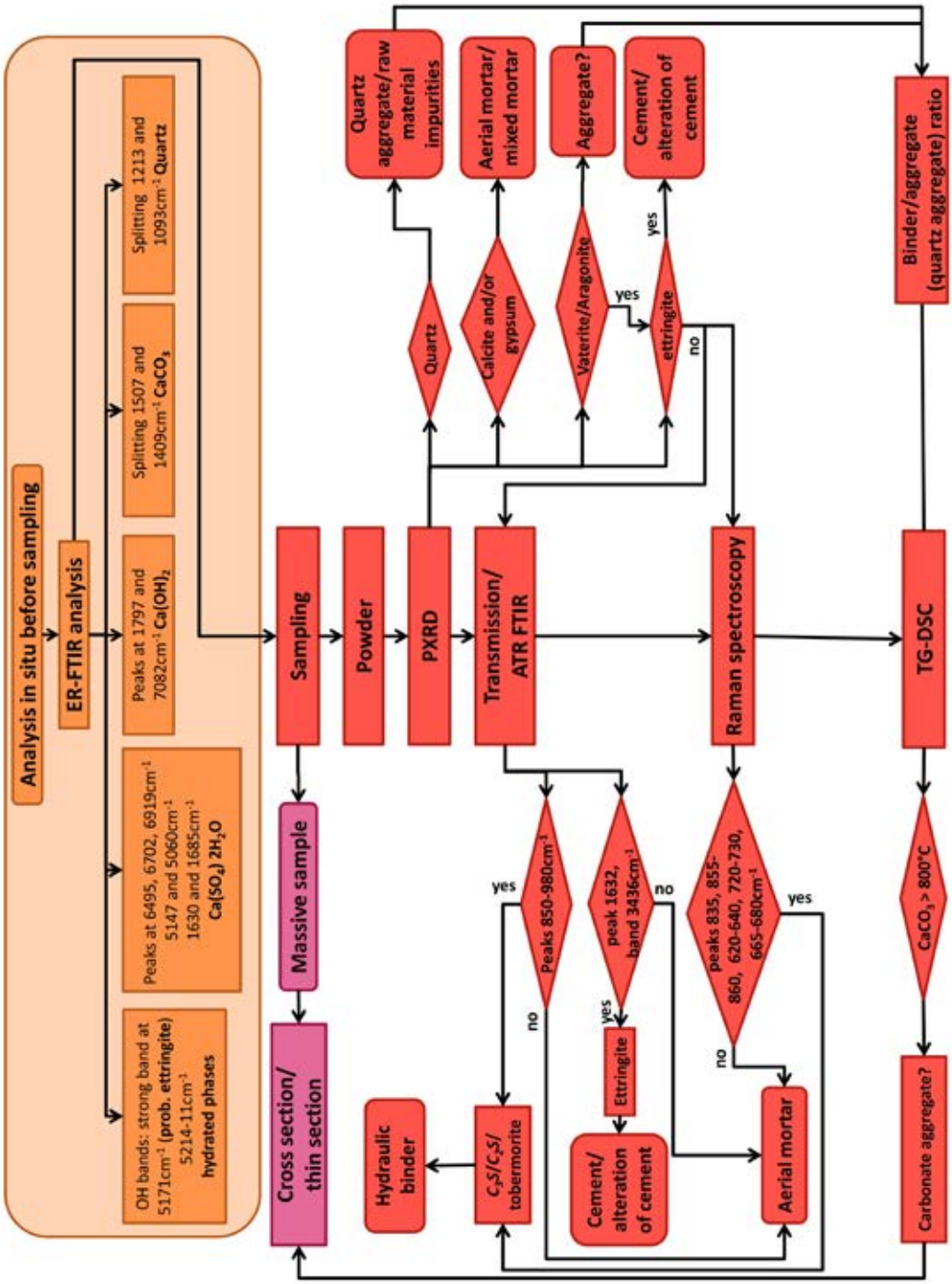
Analysis in situ before sampling
ER-FTIR analysis
OH bands: strong band at 5171cm-1 (prob. ettringite) 5214-11cm-1 hydrated phases
Peaks at 6495, 6702, 6919cm-1 5147 and 5060cm-1 1630 and 1685cm-1 Ca(SO4) 2H2O
Peaks at 1797 and 7082cm-1 Ca(OH)2
Splitting 1507 and 1409cm-1 CaCO3
Splitting 1213 and 1093cm-1 Quartz
Sampling
Massive sample
Cross section/ thin section
Powder
PXRD
Transmission/ ATR FTIR
Raman spectroscopy
TG-DSC
Quartz
Calcite and/or gypsum
Vaterite/Aragonite
ettringite
Quartz aggregate/raw material impurities
Aerial mortar/ mixed mortar
Aggregate?
Cement/ alteration of cement
Binder/aggregate (quartz aggregate) ratio
yes
no
Peaks 850-980cm-1
peak 1632, band 3436cm-1
peaks 835, 855-860, 620-640, 720-730, 665-680cm-1
CaCO3 > 800°C
Hydraulic binder
C3S/C2S/ tobermorite
Ettringite
Cement/ alteration of cement
Aerial mortar
Carbonate aggregate?

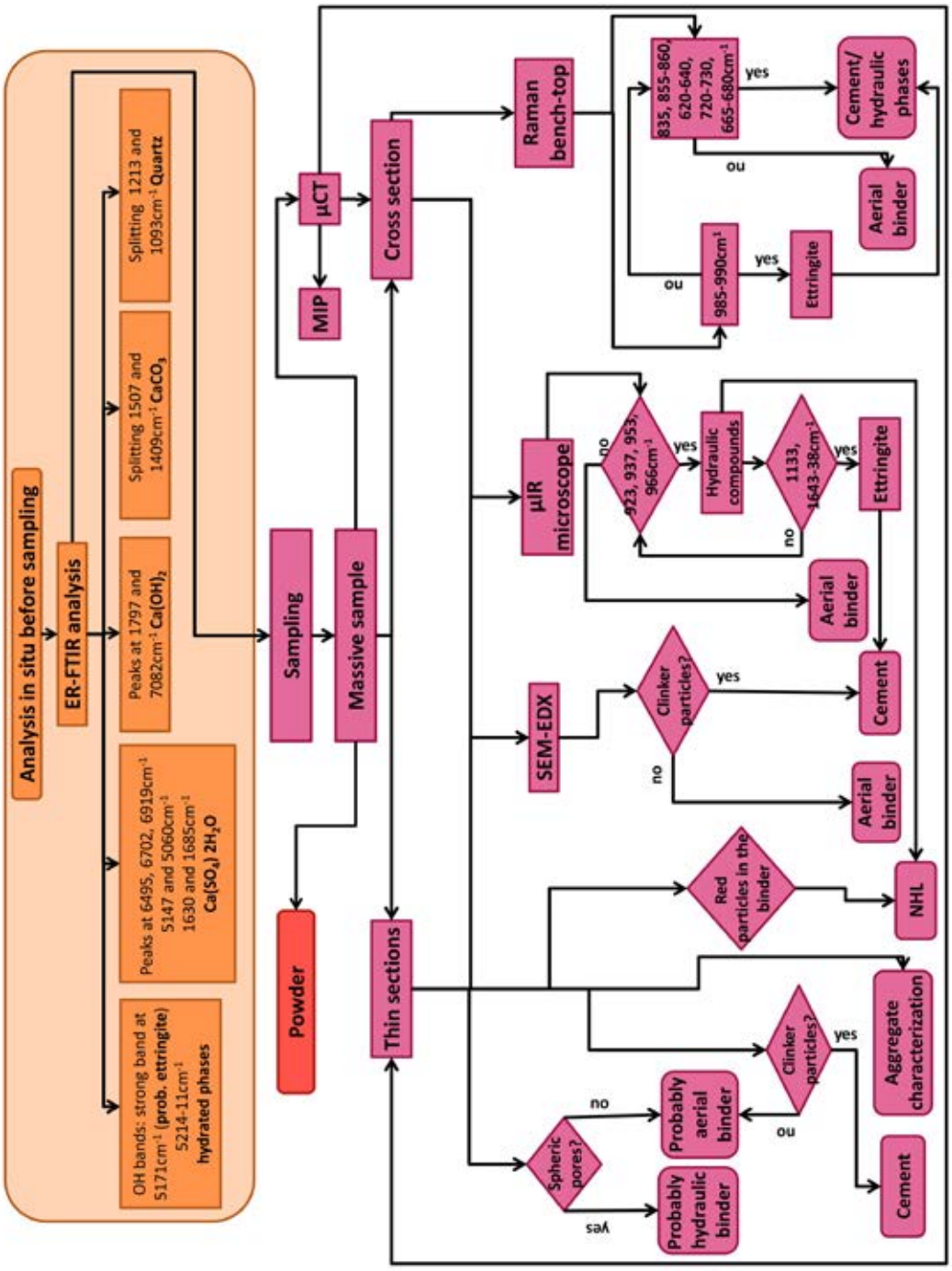
Analysis in situ before sampling
ER-FTIR analysis
OH bands: strong band at 5171cm-1 (prob. ettringite) 5214-11cm-1 hydrated phases
Peaks at 6495, 6702, 6919cm-1 5147 and 5060cm-1 1630 and 1685cm-1 Ca(SO4) 2H2O
Peaks at 1797 and 7082cm-1 Ca(OH)2
Splitting 1507 and 1409cm-1 CaCO3
Splitting 1213 and 1093cm-1 Quartz
Sampling
Powder
Massive sample
Thin sections
MIP
µCT
Cross section
Raman bench-top
µIR microscope
SEM-EDX
Spheric pores?
Probably hydraulic binder
Probably aerial binder
Clinker particles?
Cement
Aggregate characterization
Red particles in the binder
NHL
Aerial binder
Clinker particles?
Cement
Aerial binder
923, 937, 953, 966cm-1
Hydraulic compounds
1133, 1643-38cm-1
Ettringite
Aerial binder
835, 855-860, 620-640, 720-730, 665-680cm-1
Cement/ hydraulic phases
Aerial binder
985-990cm-1
Ettringite
yes
no
ou

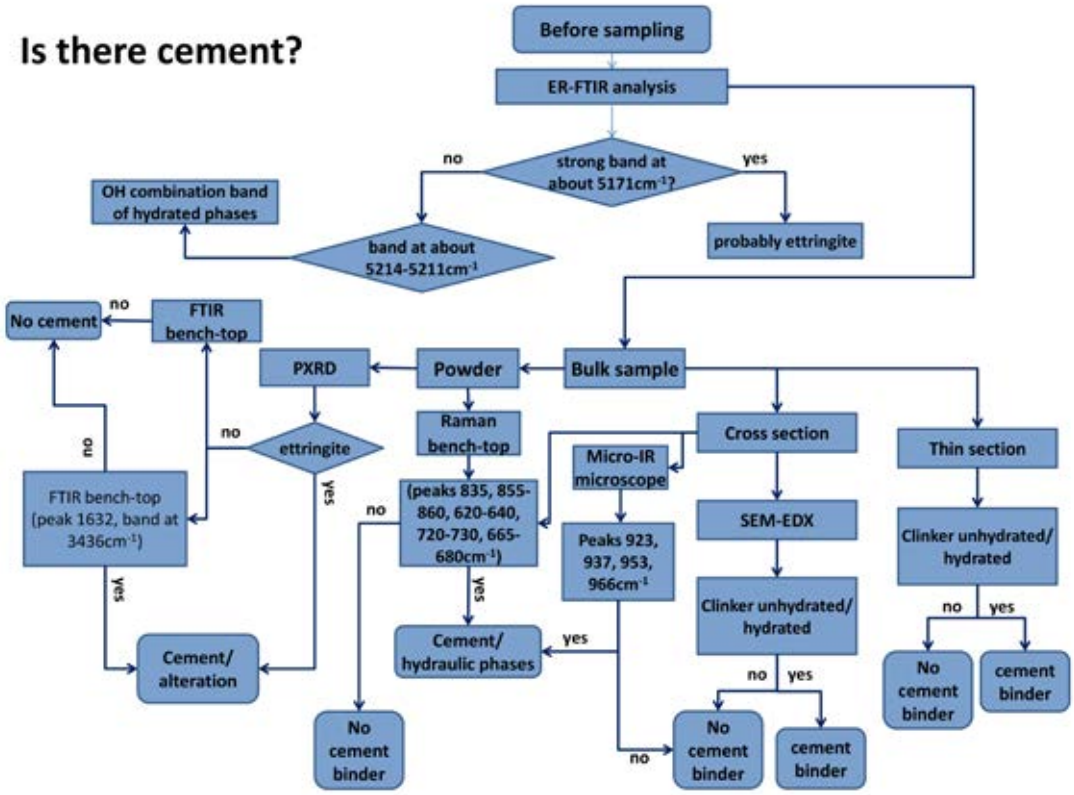

▲ *Figure 150. Analytical procedure for the identification of cement/hydraulic mortars.*

In figure 150 the analytical procedure suggested in this study to identify the presence of cement or hydraulic compounds is exemplified. In the scheme both the analyses of the cross and thin sections and the powder analysis are shown. The main diagnostic peaks are identified and they indicate the following step according to the results. The focus on mortars with cement was done because one of the most frequent questions coming from unknown samples from a heritage building is if there is cement or not (for example coming from a rejoin, or a reconstruction work). It is important to identify cement because it could damage the adjoining elements.

First of all, a screening with infrared portable instrument is recommended before sampling. Then the sample is required, to be analyzed as a massive or as a powder sample: the choice depends on the amount of sample available, the costs and the instrumentation at disposal. With the polished cross section analysis it is possible to identify clinker unhydrated relicts: in this study we found them in all the mortars and mixed mortars with cement. The same results have been obtained with the observation of thin sections too. After the powder analysis, if ettringite or calcium silicate hydrates are not detected, it does not mean that cement is not present, thus further analyses are required. FTIR analysis and Raman spectroscopy could help with the identification of hydrated products of cements. It is important to underline that the identification of hydraulic compounds in mortars with natural hydraulic lime is really hard with all the

◀ *Figure 149. Schematic analytical sequence of analysis of a bulk sample.*

techniques, and it will need further detailed studies in the future.
In this study it was possible to evaluate the application of mercury intrusion porosimetry and μ-computed tomography on a set of reference specimens for artificial building materials. From the comparison of the results of the two techniques, it is possible to see how complementary they are. Mercury intrusion porosimetry provides information on the porosity under 90μm diameter, while computed tomography gives information over 10μm. Mercury intrusion porosimetry (MIP) tends to overestimate the micro-porosity, and the computed tomography analysis tends to underestimate the micro-porosity, it is important to consider these factors while interpreting the data. Furthermore the choice between μCT or MIP depends on the questions we are trying to answer. Are we interested in micro-porosity? Macro-porosity? Or both? Consider the aim of the research, the information needed and the analytical plan?
Another key point to consider is that computed tomography has the advantage of providing information about the whole sample like the aggregate distribution or/and the presence of cracks without breaking the sample, that could be used for further investigations. In the end a 3D visualization of the results can provide helping data interpretation.
With μCT it was also possible to calculate the binder/aggregate ratio by volume. Also with the use of TG-DSC the quantitative analysis is provided, and the calculation of B/A ratio is obtained. In our specific case it is more comparable with the method we used to prepare the specimens by weight proportion (w/w) while CT tomography gives results in volume/volume. For this reason there is no direct correspondence between the results obtained, but they could anyway provide information on binder/aggregate ratio. Moreover, also the point counting performed in thin section analyses could give the ratio between pores, aggregate and binder and provide information on the distribution of the components in the sample.
Even if μCT does not provide compositional information it could suggest the presence of one or another component: for example, the sphericity of the pores could suggest the presence of a hydraulic binder. Also MIP pore size distribution can suggest the presence of one specific binder if compared to another: for example, cement tends to present low porosity while gypsum, for instance, has a very narrow pore size distribution. Anyway, these hypotheses have to be confirmed by compositional analysis.
For what concerns future developments, the comparison between different porosity measures could be improved by the evaluation of the results of other techniques such as different resolution of CT analysis, BET (Brunauer–Emmett–Teller theory), water immersion porosimetry and NMR imaging relaxometry measures. From the compositional point of view, other techniques could be added to this research. Portable instrumentations such as XRD, XRF, Raman spectroscopy have not been yet fully developed but in the future they could improve in-situ mortar analysis. The laser ablation inductively coupled plasma mass spectrometry (LA-ICP-MS) could be used on cross section either to study the stratigraphy or the border interaction between the aggregate and the binder, or to trace elements. It can provide spatial resolution thanks to the possibility of creating elemental distribution maps of the analysed area. Another technique that could improve the mortar analysis is the solid state nuclear magnetic resonance (MAS NMR), as in literature there are just few examples on the study of the hydration of cements and the gel phases that are difficult to be identified with techniques like PXRD. In the following tables (tables 49-60) are reiterated, synthesised and summarized the main advantages and drawbacks of the techniques. Moreover the quantitative analyses are an important key point when studies on mortars are carried out because it gives the quantities of the components that compose the mortars and help in the design of more compatible repair

mortars. In the future it may be useful to deepen the study of quantitative analyses with X-ray diffraction, with thermal analyses, or with X-ray fluorescence.

Powder X-ray diffraction (PXRD)

Advantages	Drawbacks
Identification of crystalline phases	No identification of gel phases
Identification of different $CaCO_3$ polymorphs.	No identification of C_2S and C_3S hydrated phases (gel).
Identification of ettringite in samples with cement and in mortars made by cement and aggregate.	difficult identification of ettringite in samples with cement in mixed mortars and samples made by two binders.
In natural hydraulic lime 3.5, the identification of hydraulic compounds is possible in the raw material.	Impossibility of distinguishing between samples with natural hydraulic lime (N) and samples with lime (C, G).
Identification or lime and gypsum when mixed together.	

Table 49. Summary of advantages and drawbacks of powder XRD analysis applied on mortars model samples.

Thermogravimetric analysis and differential scanning calorimetry (TG/DSC)

Advantages	Drawbacks
Quantitative analysis.	
Identification of the main compounds like ($CaCO_3$, $CaSO_4$ $2H_2O$, $Ca(OH)_2$).	Difficult identification of cement phases in mixed mortars.
Identification of cement phases in samples in one binder mortars.	In mixed mortars is difficult the identification of cement compouns.

Table 50. Summary of the advantages and drawbacks of thermal analysis applied to all the specimens made in this study.

Raman spectroscopy

Advantages	Drawbacks
Identification of hydraulic phases, especially if there are bands in the range: 620-740cm^{-1}.	Fluorescence.
Identification of oxides like hematite and anatase that usually are not identified by the other techniques.	Punctual analysis (a few microns); in case of inhomogeneous samples some phases could not be identified even if they are present.
Identification of unhydrated hydraulic phase also in hardened pastes.	Substances without or with a low Raman scattering are not detected.

Table 51. Summary of advantages and drawbacks of Raman spectroscopy applied to cements and natural hydraulic lime pastes and mortars.

Infrared spectroscopy (Transmission, ATR and reflection mode)

Transmission	
Advantages	**Drawbacks**
OH vibrations are more clearly shown than in ATR spectra.	After sample is mixed with KBr no other analyses are possible .
More references in literature.	
Cement identification, although if mixed it is more difficult.	
ATR	
Advantages	**Drawbacks**
The sample could be reused for other analyses.	Shift of some peaks.
Cement identification, although if mixed it is more difficult.	
Reflection	
Advantages	**Drawbacks**
No need to sample.	Splitting of some bands.
Portable.	Roughness influence into peak shape.
Two or more components of the mortars are identified, also the quartz of the aggregate.	Sensible to the composition of the first layer: problems if there is zonation.
Most of the peaks identified have the same wavenumbers as those of the peaks identified in transmission.	
Cement identification.	
The spectrum range is larger than the other two modes, so there is more information to identify the composition of the sample.	

Table 52. Summary of advantages and drawbacks of the three different infrared spectroscopies used.

Micro-infrared reflection spectroscopy (μ-FTIR)

Advantages	**Drawbacks**
Identification of hydraulic phases	It requires a carefully polished cross section, difficult to obtain for some samples
Identification of unhydrated hydraulic phase also in hardened pastes	Small areas of analysis: some phases could not be identified even if present
	The spectra often present noise, especially in the spectral range over 3500cm^{-1} and around 1650cm^{-1}

Table 53 Summary of advantages and drawbacks of μFTIR spectroscopy applied to cements and natural hydraulic lime pastes and mortars.

Thin section analysis

Advantages	Drawbacks
Identification of cement unhydrated crystals, gypsum and fly ashes.	In the mortars with two specific binders, the single components were not distinguished.
Aggregate characterization.	
It gives colour visualization of the samples	

Table 54. Summary of the advantages and drawbacks of thin sections analysis applied to all the specimens made in this study.

Microstructural analysis

μCT	
Advantages	**Drawbacks**
It can analyze the samples without destroying it.	Problem in the identification of the two binders in mixed mortars
It measure porosity over 10μm	The instruments are not diffused as MIP
3D visualization of open and closed porosity	It does not measure porosity under 10μm
It allow the analysis of the aggregate volume	
3D visualization of the aggregate and of the binder	
MIP	
Advantages	**Drawbacks**
it measure open porosity under 100μm	It is invasive and destructive (sample full of Hg)
The instruments are more diffused if compared to μCT	The samples could not be analyzed with other technique after MIP analysis.
It measure porosity under 90μm	It can damage the sample and alter the measure of porosity
	It does not measure porosity over 90μm
	It does not measure the aggregate

Table 55. Summary of advantages and drawbacks of μCT and MIP analysis applied to mortars model

Environmental scanning electron microscope (ESEM)

Advantages	**Drawbacks**
Identification of gypsum phase.	Problem in the identification of the two binders in mixed mortars.
Identification of unhydrated cement crystals in all the mortars with cements binders.	The samples have to be embedded in polished cross sections for a better identification of the components (it is a restriction for historical mortars, if there is only low quantity of sample).
Elemental map distribution.	
Identification of C_3A and/or C_4AF.	
No coating is required.	

Table 56. Summary of advantages and drawbacks of ESEM analysis applied to mortars model.

	Infrared in reflection mode (ER-FTIR)	**Infrared bench-top in transmission mode and ATR mode**	**X-Ray diffraction**	**SEM-EDX Cross sections**	**DSC – TG**	**Raman spectroscopy**
One binder	Identification of $CaCO_3$, $Ca(OH)_2$, $CaSO_4$ $2H_2O$ silicates and SiO_2. In samples with cement ettringite ($Ca_6Al_2(CaSO_4)_3$ $32(H_2O)$) and hydraulic cement is identified (by silicate bands). No clear identification of aluminates	Identification of $CaCO_3$, $Ca(OH)_2$, $CaSO_4$ $2H_2O$, silicates and SiO_2. In samples with cement binder ettringite ($Ca_6Al_2(CaSO_4)_3$ $32(H_2O)$) and tobermorite/*CSH* are identifiable. In ATR mode there is a shift in the peak position. No clear identification of the presence of aluminates in the samples.	Identification of calcite and its polymorphs, portlandite, gypsum. In samples with cement binder mineral hydraulic phases are identified: ettringite, hatrurite/larnite, mullite (in the case of CIV). *CSH* identification is not always is possible (present in a gel-like form) or tobermorite.	Performed only on hydraulic samples without the aggregate because they are the most difficult to analyze, in order to use them as reference. The identification of clinker relicts is easy. Also the interstitial phases like C_3A and C_4AF are visible. Hydration and carbonation rims are visible.	Identification of carbonate phases, gypsum, portlandite, hydrated phases of cement such as ettringite overlapped to *CSH*.	Identification of hydraulic phases of cement, both hydrated and unhydrated. Identification of calcite, portlandite, gypsum and ettringite and some oxides present in the materials as impurities. It is common to have fluorescence on the samples.

Table 57. Highlight of the main results obtained with the different techniques applied to one binder specimens.

	Infrared in reflection mode (ER-FTIR)	**Infrared bench-top in transmission mode and ATR mode**	**X-Ray diffraction**	**SEM-EDX Cross sections**	**DSC – TG**
Two binders	Identification of $CaCO_3$, $Ca(OH)_2$, $CaSO_4$ $2H_2O$ silicates and SiO_2. Difficult to distinguish the signals from one binder to the other. In samples where cement is present, ettringite is found. No clear identification of the presence of aluminates.	Identification of $CaCO_3$, $Ca(OH)_2$, $CaSO_4$ $2H_2O$, silicates and SiO_2. Difficult to distinguish the signals from one binder to the other. In samples where cement is present, ettringite is found. No clear identification of the presence of aluminates.	Identification of the main phases but impossibility to distinguish the origin of the components. In samples where one binder is made by cement, ettringite is identified in some cases.	Identification of the main element distribution and composition of the part analysed. It was not possible to distinguish the two binders mixed together. In all the samples with cement in the binder, it was possible to identify the presence of clinker relicts, in some also C_3A, C_4AF and the hydration/ carbonation rims.	The identification of the two binders is difficult; the presence of cements mixed with lime is not so evident. The presence of gypsum mixed with carbonate is well evident.

Table 58. Highlight of the main results obtained with the different techniques applied to two binder specimens.

	Infrared in reflection mode (ER-FTIR)	Infrared bench-top in transmission mode and ATR mode	X-ray diffraction	SEM-EDX Cross sections	Thin sections	DSC – TG	Raman spectroscopy
One binder and aggregate	Identification of $CaCO_3$, $Ca(OH)_2$, $CaSO_4$ $2H_2O$ silicates and SiO_2. In samples with cement binder, ettringite and bands of silicates could be related to the presence of tobermorite/*CSH*, but these latter are sometime overlapped with quartz	Identification of $CaCO_3$, $Ca(OH)_2$, $CaSO_4$ $2H_2O$, silicates and SiO_2. In samples with cement binder, ettringite and bands of silicates that could be related to the presence of tobermorite/*CSH*, but these latter are sometime overlapped with quartz.	The strongest signals are related to the aggregate (example quartz) or calcite/ magnesian calcite. Also feldspars are identified in samples with quartz sand. Presence of $CaCO_3$ polymorphs in some cases with cement binder.	Thanks to the EDX analysis on the aggregate it was possible to characterize the main elements presents in the grains and suppose the mineralogical nature of the aggregate. In all the samples with cement in the binder, it was possible to identify the presence of clinker relicts and in some also C_3A and C_4AF and the hydration / carbonation rims.	Characterization of the aggregate morphology and mineralogy. Quartz, carbonate and feldspar are identified. Characterization of pores morphology. The binder composition has been identified and when cement binder was present the clinker relicts were visible. Identification of carbonation rims.	The presence of quartz is clear. The presence of carbonate aggregate is visible, as its decomposition overlapped to the decomposition of carbonate from the binder. The aggregate carbonate decomposes at higher temperatures than the carbonate from the binder. The presence of cement is not always clear.	Identification of hydraulic phases of minerals hydrated and unhydrated. Identification of calcite, portlandite, gypsum and ettringite. It is easy to have fluorescence on the samples.

Table 59. Highlight of the main results obtained with the different techniques applied to one binder and aggregate mortars.

	Infrared in reflection mode (ER-FTIR)	**Infrared bench-top in transmission mode and ATR mode**	**X-Ray diffraction**	**SEM-EDX Cross sections**	**Thin sections**	**DSC – TG**	**Raman spectroscopy**
Two binders and aggregate	Identification of $CaCO_3$, $Ca(OH)_2$, $CaSO_4$ $2H_2O$ silicates and SiO_2. In samples where cement is present as one of the two binders, ettringite/ sulphates are identified but not in all the samples. The presence of silicates of the binder is visible, but, due to the overlapping of different bands, it is difficult the identification of a specific composition.	Identification of $CaCO_3$, $Ca(OH)_2$, $CaSO_4$ $2H_2O$, silicates and SiO_2. In samples where cement is present as one of the two binders, ettringite/sulphates are identified but not in all the samples. The presence of silicates of the binder is visible, but, due to the overlapping of different bands, it is difficult the identification of a specific composition.	Identification of the main phases, calcite/ magnesian calcite, portlandite, feldspar. Not in all the samples with the presence of cement it is possible to identify ettringite or other cement phases. It is not possible to separate the components of the aggregate from the components of the binder.	Thanks to the EDX analysis on the aggregate it was possible to characterize the main elements presents in the grains and suppose the mineralogical nature of the aggregate. In all the samples with cement in the binder, it was possible to identify the presence of clinker relicts and in some also C_3A and C_4AF and the hydration /carbonation rims.	Characterization of the aggregate morphology and mineralogy. Quartz, carbonate and feldspar are identified. Characterization of pores morphology. The identification of the two binders is difficult because they are well mixed together. When cement binder was present, the clinker relicts were visible. Identification of carbonation rims.	The presence of quartz is clear. The presence of carbonate aggregate was visible as its decomposition overlap to the decomposition of carbonate from the binder. The aggregate carbonate decomposes at higher temperatures than the carbonate from the binder. The presence of cement is not always clear.	It will be interesting to test the possibility of identification of hydraulic phases also on mixed mortars in the future developments.

Table 60. Highlight of the main results obtained with the different techniques applied to two binders and aggregate mortars.

References

[1] V.C. Farmer, ed., The Infrared Spectra of Minerals, Mineralogical Society of Great Britain and Ireland, Londan, 1974. doi:10.1180/mono-4.

[2] C. Miliani, F. Rosi, A. Daveri, B.G. Brunetti, Reflection infrared spectroscopy for the non-invasive in situ study of artists' pigments, Appl. Phys. A Mater. Sci. Process. 106 (2012) 295–307. doi:10.1007/s00339-011-6708-2.

[3] M. Vagnini, C. Miliani, L. Cartechini, P. Rocchi, B.G. Brunetti, A. Sgamellotti, FT-NIR spectroscopy for non-invasive identification of natural polymers and resins in easel paintings, in: Anal. Bioanal. Chem., 2009. doi:10.1007/s00216-009-3145-6.

[4] L. Fernández-Carrasco, D. Torrens-Martín, L.M. Morales, Sagrario Martínez-Ramírez, Infrared spectroscopy in the analysis of building and construction materials, Infrared Spectrosc. – Mater. Sci. Eng. 370 Technol. Technol. (2012) 369–382. doi:10.5772/36186.

[5] S. Gunasekaran, G. Anbalagan, S. Pandi, Raman and infrared spectra of carbonates of calcite structure, J. Raman Spectrosc. 37 (2006) 892–899. doi:10.1002/jrs.1518.

[6] M.R. Derrick, D. Stulik, J.M. Landry, Infrared Spectroscopy in Conservation Science, The Getty Conservation Institute, Los Angeles, 1999.

[7] S.N. Ghosh, S.K. Handoo, Infrared and Raman spectral studies in cement and concrete (review), Cem. Concr. Res. 10 (1980) 771–782. doi:10.1016/0008-8846(80)90005-8.

[8] D. Gastaldi, F. Canonico, E. Boccaleri, Ettringite and calcium sulfoaluminate cement: Investigation of water content by near-infrared spectroscopy, J. Mater. Sci. 44 (2009) 5788–5794. doi:10.1007/s10853-009-3812-1.

[9] L. Fernández-Carrasco, E. Vázquez, Reactions of fly ash with calcium aluminate cement and calcium sulphate, Fuel. 88 (2009) 1533–1538. doi:10.1016/j.fuel.2009.02.018.

[10] M. Torres-Carrasco, A. del Campo, M.A. de la Rubia, E. Reyes, A. Moragues, J.F. Fernández, New insights in weathering analysis of anhydrous cements by using high spectral and spatial resolution Confocal Raman Microscopy, Cem. Concr. Res. 100 (2017) 119–128. doi:10.1016/j.cemconres.2017.06.003.

[11] F. Ridi, E. Fratini, S. Milani, P. Baglioni, Near-Infrared Spectroscopy Investigation of the Water Confined in Tricalcium Silicate Pastes, J. Phys. Chem. B. 110 (2006) 16326–16331. doi:10.1021/jp060026y.

[12] D. Ergenç, L.S. Gómez-Villalba, R. Fort, Crystal development during carbonation of lime-based mortars in different environmental conditions, Mater. Charact. 142 (2018) 276–288. doi:10.1016/j.matchar.2018.05.043.

[13] M.B. Toffolo, E. Boaretto, Nucleation of aragonite upon carbonation of calcium oxide and calcium hydroxide at ambient temperatures and pressures: a new indicator of fire-related human activities, J. Archaeol. Sci. 49 (2014) 237–248. doi:10.1016/j.jas.2014.05.020.

[14] R.S.K. Lam, J.M. Charnock, A. Lennie, F.C. Meldrum, Synthesis-dependant structural variations in amorphous calcium carbonate, CrystEngComm. 9 (2007) 1226. doi:10.1039/b710895h.

[15] C.Y. Tai, F. Chen, Polymorphism of CaCO3, precipitated in a constant-composition environment, AIChE J. 44 (1998) 1790–1798. doi:10.1002/aic.690440810.

[16] V. Duchi, M. V. Giordano, M. Martini, Riesame del problema della precipitazione di calcite od aragonite da soluzioni naturali, Rend. Soc. Ital. Di Mineral. e Petrol. 34 (1978) 605–618.

[17] N. Ranjbar, C. Kuenzel, Cenospheres: A review, Fuel. 207 (2017) 1–12. doi:10.1016/j.fuel.2017.06.059.

[18] J.M. Sun, Q. Yao, X.C. Xu, Classification of micro-particles in fly ash, Dev. Chem. Eng. Miner. Process. 9 (2001) 233–238.

[19] H.F.W. Taylor, Cement chemistry. 2nd ed., 1997. doi:10.1016/S0958-9465(98)00023-7.

[20] F. Pintér, C. Gosselin, The origin, composition and early age hydration mechanisms of Austrian natural Portland cement, Cem. Concr. Res. 110 (2018) 1–12. doi:10.1016/j.cemconres.2018.04.020.

[21] J. Weber, N. Gadermayr, R. Kozłowski, D. Mucha, D. Hughes, D. Jaglin, W. Schwarz, Microstructure and mineral composition of Roman cements produced at defined calcination conditions, Mater. Charact. 58 (2007) 1217–1228. doi:10.1016/j.matchar.2007.04.025.

[22] K. Callebaut, J. Elsen, K. Van Balen, W. Viaene, Nineteenth century hydraulic restoration mortars in the Saint Michael's Church (Leuven, Belgium): Natural hydraulic lime or cement?, Cem. Concr. Res. 31 (2001) 397–403. doi:10.1016/S0008-8846(00)00499-3.

[23] E. Pecchioni, F. Fratini, E. Cantisani, Atlas of the Ancient Mortars in thin section under optical microscope, 2014.

[24] J. Weber, F. Pintér, K. Thomas, Atlas of thin sections of minerals materials in cultural heritage, (2018).

[25] M.G. Gandolfi, K. Van Landuyt, P. Taddei, E. Modena, B. Van Meerbeek, C. Prati, Environmental scanning electron microscope connected with energy dispersive X-ray analysis and Raman techniques to study proRoot mineral trioxide aggregate and calcium silicate cements in wet conditions and real time, J. Endod. 36 (2010) 851–857. doi:10.1016/j.joen.2009.12.007.

[26] A. Crumbie, G. Walenta, T. Füllmann, Where is the iron? Clinker microanalysis with XRD Rietveld, optical microscopy/point counting, Bogue and SEM-EDS techniques, Cem. Concr. Res. 36 (2006) 1542–1547. doi:10.1016/j.cemconres.2006.05.031.

[27] D. Miriello, D. Barca, A. Bloise, A. Ciarallo, G.M. Crisci, T. De Rose, C. Gattuso, F. Gazineo, M.F. La, Characterisation of archaeological mortars from Pompeii (Campania , Italy) and identi fi cation of construction phases by compositional data analysis, J. Archaeol. Sci. 37 (2010) 2207–2223. doi:10.1016/j.jas.2010.03.019.

[28] S. Martinez-Ramirez, M. Frías, C. Domingo, Micro-Raman spectroscopy in white portland cement hydration: Long-term study at room temperature, J. Raman Spectrosc. 37 (2006) 555–561. doi:10.1002/jrs.1428.

[29] M. Tarrida, M. Madon, B. Le Rolland, P. Colombet, An in-situ Raman spectroscopy study of the hydration of tricalcium silicate, Adv. Cem. Based Mater. 2 (1995) 15–20. doi:10.1016/1065-7355(95)90035-7.

[30] J. Higl, M. Köhler, M. Lindén, Confocal Raman microscopy as a non-destructive tool to study microstructure of hydrating cementitious materials, Cem. Concr. Res. 88 (2016) 136–143. doi:10.1016/j.cemconres.2016.07.005.

[31] J. Ibáñez, L. Artús, R. Cuscó, Á. López, E. Menéndez, M.C. Andrade, Hydration and carbonation of monoclinic C_2S and C_3S studied by Raman spectroscopy, J. Raman Spectrosc. 38 (2007) 61–67.

doi:10.1002/jrs.1599.

[32] D. Torréns-Martín, L. Fernández-Carrasco, S. Martínez-Ramírez, J. Ibáñez, L. Artús, T. Matschei, Raman spectroscopy of anhydrous and hydrated calcium aluminates and sulfoaluminates, J. Am. Ceram. Soc. 96 (2013) 3589–3595. doi:10.1111/jace.12535.

[33] I.G. Richardson, A. V. Girão, R. Taylor, S. Jia, Hydration of water- and alkali-activated white Portland cement pastes and blends with low-calcium pulverized fuel ash, Cem. Concr. Res. 83 (2016) 1–18. doi:10.1016/j.cemconres.2016.01.008.

[34] J. Skibsted, C. Hall, Characterization of cement minerals, cements and their reaction products at the atomic and nano scale, Cem. Concr. Res. 38 (2008) 205–225. doi:10.1016/j.cemconres.2007.09.010.

[35] K. Garbev, P. Stemmermann, L. Black, C. Breen, J. Yarwood, B. Gasharova, Structural features of C-S-H(I) and its carbonation in air-A Raman spectroscopic study. Part I: Fresh phases, J. Am. Ceram. Soc. 90 (2007) 900–907. doi:10.1111/j.1551-2916.2006.01428.x.

[36] Y. Aono, F. Matsushita, S. Shibata, Y. Hama, Nano-structural Changes of C-S-H in Hardened Cement Paste during Drying at 50°C, J. Adv. Concr. Technol. 5 (2007) 313–323. doi:10.3151/jact.5.313.

[37] S. Vecchio, A. La Gmestra, A. Frezza, C. Ferragina, The use of thermoanalytical techniques in the characterization of ancient mortars, Thermochim. Acta. 227 (1993) 215–223. doi:10.1016/0040-6031(93)80264-B.

[38] G. Biscontin, M. Pellizon Birelli, E. Zendri, Characterization of binders employed in the manufacture of Venetian historical mortars, J. Cult. Herit. 3 (2002) 31–37. doi:10.1016/S1296-2074(02)01156-1.

[39] A. Bakolas, G. Biscontin, V. Contardi, E. Franceschi, A. Moropoulou, D. Palazzi, E. Zendri, Thermoanalytical research on traditional mortars in venice, Thermochim. Acta. 269–270 (1995) 817–828. doi:10.1016/0040-6031(95)02574-X.

[40] A. Bakolas, G. Biscontin, A. Moropoulou, E. Zendri, Characterization of structural byzantine mortars by thermogravimetric analysis, Thermochim. Acta. 321 (1998) 151–160. doi:10.1016/S0040-6031(98)00454-7.

[41] A. Moropoulou, A. Bakolas, K. Bisbikou, Investigation of the technology of historic mortars, J. Cult. Herit. 1 (2000) 45–58. doi:10.1016/S1296-2074(99)00118-1.

[42] D.L. Hudson-Lamb, C.A. Strydom, J.H. Potgieter, The thermal dehydration of natural gypsum and pure calcium sulphate dihydrate (gypsum), Thermochim. Acta. 282–283 (1996) 483–492. doi:10.1016/0040-6031(95)02819-6.

[43] J. Dweck, P.M. Buchler, A.C.V. Coelho, F.K. Cartledge, Hydration of a Portland cement blended with calcium carbonate, Thermochim. Acta. 346 (2000) 105–113. doi:10.1016/S0040-6031(99)00369-X.

[44] L.M. Barcina, A. Espina, M. Sufirez, J.R. Garc, J. Rodr, Characterization of monumental carbonate stones by thermal analysis (TG, DTG and DSC), Science (80-.). 290 (1997) 181–189.

[45] International Organization for Standardization, ISO 5807:1985 Information processing — Documentation symbols and conventions for data, program and system flowcharts, program network charts and system resources charts, (1985).

CHAPTER 5

Conclusions

In conclusion, this research provides information to be interpreted and used from different perspectives. The formulation of the question to be answered is of crucial importance. In fact, this work could present different levels of interpretation depending on the end user. It may result specific for a conservator scientist who has to carry out the analysis, because it helps him/her in choosing the analytical procedure and in interpreting the results.

It could also be used by a restorer, who needs the full knowledge of the materials concerned by the conservation work; in this case the collaboration with a conservation scientist is needed, as the flow charts here designed suggest which laboratory should be contacted for the analyses and allow to better understand which result could be obtained following the different procedures. Furthermore, it helps the restorer to better comprehend the possible analyses that could be carried out and what the conservator scientist is proposing as diagnostic campaign.

The proposed protocols depend also on the typology and amount of the samples.

This research of course does not solve all the problems associated with the analyses of mortars; in fact, some crucial problems remain open, such as the difficulties in separating the aggregate signals from those from the binder, or the identification of the mixed mortars because the presence of each of the components is not always clearly determined. Nevertheless, it is important to underline that this research provides an improvement in the study of the composition of the mortars, building up the possible answers by different techniques when applied to a set of known composition specimens. Moreover, the applications of innovative and not diffused techniques such as ER-FTIR, μFTIR and Raman spectroscopy or the combination of μCT and MIP provides new data for the research community on the characterization of mortars.

If we compare our protocol proposal with those already published, we can underline some differences. First of all, we considered a wider set of analytical techniques, also those not available at the publishing time of some protocols (for example Normal 27/88). In case of RILEM [1–4], the authors divided the research in mineralogical and chemical characterization. With regards to the mineralogical characterization, they considered XRD, microscopic observations (thin sections), SEM and thermal analysis, while they reserved only a mention to infrared spectroscopy. Moreover, they reported some examples for a selection of these techniques explaining some of the results. On the other hand, in the chemical characterization they mainly focus on wet chemistry separation methods without considering infrared or Raman spectroscopy. In detail in the Report of RILEM TC 167-COM the "Characterization of old mortars with respect to their repair" in chapter 2 they divide the characterization of mortars in the following way: In-situ visual analysis and practical sampling of historic mortars, mineralogical characterization of historic mortars, chemical characterization of historic mortars, mechanical tests on mortars and assemblages and porosity of mortars. After the chemical and mineralogical characterization the committee proposed

two flow charts similar to which we produced. These flow chart are more detailed if compared to the previous one [5–7], but still lack in analytical techniques like Raman spectroscopy or portable instruments. Furthermore these flow charts are not evaluating the differences between the different modalities of application of the techniques cited (i.e. FTIR in transmission or ATR or portable). Moreover in RILEM TC 167-COM also porosity characterization is considered underling some of the limitations and advantages that we have experimented in this research,

In standard normatives such as ASTM C114, UNI 11088, UNI 11089 and UNI 11189 [8–11], the models refer only to wet chemistry methods to estimate each component of mortars. These procedures are time consuming and require a certain amount of samples that at the end of the analysis will be destructed, reducing the possibility to perform other analyses on the same samples; moreover, the analyses are destructive that could be a severe restriction in case of a procedure applied on Cultural Heritage.

In the proposal by Alessandrini et al., Normal 27/88 and Veiga et al., the authors did not create a detailed flow chart as guide for the end user [1,4,5,7,12,13], but provide just general information on the results that could be obtained with each technique; the authors did not face the problems that could occur with different typology of mortars (mortars with on single binder or mixed mortars).

In the flow charts here proposed, we are confident that some problems in the identification of the different components have been fully detailed, suggesting also an alternative analysis on the basis of the results. The protocols propose innovative analyses to improve the studies on mortars. Moreover, we suggest for the first time the use of portable instruments as the first step before sampling, in order to collect some materials information prior to the sampling step.

In conclusion the significant outcomes of this work are:

- the flow charts proposed
- the analytical method used
- the comparison between different techniques
- the evaluation of the ability of the technique in the identification of the composition
- use of portable infrared on mortar samples
- application of tomography and mercury intrusion porosimetry on mortars.

References

[1] P.B. Middendorf, J.J. Hughes, K. Callebaut, G. Baronio, I. Papayianni, Investigative methods for the characterisation of historic mortars. Part 2: Chemical characterisation, Mater. Struct. - RILEM TC 167-COM Characterisation Old Mortars with Respect to Their Repair. 38 (2005) 771–780. doi:10.1617/14282.

[2] B. Middendorf, J.J. Hughes, K. Callebaut, G. Baronio, I. Papayianni, Investigative methods for the characterisation of historic mortars—Part 1: Mineralogical characterisation, Mater. Struct. - RILEM TC 167-COM 'haracterisation Old Mortars with Respect to Their Repair. 38 (2005) 761–769. doi:10.1007/BF02479289.

[3] R.P.J. van Hees, L. Binda, I. Papayianni, Toumbakari, Characterisation and damage analysis of old mortars, Mater. Struct. 37 (2004) 644–648. doi:10.1007/BF02483293.

[4] R.T. Committee, RILEM TC 203-RHM: Repair mortars for historic masonry, Mater. Struct. 45 (2012) 1295–1302. doi:10.1617/s11527-012-9917-z.

[5] G. Alessandrini, C. Tedeschi, Le malte e la conservazione: conoscenza e normativa, Kermes La Riv. Del Restauro. (2009).

[6] Normal 27/88 : Caratterizzazione di una malta, (1988) 10.

[7] M.R. Veiga, J. Aguiar, A.S. Silva, F. Carvalho, Methodologies for characterisation and repair of mortars of ancient buildings, Hist. Constr. Int. Semin. (2001) 353–362.

[8] ASTM International, ASTM C114 - 18 - Standard Test Methods for Chemical Analysis of Hydraulic Cement, (2018). doi:10.1520/C0114-18.

[9] Ente italiano di normalizzazione, UNI 11088:2003 - Cultural heritage - Ancient mortar and mortar for restoration - Chemical characterization of a mortar - Determination of siliceous aggregate and of some soluble analytes content, (2003).

[10] Ente italiano di normazione, UNI 11089:2003 - Cultural heritage - Ancient mortar and mortar for restoration - Estimate of the composition of some kind of mortars, (2003).

[11] Ente italiano di normazione, UNI 11189 Beni culturali – Malte storiche e da restauro – Metodi di prova per la caratterizzazione chimica di una malta – Analisi chimica; Cultural heritage, Historical and repair mortars - Test methods for chemical characterisation of a mortar - Chemical, (2013) 2013.

[12] G. Martinet, B. Quenee, Proposal for useful methodology for the study of ancient mortars, in: P. Bartos, C. Groot, J. Hughes (Eds.), Int. RILEM Work. Hist. Mortars Charact. Tests Paisley, Scotland, 12th-14th May 1999, 2010: pp. 81–91.

[13] E. Goins, A new protocol for the analysis of historic cementicius material, in: P. Bartos, C. Groot, J.J. Hughes (Eds.), Int. RILEM Work. Hist. Mortars Charact. Tests, RILEM Publications SARL, 1999: pp. 71–79.

Ringraziamenti

Il dottorato è come una "scuola di vita", e penso proprio che questa frase descriva questo mio percorso. Di questa esperienza oltre alle conoscenze scientifiche e culturali che mi hanno arricchito, conservo nuove amicizie e momenti di crescita. Inoltre spero di non perdere mai la mia curiosità e l'entusiasmo per le cose che mi ha portato fin qui.

Vorrei ringraziare innanzi tutto Laura Rampazzi, Cristina Corti, Antonio Sansonetti, per avermi seguita in questo percorso, per il supporto e la fiducia datomi.

E' con estrema gratitudine che ringrazio in particolar modo Laura Rampazzi per avermi guidato, consigliato e per avermi dato questa possibilità di crescita. Ringrazio Cristina Corti, per avermi seguito nelle analisi, consigliato ed essere stata sempre disponibile nei miei confronti e avermi aiutata. Ringrazio Antonio per avermi seguito dalla mia tesi magistrale a qui, in questo nuovo percorso per avermi dato consigli e suggerimenti.

Un ringraziamento particolare va ai commissari, e ai revisori per il dottorato europeo che con i loro commenti e i loro suggerimenti hanno contribuito ad arricchire questo lavoro di ricerca.

Un grande ringraziamento va a Tim de Kock che è stato sempre presente, che mi ha supportato al meglio e da cui ho appreso molto. Ringrazio inoltre Veerle Cnudde per avermi dato la possibilità di lavorare con il suo gruppo di ricerca. Vorrei inoltre ringraziare Tim, Geraldine, Lorentz, Maxim, Arjen, Benjamin, Stefanie, Redouane, Aleksandra (Ola) per aver reso piacevole la mia permanenza a Gent e per avermi fatto sentire parte del gruppo.

Un ringraziamento particolare va a Cristina Tedeschi del Dipartimento di Ingegneria Civile e Ambientale del Politecnico di Milano per avermi seguito dalla tesi magistrale, per avermi sostenuto anche durante il dottorato e per il supporto tecnico che mi ha dato e un ringraziamento anche Mariagiovanna Taccia per il suo supporto tecnico.

Ringrazio inoltre Farkas Pintér, Roberto Bugini e Angelo Maspero per la loro disponibilità, il supporto datomi, il tempo che sono stati capaci di dedicarmi e per avermi aiutato in questo lavoro di ricerca.

Un sentito ringraziamento va anche all'Istituto di Scienze del Patrimonio Culturale del Consiglio Nazionale delle Ricerche (ISPC-CNR), in particolar modo a Claudia Conti, Alessandra Botteon ed Elena Possenti per l'aiuto nelle analisi di spettroscopia Raman e micro-FTIR svolte assieme e a Riccardo Negrotti per il supporto alle analisi di porosimetria a intrusione di mercurio. Ringrazio sinceramente il professor N. Masciocchi e la prof.ssa S. Galli per avermi permesso di compiere le analisi di diffrazione, mentre, per quanto riguarda le analisi tomografiche ringrazio il centro per le analisi tomografiche dell'Università di Gent (Gent University Centre for Tomography (UGCT)) e tutti i suoi componenti.

Vorrei anche ringraziare tutti i docenti che hanno avuto un ruolo fondamentale, nella mia formazione

sia a Milano, Parma e Como. Mentre un profondo ringraziamento va a tutti i componenti del gruppo di chimica analitica dell'Università di Como e agli altri dottorandi con cui ho condiviso momenti felici e più difficili. Ringrazio anche i compagni di viaggio in treno, perché fare due chiacchere o farsi quattro risate in treno può rendere più piacevole il viaggio.

Un ringraziamento particolare va a Francesca, Giulia, Rebecca, Kiko, Alessandro, Gregorio, Martino, Simone, Laura, Cristina, Barbara, Angelo, Eva e Monica. Un sentito ringraziamento va anche a Carola che è stata di grande aiuto durante le analisi in spettroscopia infrarossa.

Un particolare ringraziamento va ad Antonella, Ivan e Giulia che con i loro svariati contributi mi hanno seguito, con passione, in questo lavoro. Il mio percorso completo non sarebbe stato possibile senza di loro. Ringrazio in particolar modo Giulia soprattutto in quest'ultimo periodo di scrittura.

Un grazie profondo ad Andrea, per aver condiviso con me questa esperienza, per essermi stato accanto in tutti i momenti, per aver condiviso con me i mesi trascorsi all'estero per averli trasformati in un'esperienza piacevole e per averla condivisa assieme.

Vorrei inoltre ringraziare tutti, e per farlo, concludo prendendo in prestito una frase da Oscar Wilde:

"*Io non voglio cancellare il mio passato perché nel bene o nel male mi ha reso quello che sono oggi.*
Anzi, ringrazio chi mi ha fatto scoprire l'amore e il dolore,
chi mi ha amato e usato, chi mi ha detto "ti voglio bene" credendoci
e chi invece l'ha fatto solo per i suoi sporchi comodi.
Io ringrazio me stesso per aver trovato sempre la forza di rialzarmi e andare avanti, sempre".

Valentina Brunello

Acknowledgements

PhD is like a "school of life" and I really think this sentence perfectly describes this path. In addition to the scientific and cultural knowledge that enriched me, I gained new friendships and moments of growth during these years. I hope I will never lose my curiosity and enthusiasm for the things that brought me here.

First of all, I would like to thank Laura Rampazzi, Cristina Corti and Antonio Sansonetti for following me along this path, for the support and trust given to me. It is with extreme gratitude that I especially thank Laura Rampazzi for guiding, advising and for giving me this opportunity of growth. I thank Cristina Corti for following me in the analyses, advising me and always being helpful. I thank Antonio for following me from my master's thesis until now, in this new path, and for giving me advice and suggestions.

A special thanks goes to the commissioners and to the referees for the European doctorate, who, with their comments and suggestions, have contributed to enriching this research work.

A big thank-you goes to Tim de Kock who has always been present, who has supported me as best as he could and from whom I learned a lot. I also thank Veerle Cnudde for giving me the opportunity to work with her research team.
I would also like to thank Tim, Geraldine, Lorentz, Maxim, Arjen, Benjamin, Stefanie, Reduanne, Aleksandra (Ola) for making my stay in Gent pleasant and for making me feel part of the group.

A special thanks goes to Cristina Tedeschi of the Department of Civil and Environmental Engineering of the Polytechnic of Milan for having followed me since my master's thesis, for supporting me also during the PhD and for the technical support that she gave me. I would also like to thank Mariagiovanna Taccia for her technical support.

I also thank Farkas Pintér, Roberto Bugini and Angelo Maspero for their helpfulness, the support they gave me, the time they have been able to dedicate to me and for helping me in this research work.
A heartfelt thanks also goes to the Institute of Cultural Heritage Sciences of the National Research Council (ISPC-CNR), in particular to Claudia Conti, Alessandra Botteon and Elena Possenti for their help with Raman and micro-FTIR spectroscopy and the analyses carried out together; a thanks goes also to Riccardo Negrotti for his support during the mercury intrusion porosimetry analyses. I sincerely thank Professor N. Masciocchi and Prof. S. Galli for allowing me to perform the diffraction analyses, while, as regards the tomographic analyses, I would like to thank the Centre for Tomographic Analyses of the University of Gent (Gent University Center for Tomography (UGCT)) and all its members.

I would also like to thank all the teachers who have played a fundamental role in my training in Milano, Parma and Como. A deep thank-you goes to all the members of the analytical chemistry group of the University of Como and to the other PhD students with whom I shared both happy and difficult moments. I also thank my travelling friends my fellow commuters: thank you because having a chat or a laugh during our train trips could make the journey more pleasant.

A special thanks goes to Francesca, Giulia, Rebecca, Kiko, Alessandro, Gregorio, Martino, Simone, Laura, Cristina, Barbara, Angelo, Eva and Monica. A heartfelt thanks also goes to Carola who has been very helpful during the infrared spectroscopy analyses.

A special thanks goes to Antonella, Ivan and Giulia who, with their various contributions, have followed me with passion in this work. My full path would not have been possible without them. I thank Giulia especially in this last period of writing.

Last but not least, to Andrea: thank you for sharing this experience with me, for having been always with me and by my side. Thank you for sharing with me the experience of the months spent abroad and for turning them into a pleasant experience. Thank you for sharing it all together.

I would really like to thank everyone, and to do it, I conclude by borrowing a quote from Oscar Wilde:

"I don't want to erase my past because for good and for bad it has made me the man I am.
I thank those who made me discover love and grief,
those who have loved me and those who have used me,
those who told they loved me, meaning it, and those who did only to play their dirty games.
And I thank myself for finding the strength to rise again and move on, always."

Valentina Brunello